Search for BSM $A/H \rightarrow \tau\tau$ in the Fully Hadronic Decay Channel with ATLAS

Dissertation

zur Erlangung des mathematisch-naturwissenschaftlichen Doktorgrades
„Doctor of Philosophy"
der Georg-August-Universität Göttingen

im Promotionsstudiengang Physik
der Georg-August University School of Science (GAUSS)

vorgelegt von

Lino Gerlach

aus Kreuztal

Göttingen, 2021

Betreuungsausschuss

Prof. Dr. Ariane Frey
Prof. Dr. Steffen Schumann
Prof. Dr. Stan Lai

Mitglieder der Prüfungskommission:

Referent:	Prof. Dr. Stan Lai II. Physikalisches Institut, Georg-August-Universität Göttingen
Koreferentin:	Prof. Dr. Arnulf Quadt II. Physikalisches Institut, Georg-August-Universität Göttingen

Weitere Mitglieder der Prüfungskommission:

Prof. Dr. Ariane Frey
II. Physikalisches Institut, Georg-August-Universität Göttingen

Prof. Dr. Laura Covi
Institut für Theoretische Physik, Georg-August-Universität Göttingen

Prof. Dr. Steffen Schumann
Institut für Theoretische Physik, Georg-August-Universität Göttingen

Prof. Dr. Hans Hofsäss
II. Physikalisches Institut, Georg-August-Universität Göttingen

Tag der mündlichen Prüfung: 02.11.2021

Referenz: II.Physik-UniGö-Diss-2021/04

Search for BSM $A/H \to \tau\tau$ in the Fully Hadronic Decay Channel with ATLAS

Abstract

In 2012, a scalar boson was found at CERN that is consistent with the properties of the Higgs boson predicted by the Standard Model (SM) of particle physics. Some theories, in particular supersymmetric models, also predict the existence of additional heavier neutral Higgs bosons. The decays of these heavy Higgs bosons to a pair of τ-leptons can be significant because of the relatively large mass of the τ-lepton and additional effects of two-Higgs-doublet models that can enhance the coupling to down-type fermions. Searches for heavy neutral Higgs bosons, A/H, as predicted by the MSSM are performed using a 139 fb^{-1} dataset recorded at the ATLAS detector between 2015 and 2018 at a centre-of-mass energy of $\sqrt{s} = 13$ TeV. The particle is assumed to decay into a pair of τ-leptons and the all-hadronic final state is considered for this search. The results are interpreted in different benchmark scenarios, such as the hMSSM. No excess over the SM background was observed.

Contents

CHAPTER 1

Introduction

The Standard Model of particle physics (SM) is a theory describing the known fundamental constituents of nature as well as three of the four forces acting upon them. It has been tested at many independent experiments and so far, every measurement made is consistent with its predictions. With the discovery of the Higgs boson at the LHC in 2012 [1–3], every particle predicted by the SM has been experimentally detected. Nonetheless, there are observations that cannot be understood in the context of the SM. Therefore, physics *beyond the Standard Model* (BSM) must exist.

Many promising BSM theories include modifications to the Higgs sector predicting different detectable deviations from the SM, such as altered properties of the Higgs boson with a mass of 125 GeV. So far, however, all results point to this particle being consistent with the predictions of the SM. Another consequence of an extended Higgs sector could be the existence of additional (heavier) scalar particles. The coupling of these heavy Higgs bosons to other particles would depend on the particles' mass, as in the case for the SM Higgs boson whose decay into a pair of τ-leptons has the highest branching fraction of any leptonic decay mode [4]. Furthermore, the mixing of different Higgs fields in so-called two-Higgs-doublet models (parametrized by $\tan\beta$) could enhance the coupling to down-type fermions [5], which makes the decay channel with two τ-leptons very promising.

Since τ-leptons are heavier than the lightest quarks, they are the only leptons in the SM that can decay into final states with hadrons. These hadronic decays lead to signatures similar to those of pure quark-gluon-interactions, making it difficult to distinguish them from such backgrounds. For this reason, elaborate techniques are deployed for the identification of hadronic τ-lepton decays and the corresponding background estimates.

In this thesis, searches for heavy BSM Higgs bosons decaying into a pair of τ-leptons are described. Focus is put on the fully hadronic decay channel, although the combination with the semi-leptonic decay channel is also described. The considered data was taken between 2015 and 2018 by the ATLAS detector at a centre-of-mass energy of $\sqrt{s} = 13$ TeV corresponding to an integrated luminosity of 139 fb^{-1}.

The outline of this thesis is as follows. In Chapter 2, the SM is explained briefly. Afterwards, problems with the SM and how they can be addressed are elaborated upon in Chapter 3. In Chapter 4, the experimental apparatus, namely the LHC and the ATLAS detector, are discussed (including Monte Carlo generators and detector simulation) before the focus is placed on the reconstruction of particles and other objects from signatures in the detector in Chapter 5. Chapter 6 details the measurement of τ-lepton identification efficiency, an analysis that was conducted by the author of this thesis in order to qualify as a full member of the ATLAS collaboration. The analysis techniques in the search for $H \to \tau\tau$ are described in Chapter 7 before Chapter 8 lists changes to these techniques which improve the sensitivity of the search. A conclusion is drawn in Chapter 9.

CHAPTER 2

The Standard Model of particle physics

This chapter describes the theoretical foundations of the SM. As mentioned in Chapter 1, it describes a set of elementary particles and their interactions, namely three of the four known fundamental forces: the strong interaction, the weak interaction and the electromagnetic interaction [6–8]. Gravity is the only force that cannot be described in the context of the SM. Considering the fact that gravity is much weaker than the other three forces, it can be neglected in most cases, making the SM very well suited for describing physics at typical energy scales of particle accelerators. The mathematical framework in which the SM is formulated is known as quantum field theory, where particles are represented as excitations of omnipresent fields.

In the following sections, special emphasis will be put on the particle content of the SM, its internal symmetries and the Higgs mechanism. Since τ-leptons play an important role throughout this thesis, they will be described in more detail than other particles. Lastly, shortcomings of the SM which motivate the search for BSM phenomena will be discussed.

2.1. Particle content of the SM

The elementary particles predicted by the SM can be classified into two groups. The first group are the fermions with half integer values of spin, making up all known matter in the universe. The second group are the bosons with integer values of spin. They act as mediators of the fundamental forces. The Higgs boson plays a special role, being the only scalar particle in the SM with a spin of 0. The fermions can be further split into leptons that interact via the weak force and quarks which also partake in the strong force. There

are three generations of quarks and leptons alike. Each generation contains an "up"- and a "down"-type particle with a weak isospin of $+\frac{1}{2}$ and $-\frac{1}{2}$, respectively.
In the case of leptons, the three down-type particles are the electron, e^-, the muon, μ^-, and the tau lepton, τ^-, each possessing a charge of $Q = -1$. The up-type leptons are the neutrinos, denoted as ν_e, ν_μ, and ν_τ. Unlike their down-type counterparts, neutrinos are electrically neutral, meaning they exclusively interact via the weak force. The leptons are often listed as contents of three doublets in order to visualize their internal relations like so:

$$\begin{pmatrix}\nu_e \\ e^-\end{pmatrix} \begin{pmatrix}\nu_\mu \\ \mu^-\end{pmatrix} \begin{pmatrix}\nu_\tau \\ \tau^-\end{pmatrix}.$$

For quarks, the up-type particles are referred to as up quark, u, charm quark, c, and top quark, t, and have an electrical charge of $Q = +2/3$. The down type particles, down quark, d, strange quark, s, and bottom quark, b, have an electrical charge of $Q = -1/3$. Hence, applying the same grouping scheme as for the leptons, the quarks can be listed as

$$\begin{pmatrix}u \\ d\end{pmatrix} \begin{pmatrix}c \\ s\end{pmatrix} \begin{pmatrix}t \\ b\end{pmatrix}.$$

The generations of fermions only differ in their mass. With the exception of the neutrinos, the mass of the fermions increases from first to third generation. For this reason, any charged fermion will decay into its corresponding first generation version, explaining why all stable matter consists of first generation fermions: atoms are made of up- and down-quarks forming protons and neutrons in the nuclei and electrons around it.
There is an antiparticle, $\overline{f}$, for any fermion, f, of the SM. Particles and antiparticles have opposite electric charge, but the same mass.
The spin-1 bosons of the SM can be grouped by the interaction which they mediate: The photon, γ, is responsible for the electromagnetic force. The weak interaction is mediated by $W^\pm$ and Z bosons. Finally, the force carriers of the strong interaction are the eight gluons. The complete set of particles of the SM can be seen in Figure 2.1.

2.2. Gauge symmetries of the SM

Symmetries play an important role in any mathematical formulation of nature. In the following, special emphasis will be placed on how interactions between particles can be introduced by exploiting certain symmetries. As already mentioned, the SM is a quantum field theory containing fermionic and bosonic fields. Like in any quantum field theory, all relevant information about a physical system is contained in the *Lagrange density*, $\mathcal{L}$ (often referred to as *Lagrangian*), as the equations of motion can be derived from it.
A Lagrangian can be constructed so that it is invariant under certain symmetry groups. According to the Yang-Mills theory [10], this can be achieved - among others - for any special unitary group $SU(N)$ (and $U(1)$). Assume a symmetry group with transformations of the form $U = e^{ig\theta^a T_a}$, where T_a are the generators fulfilling the commutation

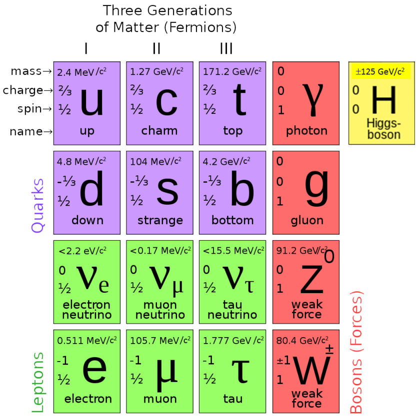

Figure 2.1.: Particle content of the SM [9].

relations $[T_b, T_c] = i f^a_{bc} T_a$ and f^a_{bc} are called the *anti-symmetric structure constants*. In order for $\mathcal{L}$ to be invariant under the transformation $\psi \to U\psi$, the covariant derivative must take the form

$$\partial_\mu \to D_\mu := \partial_\mu + igA^a_\mu T_a, \tag{2.1}$$

where g is referred to as the *coupling constant*. The number of newly introduced vector fields A^a_μ corresponds to the number of generators of the respective symmetry group. A field tensor has to be defined as

$$F^a_{\mu\nu} = \partial_\mu A^a_\nu - \partial_\nu A^a_\mu + g f^a_{bc} A^b_\mu A^c_\nu. \tag{2.2}$$

The last term in Eq. 2.2 does not appear in the case of Abelian symmetry groups like $U(1)$, as their structure constants are zero. In the case of non-Abelian gauge groups, however, it leads to terms containing third and fourth powers of the vector fields, implying self-coupling of the latter.

When applying this procedure to create a Lagrangian that is invariant under the symmetry group $SU(2)$, one finds the Lagrangian of the weak interaction. In this case, there are three generators: the Pauli matrices, correctly predicting the existence of three gauge boson fields and phenomena such as self-interaction of these. However, this would assume the emerging bosons to be massless, contradicting the experimental findings on $W^\pm$ and Z bosons. A mechanism known as *electroweak symmetry breaking* can solve this contradiction. It is explained in more detail in Sec. 2.3. There is another caveat to the weak interaction: it only affects left-handed chiral spinors of the form $\psi_L = \frac{1}{2}(1 - \gamma^5)\psi$.

In the case of $SU(3)$, there are eight generators represented by the Gell-Mann matrices. When following the procedure, one finds the Lagrangian of the strong interaction, mediated via the eight gluons. The theory is known as *quantum chromodynamics* (QCD).

All in all, the gauge group of the SM is the unitary product group $SU(3)_C \times SU(2)_L \times U(1)_Y$, where the indices denote the charges of the three interactions, respectively. These

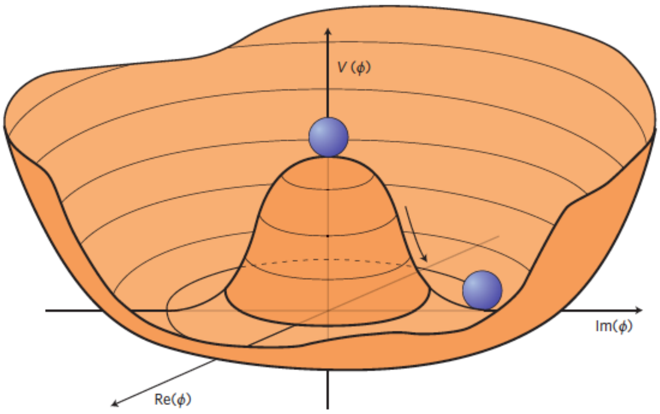

Figure 2.2.: Graphical depiction of the Higgs potential. The vacuum state is around the circle at the bottom. Since the state of lowest energy is shifted from zero, the symmetry is spontaneously broken.

are the colour charge of the strong interaction, C and two charges that emerge from the electroweak combination: the weak isospin, L, and the hypercharge, Y. Furthermore, the gauge group of the SM is *renormalizable* [11, 12]. It is a crucial property which not every local gauge theory possesses, allowing for qualitative statements by avoiding divergencies.

2.3. Electroweak symmetry breaking

If the electroweak symmetry of the SM was unbroken, the gauge fields of the electroweak force, $W^{1,2,3}$ and B^0, would be in a one-to-one correspondence with massless particles. Since $m(W^{\pm}) = 80.385 \pm 0.015$ GeV and $m(Z) = 91.1876 \pm 0.0021$ GeV [9], this is evidently not the case. Introducing explicit mass terms to the Lagrangian would, however, spoil the local gauge invariance of the SM. This problem can be solved by the Brout-Englert-Higgs (BEH) mechanism [13–15], or the Higgs mechanism for short. At its core lies the idea that the electroweak symmetry is broken. To achieve this, a new complex scalar $SU(2)$ doublet field, ϕ, with a hypercharge of $Y_\phi = 1$ is introduced:

$$\phi = \begin{pmatrix} \phi^+ \\ \phi^0 \end{pmatrix} = \frac{1}{\sqrt{2}} \begin{pmatrix} \phi_1 + i\phi_2 \\ \phi_3 + i\phi_4 \end{pmatrix}.$$

This is called the Higgs field. According to the procedure described in Section 2.2, a Lagrangian that is invariant under local transformations of the $U(1) \times SU(2)$ group can be constructed from this:

$$\mathcal{L}_{\text{Higgs}}^{\text{kinetic}} = (D_\mu \phi)^\dagger (D^\mu \phi), \tag{2.3}$$

where the covariant derivative must take the form

$$D_\mu = \partial_\mu + g\frac{\sigma_a}{2}W_\mu^a + ig'\frac{1}{2}B_\mu.$$

In order to break the symmetry, a potential is introduced to the Lagrangian:

$$\mathcal{L}_{\text{Higgs}} = (D_\mu\phi)^\dagger(D^\mu\phi) - V(\phi), \tag{2.4}$$

where $V(\phi)$ is defined as

$$V(\phi) = \mu^2\phi^\dagger\phi + \lambda(\phi^\dagger\phi)^2,$$

and $\lambda > 0$ is assumed to guarantee that the potential is bound from below. If $\mu^2 > 0$, $V(\phi)$ has the trivial global minimum at $\phi_i = 0$, $\forall i \in \{1,2,3,4\}$ and the symmetry is preserved. If, however, $\mu^2 < 0$, the global minimum lies instead at

$$\sum_i \phi_i^2 = -\frac{\mu^2}{\lambda} =: v^2,$$

breaking the $U(1) \times SU(2)$ symmetry. The newly introduced v is referred to as the *vacuum expectation value* (vev) of ϕ. In two dimensions, this would correspond to a ring around the centre with radius v, as it can be seen in Figure 2.2, where the shape of $V(\phi)$ is graphically displayed. For simplicity the state

$$\phi_0 := \frac{1}{\sqrt{2}}\begin{pmatrix} 0 \\ v \end{pmatrix}$$

will be considered as the ground state in the following. It can be shown that in this ground state, the Lagrangian in Eq. 2.4 is invariant under a linear combination of the hypercharge operator, Y, and the third component of the weak isospin, T^3, known as the electric charge, Q:

$$Q = T^3 + \frac{Y}{2}$$

Hence, the electroweak symmetry breaking (EWSB) breaks the $U(1) \times SU(2)$ symmetry of the electroweak interaction to create the $U(1)$ symmetry of the electromagnetic interaction:

$$U(1)_Y \times SU(2)_L \xrightarrow{\text{EWSB}} U(1)_{EM}.$$

ϕ can be expressed as an expansion around ϕ_0 by the amount v:

$$\phi = \frac{1}{\sqrt{2}}\begin{pmatrix} 0 \\ v + h \end{pmatrix},$$

a choice that is known as the *unitary gauge*. Applying the covariant derivative as defined in Eq. 2.1 and exploiting the algebra of the Pauli matrices, one finds

$$D_\mu \phi = \frac{1}{2\sqrt{2}} \begin{pmatrix} ig(W_\mu^1 - iW_\mu^2) \\ 2\partial_\mu - igW_\mu^3 + ig'B_\mu \end{pmatrix} (v+h).$$

From this, the Higgs Lagrangian as defined in Eq. 2.4 can be derived, containing the following mass terms (terms of the form $\frac{1}{2}m^2 F_\mu F^\mu$) proportional to v^2:

$$\mathcal{L}^m_{\text{Higgs}} = \frac{v^2}{8} \left[g^2 (W_\mu^1 + iW_\mu^2)(W^{1\mu} - iW^{2\mu}) + (gW_\mu^3 - g'B_\mu)(gW^{3\mu} - g'B^\mu) \right]. \tag{2.5}$$

New fields $W_\mu^\pm$, Z_μ, and A_μ can be defined as linear mixtures of the ones above to make the mass terms appear in a more direct manner:

$$W_\mu^\pm := \frac{W_\mu^1 \mp iW_\mu^2}{\sqrt{2}}; \qquad Z_\mu := \frac{gW_\mu^3 - g'B_\mu}{\sqrt{g^2 + g'^2}}; \qquad A_\mu := \frac{g'W_\mu^3 + gB_\mu}{\sqrt{g^2 + g'^2}}, \tag{2.6}$$

so that the following mass terms arise:

$$\mathcal{L}^{m\prime}_{\text{Higgs}} = \frac{1}{2}\left(\frac{vg}{2}\right)^2 (W_\mu^- W^{-\mu} + W_\mu^+ W^{+\mu}) + \frac{1}{2}\left(\frac{v\sqrt{g^2 + g'^2}}{2}\right)^2 Z_\mu Z^\mu.$$

From this, the following masses for the fields can be read off:

$$m_{W^\pm} = \frac{vg}{2}; \qquad m_Z = \frac{v\sqrt{g^2 + g'^2}}{2}; \qquad m_A = 0.$$

The Lagrangian also contains terms of the form VVh and $VVhh$, where V can be either $W^\pm$ or Z. These give rise to triple and quartic couplings between Higgs bosons and the gauge bosons. It can be shown that the coupling of a gauge boson to the Higgs boson is proportional to the gauge boson's mass. Furthermore, the Higgs boson can interact with itself. This can be seen by developing the Higgs potential around its minimum:

$$V(h) = \lambda v^2 h^2 + \lambda v h^3 + \frac{\lambda}{4} h^4.$$

From this, the mass of the Higgs boson, $m_h^2 = 2\lambda v^2$, as well as the coupling strengths for the triple ($g_{hhh} = \lambda v$) and quartic self-interaction ($g_{hhhh} = \frac{\lambda}{4}$) can be read off. The whole procedure of electroweak symmetry breaking is described by four parameters: g, g', μ, and λ, which have all been determined experimentally. In particular, from measurements of m_W and g, the vacuum expectation of the Higgs field is found to be [9]

$$v = 246 \text{ GeV}. \tag{2.7}$$

What is left to explain is why fermions can possess a non-vanishing mass. Adding explicit mass terms of the form

$$-m_f \overline{\psi}\psi = -m_f(\overline{\psi}_R \psi_L + \overline{\psi}_L \psi_R)$$

would break the gauge invariance of the Lagrangian due to the different transformation behaviours of ψ_L ($SU(2)$ doublet) and ψ_R (singlet). However, terms of the form $\overline{\psi}_L\phi$ are invariant as left-handed spinors and the Higgs field transforms in the same way. Hence, an invariant Lagrangian of the form

$$\mathcal{L}_{\text{Yukawa}} = -g_f(\overline{\psi}_L\phi\ \psi_R + \overline{\psi}_R\phi^\dagger\psi_L)$$

can be constructed. This is known as the Yukawa mechanism. In the case of down-type fermions, inserting the unitary gauge leads to

$$\mathcal{L}_{\text{Yukawa}} = -\frac{g_f v}{\sqrt{2}}(\overline{\psi}_L\psi_R + \overline{\psi}_R\psi_L) - \frac{g_f h}{\sqrt{2}}(\overline{\psi}_L\psi_R + \overline{\psi}_R\psi_L),$$

resembling two explicit mass terms. For up-type fermions, a different gauge of the Higgs field has to be chosen, but the rest is analogous. To make the mass terms obvious, the free coupling constant is chosen to be

$$g_f = \sqrt{2}\frac{m_f}{v}, \tag{2.8}$$

resulting in

$$\mathcal{L}_{\text{Yukawa}} = -m_f\overline{\psi}\psi - \frac{m_f}{v}\overline{\psi}\psi h.$$

The first term shows that massless fermion fields acquire a mass by interacting with the non-vanishing vacuum expectation value of the Higgs field. The second term implies that fermions couple to the Higgs boson and that the coupling strength is proportional to the fermion's mass.

2.4. The Higgs sector of the SM

At the conditions of the LHC, the four leading production mechanisms of the Higgs boson are gluon-gluon fusion (ggF), vector-boson fusion (VBF), associated production with a vector boson (VH, sometimes referred to as *Higgs-Strahlung*) and associated production with top quarks (ttH). The corresponding Feynman diagrams can be seen in Figure 2.3. Since the Higgs boson couples exclusively to massive particles, the ggF production is only possible via a loop. The dominant contribution in this loop arises from top quarks and all vertices in the leading four production processes involve a top quark or a weak gauge boson (W or Z) because of their high mass. For the same reason, decays of the Higgs boson into final states with heavy particles have a high branching ratio. Since the b quark is the heaviest particle in the SM that is less than half the Higgs boson's mass, the $h \to b\bar{b}$ channel has the largest branching ratio at 0.582 [9]. The relative contribution of each of the production processes and the branching fractions of its decay modes depend on the Higgs boson's mass, as can be seen in Figure 2.4. These dependencies are important for this thesis since a search for heavier versions of the Higgs boson is performed.

Figure 2.3.: Feynman diagrams of the four leading production mechanism of the Higgs boson at the LHC: *a*) gluon-gluon fusion (ggF), *b*) vector-boson fusion (VBF), *c*) associated production with a vector boson (VH) and *d*) associated production with top quarks (ttH).

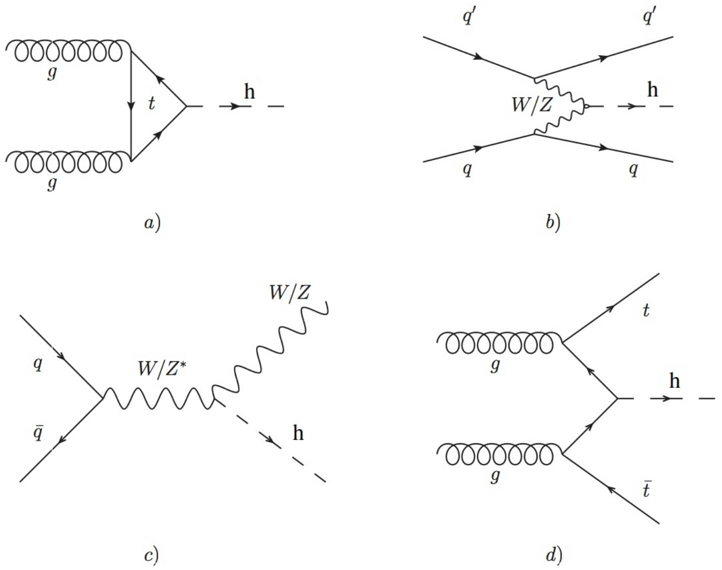

Experimental results on various production cross sections and decay branching ratios of the Higgs boson are summarized in Figure 2.5. So far, all findings are compatible with the predictions of the SM. The data also supports the hypothesis that the Higgs boson has a spin of zero and an even parity [16, 17].

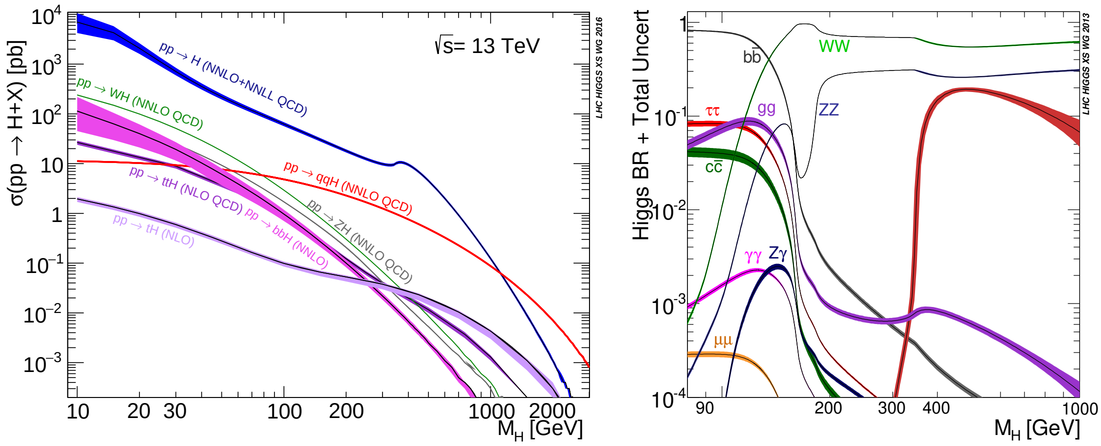

Figure 2.4.: Higgs boson production cross sections and decay branching ratios at $\sqrt{s} = 13$ TeV [18].

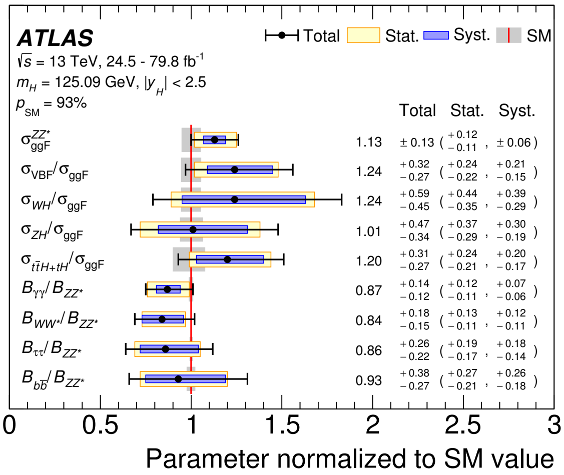

Figure 2.5.: Results of a simultaneous fit for σ^{ZZ}_{ggF}, $\sigma_{VBF}/\sigma_{ggF}$, σ_{WH}/σ_{ggF} σ_{ZH}/σ_{ggF}, $\sigma_{t\bar{t}H+tH}/\sigma_{ggF}$, $B_{\gamma\gamma}/B_{ZZ}$, B_{WW}/B_{ZZ}, $B_{\tau\tau}/B_{ZZ}$, and B_{bb}/B_{ZZ}. The fit results are normalized to the SM predictions. The black error bars, blue boxes and yellow boxes show the total, systematic, and statistical uncertainties in the measurements, respectively. The gray bands show the theory uncertainties in the predictions [19].

2.5. The τ-Lepton

The τ-lepton is the heaviest lepton in the SM. For this reason, it plays an important role when investigating the Higgs sector since the Higgs boson's coupling to a fermion depends linearly on the fermion's mass. According to some BSM theories, hypothetical heavy Higgs bosons could have an enhanced coupling to down-type fermions, giving further motivation for searches for final states containing τ-leptons.
With a mass of 1776.86 ± 0.12 MeV [9], τ-leptons are the only leptons in the SM that are heavier than first generation quarks. Therefore, they are the only leptons that can decay into hadrons. Although a ν_τ is produced in every case, these decays are referred to as *hadronic*. Hadronic decays contain mainly pions in the final state and make up 64.79 ± 0.14 % of all τ-lepton decays. Because of charge conservation, there must be an odd number of charged hadrons in the final state. The number of neutral hadrons can vary between 0 and 11 with decreasing probability. Decays with one charged hadron (one-prong, 1P) or three charged hadrons (three-prong, 3P) have a total branching fraction of 49.04 ± 0.10 % and 15.21 ± 0.06 %, respectively [9]. Decays with five or more charged hadrons only make up 0.55 ± 0.13 % of all τ-lepton decays. The other two decay channels are purely leptonic. Because of lepton universality, the electron ($\nu_\tau \overline{\nu_e} e$) and muon final states ($\nu_\tau \overline{\nu_\mu} \mu$) occur with very similar branching fractions of 17.82 ± 0.04 and 17.39 ± 0.04, respectively. Figure 2.6 shows an overview of the four leading decay modes and their branching fractions.

Figure 2.6.: Branching fractions of τ-lepton decays (rounded) [9].

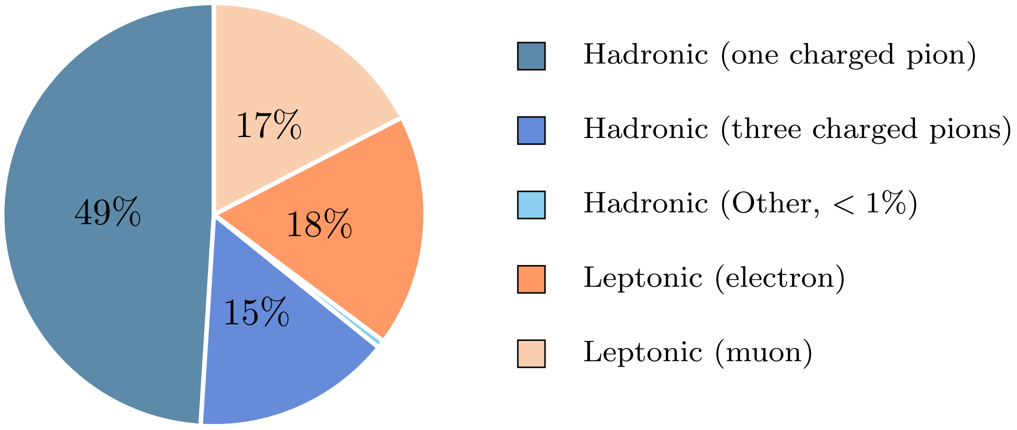

With an average lifetime of $(2.903 \pm 0.005) \cdot 10^{-13}$ s, τ-leptons have a proper decay length of roughly 87 μm and usually decay before possibly being detected. Therefore, the reconstruction and identification of hadronic τ-lepton decays are based on the decay products which form a jet-like signature in the detector as depicted in Figure 2.7. These jets are on average more narrow than those initiated by a quark or gluon. Furthermore, the origin of a jet of a hadronic τ-lepton decay is shifted from the position where the τ-lepton was created. This phenomenon is known as a *displaced vertex*. Both of the aforementioned properties are used, among others, in order to distinguish hadronic τ-lepton decays from background. The techniques and algorithms for this task are described in Section 5.5.

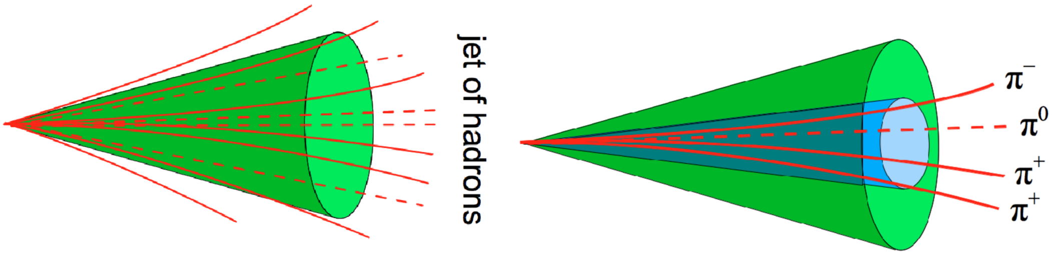

Figure 2.7.: A jet from QCD processes (left) and a jet caused by a hadronically decaying τ-lepton, which is narrower (right).

CHAPTER 3

Physics Beyond the Standard Model

As mentioned in Chapter 1, the SM is very successful at describing particle physics at typical energy scales of human-made particle colliders. With the discovery of the Higgs boson, every particle predicted by the SM has been found and vice versa. The SM has been tested experimentally in countless independent measurements, and no collider physics measurement contradicts it. However, some observations cannot be understood in the context of the SM. Therefore, physics *beyond the Standard Model* (BSM) must exist. These modifications or extensions to the SM can concern almost any part of the theoretical foundation of the SM. Emphasis will be put on BSM theories that predict the existence of additional heavy Higgs bosons or other resonances that could decay into final states with two τ-leptons and are therefore relevant for this thesis.
Firstly, a selection of problems of the SM is listed to motivate BSM theories in Section 3.1. Then, the basic concepts of Supersymmetry (SUSY) are explained as an example for a BSM theory predicting the existence of additional Higgs bosons and potentially resolving problems of the SM in Section 3.2. Lastly, Section 3.3 discusses models that predict the existence of a heavier version of the Z boson, referred to as Z', as such a particle could also decay into a di-τ final state.

3.1. Problems with the SM

The following list is a selection of problems with the SM which are relevant for this thesis. In other words: inconsistencies that could potentially be resolved by BSM theories that also predict the existence of additional Higgs bosons. These problems can be grouped into three categories: it is not valid above a certain energy scale (Quantum Gravity), it is inconsistent with astronomical observations (Dark Matter), and its free parameters must have finely tuned values to match the observations (hierarchy problem).

3.1.1. Quantum Gravity and the Planck Scale

The fact that the SM only incorporates three of the four known fundamental forces can be attributed to the incompatibility of general relativity with quantum mechanics. Designing a quantum field approach analogous to that of the other three forces of the SM is unfeasible since gravity is perturbatively not renormalizable [20]. However, the fact that the SM cannot incorporate gravity only becomes prominent when investigating particles at energy scales where the spatial resolution is close to the particle's Schwarzschild radius, $r = \frac{2Gm}{c^2}$ [21]. To estimate where this scale lies, consider the Heisenberg uncertainty principle in the form

$$\Delta x \cdot \Delta p \geq \frac{\hbar}{2}. \tag{3.1}$$

Restricting the particle's position increases its momentum and, with it, the corresponding energy and mass. For a sufficiently small Δx, the particle's mass will be high enough to form a black hole. The value of Δx, where the local restriction of a particle is equal to its Schwarzschild radius, is known as Planck length:

$$l_{Pl} := \sqrt{\frac{G\hbar}{c^3}} \approx 1.6 \cdot 10^{-35} \text{ m}. \tag{3.2}$$

The Planck energy, $E_{Pl} \approx 10^{19}$ GeV, is defined as the corresponding energy uncertainty. Simply put, the SM does not hold for processes at energies above 10^{19} GeV since a quantum mechanical treatment of gravity would be needed in that case. Theoretical concepts that could provide a framework to explain quantum gravity often assume SUSY (see Section 3.2) to be realized in nature, such as superstring theory [22].

3.1.2. Dark Matter

Already in the first half of the 20-th century, astronomers discovered that the rotational velocities of stars as a function of their distance to the centre of the galaxy (galaxy rotation curves) are not compatible with predictions from general relativity and common assumptions about the distribution of mass within galaxies [23,24]. There are two possible explanations for this ostensible contradiction: the theory of general relativity is wrong, or the mass distribution within galaxies is significantly different than assumed. The search for alternatives to general relativity is currently a broad research topic [25] but will be neglected in the following.

Different scenarios concerning how matter could be distributed within galaxies can be assumed to predict the corresponding galaxy rotation curves. However, none of these scenarios can explain the observed behaviour. This led to the proposal that stars, gas clouds, black holes, and other known objects are not the only contributors to the galaxy's

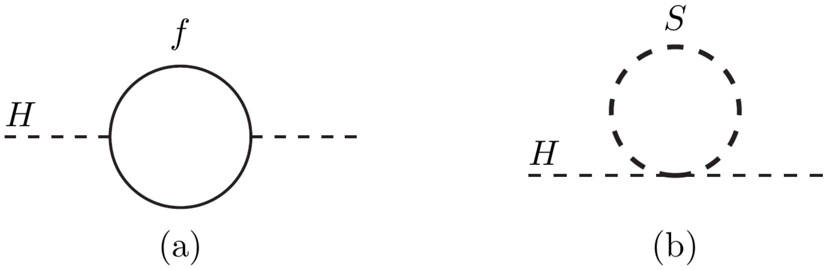

Figure 3.1.: One-loop quantum corrections to the Higgs squared mass parameter m_H^2, due to (a) a Dirac fermion f, and (b) a scalar S [29].

mass. Thus, there must be some invisible (*dark*) matter that predominantly interacts gravitationally. By now, more observations hint at the existence of Dark Matter in the context of gravitational lensing [26] and the cosmic microwave background [27]. From cosmological observations, one can estimate that Dark Matter makes up roughly 85% of all matter in the universe [28].
If SUSY occurs in nature, it could explain Dark Matter by predicting a stable particle that exclusively interacts gravitationally with the particles of the SM.

3.1.3. Hierarchy problem

Another issue for which the SM provides no satisfying explanation is the so-called *hierarchy* problem. It refers to the fact that the value of the Higgs boson mass is not at a natural scale. During its calculation, fermionic loop corrections on the Higgs mass need to be taken into account up to the highest energy scale for which the theory holds (cut-off scale or ultraviolet limit), which, in the case of the SM, is the Planck Energy, E_{Pl} (see Section 3.1.1).

$$\Delta m_H^2 \approx \int^{E_{Pl}} d^4 f(k, \text{external momenta}).$$

The observed mass of roughly 125 GeV can only be obtained by fine-tuning the squared mass by a value Δm_H^2 which depends quadratically on the cut-off scale:

$$\Delta m_H^2 = \frac{\lambda_f^2}{16\pi^2}[-2E_{Pl}^2 + ...] \propto E_{Pl}^2 \approx 10^{38}\ \text{GeV}^2.$$

This leads to fine-tuning that is of a much larger order than the observed mass. Analogous phenomena indicate a deeper physical principle behind the fine tuned value of m_H. In the case of the hierarchy problem, the realization of SUSY would lead to bosonic fields that contribute to the loop corrections with the same absolute value but the opposite sign so that their effects cancel out and only minor fine-tuning is needed. In this case, the theory's prediction of m_H does not have to be fine-tuned so strongly to match the experimental observations. Figure 3.1 schematically depicts such quantum loop contributions of a Dirac fermion and a scalar separately.

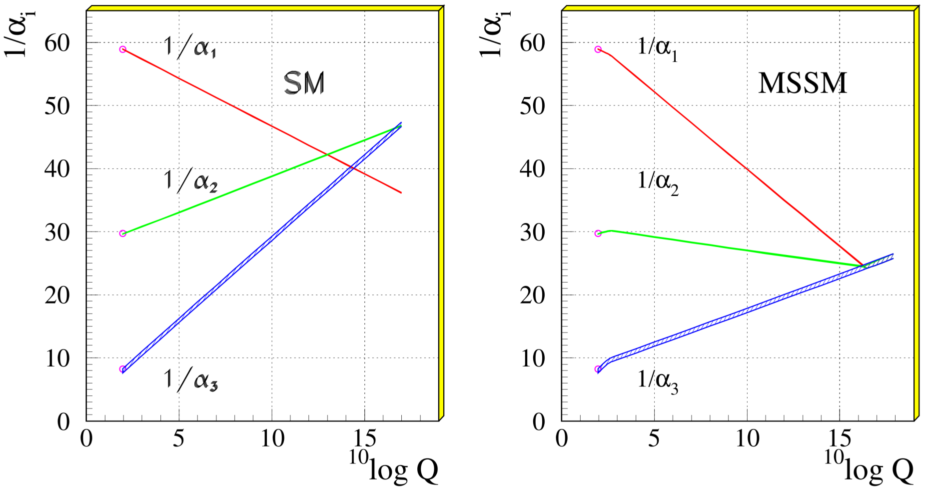

Figure 3.2.: Unification of the running coupling constants in the SM and the MSSM [31].

3.1.4. Gauge-coupling unification

Since in the SM, the electromagnetic and the weak force can be unified in the context of the electroweak theory, many theorists believe that a single, unified theory can describe all three forces of the SM at high energies. Such models are often referred to as Grand Unified Theories (GUT) [30]. One necessary prerequisite for a GUT is the unification of the three coupling constants, determined by the renormalization group equation. In the case of the SM, however, the coupling constants do not meet in one point. If SUSY occurs in nature, the coupling constants would meet at one point, laying the foundation for a possible GUT. Figure 3.2 shows the different behaviours of the coupling constants as a function of the logarithmic energy scale, log Q.

3.2. Supersymmetry

A very promising BSM theoretical framework that could solve the problems of the SM mentioned in Section 3.1 is SUSY. It predicts undiscovered supersymmetric partners for the particles of the SM and will be discussed in the following.

3.2.1. SUSY and its Generators

SUSY is a symmetry between bosonic and fermionic fields. Its generators, which will be denoted as Q and $Q^\dagger$ in the following, turn fermionic states into bosonic ones and vice versa:

$$Q\,|Boson\rangle = |Fermion\rangle \qquad Q\,|Fermion\rangle = |Boson\rangle\,.$$

Since they change the spin of particles by half-integer values, they must act as fermionic operators and anti-commute. The Haag-Łopuszański-Sohnius-Theorem [32] states that SUSY is the only nontrivial extension to the symmetry group of space-time translations, the Poincaré group with generators P^μ. Other interesting implications of this theorem concern the SUSY generators themselves. They must act as spin-1/2 objects (e.g. spin-3/2 is ruled out) and fulfill the following schematic algebra [29]:

$$\begin{aligned}\{Q, Q^\dagger\} &= P^\mu \\ \{Q, Q\} &= \{Q^\dagger, Q^\dagger\} = 0 \\ [P^\mu, Q] &= [P^\mu, Q^\dagger] = 0.\end{aligned}$$

It should be noted that SUSY provides the only possible way to combine an internal symmetry with the Poincaré group in a nontrivial way, which is further motivation for this model.

The irreducible representations of the SUSY algebra are called *supermultiplets*. Bosonic and fermionic fields that are related to each other by Q and $Q^\dagger$ are known as *superpartners*. Since Q and $Q^\dagger$ commute with any other generator of gauge transformation, they leave the corresponding quantum numbers untouched. Therefore, superpartners must have the same electric charge, weak isospin, and colour degrees of freedom. In particular, $[P^\mu, Q] = [P^\mu, Q^\dagger] = 0$ leads to $[P^2, Q] = [P^2, Q^\dagger] = 0$. Considering $p^\mu p_\mu = m^2$, this implies that, if SUSY were unbroken, superpartners would have the same mass.

3.2.2. Minimal Supersymmetric Standard Model

In any supersymmetric extension of the SM, each fundamental particle is in either a chiral or a gauge supermultiplet, and each fundamental particle must have a superpartner with spin differing by 1/2 unit. The *Minimal Supersymmteric Standard Model* (MSSM) is the supersymmetric theory that predicts the fewest additional particles to the SM. It assumes two Higgs doublets and one superpartner (sparticle) for each particle in the SM. The resulting field content can be seen in Figure 3.3. Since the Higgs boson is a scalar boson, it must reside in a chiral supermultiplet. One chiral supermultiplet would, however, lead to the electroweak gauge symmetry suffering from a gauge anomaly. To prevent the anomaly from occurring, the so-called *anomaly trace* must satisfy $\mathrm{Tr}[T_3^2 Y] = \mathrm{Tr}[Y^3] = 0$, where T_3 and Y are the third component of the weak isospin and the hypercharge, respectively. In the SM, this condition is fulfilled when summing over all fields with non-vanishing hypercharge. Adding a single fermionic partner of the Higgs boson with $|Y| = \frac{1}{2}$ would, however, spoil this condition. Therefore, two Higgs doublets with $Y = \pm\frac{1}{2}$, respectively, are needed for their contributions in the anomaly trace to cancel out [29].

Furthermore, the superpotential, whose derivatives occur in the Lagrange density, must be a holomorphic function of the included fields in any supersymmetric theory[1]. Therefore, terms like $H_u^* H_u$ or $H_d^* H_d$ analogous to the Higgs mass term in the Lagrange density

---

[1] A function $f(z, z^*) : U \to \mathbb{C}$ is holomorphic if and only if it is differentiable and $\frac{\partial f}{\partial z^*} = 0$ holds.

Names		spin 0	spin 1/2
squarks, quarks	Q	$(\widetilde{u}_L\ \ \widetilde{d}_L)$	$(u_L\ \ d_L)$
(×3 families)	$\overline{u}$	$\widetilde{u}_R^*$	$u_R^\dagger$
	$\overline{d}$	$\widetilde{d}_R^*$	$d_R^\dagger$
sleptons, leptons	L	$(\widetilde{\nu}\ \ \widetilde{e}_L)$	$(\nu\ \ e_L)$
(×3 families)	$\overline{e}$	$\widetilde{e}_R^*$	$e_R^\dagger$
Higgs, higgsinos	H_u	$(H_u^+\ \ H_u^0)$	$(\widetilde{H}_u^+\ \ \widetilde{H}_u^0)$
	H_d	$(H_d^0\ \ H_d^-)$	$(\widetilde{H}_d^0\ \ \widetilde{H}_d^-)$

Names	spin 1/2	spin 1
gluino, gluon	$\widetilde{g}$	g
winos, W bosons	$\widetilde{W}^\pm\ \ \widetilde{W}^0$	$W^\pm\ \ W^0$
bino, B boson	$\widetilde{B}^0$	B^0

Figure 3.3.: Field content of the MSSM [29]. Like in the SM, fields can mix to form mass eigenstates that are observed as particles.

of the SM are forbidden. Instead,

$$\mu H_u H_d \tag{3.3}$$

appears in the MSSM Lagrangian as a mass term. For the same reason, Yukawa coupling terms in the MSSM Lagrangian like $\bar{u}QH_u$ cannot be replaced by terms such as $\bar{u}QH_d*$. Therefore, only a $Y = +1/2$ Higgs field (H_u) can Yukawa couple to up-type quarks, and only a $Y = -1/2$ Higgs field (H_d) can couple to down-type quarks and charged leptons. This is why there must be two Higgs supermultiplets in the MSSM.

Another interesting property of the MSSM is the behaviour of the coupling constants. If the masses of the sparticles are in the order of 1 TeV, the renormalization group allows them to meet in one point, giving way to a possible unification of all three forces [30]. This is displayed in Figure 3.2.

3.2.3. SUSY Breaking and the MSSM Higgs Sector

If SUSY were unbroken, superpartners would have the identical mass, and sparticles would have been found already. Therefore, SUSY must be a broken symmetry, most likely spontaneously broken, as in the case of the electroweak symmetry. This means that $\mathcal{L}$ is invariant, but the vacuum state is not, hiding the symmetry at low energies. This symmetry breaking can be achieved by extending the theory by new particles and interactions at very high mass scales. However, there is no consensus on how this should

be done precisely and a variety of different mechanisms were proposed (e.g. GMSB, SUGRA [29]).
Like in the SM, the symmetry breaking leads to splitting and mixing between gauge and mass eigenstates. As mentioned above, the Higgs scalar fields consist of two complex $\mathrm{SU}(2)_L$ doublets, which lead to eight degrees of freedom. Electroweak symmetry breaking creates three Goldstone bosons $G^0, G^\pm$, which become the longitudinal modes of Z^0 and $W^\pm$. The remaining five Higgs mass eigenstates are:

- Two CP-even neutral scalars h^0, H^0,
- One CP-odd neutral scalar A^0,
- One charged scalar H^+ and its conjugate H^-.

3.2.4. R-parity

In the MSSM, the Lagrange density can be extended by additional gauge invariant terms. These will, however, violate either Baryon number (B) or Lepton number (L) conservation, which would lead to proton decay. Since this has not been experimentally observed yet, an additional mechanism is needed to explain this behaviour. In the SM, Lepton and Baryon number conservation is not introduced as a fundamental principle but rather follows from the properties of the interactions. To keep the MSSM consistent with experimental results, a new conserved quantum number, R-parity, is introduced according to

$$P_R = (-1)^{3(B-L)+2s}. \tag{3.4}$$

Particles of the SM will have $P_R = 1$, whereas their superpartners will have $P_R = -1$. This explains B and L conservation and makes the lightest supersymmetric particle (LSP) stable, which is crucial when considering it as a candidate for Dark Matter.

3.2.5. MSSM parameter space

The most general form of the MSSM has 120 additional free parameters compared to the SM. The vast majority of which (105 out of 120) arise from SUSY breaking [29]. The high number of free parameters makes it nearly impossible to exclude the theory in general. However, many of these parameters could lead to effects such as flavour changing neutral currents or new sources of CP violation. None of these effects have been observed, tightly constraining many parameters of the MSSM. Designing the theory to make the LSP a candidate for Dark Matter applies further restrictions. It must be a neutralino (electrically neutral mixture of $\tilde{W}$ and $\tilde{B}$ fields) or gravitino, and its mass must lie within a certain range [34]. This narrows down the free parameter space of the MSSM to a degree, where only two non-SM parameters are necessary to describe the Higgs sector at tree level. These are often chosen to be

- m_A, the mass of the CP-odd neutral scalar,

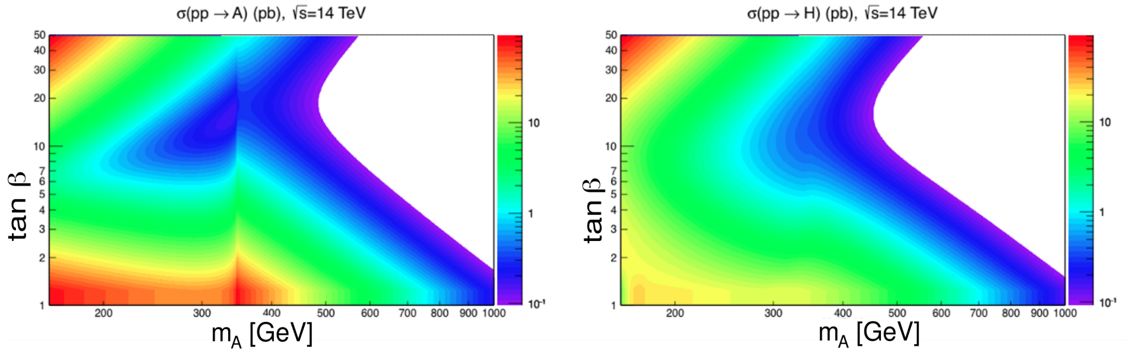

Figure 3.4.: Predicted production cross section of the heavy Higgs bosons A (left) and H (right) for proton-proton collisions at $\sqrt{s} = 14$ TeV in the $\tan\beta$–m_A plane. Gluon-gluon-fusion and b-associated production have been considered [33].

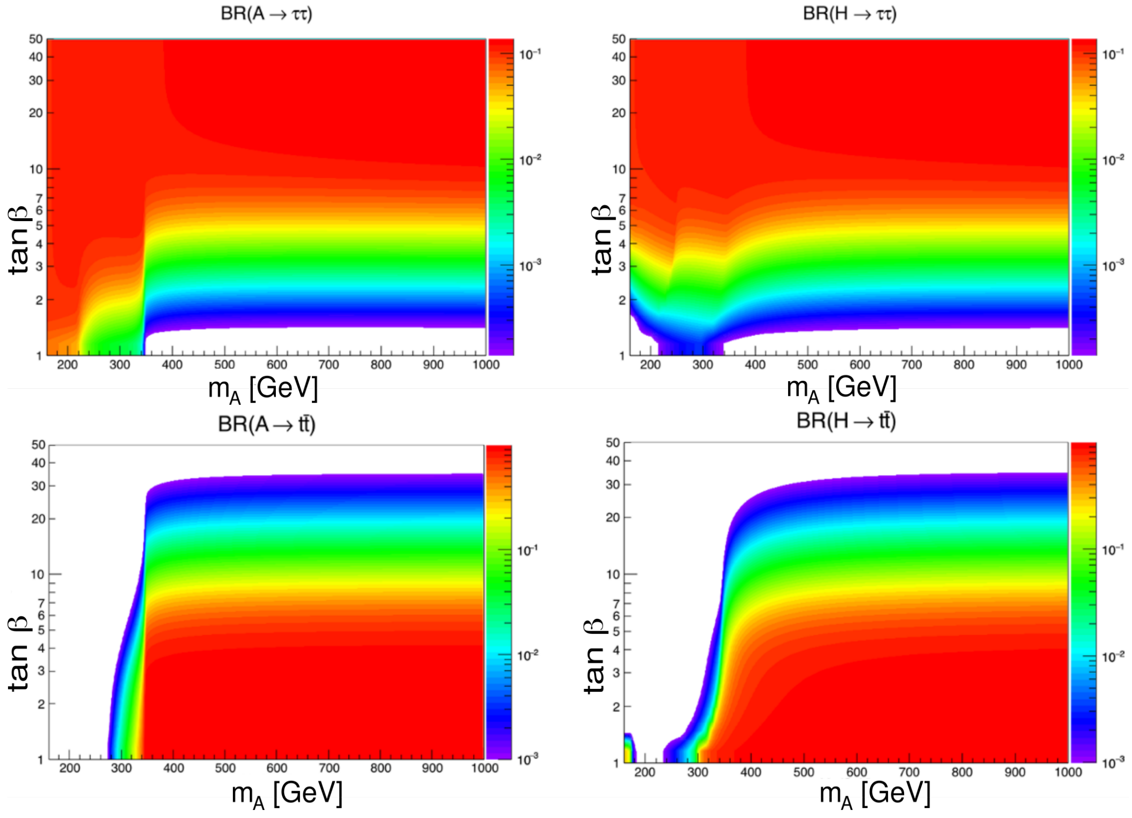

Figure 3.5.: Predicted branching ratios of the heavy Higgs bosons A (left) and H (right) into τ-leptons (top) and top quarks (bottom) in the $\tan\beta$–m_A plane [33].

- $\tan\beta = \frac{<H_u^0>}{<H_d^0>}$, the ratio of the two Higgs vacuum expectation values.

Beyond tree level, there are additional parameters that affect the Higgs sector. Depending on the choice of these, different MSSM benchmark scenarios are defined. Most of these scenarios identify the lighter of the two CP-even neutral Higgs scalars, h^0, as the SM-like scalar particle with a mass of 125 GeV. However, this can be achieved in different ways. In the m_h^{max} scenario, for example, the benchmark parameters are chosen such that the mass of the light CP-even scalar, h^0, is maximized for fixed $\tan\beta$ and m_A to make it match the observed value [35]. Another approach is the $m_h^{\text{mod+}}$ scenario. Here, the mixing of the stop fields (the supersymmetric partners of the top quark fields) is chosen in a way to maximize the region in $\tan\beta$ that is compatible with the observed Higgs mass value [36]. The soft SUSY-breaking mass scale is usually chosen to be $M_{\text{SUSY}} = 1$ TeV in both of these scenarios.

Another approach is known as the hMSSM scenario, where the value of m_h is used to predict the other masses and coupling parameters without referencing the soft SUSY-breaking parameters [37]. Figure 3.4 shows the predicted production cross section for the heavy Higgs bosons A/H at the LHC in the $m_A - \tan\beta$ plane for the hMSSM scenario. Special effects occur when on-shell pairs of top quarks have to be considered around $m_A = 2m_t \approx 350$ GeV.

In any case, the $m_A - \tan\beta$ plane is an appropriate parameter space for exclusion limits regarding the MSSM Higgs sector. Large values of $\tan\beta$ would also lead to enhanced coupling of the neutral Higgs scalars, H^0 and A^0, to down-type fermions, resulting in increased branching fractions to τ-leptons and b quarks, as can be seen in Figure 3.5. This has inspired many searches for a scalar boson in $\tau\tau$ and bb final states.

In this thesis, exclusion limits in the $\tan\beta - m_A$ plane on the $m_h^{\text{mod+}}$ and hMSSM scenario will be presented. Figure 3.6 shows a summary of hMSSM exclusion limits set in this plane by eight different ATLAS publications. No excess over the SM has been observed. As expected, low resonance masses are excluded already, and the limits on large values of $\tan\beta$ are dominated by searches for final states with down-type fermions. However, a large part of the phase space compatible with phenomenology has not been excluded yet.

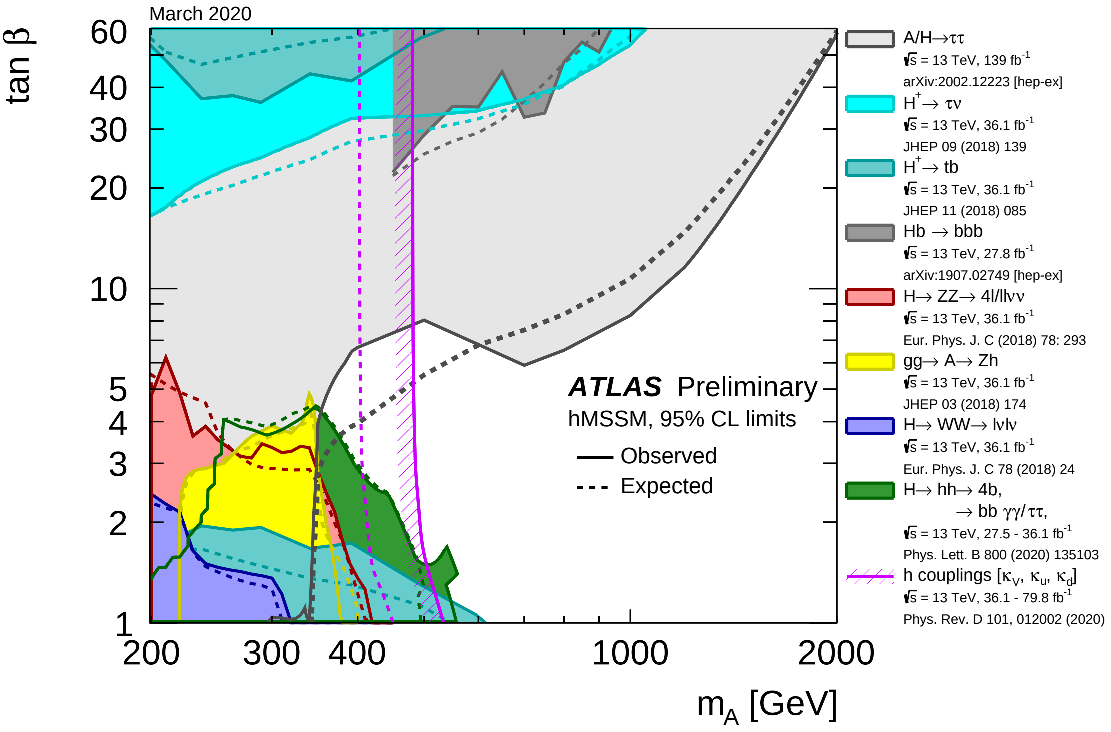

Figure 3.6.: Exclusion limits at 95% CL in the $[m_A, \tan\beta]$ plane of the hMSSM model set by direct searches for heavy Higgs bosons. Solid (dashed) lines indicate the observed (expected) values [38].

3.3. Z' models

Several BSM models predict the existence of a heavy Z' boson in addition to the SM Z boson with $m_Z = 91$ GeV [39–42]. These hypothetical particles are predicted as a result of extending the electroweak gauge group while preserving lepton universality [43]. Such extensions to the gauge group of the SM are well motivated. For example, the symmetry groups $SO(10)$ and E_6 can be broken down to $SU(3) \times SU(2) \times U(1) \times U(1)'$, providing a basis for a GUT.

The most frequently used benchmark scenario is known as the *Sequential Standard Model* (SSM) [44]. It assumes a single additional Z' boson whose couplings are identical to those of its SM-like counterpart. Some models, however, predict that the Z' boson could preferably couple to third-generation fermions [45–48], motivating searches in the di-τ final state. The increased coupling to third-generation fermions could also explain the high mass of the top quark, a phenomenon that remains unexplained in the context of the SM. One such model is the *Strong Flavour Model* (SFM) [46,48], which also predicts the existence of a heavy W' boson.

CHAPTER 4

The ATLAS detector at the LHC

The European Organization for Nuclear Research (CERN) is the largest institution for particle physics worldwide. It was founded in 1954 near Geneva, Switzerland, and hosts many experiments that have achieved groundbreaking discoveries. These include the discovery of W and Z boson in 1983 at the UA1 and UA2 experiments [49], the determination of the number of light neutrino families at the Large Electron-Positron Collider (LEP) [50], the discovery of direct CP violation in the NA49 experiment in 1999 [51], and the discovery of the Higgs boson in 2012 at ATLAS and CMS [1–3].

The following Chapter details the experimental setup that was used to take the data analyzed in this thesis. The machine that accelerates and collides the protons, the Large Hadron Collider (LHC) [52], is described in Section 4.1. Section 4.2 covers the ATLAS detector [53], the largest particle detector at CERN. Lastly, event generation and the Worldwide LHC Computing Grid (WLCG) are detailed in Section 4.3 and Section 4.4, respectively.

4.1. The Large Hadron Collider

The LHC is the largest and most powerful particle accelerator in the world. For most of the time, it collides protons with one another - there are, however, dedicated heavy ion runs, as well. It lies within a 27 km long, nearly circular tunnel at a depth of around 100 m underground. Superconducting magnets create a strong magnetic field that forces the beams of particles on their trajectory. Roughly 1200 dipole niobium-titanium magnets guarantee nearly circular motion, while 392 quadrupole, 688 sextupole, and 168 octupole magnets are responsible for the beams' collimation. The magnets are cooled to

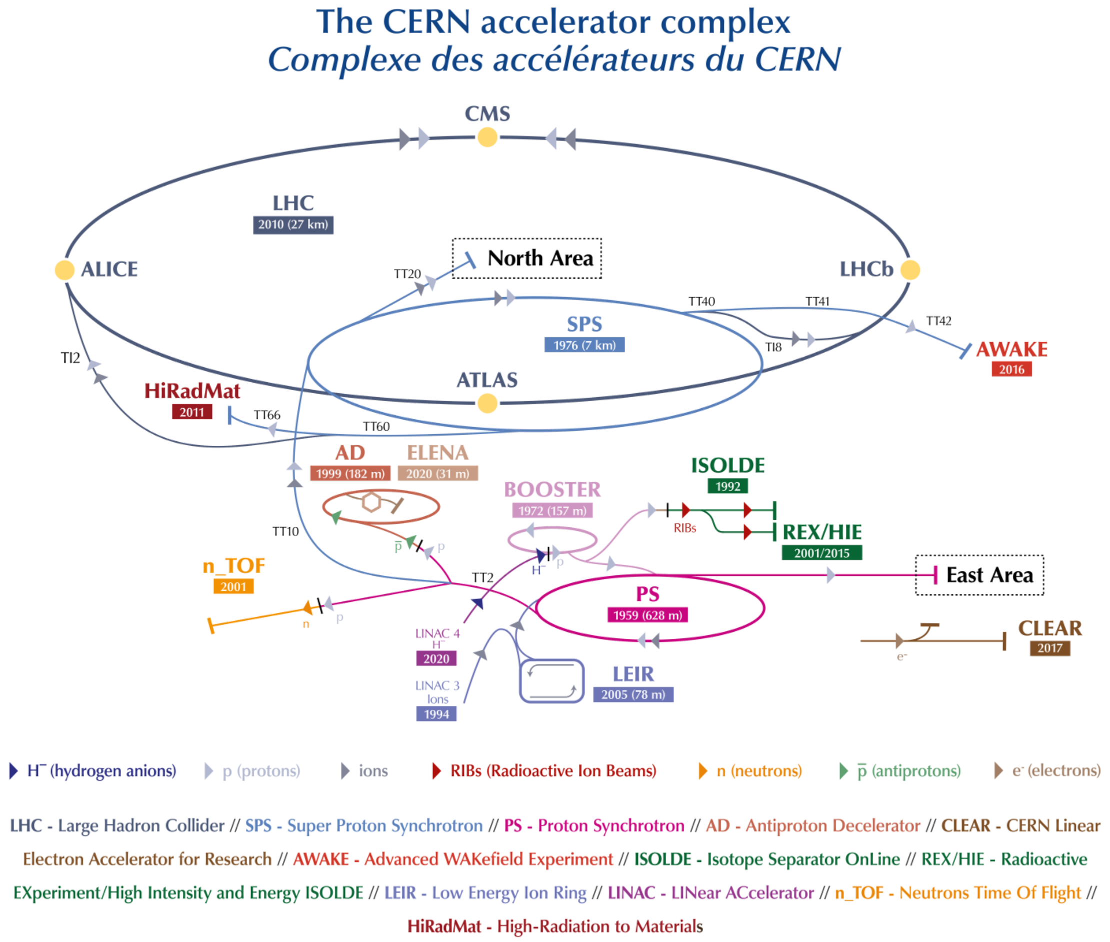

Figure 4.1.: A schematic display of the acceleration complex at CERN [54].

a temperature of 1.9 K and produce a magnetic field of up to 8.3 T. The protons traverse the LHC in two beams, flying in opposite directions. Each beam consists of bunches of roughly 10^{11} particles each. These bunches are spaced at 25 ns intervals, resulting in 2808 bunches per beam. The beam pipe houses a near-perfect vacuum, the largest of its purity worldwide. High-frequency electric fields are used to accelerate the protons to an energy of 6.5 TeV[1].

Protons pass an array of smaller accelerators before being injected into the LHC. An overview of this accelerator complex can be seen in Figure 4.1. Firstly, electrons are stripped from Hydrogen atoms to obtain free protons. These are then accelerated to 50 MeV by the linear accelerator LINAC2. After this, the Proton Synchrotron Booster (PSB) increases the protons' energy to 1.4 GeV. Lastly, Proton Synchrotron (PS) and Super Proton Synchrotron (SPS) accelerate the protons to 26 GeV and 450 GeV, respectively.

Stable beams were achieved at the LHC for the first time in 2008. Due to an accident, however, the operation had to be suspended for more than a year. After the relaunch in late 2009, the performance of the LHC was increased step-by-step, leading to stable beams with a centre-of-mass energy of $\sqrt{s} = 7$ TeV in 2011. During that year, ATLAS and CMS recorded roughly 5 fb^{-1} of data. One year later, $\sqrt{s}$ increased to 8 TeV for eight months before the machine was turned off for the planned *Long Shutdown*, marking the end of Run 1. ATLAS and CMS recorded roughly 20 fb^{-1} of data at $\sqrt{s} = 8$ TeV during Run 1. The end of the Long Shutdown in 2015 marked the start of Run 2 with proton-proton collisions at $\sqrt{s} = 13$ TeV. That data-taking period lasted until 2018 and produced roughly 139 fb^{-1} of data for each of the ATLAS and CMS experiments. The time-dependent integrated luminosity at ATLAS for proton-proton collisions for each year is displayed in Figure 4.2.

At the LHC, there are four points at which the beams cross, and proton collisions occur. A detector is placed around each of these points to observe the newly created particles. ATLAS (A Toroidal LHC ApparatuS) [56] and CMS (Compact Muon Solenoid) [57] are the largest experiments at CERN, serving as multi-purpose detectors. Both were designed to detect the Higgs boson, conduct SM precision measurements, and contribute to searches for BSM physics. The other two detectors are optimized for a specific task. LHCb (LHC beauty) [58] detects B-hadrons in a forward region to study CP-violation and find an explanation for the matter-antimatter asymmetry in our universe. ALICE (A Large Ion Collider Experiment) [59] focuses on heavy ion collisions to understand quark-gluon plasma and the process of hadronization. Smaller experiments surrounding the four previously mentioned ones are: TOTEM (TOTal cross section, Elastic scattering and diffraction dissociation Measurement) [60] measuring the total cross section of proton collisions, MoEDAL (Monopole & Exotics Detector at the LHC) [61] searching for magnetic monopoles, and LHCf (LHC forward) [62] investigating forward regions and cosmic rays.

---

[1] The LHC was originally designed to achieve proton energies of 7 TeV. However, this value has not been reached yet. Recent developments seem to make this possible for the future, though.

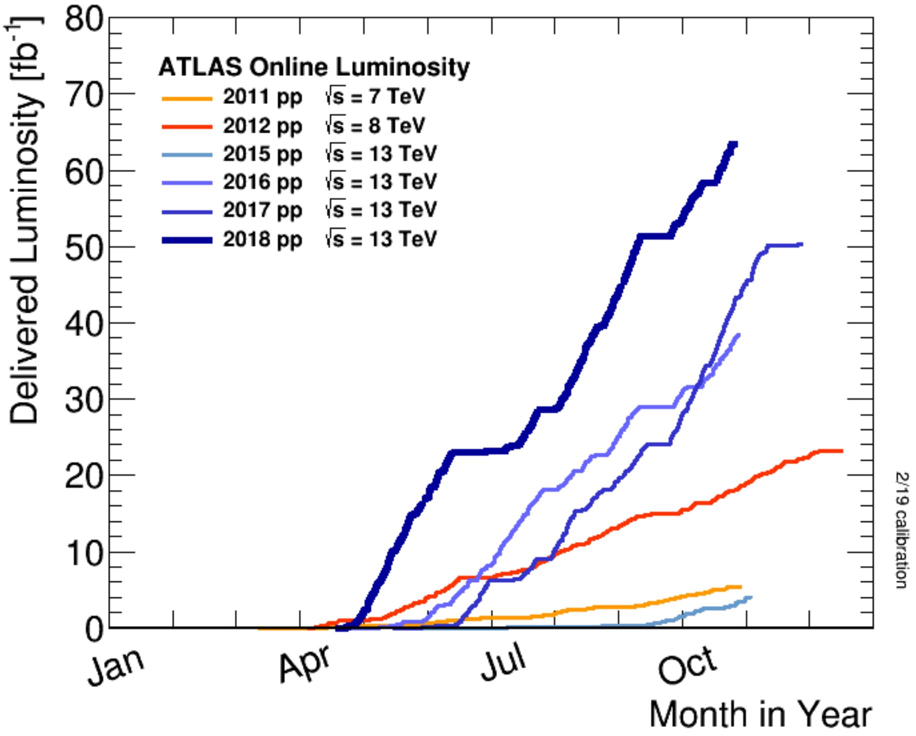

Figure 4.2.: Integrated luminosity of data taken by the ATLAS detector between 2011 and 2018 [55].

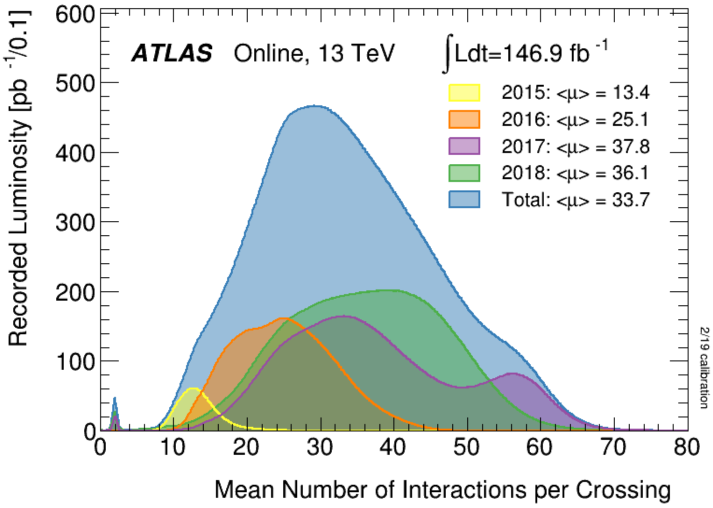

Figure 4.3.: Average number of interactions per bunch crossing for the different data-taking years of Run 2 [55].

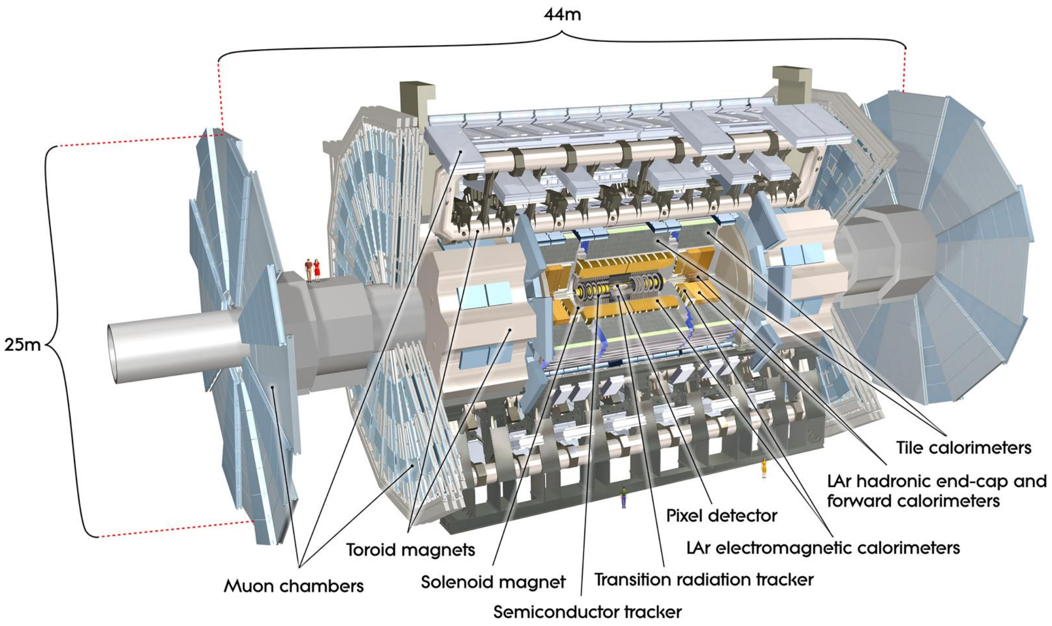

Figure 4.4.: A schematic display of ATLAS and its subdetectors. The humans are depicted for scale purposes ©CERN.

Scientists aim to collimate the beams further to increase the instantaneous luminosity, leading to a larger dataset. Figure 4.3 shows the resulting increase in the average number of proton collisions per bunch crossing for the different data-taking years of Run 2. Since usually only the proton collision with the highest energy transfer is considered by the detectors, most of the proton collisions are background known as *pile-up*.

4.2. The ATLAS detector

The ATLAS detector is rotationally symmetric around the beam axis. It is the largest detector at CERN, with a length of 44 m and a diameter of 25 m. However, in terms of weight, it is second to CMS at 7000 t. Figure 4.4 shows a schematic display of ATLAS and its subdetectors. From inside out these are the *Inner Detector*, recording tracks of charged particles, the *calorimeters*, measuring the deposited energy of electrons, jets, and photons, and the *muon system*, precisely tracing back the trajectories of muons. The various subdetectors will be described in more detail in the following. Firstly, however, the coordinate system used at ATLAS is described in Section 4.2.1.

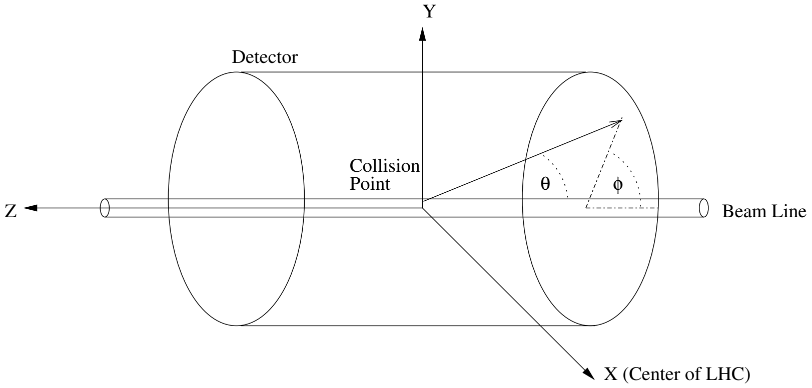

Figure 4.5.: Coordinate system of the ATLAS detector [63].

4.2.1. The ATLAS coordinate system

Because of its cylindrical structure, ATLAS uses a (right-handed) coordinate system where the beam direction defines the z-axis, the x-axis points towards the centre of the LHC, and the y-axis points upwards. The azimuthal angle ϕ lies in the plane perpendicular to the z-axis. Variables such as the *transverse momentum*, p_T, or the *transverse energy*, E_T, refer to the projection onto this plane. The polar angle θ is measured from the beam-axis. Instead of θ, however, the rapidity

$$y \equiv \frac{1}{2} \ln \left(\frac{E - p_L}{E + p_L} \right)$$

is often used, since intervals in y are invariant under Lorentz boosts along the z-axis. Here, p_L is the longitudinal momentum, so the projection of $\vec{p}$ on the z-axis. In the ultra-relativistic limit, y is equal to the pseudo-rapidity, defined as

$$\eta \equiv -\ln \left(\tan \frac{\theta}{2} \right) .$$

Angular distances are measured in units of

$$\Delta R \equiv \sqrt{(\Delta\eta)^2 + (\Delta\phi)^2}.$$

The coordinate system is schematically displayed in Fig. 4.5.

4.2.2. Inner Detector

The innermost subdetector of ATLAS is known as the *Inner Detector* (ID) and is responsible for the reconstruction of tracks and vertices. It is engulfed by a 2 T magnetic field which forces charged particles on a bent trajectory, allowing to indirectly measure momenta, charges and masses of particles, and aiding with the identification of electrons. To do so, it possesses a very high granularity, allowing for a precise spatial resolution.

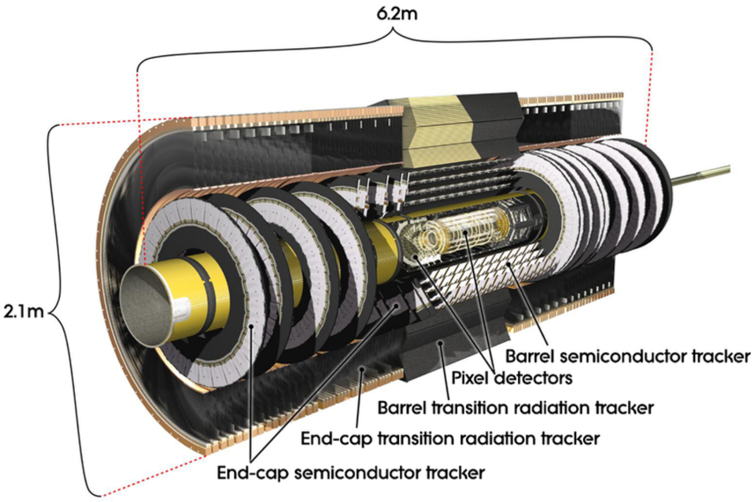

Figure 4.6.: The layout of the ATLAS inner detector ©CERN.

In order to withstand the large amount of radiation so close to the beam collisions and to affect the particles' trajectories as little as possible, the ID was designed to contain the lowest possible amount of interacting material. Covering a range of $|\eta| \in [0, 2.5]$, it reaches a relative momentum resolution of

$$\frac{\sigma_{p_\mathrm{T}}}{p_\mathrm{T}} = 0.04\% \cdot p_\mathrm{T}[\mathrm{GeV}] \oplus 2\%.$$

Its layout can be seen in Figure 4.6. It consists of three subdetectors: *Pixel Detector*, *Semiconductor Tracker* (SCT) and *Transition Radiation Tracker* (TRT). They will be described in the following.

Pixel Detector The innermost subsystem of the ID is the Pixel Detector. It consists of over 80 million semiconductor silicon pixels with a size of 50×400 μm^2, each. Between Run 1 and Run 2, an additional layer, the Insertable B-Layer (IBL) [64] was inserted between the existing three cylindrical layers and the beam pipe at a distance of roughly 2 cm from the beam crossing. With an additional 10 million pixels of size 50×250 μm^2, each, its purpose is to improve the reconstruction of secondary vertices that occur in decays of b-quarks and τ-leptons. The spatial resolution of the Pixel Detector is 10 μm in the transverse plane and 115 μm in z-direction.

Semiconductor Tracker Around the Pixel Detector lies the SCT. It consists of 4 layers of silicon microstrips in the barrel and 9 in the endcaps. Each strip has a size of 80 μm $\times$ $(6 - 12)$ cm. With over 6 million readout channels, the SCT achieves a spatial resolution of 16 μm in the transverse plane and 580 μm in z-direction.

Transition Radiation Tracker The outermost part of the ID is the TRT. It comprises roughly 370 000 straw tubes parallel (orthogonal) to the beam pipe in the barrel (endcap) region with a radius of 2 mm and a length of 144 (37) cm. These tubes lie within a transition-radiation detector and contain a mixture of Xe, CO_2, and O_2, as well as a wire in the middle. When a charged particle passes two gases with different diffraction indices, it produces transition-radiation photons. These then ionize the gas in the tubes, which causes an electrical current from the shell to the wire. The amplitude of this signal is proportional to the Lorentz factor γ. Hence, the TRT is very effective at distinguishing electrons from pions, with deteriorating performance with increasing $|\eta|$.

4.2.3. Calorimeters

Calorimeters measure the energy of a particle by inducing electromagnetic or hadronic showers. For a good resolution, all products of a shower must be contained in the system. The size of such a shower is proportional to the logarithm of the energy of the incoming particle and the radiation length of the material in the calorimeter, X_0, defined as the distance after which the energy of the particle decreased to $1/e$ of its original value. Therefore, calorimeters usually contain much dense material. The ATLAS calorimeter system uses two different types of calorimeters. The outer hadronic calorimeter (HCal) is a tile calorimeter. The electromagnetic calorimeter (ECal), the forward calorimeter (FCal), and the endcap of the HCal are liquid Argon (LAr) calorimeters. The overall layout of the ATLAS calorimeter system is schematically displayed in Figure 4.7. In general, ATLAS only deploys *sampling* calorimeters. Here, a combination of active material for the readout and a passive material to induce showering is used. Active and passive material are arranged in an alternating manner.

Electromagnetic Calorimeter The ECal uses Lead plates as an absorber and liquid Argon as the active material. Electromagnetic showers that are induced when a Lead plate is struck by a particle ionize the Argon atoms, producing a signal. The ECal has a thickness of $23X_0$, stopping almost any incoming photon or electron, and a resolution varying between 0.025×0.025 and 0.1×0.1 in terms of $\Delta\eta \times \Delta\phi$, depending on $|\eta|$, amounting to about 180,000 readout channels. This high resolution is particularly crucial for the reconstruction of photons, since they produce no tracks in the inner detector. The ECal can be split into the barrel region, with a coverage of $|\eta| < 1.475$, and the endcap region, with a coverage of $1.375 < |\eta| < 3.2$. The barrel consists of two identical halves that are separated by a 4 mm wide gap. The transition region between the barrel and the endcap region ($1.37 < |\eta| < 1.52$) is called the *crack-region*, and possesses a significantly reduced resolution. Showers that started before the first layer of absorber material are detected by the dedicated presampler LAr layer, which is 11 mm thick and covers a range of $|\eta| < 1.8$. Assuming the complete shower develops within the calorimeter, the relative

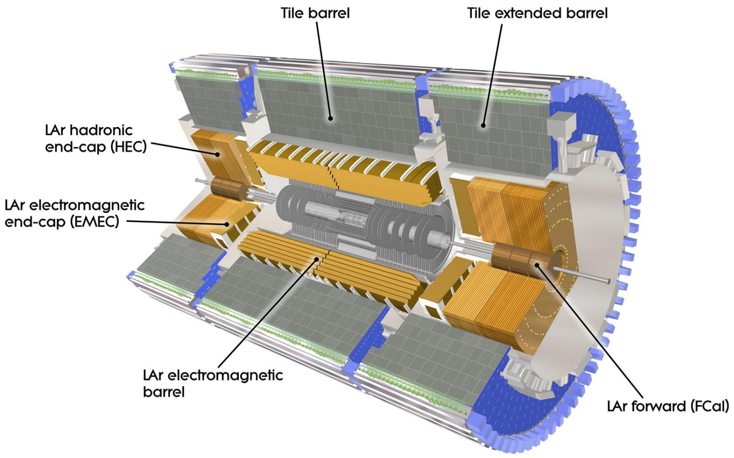

Figure 4.7.: A schematic depiction of the ATLAS calorimeters ©CERN.

energy resolution of the ECal can be written as

$$\frac{\sigma}{E[\mathrm{GeV}]} = \frac{0.1}{\sqrt{E[\mathrm{GeV}]}} \oplus 0.01 \oplus \frac{0.3}{E[\mathrm{GeV}]}. \tag{4.1}$$

Hadronic Calorimeter In contrast to the ECal, the HCal uses different materials in the barrel and the endcaps. In the barrel, the passive material is steel, and scintillating tiles make up the active material. It covers $|\eta| < 1.7$ with 5760 readout channels, and has a $\Delta\eta \times \Delta\phi$ granularity of 0.1×0.1. In the endcaps, the HCal uses a combination of liquid Argon and Copper, covering the region $1.5 < |\eta| < 3.2$ with a granularity between 0.1×0.1 and 0.2×0.2, depending on $|\eta|$, resulting in 4092 readout channels. Analogous to Equation 4.1, the HCal has a relative energy resolution of

$$\frac{\sigma}{E[\mathrm{GeV}]} = \frac{0.5}{\sqrt{E[\mathrm{GeV}]}} \oplus 0.03.$$

Forward Calorimeter The very forward region of the ATLAS detector ($3.1 < |\eta| < 4.9$) is covered by the *Forward Calorimeter* (FCal) which uses liquid Argon as an active material and Copper (Tungsten) as a passive material for the electromagnetic (hadronic) detection. Its relative energy resolution is

$$\frac{\sigma}{E[\mathrm{GeV}]} = \frac{1}{\sqrt{E[\mathrm{GeV}]}} \oplus 0.1.$$

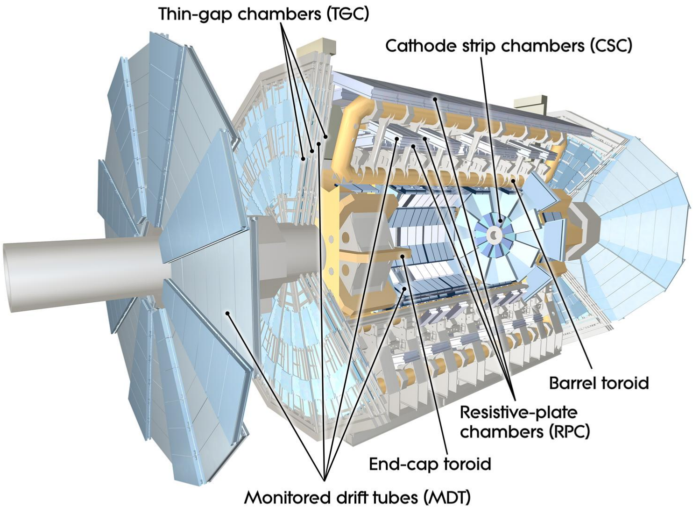

Figure 4.8.: The layout of the ATLAS muon system ©CERN.

4.2.4. Muon System

The energy loss of a particle when passing through matter decreases quickly with its mass (e.g. Bremsstrahlung: $\Delta E \propto \frac{1}{m^4}$). Therefore, muons only lose a negligible fraction of their energy in the ID and calorimeter system. For this reason, a dedicated muon spectrometer is installed at the outermost layer so that other particles will not reach it. It is split into a barrel and an endcap. Two strong endcap magnets provide bending power for muon tracks, which, combined with the three cylindrical layers of high precision tracking chambers, lead to an excellent muon momentum resolution. Figure 4.8 shows the layout of the ATLAS muon system. A combination of four detector types is deployed, amounting to roughly a million readout channels. These are *Monitored drift tubes* (MDT), *Cathode Strip Chambers* (CSC), *Resistive Plate Chambers* (RPC), and *Thin-Gap Chambers* (TGC), leading to an overall relative p_T resolution of $2-3$ % for typical muon energies that deteriorates to 10% at $p_{\mathrm{T}} = 1$ TeV [56].

Monitored drift tubes The MDTs are used for measuring the muon momenta precisely, covering a range of $|\eta| < 2$ with a radial orientation. Each tube has a spatial resolution of roughly 80 μm. Because of their slow readout, MDTs and CSTs are not suited to support trigger decisions.

Cathode Strip Chambers The CSTs aid the MDTs in the precision tracking, extending what is covered by the region $2.0 < |\eta| < 2.7$. Multiwire proportional chambers with strip-shaped cathodes offer a 40 μm × 5 mm resolution in terms of $z \times r$.

Resistive plate chambers Unlike MDTs and CSTs, RPCs and TGCs have a rapid readout of 15−25 ns. Therefore, the muon trigger system exclusively relies on the tracking information of the latter two. Covering a region of $|\eta| < 1.05$, RPCs are gas detectors that measure the degree of ionization caused by highly energetic charged particles.

Thin-gap chambers TGCs are multiwire proportional chambers and cover a region of $1.05 < |\eta| < 2.4$. Apart from their contribution to the trigger system, they also complement the measurement of the MDTs by providing the second, azimuthal coordinate.

4.2.5. Trigger System

With bunch crossings occurring at a frequency of 40 MHz, recording each one would amount to roughly 60 TB of data per second. Current technology cannot process such large quantities of data. Therefore, ATLAS deploys a *trigger* system that quickly marks interesting events for further processing, neglecting the rest and reducing the data rate to the order of 1 GB per second. It consists of two steps: *Level 1* (L1) and *High Level Trigger* (HLT) [65].
Since the reconstruction of tracks is computationally intensive, the L1 neglects information from the ID to handle the high rate of events. Instead, only data from the calorimeters and the fast parts of the muon system (RPCs and TPCs) are considered. The L1 reduces the event rate to approximately 100 kHz, accepting only events with large energy deposits or muon tracks. The geometric parts of the detector where these occurred are defined as regions of interest (ROIs) and passed to the HLT as input. Dedicated versions of the HLT then use the complete detector information to identify signatures of electrons, photons, muons, hadronic τ-lepton decays, jets, b-quark-induced jets, missing transverse momentum, respectively. An event is neglected if none of the previously mentioned signatures is found. The criteria of the HLT tighten with increasing instantaneous luminosity to keep the rate of stored events around 1 kHz.

4.3. Event simulation

To make a scientific statement about a theory, its predictions must be compared to experimental data. Therefore, simulations are necessary. In high energy physics, *Monte Carlo* (MC) simulations model the quantum mechanical randomness according to underlying probability distribution functions. At ATLAS, proton-proton collisions are simulated according to the SM or relevant BSM theories [66]. The chain from first-principal theoretical calculations based on quantum field theory to a dataset comparable to experimental findings consists of several independent steps explained in the following.

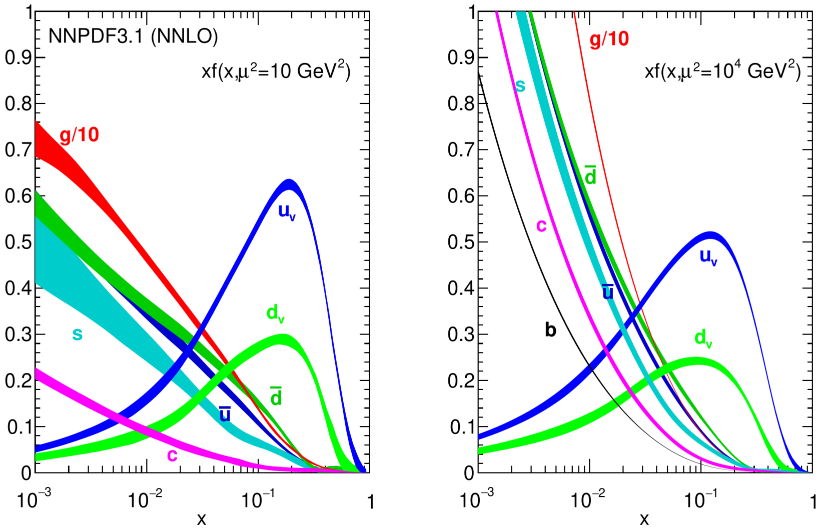

Figure 4.9.: NNLO PDFs, evaluated at $\mu^2 = 10$ GeV^2 (left) and $\mu^2 = 10^4$ GeV^2 (right). The gluon PDFs are scaled down by a factor of ten [67].

Parton Distribution Functions Protons consist of two u quarks and one d quark, the *valence* quarks. However, depending on the protons' energy, the strong interaction between the valence quarks can lead to additional quarks and gluons playing a role in proton-proton collisions. These additional particles are referred to as *sea* quarks and gluons. Together with the valence quarks, they make up the partons. Since the coupling strength of the strong interaction decreases with the energy, the partons are basically free particles - a principle known as asymptotic freedom. The probability f_a of a particle of type a taking part in the primary interaction of a proton-proton collision can be quantified by *Parton Distribution Functions* (PDFs). They are parametrized in terms of x and μ. Here, x is the fraction of the proton momentum carried by the individual particle, and μ is the order of magnitude of the transferred momentum in the collision. Next-to-next-to-leading order (NNLO) calculations of such PDFs are displayed in Figure 4.9.

Matrix Element calculation The first step of simulating particle collisions is calculating the corresponding scattering matrix. Its elements are often abbreviated as the Matrix Elements (MEs). To do so, a renormalization scale, has to be defined to bypass ultraviolet divergencies. Then the ME can be calculated *pertubatively*, using iteratively higher orders of the coupling strength α to increase the precision. The power of α corresponds to the number of interactions considered in the respective Feynman diagram. The first approximation, known as *leading-order* (LO), corresponds to assuming the minimum number of interaction vertices necessary for the transition from the initial to the final state. Next-to-leading-order (NLO) calculations also contain the second-lowest possible number of vertices and so on. In combination with a Monte Carlo (MC) simulation for the particles and their kinematics, this step of the simulation chain is known as *parton level* or *generator level*.

Parton shower Parton showering occurs when highly energetic partons emit gluons or form quark-antiquark pairs. The process continues until their energy is low enough for hadronization, typically around 1 TeV [68]. When simulating parton showering perturbatively, a cut-off energy scale has to be introduced. Below this so-called *factorization scale*, a perturbative approximation does not hold anymore as α_S increases with decreasing energy, leading to divergencies.

Hadronization When a parton's energy is low enough, it will start forming colour-neutral states, a process known as hadronization. Since this cannot be simulated perturbatively, a more phenomenological approach is deployed. The most frequently used approaches to simulate this process are known as *string dynamics* [69] and *cluster model* [70]. The simulations are adjusted via parameters that are determined experimentally. A complete set of such parameters is referred to as a *tune* [71, 72].

Underlying event After the initial scattering, the residual partons of the protons will also undergo parton showering and eventually form new hadrons. This phenomenon is known as the *underlying event*. Similar to the hadronization described above, the underlying event is simulated with the help of simplified models [73,74] and corresponding experimentally determined tunes.

Pile-up reweighting Only the primary interaction vertex is fully simulated in each event. For the simulation of pile-up, two distinct cases are considered: *in-time pile-up*, where the secondary collisions occur in the same bunch crossing, and *out-of-time pile-up*, where the signatures originate from collisions in previous or following bunch crossings. Both in-time pile-up and out-of-time pile-up are simulated by superimposing simulated events with and without hard-scattering. Additionally, simulated events are reweighted to match the pile-up in recorded data. Due to the very different conditions of the respective year of data-taking, these event weights can be large, deteriorating the statistical power of the dataset. Therefore, simulated events used in this thesis are split into three *campaigns*: *mc16a*, *mc16d*, and *mc16e* correspond to data taken in 2015-2016, 2017, and 2018, respectively. The ratio of simulated events across the three campaigns matches that in the recorded data to maximize the statistical power.

Detector simulation All previously mentioned steps are at the so-called *truth-level*, meaning they contain perfect information about all particles involved and their trajectories. However, a simulation must also take the detector response into account to make the predictions commensurable to the recorded data.

The ATLAS detector is modelled using the software package Geant4 [75]. This includes a detailed digital replica of the complete construction and a simulation of the interactions of particles with it. With this approach, simulations on truth-level can be used as input to create HITS files containing the information that each readout channel would receive. After a dedicated digitization simulation, the proton-proton collisions are represented in a format that can be compared to recorded data, meaning that further processing like reconstruction, identification and energy calibration of particle signatures can be applied to simulated and recorded data alike.

The detector simulation is the computationally most intensive part of the complete chain of simulating proton-proton collisions. Therefore, a simplified detector simulation known as AtlFast-II was developed [76]. It deploys parametrizations of hadronic showers in the calorimeters. Simulated samples after the detector simulation are referred to as *reconstruction-level*.

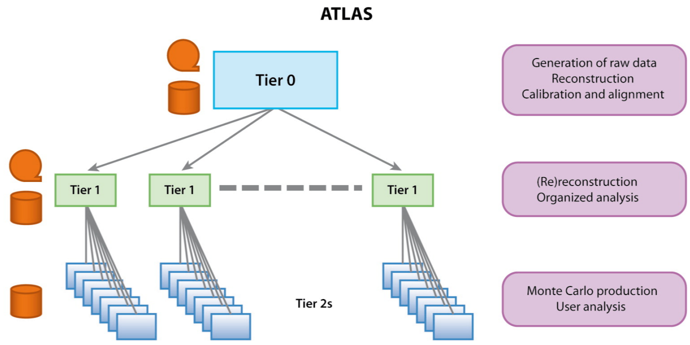

Bird I. 2011.
Annu Rev. Nucl. Part. Sci. 61:99–118

Figure 4.10.: The ATLAS computing model [80].

4.4. The worldwide LHC computing grid

The amount of data produced at the LHC is tremendous, with roughly 15 PB per year. In addition to analyzing proton-proton collisions, computationally intensive simulations are also carried out. The vast demand for computing power and the desired global accessibility of the data lead to the development of a worldwide grid, the *WLCG* (Worldwide LHC Computing Grid) [77, 78]. Figure 4.10 shows the computing model for ATLAS. All partaking computing clusters are categorized in Tiers 0 to 3 [79] explained in the following.

- The Tier 0 centre at CERN accepts the data streaming from the experiments at full rates. It must also save them to tape for archiving. A backup of the data spreads among all Tier 1 centres. In order to make that data transfer possible, dedicated network connections to Tier 1 centres, with a bandwidth of 10 GB/s, have been established. It also provides a large computing cluster and operates the rest of the grid.
- There are thirteen Tier 1 sites spread across North America, Europe, and Asia. Due to their essential role within the grid, Tier 1 sites are usually located at institutions with experience in large-scale data management. Each site has to store a previously agreed part of the raw and simulated data from Tier 0.
- Each Tier 1 site supports several Tier 2 centres that analyze a share of the data and provide computing resources for Monte Carlo simulations. Tier 2 sites do not archive crucial data, allowing for small service teams to run them. The university of Göettingen provides a Tier 2 centre known as *GoeGrid*.
- Tier 3 sites provide computing resources for end-user analysis. The scope of their hardware varies enormously, ranging from a few CPUs to extensive national analysis facilities.

CHAPTER 5

Object reconstruction and identification

Many particles produced at the LHC have proper decay lengths below 1 mm, decomposing before reaching the innermost layer of the ATLAS detector. Therefore, only a small number of particle types can be directly detected. Figure 5.1 shows the trajectories of different long-lived particles and how they interact with the detector material of the various subsystems.

In a broader sense, ATLAS reconstructs physics-related *objects* and uses these to draw conclusions on the primary particles indirectly. In the first step, universal entities closely related to the detector signatures, such as tracks, vertices, and energy clusters in the calorimeter, are reconstructed. From this, more complex objects like electrons, muons, jets, τ-leptons, and missing transverse momentum are reconstructed[1].

Although sometimes bearing the same name, the reconstructed objects are not to be confused with the actual particles causing the respective signature in the detector. Information on the latter is only available in simulations - not in recorded data. However, as mentioned in Section 4.3, the reconstruction is performed on recorded and simulated data, alike. An object correctly reconstructed from a particle of the same kind is referred to as *true*. Wrongfully reconstructed objects (e.g. a quark- or gluon-initiated jet reconstructed as a hadronically decaying τ-lepton) are known as *fake*.

After the actual reconstruction, the additional steps of calibration and identification are performed for determining precise kinematics and better background rejection, respectively. The various algorithms are discussed in the following. Only objects relevant in this thesis are considered, where particular emphasis is put on hadronically decaying τ-leptons as they play an essential role.

---

[1] No distinction is made between particles and anti-particles in the names of reconstructed objects

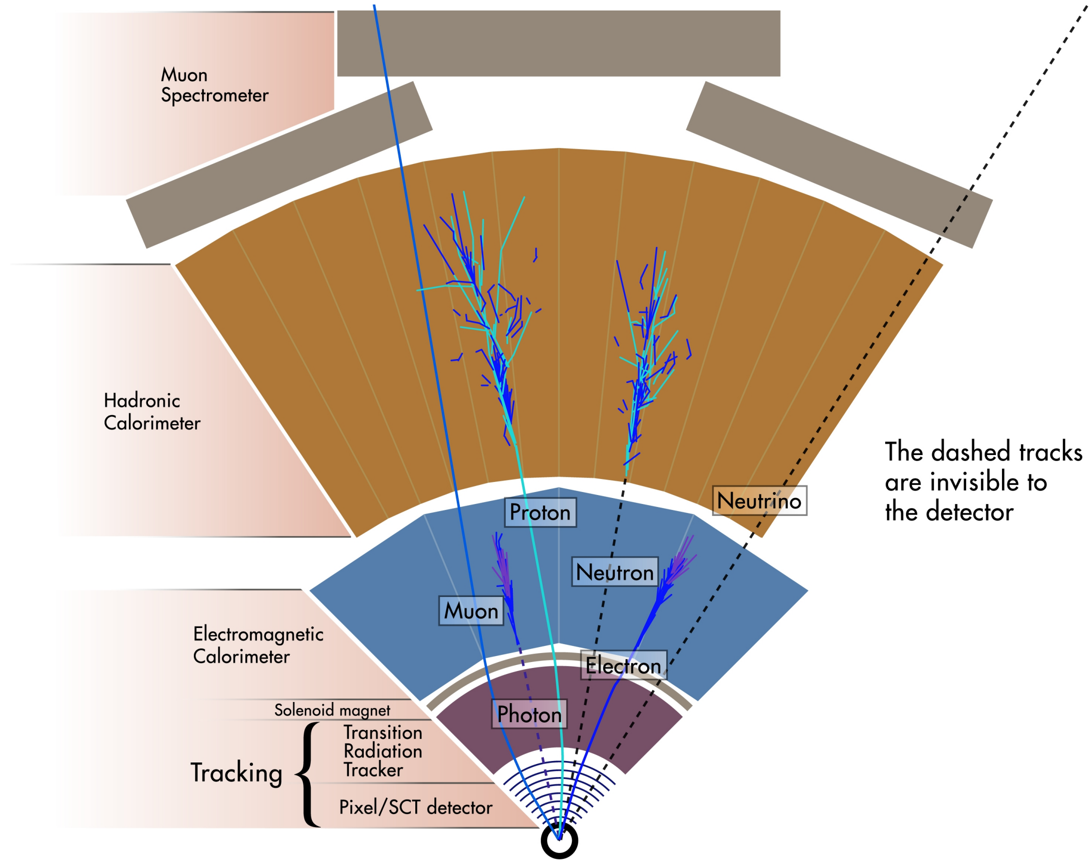

Figure 5.1.: Schematic display of trajectories of long-lived particles at ATLAS and their interactions with the various sub-detectors ©CERN.

5.1. Tracks and vertices

Tracks are reconstructed from hits in the layers of the ID caused by charged particles [81]. The ratio of charge to momentum of a particle, q/p, defines the curvature of its trajectory induced by the magnetic field. The only additional degrees of freedom of a track are the following four geometric properties:

- the transverse impact parameter, d_0, defined as the closest distance between the interaction point and the track's projection onto the transverse plane,
- the longitudinal impact parameter, z_0, defined as the closest distance between the interaction point and the track's projection onto the beam axis,
- the track's azimuthal angle, ϕ,
- the track's polar angle, η.

The reconstruction of tracks starts with assembling clusters from raw measurements of the pixel and SCT detectors. Pixels and strips with deposited energy exceeding a certain threshold are grouped using a connected component analysis [82]. The clusters are used to define *space-points*, representing the location where the charged particle passed through the active material of the respective layer of the ID.

An iterative track-finding algorithm seeded from the previously determined space-points identifies combinatorial possibilities to form tracks passing through at least three of them. Then, a staged pattern-recognition algorithm is deployed. A first loose selection narrows down the candidates before the *ambiguity-solver* assigns a relative *track score* to each track by comparing them with each other. A fit then also takes information from the TRT to find the most likely actual trajectories of particles. The fitted tracks that pass the ambiguity solver again are added to the final selection of tracks.

After a final set of tracks has been reconstructed, the primary vertex (PV) is sought to be identified [83, 84]. The procedure can be divided into two steps: vertex finding and vertex fitting. The former being the association of tracks to a vertex, and the latter being the precise determination of the vertex's position.

The vertex finding algorithm deploys a fit to find the most likely vertex position. An iterative approach is used where the least suitable tracks are assigned a lower weight before recomputing the vertex position. The seed position of this fit is determined in the transverse plane by the centre of the beam spot. In z-direction, the mode of the z_0 distribution of all tracks is used. Once the fit converged on a vertex position, tracks that are incompatible with that result are removed. The remaining tracks are used to find the position of the next vertex. The procedure is repeated until no tracks are left.

The sum of p_{T}^2 of all associated tracks, Σp_{T}^2, is calculated for each reconstructed vertex. The vertex with the highest Σp_{T}^2 is chosen as the PV. All other vertices are classified as either pile-up or secondary vertices. The distinction between the latter two is based on the relative position concerning the beam spot. The beam spot is reconstructed approximately every ten minutes of data taking via maximum-likelihood fit to the distribution of primary vertices.

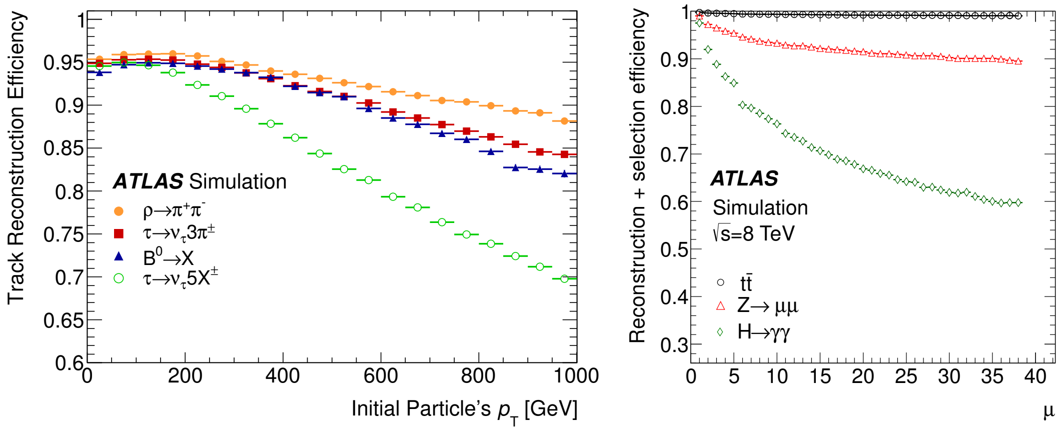

Figure 5.2.: Single-track reconstruction efficiency as a function of the initial particle's p_T [81] (left) and efficiency to reconstruct and then select the hard-scatter PV as a function of the average number of pp interactions per bunch crossing, μ, for different physics processes [83] (right).

The track reconstruction efficiency is defined as the fraction of charged particles traversing the ID that is correctly reconstructed as such. It is displayed in Figure 5.2 for different track-inducing decays as a function of the mother particle's p_T. The Figure also shows the fraction of events where the PV is reconstructed and subsequently correctly selected as a function of the average number of pp interactions. Both plots serve as a measure of the performance of the respective process.

5.2. Electrons

When passing through the detector, electrons leave a track in the ID and shower in the ECal. Therefore, the reconstruction and identification of electrons utilize information from those two subsystems. The reconstruction is started if a local energy cluster in the ECal exceeds $E_\mathrm{T} > 2.5$ GeV [85]. Areas of 3×7 (5×5) cells in terms of $\eta \times \phi$ in the barrel (endcap) are considered for this. A sliding-window algorithm is deployed for the clustering [86]. As a next step, tracks that fulfill $p_\mathrm{T} > 0.5$ GeV are geometrically selected, meaning their virtual extension has to pass through the respective energy cluster to be considered a part of the reconstructed electron. The four-momentum is established by combining the energy deposit in the cluster with the weighted average three-momentum of all tracks and must fulfill $|d_0|/\sigma(d_0) < 5$ and $z_0 \sin(\theta) < 0.5$ mm. Like for most objects that are reconstructed using calorimeter information, any electron must lie inside the precision region of the detector ($|\eta_\mathrm{cluster}| > 2.47$) and outside the crack-region ($1.37 < |\eta_\mathrm{cluster}| < 1.52$).

A multivariate approach is deployed to discriminate true electrons from backgrounds, such as jets and photons wrongfully reconstructed as electrons [87]. The input features include low-level tracking- and calorimeter-based information and high-level variables constructed from both of them. A signal (background) probability density functions, $P_{S(B),i}$, is simulated for each input feature i. Any reconstructed electron is then assigned a likelihood score, d_L, according to

$$d_L = \frac{L_S}{L_S + L_B}, \qquad L_{S(B)}(\boldsymbol{x}) = \prod_i^n P_{S(B),i}(x_i),$$

where x_i is the i-th out of n features. The classification is performed by requiring the electron to surpass a certain lowest likelihood score. Three operating points with increasing cut value are defined: *loose*, *medium*, and *tight*.

An additional requirement is imposed to discriminate primary (prompt) from non-prompt electrons. The latter arise from semileptonic decays of heavy quarks or hadrons, or photons converting into electron-positron-pairs, and are considered an additional source of background. A gradient isolation is deployed, which imposes $|\eta|$ dependent restrictions on the energy fraction deposited in a $\Delta R = 0.2$ cone around the energy cluster of the electron [85]. Similarly, track transverse momenta in a cone of p_T dependent size around the electron must meet some $|\eta|$ dependent requirements so that the overall efficiency of the gradient isolation amounts to 90(99)% for electrons with a p_T of 25(50) GeV.

It has to be considered that the reconstruction and identification of objects can perform differently on recorded versus simulated data. Therefore, *scale factors* are introduced, defined as the ratio of the classification efficiency on data to that on Monte Carlo (MC) simulated events:

$$SF = \frac{\epsilon_\mathrm{data}}{\epsilon_\mathrm{MC}}. \tag{5.1}$$

Applying the scale factor and its uncertainty to simulated electrons passing the respective classification allows comparing simulated and recorded data directly. Analogous scale factors are also derived and applied to other objects. In the case of electrons, they are measured in $Z \to e^+e^-$ and $J/\Psi \to e^+e^-$ events using a *tag-and-probe*-approach [87]. Similarly, the reconstructed energy is to be accounted for possible differences between data and simulated electrons. This is known as *energy calibration* [88].

Figure 5.3 shows the reconstruction and identification efficiency for electrons as a function of E_T. The reconstruction efficiency is plotted for each separate step and the reconstruction of the energy cluster can be seen to be the largest source of inefficiency. Reconstruction and identification are almost fully efficient for larger values of E_T.

5.3. Muons

Being roughly two hundred times heavier than electrons, muons lose a significantly lower fraction of their energy when passing through matter. Therefore, they are referred to as minimum ionizing particles and are not stopped in the calorimeters, reaching the outermost layer of the detector, the Muon System (MS). Tracks are reconstructed in

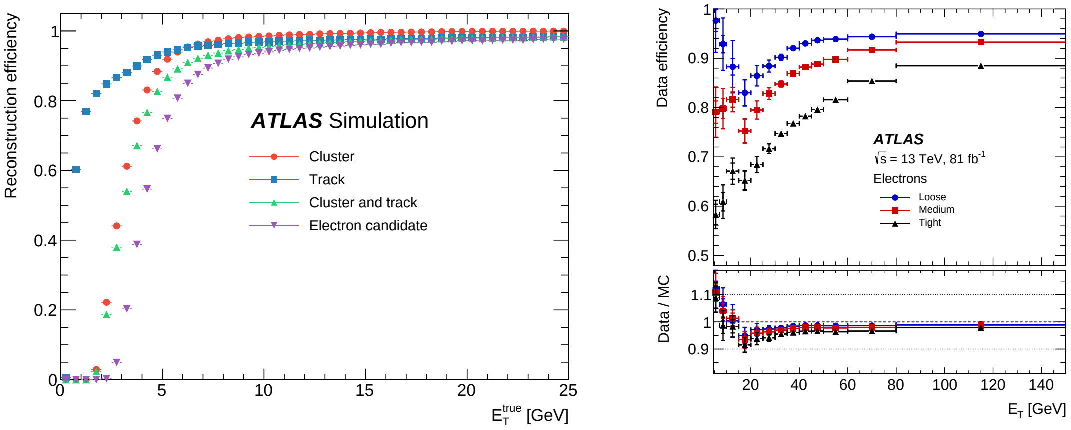

Figure 5.3.: Efficiency for each step of the electron reconstruction and the combination of them (left) and identification efficiency as a function of E_{T} (right) [89].

the MS and the ID independently. Muon tracks are then combined with an *outside-in* approach, where tracks in the MS initiate the process and are then sought to be combined with those in the ID to determine the muon's trajectory [90].

The main challenge of the muon identification is to discriminate non-prompt from prompt muons. In contrast to the former, non-prompt muons often exhibit a kink in their trajectory, making the tracks in the ID and those in the MS less compatible. Three variables providing good separation are used in a cut-based approach:

- *q/p significance*, defined as the absolute difference between the ratio of charge and momentum of a muon measured in the ID and the MS and weighted by the inverse squared uncertainties,
- $\rho\prime$, the absolute difference between the measurements of transverse momentum by the ID and the MS, and normalized to the combination of the two,
- normalized χ^2 of the combined track fit.

The four working points *loose*, *medium*, *tight*, and *high-p_T* are distinguished depending on the strictness of the cuts applied on the aforementioned variables.

Additional isolation criteria provide further suppression of muons originating from hadron decays. The *gradient* working point is defined analogously to the electron *gradient* isolation mentioned in Section 5.2. It provides an efficiency of 95(99)% at $p_{\mathrm{T}} = 25(60)$ GeV for muons [90].

As for the electron candidates, the reconstruction and identification of muons require scale factors to be derived. $Z \to \mu\mu$ and $J/\Psi \to \mu\mu$ events are analyzed with a tag-and-probe approach to determine the necessary efficiencies on recorded data. Figure 5.4 shows the efficiency defined as the fraction of muons that are correctly reconstructed and subsequently pass the *medium* identification requirement as a function of p_{T}. The

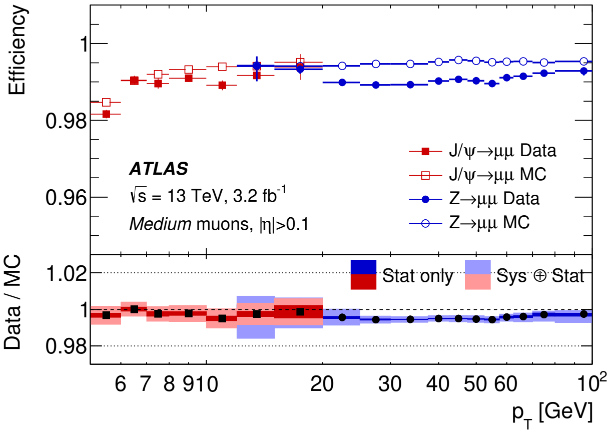

Figure 5.4.: Reconstruction efficiency for the *medium* working point muon selection versus muon p_{T}. The error bars in the upper plot only contain the statistical uncertainty. The ratio plot shows statistical and systematic uncertainties [90].

bottom panel shows the ratio of these efficiencies on recorded to simulated data, allowing the display of the product of reconstruction and identification scale factors.
Analogous to the energy calibration of electrons, the transverse momentum of muon candidates is also corrected. This is achieved by a maximum-likelihood fit of the invariant mass of the muon pair in $Z \to \mu\mu$ and $J/\Psi \to \mu\mu$ events [90].

5.4. Jets

Highly energetic quarks and gluons lead to collimated *jets* of colourless hadrons in the detector because of parton showering and subsequent hadronization. Since the LHC is a hadron collider, almost all events possess jets in the detector, making their reconstruction and calibration crucial.

5.4.1. Clustering and the anti-k_t algorithm

The first step in the reconstruction of jets is to identify calorimeter cells whose signal is above a noise threshold. These are then grouped with the help of a clustering algorithm to form what is referred to as TopoClusters [91]. The name comes from the term topological, referencing the fact that the clustering happens solely according to the three-dimensional position of the respective cell. A dedicated jet clustering algorithm, known as anti-k_t algorithm, is deployed to group TopoClusters into jets [92]. It belongs to the broader group of sequential recombination jet algorithms, which compare and possibly combine *entities* that can be single TopoClusters or combinations of them, referred to as *pseudo-*

jets. First, a generalized distance measure is defined according to

$$d_{ij} = \min\left(p_{\mathrm{T}i}^{2p}, p_{\mathrm{T}j}^{2p}\right)\frac{\Delta R_{ij}^2}{R^2}, \qquad d_{i\mathrm{B}} = \frac{1}{p_{\mathrm{T}i}^2}, \qquad \Delta R_{ij}^2 = (\phi_i - \phi_j)^2 + (\eta_i - \eta_j)^2, \quad (5.2)$$

where R is the radius-parameter (often chosen to be $R = 0.4$), d_{ij} is the distance measure between entities i and j, and $d_{i\mathrm{B}}$ is the distance measure between entity i and the beam. If the smallest of all combinatorically possible distances is between two entities, they are merged. If, however, the smallest possible distance is $d_{i\mathrm{B}}$, the entity i is labelled as a jet, removed from the list of entities, and the distances are recalculated. This procedure is repeated until no entities are left. The parameter choice $p = -1$ in the definition of the distance measure in Eq. 5.2 is what sets the anti-k_t algorithm apart from other sequential recombination jet algorithms like the *Cambridge/Aachen* algorithm [93] ($p = 0$) or the *inclusive* k_t algorithm [94] ($p = 1$).

The anti-k_t algorithm has properties that make it better suited for ATLAS than other jet clustering algorithms. The negative exponent leads to a preferred symmetrical clustering around particles with a large momentum. Furthermore, the anti-k_t algorithm is infrared and collinear (IRC) safe, meaning that the reconstructed jet does not change much when adding a further soft particle in the parton final state or when substituting one particle with two collinear particles.

5.4.2. Energy calibration

Since not all of the energy that a particle or jet loses in a calorimeter is recorded, extensive energy calibration must be conducted. At ATLAS, the energy of a reconstructed jet is adjusted in several steps to match that of the underlying truth-jet [95]. Firstly, the jet is assumed to have originated in the previously reconstructed PV rather than the centre of the detector. The effect is estimated from MC simulation, altering the jet's four-momentum while keeping its energy unchanged. The impact of in-time and out-of-time pile-up on the energy scale is estimated based on the reconstructed jet area [96] and MC simulations, respectively. After these steps, MC studies are used to derive $|\eta|$ dependent *energy response functions*, matching the reconstructed to the underlying truth-jet energy scale. Then, the *global sequential calibration* (GSC) is applied, taking information from all sub-detectors into account and correcting for possible neglected biases caused by jet flavour and energy leakage outside of the calorimeter. The last step is referred to as the *in-situ* calibration. It is only applied to jets in recorded data accounting for differences between the latter and simulated jets.

5.4.3. Jet-vertex-tagger

The suppression of pile-up jets that are falsely reconstructed as jets originating from the PV is crucial. A multivariate technique, the *jet-vertex-tagger* (JVT), is deployed for this task [97]. It calculates a two-dimensional likelihood from the two variables corrJVF and R_{p_T} to form a well-separating discriminant. The former is defined as the scalar transverse

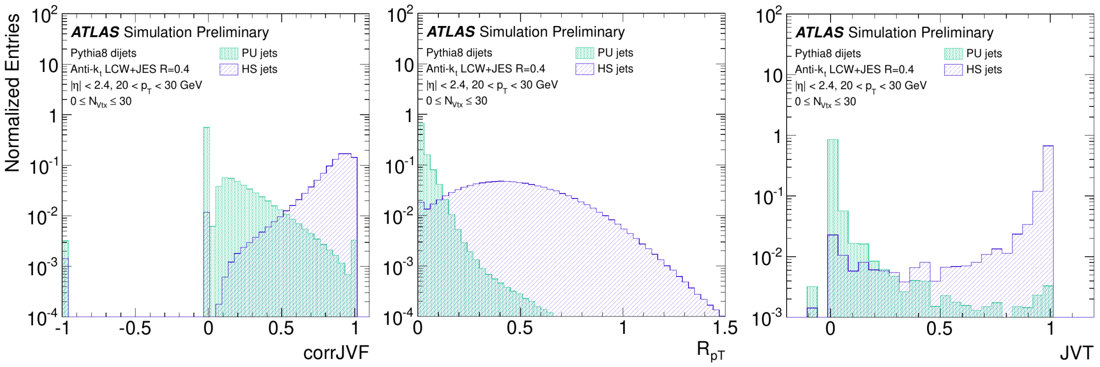

Figure 5.5.: Distributions of the two input variables of the JVT-algorithm corrJVF (left) and R_{p_T} (middle), as well as the resulting final discriminant (right). Each variable is plotted for hard scatter (HS) jets from the PV and for pile-up tracks, separately [97].

momentum sum of the tracks that are associated with the jet and originate from the PV divided by the scalar p_T sum of all associated tracks weighted by the number of vertices in the event:

$$\mathrm{corrJVF} = \frac{\sum_m p_{\mathrm{T},m}^{track}(\mathrm{P}V_0)}{\sum_l p_{\mathrm{T},l}^{track}(\mathrm{P}V_0) + \frac{\sum_{n\geq 1}\sum_l p_{\mathrm{T},l}^{track}(\mathrm{P}V_n)}{(k\cdot n_{\mathrm{track}}^{\mathrm{PU}})}},$$

where $\mathrm{P}V_0$ is the PV, $\mathrm{P}V_j$ are all other vertices, $n_{\mathrm{track}}^{\mathrm{PU}}$ is the number of all tracks not associated to the PV, and k is tuning parameter, usually defined as $k = 0.01$. R_{p_T}, on the other hand, is defined as the scalar p_T sum of tracks associated to the jet and the PV divided by the jet p_T after the complete aforementioned calibration:

$$R_{p_\mathrm{T}} = \frac{\sum_k p_{\mathrm{T},k}^{track}(\mathrm{P}V_0)}{p_\mathrm{T}^{\mathrm{jet}}}.$$

The distributions of corrJVF and R_{p_T} are displayed in Figure 5.5 alongside the resulting JVT score. Since the JVT uses information from the ID, it is only applicable to central jets with $|\eta| < 2.4$. More forward jets are analyzed by the dedicated *forward JVT* [98]. The latter analyzes information on the jet shape from the forward calorimeters and extrapolates the JVT based on topological correlations among the particles originating from a pile-up interaction.

5.4.4. Identification of *b*-jets

Jets containing hadrons with *b*-quarks, referred to as *b*-jets, play a unique role within ATLAS. Specific properties of these hadrons make identifying *b*-jets possible, a process

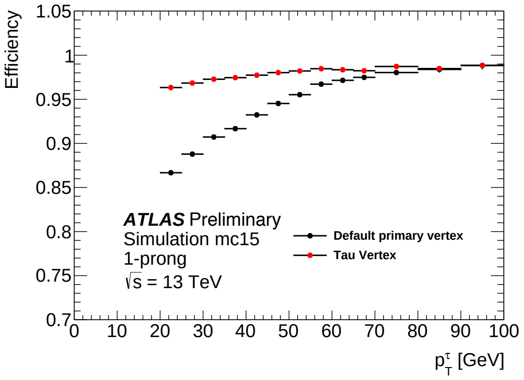

Figure 5.6.: Efficiency for correct production vertex assignment in 1-prong tau decays for the tau reconstruction algorithm and the default choice of the vertex with the highest $\sum p_T^2$, as a function of $\tau_{\text{had-vis}}$ p_T (left) and of the number of reconstructed vertices in the event (right) [101].

known as b-tagging. The most important of these properties is the relatively long average lifetime of roughly $\tau_B = 1.5$ ps [9], corresponding to a proper decay length of 0.5 mm. Thus, the decay products of b-hadrons can often be associated with a displaced vertex. Additionally, b-hadron decays often decay semi-leptonically, producing electrons or muons in the final state that exhibit a significant transverse momentum relative to the jet axis due to the high mass of the mother particle. The two most frequently used b-tagging algorithms are the *MV2c10* algorithm [99] and the *DL1r* [100] algorithm. The former deploys a boosted decision tree (BDT) that combines the output of several sub-classifiers. DL1r, on the other hand, uses a more modern deep learning approach. A recurrent neural network (RNN) was trained such that it performs better than the MV2c10 algorithm, particularly for high values of p_{T}.

5.5. Hadronically decaying τ-leptons

As mentioned in Section 2.5, τ-leptons usually decay before reaching the innermost layer of the detector into a leptonic (τ_{lep}, BR≈35%) or a hadronic (τ_{had}, BR≈65%) final state with at least one neutrino. Electrons and muons from leptonic τ decays cannot be distinguished from those of other origins. Therefore, no dedicated reconstruction algorithms for leptonically decaying τ-leptons exist. However, hadronic τ decays produce distinct signatures in the detector that can be reconstructed as objects. These are referred to as $\tau_{\text{had-vis}}$ candidates, where the index '$_{\text{vis}}$' excludes the neutrino in the final state that is not reconstructed [101].

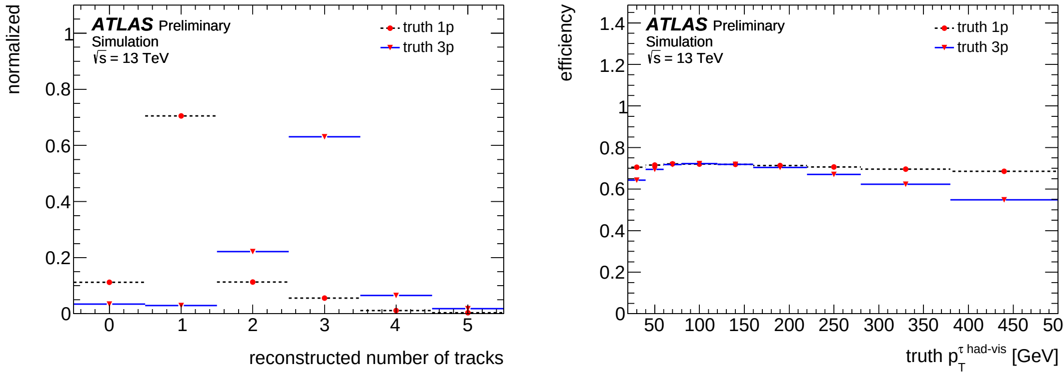

Figure 5.7.: Number of reconstructed tracks for $\tau_{\text{had-vis}}$ candidates from true 1-prong and 3-prong tau decays (left) and efficiency for reconstructing the same number of tracks as the number of charged decay products of the tau lepton as a function of $\tau_{\text{had-vis}}$ p_T (right) [101].

5.5.1. Reconstruction

The reconstruction of a $\tau_{\text{had-vis}}$ candidate starts with a *seed jet*. These are jets that were reconstructed by the anti-k_t algorithm with a radius parameter of $R = 0.4$. In contrast to the jets described in Section 5.4, seed jets for the $\tau_{\text{had-vis}}$ reconstruction are calibrated using the *local hadronic calibration* (LC) [91]. Additionally, seed jets must fulfill the requirements $p_{\text{T}} > 10$ GeV and $|\eta| < 2.5$ to be selected. Again, the crack-region $1.37 < |\eta| < 1.52$ is excluded.

After the seed jet was established, the dedicated *vertex association* takes place. Its goal is to identify the vertex at which the τ-lepton was produced (TV) rather than the PV of the event. Knowing the TV later allows associating tracks to the τ_{had} decay more precisely and suppressing the contribution from pile-up tracks. For the vertex association, the algorithm explained in Section 5.1 is used, with the requirement that the tracks must lie inside a $\Delta R = 0.2$ cone around the seed jet axis. Afterwards, the impact parameters of the $\tau_{\text{had-vis}}$ candidate are recalculated with respect to the TV. Figure 5.6 shows the efficiency of correctly assigning the τ_{had} production vertex for 1-prong $\tau_{\text{had-vis}}$ candidates as a function of p_{T} and the number of vertices in the event. It can be seen that for low values of p_{T} and large numbers of vertices, the dedicated tau-vertex-association is an improvement of the standard PV association.

Only tracks that lie inside the core region, defined as a $\Delta R = 0.2$ cone around the jet axis, are associated to the $\tau_{\text{had-vis}}$ candidate. Furthermore, each track must fulfill the following criteria:

- $p_{\text{T}} > 1$ GeV,
- at least two associated hits in the Pixel Detector (including the IBL),
- at least seven hits in total in the Pixel- and the SCT detectors,

- $|d_0| < 1.0$ mm,
- $z_0 \sin(\theta) < 1.5$ mm.

The selection mentioned above was optimized to maximize the fraction of 1-prong and 3-prong tau decays reconstructed with the correct charged particle multiplicity [101]. Figure 5.7 shows the number of reconstructed tracks for simulated 1-prong and 3-prong decays and the overall efficiency of the $\tau_{\text{had-vis}}$ reconstruction as a function of p_{T}. It appears that high-p_{T} 3-prong decays are sometimes falsely reconstructed as having only two associated tracks. This can happen when, due to the considerable boost of the decay products, two tracks are so close that the detector cannot resolve them.

5.5.2. Energy calibration

The energy estimation of a $\tau_{\text{had-vis}}$ candidate starts by taking the seed jet's original LC calibration that already accounts for dead material in the calorimeters and deposits too low to trigger the formation of TopoClusters. Then, two additional corrections are applied to arrive at the *baseline* calibration, entirely based on information from the calorimeters. The first one takes pile-up into account, whereas the second one estimates the effect of decay products not reaching the calorimeter. Both corrections are quantified via a single function depending on $|\eta|$ and the number of primary vertices, N_{PV}.

The baseline energy calibration generally performs well but has a poor resolution for low-p_{T} $\tau_{\text{had-vis}}$ candidates [102]. For this reason, a tracking-based reconstruction algorithm for the hadrons in a τ_{had} decay was developed, known as Tau Particle Flow (TPF) [103]. A boosted regression tree (BRT) then combines the baseline calibration with the tracking-based TPF and more low-level variables to provide a solid energy estimate for $\tau_{\text{had-vis}}$ candidates across a large p_{T} spectrum.

The four-momentum of the $\tau_{\text{had-vis}}$ candidate is recalculated after the energy calibration assuming a vanishing mass.

5.5.3. Identification

After all the previously mentioned reconstruction steps, most $\tau_{\text{had-vis}}$ candidates are actually *fakes* stemming from quark- or gluon-initiated jets falsely reconstructed as hadronically decaying τ-leptons. An additional identification algorithm, referred to as τ_{had}-ID, is deployed to discriminate these fakes from true τ-leptons. More precisely, two different BDT-based classifiers exist for 1-prong and 3-prong $\tau_{\text{had-vis}}$ candidates, respectively. The input features are twelve high-level input variables based on the TopoClusters and tracks in the core ($\Delta R < 0.2$) or isolation ($0.2 < \Delta R < 0.4$) region, where not all of them are used for both classifiers [101]. Most of the input features quantify the shape and internal energy distribution of the jet. However, also the displacement of the TV with respect to the PV is exploited. The central energy fraction, f_{cent}, provides the best separation power. It is defined as the fraction of calorimeter transverse energy deposited in the central region ($\Delta R < 0.1$) to all energy deposited in the core region. The classifiers are

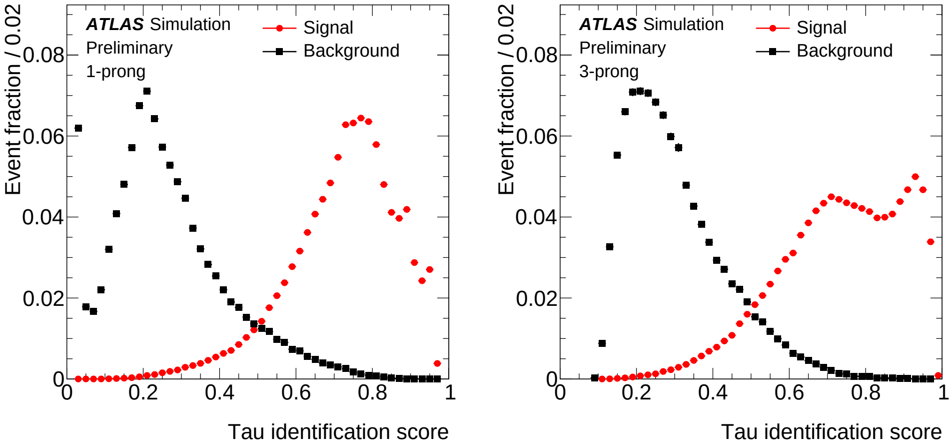

Figure 5.8.: Distribution of the BDT-based τ_{had}-ID score for true (red) and misidentified (black) 1-prong (left) and 3-prong (right) $\tau_{\text{had-vis}}$ candidates [102].

trained on simulated $Z/\gamma^* \rightarrow \tau\tau$ and di-jet events as signal and background, respectively. Figure 5.8 shows the distribution of the BDT-based τ_{had}-ID score for true and misidentified as well as for 1-prong and 3-prong $\tau_{\text{had-vis}}$ candidates evaluated on simulated data. The τ_{had}-ID score as shown here is often flattened vs p_{T}, and subsequently, the x-axis is transformed so that the signal exhibits a perfectly flat distribution. After these steps, requiring a $\tau_{\text{had-vis}}$ candidate to exceed a given τ_{had}-ID score (ϵ) corresponds directly to tuning the classifier to the signal efficiency ϵ. Based on this, a set of working points for the $\tau-$ID are defined. A summary of their signal efficiencies and background rejections is shown in Table 5.1.

In 2019, a new τ_{had}-ID classification algorithm was introduced [104]. It is based on a recurrent neural network (RNN) and uses twelve high-level input variables almost identical to those of the BDT-based classifier mentioned above. However, the recurrent structure of the network in combination with long short-term memory architecture [105] allows processing sequences of a priori unknown length. Therefore, the RNN-based classifier

	Signal efficiency		Background rejection BDT		Background rejection RNN	
Working point	1-prong	3-prong	1-prong	3-prong	1-prong	3-prong
Tight	60%	45%	40	400	70	700
Medium	75%	60%	20	150	35	240
Loose	85%	75%	12	61	21	90
Very loose	95%	95%	5.3	11.2	9.9	16

Table 5.1.: List of defined working points with fixed true $\tau_{\text{had-vis}}$ selection efficiencies and the corresponding background rejection factors for misidentified $\tau_{\text{had-vis}}$ in dijet events for the BDT and RNN classifiers [104].

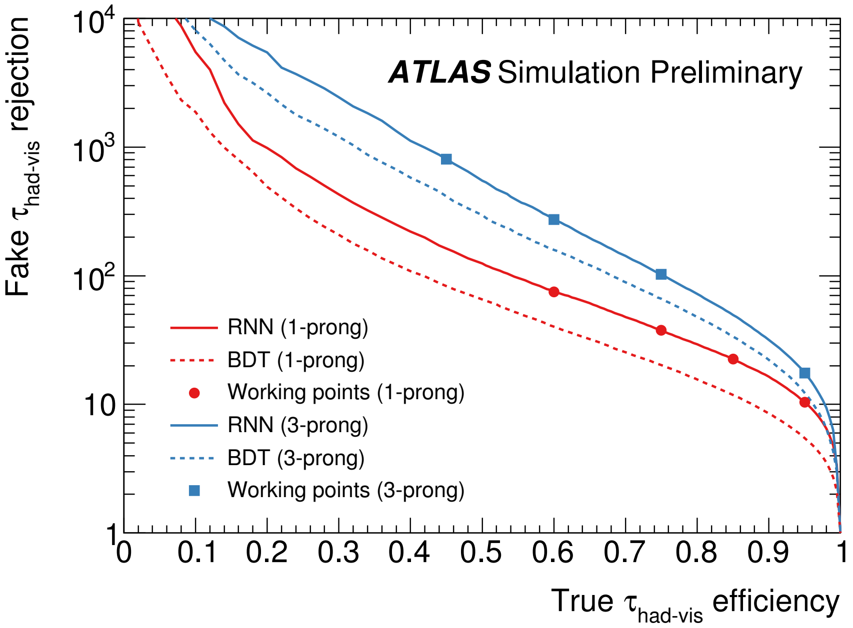

Figure 5.9.: Rejection power for quark and gluon jets misidentified as $\tau_{\text{had-vis}}$ (fake $\tau_{\text{had-vis}}$) depending on the true $\tau_{\text{had-vis}}$ efficiency. Shown are the curves for 1-prong (red) and 3-prong (blue) $\tau_{\text{had-vis}}$ candidates using the RNN-based (full line) and the BDT-based (dashed line) identification algorithms. The markers indicate the four defined working points Tight, Medium, Loose and Very loose with increasing signal selection efficiencies [104].

can also take low-level input variables based on each track or TopoCluster associated with the $\tau_{\text{had-vis}}$ candidate into account, significantly improving its performance compared to that of the BDT-based classifier.

Figure 5.9 shows the background rejection power as a function of the signal efficiency for both classifiers and split into 1-prong and 3-prong $\tau_{\text{had-vis}}$ candidates evaluated on simulated data. Across all working points, the background rejection of the RNN-based classifier is roughly twice as high as that of the BDT-based one, corresponding to a roughly four-fold background reduction in searches for $\tau_{\text{had}}\,\tau_{\text{had}}$ final states.

Quark- or gluon-initiated jets are not the only source of fakes. Electrons can also be falsely reconstructed as $\tau_{\text{had-vis}}$ candidates. Hence, $\tau_{\text{had-vis}}$ candidates inside a $\Delta R = 0.4$ cone around a reconstructed electron are rejected if the latter passes the very loose (95% signal efficiency) electron identification working point as explained in Section 5.2.

5.5.4. Truth-matching

On simulated data, $\tau_{\text{had-vis}}$ candidates that originate from actual hadronically decaying τ-leptons can be marked as such via a process known as *truth-matching*. A $\tau_{\text{had-vis}}$ candidate counts as truth-matched if its momentum vector lies within a $\Delta R = 0.2$ cone around the momentum of a τ-lepton on truth-level. $\tau_{\text{had-vis}}$ candidates that are not truth matched most likely originate from a quark- or gluon-initiated jet and are referred to as *fakes*.

5.6. Missing transverse momentum

As neutrinos do not interact with the detector material, they do not cause any signal and cannot be measured directly. They can, nonetheless, be reconstructed indirectly due to the conservation of momentum. As mentioned in Section 4.3, partons carry a random fraction of the momentum along the beam axis of the proton at the LHC. Their transverse momentum, however, is approximately zero. Therefore, the transverse component of the four-momenta of all outgoing particles of a given proton collision must add up to zero. Any significant deviation from that indicates an undetected particle (e.g. a neutrino) carrying away the *missing transverse momentum*. It is calculated as the negative vectorial sum of the transverse components of all reconstructed photons, electrons, muons, jets, and τ-leptons, and the *soft* contribution. The latter corresponds to the sum of all tracks in the ID that are not associated with any of the previously mentioned reconstructed objects [106]:

$$E_i^{\text{miss}} = -\left(p_i^{\text{soft}} + \sum_r p_i^r\right),$$

where i can be x or y. Its absolute value is referred to as the *missing transverse energy*, $E_{\text{T}}^{\text{miss}}$.

5.7. Object overlap removal

A single true object can spark the creation of multiple, geometrically overlapping reconstructed objects. Therefore, an *overlap removal* is performed after the reconstruction according to a set of rules to avoid ambiguities. Most of these rules depend on the value of ΔR between two reconstructed objects, where the object with the lower reconstruction efficiency is usually removed from the event. The following criteria are relevant for this thesis:

- jets within $\Delta R < 0.2$ of a $\tau_{\text{had-vis}}$ candidate are removed,
- jets within $\Delta R < 0.4$ of an electron or muon are removed,
- $\tau_{\text{had-vis}}$ candidates within $\Delta R < 0.2$ of an electron or muon are removed,
- electrons within $\Delta R < 0.2$ of a muon are removed.

CHAPTER 6

Measurement of τ_{had} identification efficiency

As τ-leptons play an important role in many measurements and searches within and beyond the SM at ATLAS, the τ_{had}-ID algorithms described in Section 5.5.3 are widely used across the collaboration. Therefore, it is imperative to understand the algorithms' performance on simulated and recorded data. A scale factor is introduced, defined as the ratio of the efficiency on recorded data to that on MC simulated hadronic τ-decays:

$$SF = \frac{\epsilon_{data}}{\epsilon_{MC}}, \tag{6.1}$$

where the efficiency is defined as the fraction of true $\tau_{\text{had-vis}}$ candidates that are correctly classified as such and pass the identification:

$$\epsilon = \frac{\tau_{\text{had-vis}}(\text{true, pass})}{\tau_{\text{had-vis}}(\text{true})}. \tag{6.2}$$

Applying this scale factor and its uncertainties to simulated τ_{had} decays allows a direct comparison with recorded data.
The scale factors are binned in different quantities of the $\tau_{\text{had-vis}}$ candidate to cover possible biases of the respective τ_{had}-ID algorithm. For the RNN-based τ_{had}-ID, these are

- Transverse momentum ($p_T[\text{GeV}] \in (20, 25] \vee (25, 30] \vee (30, 40] \vee (40, \infty]$),
- Number of prongs (1 or 3),
- Working point of the τ_{had}-ID (*loose*, *medium*, or *tight*).

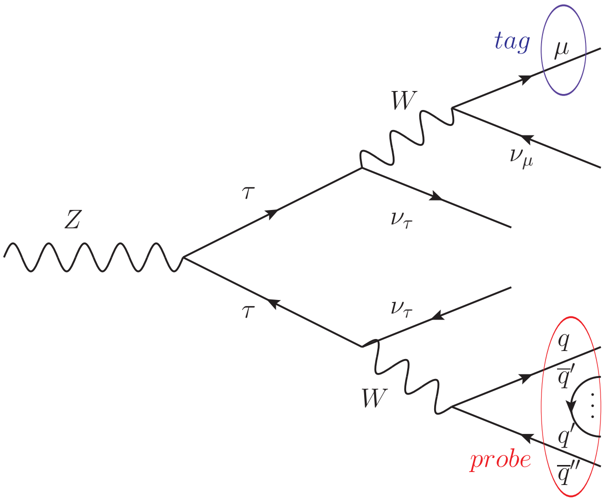

Figure 6.1.: The tag-and-probe method: $Z \to \tau_\mu \tau_{\text{had}}$ events are tagged by the muon. The τ_{had} is probed for the measurement.

For the BDT-based τ_{had}-ID, it was found that the signal modelling depends strongly on the region of the detector in which the $\tau_{\text{had-vis}}$ candidate was reconstructed. Therefore, the scale factors are provided in the following binning:

- Barrel ($|\eta| < 1.37$) vs endcap ($|\eta| < 1.52$),
- Number of prongs (1 or 3),
- Working point of the τ_{had}-ID (*loose*, *medium*, or *tight*).

The biggest challenge in experimentally determining the scale factors as defined in Eq. 6.1 is to estimate the number of true $\tau_{\text{had-vis}}$ candidates on recorded data and the corresponding uncertainties. To do so, a *tag-and-probe* approach in a dataset enriched in $Z \to \tau_\mu \tau_{\text{had}}$ events is deployed. The background estimate exploits the different charge correlations of signal and background. The contribution of true $\tau_{\text{had-vis}}$ candidates is estimated via a maximum likelihood fit of $|\Delta\eta(\mu, \tau_{\text{had-vis}})|$. The fit results are then used to extract the scale factors and the corresponding uncertainties. The different steps are described in more detail in the following.

6.1. Event selection

The considered data was recorded between 2016 and 2018 at a centre-of-mass energy of $\sqrt{s} = 13$ TeV corresponding to an integrated luminosity of roughly $\int L\ dt = 136\ \text{fb}^{-1}$. To maximize the fraction of true $\tau_{\text{had-vis}}$ candidates, $Z \to \tau_\mu \tau_{\text{had}}$ events are analyzed where one τ-lepton decays into a muon, and the other one decays hadronically. What is referred to as a tag-and-probe technique exploits the high reconstruction efficiency and

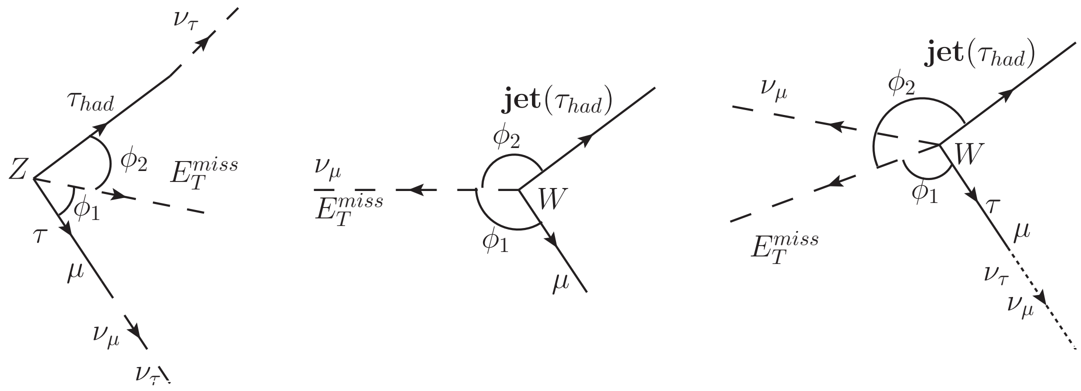

Figure 6.2.: Schematic depiction of kinematics in the transverse plane for three different processes contributing in the signal region. From left to right: $Z \to \tau_\mu \tau_{\text{had}}$, $W(\to \mu\nu_\mu)$+jet, $W(\to \tau\nu_\tau)$+jet. The following notation is used: $\phi_1 = \phi(E_{\text{T}}^{\text{miss}}) - \phi(\mu)$, $\phi_2 = \phi(E_{\text{T}}^{\text{miss}}) - \phi(\tau_{\text{had-vis}})$.

background rejection for muons at ATLAS. An event is ‘tagged’ by the existence of a muon, marking it for further analysis. The $\tau_{\text{had-vis}}$ candidate is then used as the ‘probe’ - the object on which the actual measurement is conducted. The Feynman diagram of this decay can be seen in Figure 6.1.

The following describes the requirements that must be met for an event to be accepted in the signal region (SR). One of the muon triggers `HLT_mu26_ivarmedium` and `HLT_mu50` must have fired[1]. There must be exactly one reconstructed muon, one $\tau_{\text{had-vis}}$ candidate and no reconstructed electron. The muon must also be geometrically matched to the respective trigger that fired[2], pass the *medium* identification requirement, and its transverse momentum must lie between 27.3 and 40 GeV. Furthermore, the muon must pass the ‘FCTightTrackOnly_FixedRad’ isolation criterion. The absolute value of the charge of the $\tau_{\text{had-vis}}$ candidate must be exactly one, and it must lie in the fiducial volume of the detector ($|\eta| < 2.47$). The transverse mass between the muon and the missing transverse momentum must be smaller than 50 GeV ($m_T(\mu, E_{\text{T}}^{\text{miss}}) < 50$ GeV) and the sum of the cosines of $\Delta\phi$ between the missing transverse energy and the $\tau_{\text{had-vis}}$ candidate and the missing transverse momentum and the muon must be greater than -0.15:

$$\sum \cos(\Delta\phi) = \cos(\phi(E_{\text{T}}^{\text{miss}}) - \phi(\mu)) + \cos(\phi(E_{\text{T}}^{\text{miss}}) - \phi(\tau_{\text{had-vis}})) > -0.15.$$

The cut on $\sum \cos(\Delta\phi)$ suppresses the contribution from the W+jets process. This is apparent when considering Figure 6.2, which schematically depicts the transverse kinematics of this background contribution and the signal, $Z \to \tau_\mu \tau_{\text{had}}$. Only for the latter,

---

[1] HLT is short for ’high level trigger’. ’mu50’ and ’mu26’ refer to a muon whose p_{T} exceeds 50 or 26 GeV on trigger level, respectively. ’ivarmedium’ refers to the online ID requirement of that trigger.

[2] Similar to the truth-matching for $\tau_{\text{had-vis}}$ candidates described in Section 5.5.4, a muon is matched to a trigger if their four-momenta lie within a $\Delta R = 0.2$ cone.

the angles $\phi_1 \equiv \phi(E_{\mathrm{T}}^{\mathrm{miss}}) - \phi(\mu)$ and $\phi_2 \equiv \phi(E_{\mathrm{T}}^{\mathrm{miss}}) - \phi(\mu)$ tend to have values below 90°, leading to primarily positive values of $\sum \cos(\Delta\phi)$.
Additionally, the visible mass of the muon-$\tau_{\text{had-vis}}$-system must lie within 45 and 90 GeV ($45 < m_{\text{vis}} < 90$ GeV), a requirement known as the Z-mass-window-cut. The muon and the $\tau_{\text{had-vis}}$ candidate must be back-to-back ($\Delta\phi(\mu, \tau_{\text{had-vis}}) > 2.4$), and there must be one or more primary vertices but no b-tagged jet. The signal process $Z \to \tau_\mu \tau_{\text{had}}$ is charge asymmetric, meaning that the tag (μ) and the probe ($\tau_{\text{had-vis}}$) are expected to have opposite electric charges. Enforcing it in the event selection is referred to as the opposite sign (OS) requirement in the signal region.
The signal region is further split depending on some properties of the $\tau_{\text{had-vis}}$ candidate:

- two prong bins (1-prong and 3-prong),
- four disjoint slices of the $\tau-$ID score,
- only for the RNN-based τ_{had}-ID: four p_T bins (20-25, 25-30, 30-40, >40 GeV),
- only for the BDT-based τ_{had}-ID: two $|\eta|$ bins (< 1.37 and > 1.52).

The four disjoint slices of the $\tau-$ID score are constructed from the working points mentioned in Section 5.5.3. For example, the *loose-not-medium* slice contains all $\tau_{\text{had-vis}}$ candidates that pass the *loose* requirement, but fail the *medium* one, corresponding to the $\tau-$ID score interval [0.75, 0.85] for 1-prong and [0.6, 0.75] for 3-prong $\tau_{\text{had-vis}}$ candidates. The other three slices (*not-loose*, *loose-not-medium*, *tight*) are constructed analogously.
This results in 32 (16) disjoint categories in the signal region for the RNN(BDT)-based τ_{had}-ID. Four control regions for every category of the signal region are important for the background estimate (see Section 6.2). They are explained in the following, where only differences to the signal region are mentioned.

The QCD control region can be retrieved from the signal region by inverting the muon isolation requirements.

The Top Control Region is defined by inverting the b-veto into a b-tag. Furthermore, the upper limit on the muon p_T, the Z-mass-window-cut, and the back-to-back requirement are neglected. Additionally, the transverse mass between the muon and the missing transverse energy has to be greater than 40 GeV ($m_{\mathrm{T}}(\mu, E_{\mathrm{T}}^{\mathrm{miss}}) > 40$ GeV).

The W control region requires the transverse mass between the muon and the missing transverse energy to be greater than 60 GeV ($m_{\mathrm{T}}(\mu, E_{\mathrm{T}}^{\mathrm{miss}}) > 40$ GeV)) and the missing transverse energy itself to exceed 30 GeV ($E_{\mathrm{T}}^{\mathrm{miss}} > 30$ GeV). Also, the sum of cosines has to be below zero ($\sum \cos(\Delta\phi) < 0$) and the back-to-back-requirement is dropped.

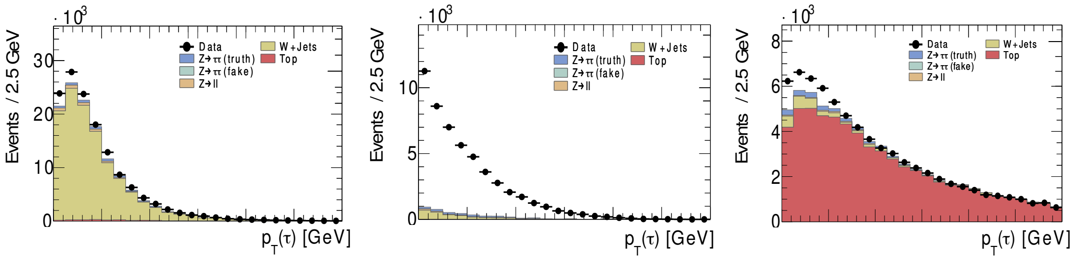

Figure 6.3.: Pre-fit $p_{\mathrm{T}}(\tau)$ distribution for 1-prong in the p_{T} and τ_{had}-ID inclusive control regions. From left to right: W control region, QCD control region, and Top control region.

The high-m_{vis} control region is like the signal region but the cut on the Z-mass-window-cut is replaced by a cut that requires the visible mass to be greater than 100 GeV. Like the QCD control region, the high-m_{vis} control region is dominated by the SS contribution. This additional control region helps to understand the SS contribution in a region that kinematically differs from the signal region but applies the same isolation requirement on muon, which proved beneficial for the likelihood-maximization described in Section 6.3.

Figure 6.3 shows the p_{T}- and τ_{had}-ID-inclusive $|\Delta\eta(\mu, \tau_{\mathrm{had\text{-}vis}})|$ distributions in the QCD, Top, and W control regions for 1-prong $\tau_{\mathrm{had\text{-}vis}}$ candidates. The different contributions are taken directly from MC simulations. The mismatch between simulation and data is due to the absence of an estimate for the multijet contribution.

6.2. Background estimate

The background estimate described in the following is conducted independently for each category of the signal region. It can be used to model any distribution. Often, the variable $|\Delta\eta(\mu, \tau_{\mathrm{had\text{-}vis}})|$ is shown. It is used as the input for the maximum-likelihood fit described in Section 6.3. Four main background processes have to be considered for this analysis:

- QCD (multijet),
- W+jets,
- Top (single top & top-antitop ($t\bar{t}$) events),
- $Z \to \ell\ell$(where ℓ can be an electron or a muon).

Like in most analyses, the QCD background is estimated with a data-driven technique. For all other backgrounds, MC simulated events are used. A full list of the samples used in this analysis can be found in Appendix B.1. The data yield in the opposite-sign (OS)

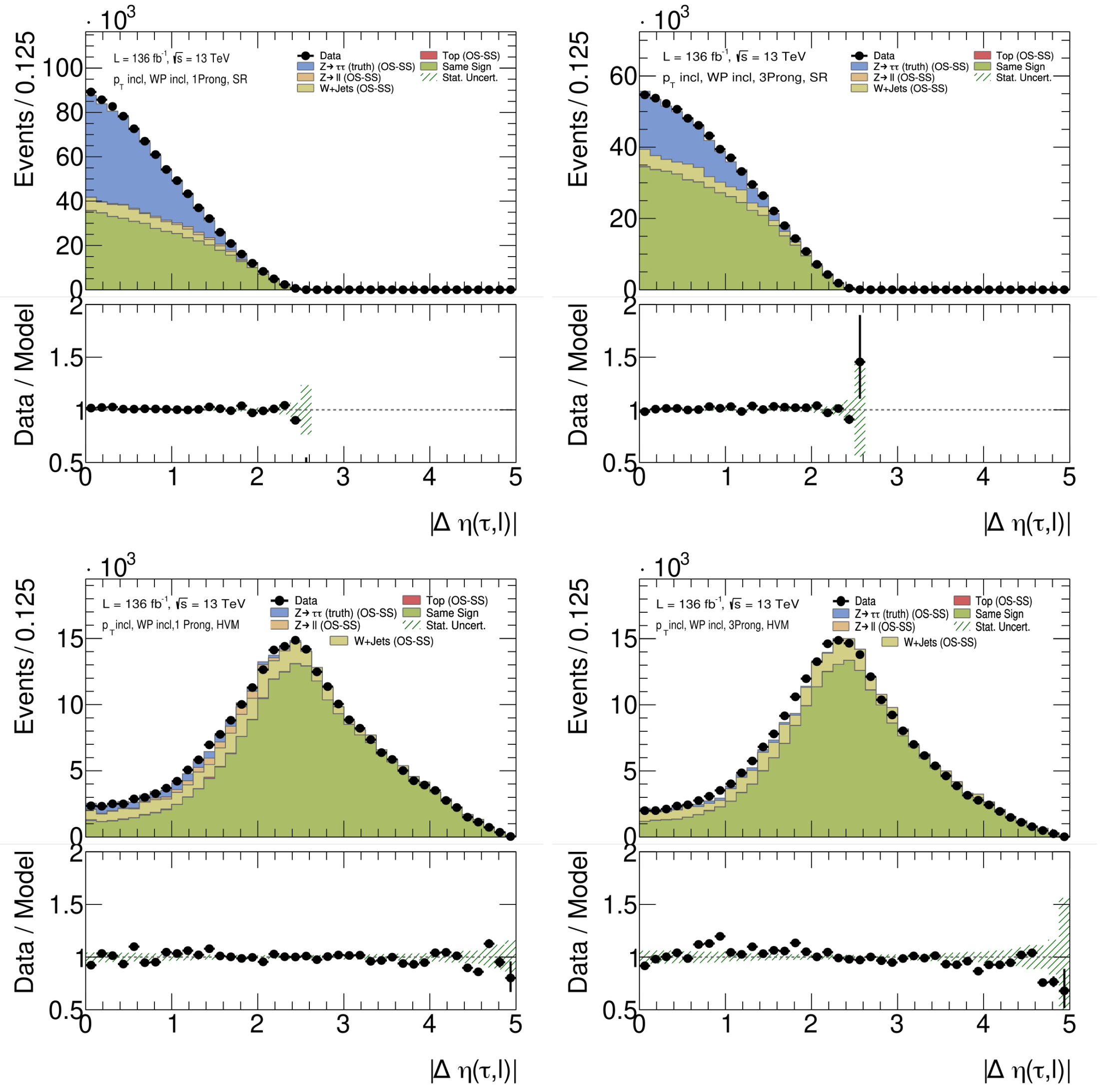

Figure 6.4.: Pre-fit $|\Delta\eta(\mu, \tau_{\text{had-vis}})|$ distribution for p_{T}- and τ_{had}-ID inclusive case. The figure is split into 1-prong versus 3-prong (left and right) and signal region versus high-m_{vis} region (top and bottom).

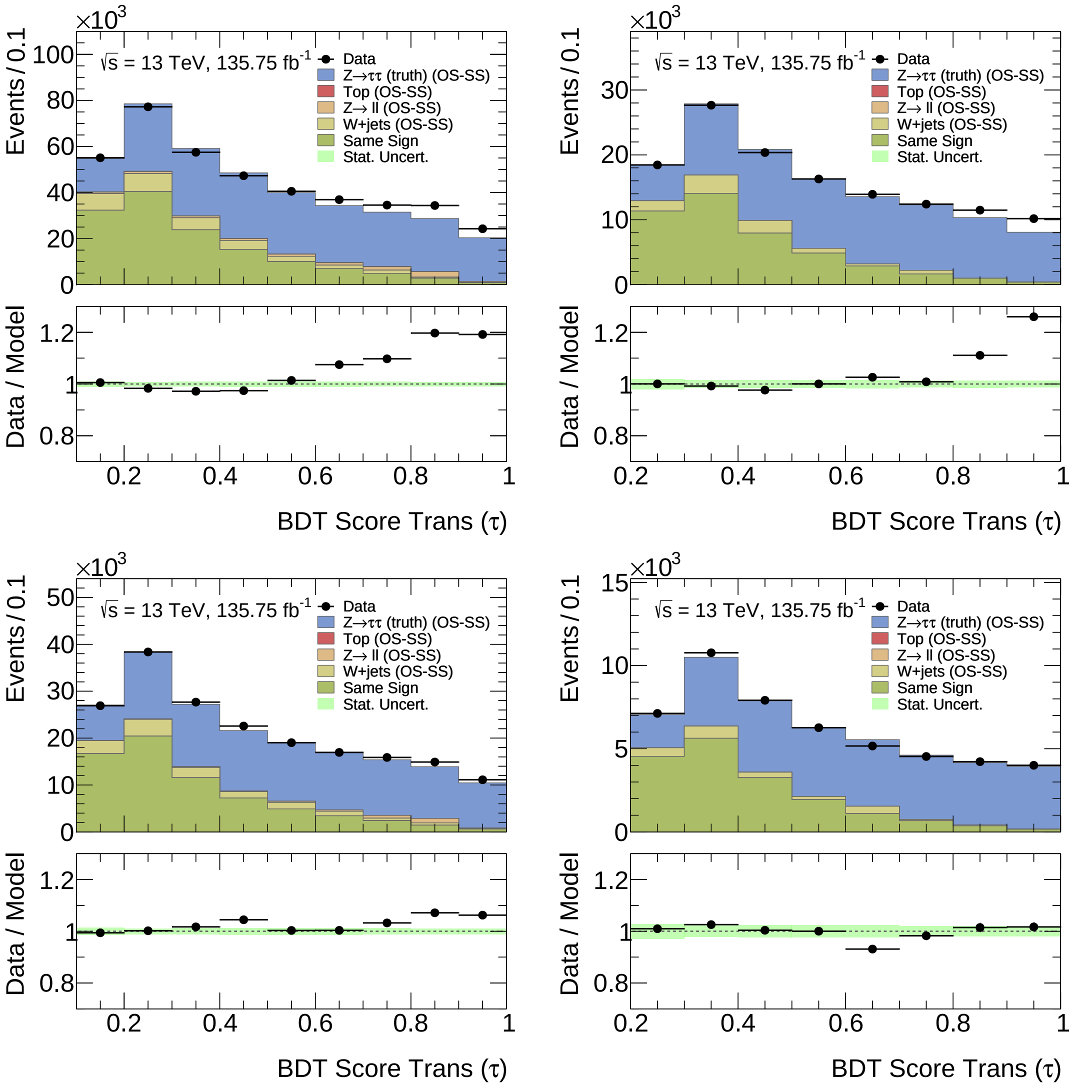

Figure 6.5.: Pre-fit τ_{had}-ID score distribution for the BDT-based classifier in the p_{T} inclusive signal region. The figure is split into 1-prong versus 3-prong (left and right) and low versus high $|\eta|$ (top and bottom).

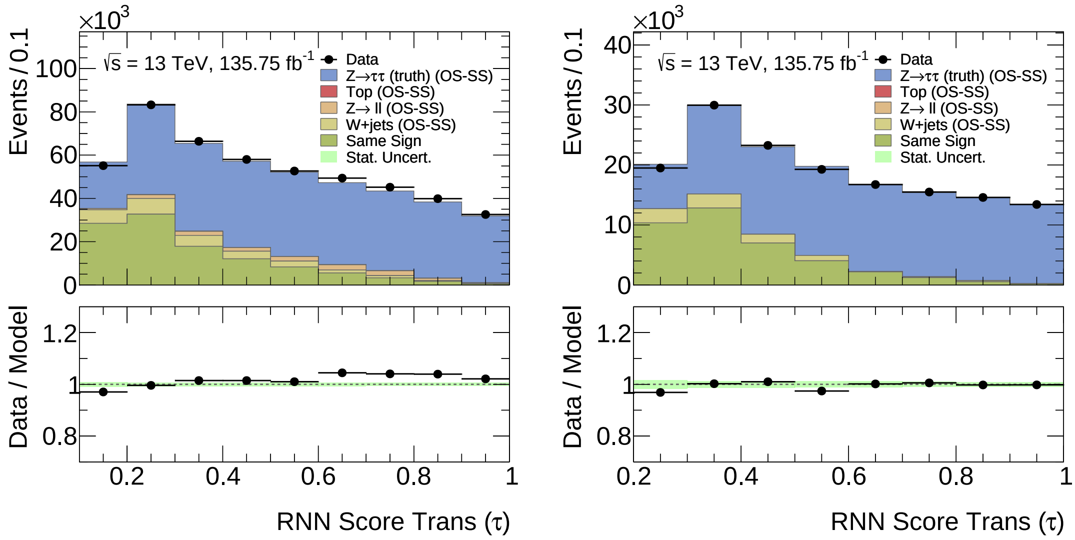

Figure 6.6.: Pre-fit τ_{had}-ID score distribution for the RNN-based classifier in the p_{T} inclusive signal region. The figure is split into 1-prong versus 3-prong (left and right).

signal region can be split into the different processes and is approximated by

$$N^{\text{OS}}_{\text{data}} = N^{\text{OS}}_{\text{QCD}} + N^{\text{OS}}_{Z\to\tau\tau} + N^{\text{OS}}_{Z\to\ell\ell} + k^{\text{OS}}_{W} \times N^{\text{OS}}_{W} + k^{\text{OS}}_{\text{Top}} \times N^{\text{OS}}_{\text{Top}}. \tag{6.3}$$

Here, k^{OS}_{W} and $k^{\text{OS}}_{\text{Top}}$ are referred to as k-factors. They are introduced to account for a possible mismodelling of the normalization of a given process and defined as the ratio of data to MC simulated events after subtracting backgrounds (BG) in the respective control region:

$$k_i = \frac{\text{Data} - \text{BG}_i}{\text{MC}}, \qquad i \in [W,\ \text{Top}].$$

Since the QCD contribution is almost charge symmetric, it can be estimated from the same-sign (SS) data yield after the subtraction of the contributions from all other processes:

$$N^{\text{OS}}_{\text{QCD}} = R_{\text{QCD}} \times (N^{\text{SS}}_{\text{data}} - N^{\text{SS}}_{Z\to\tau\tau} - N^{\text{SS}}_{Z\to\ell\ell} - k^{\text{SS}}_{W} \times N^{\text{SS}}_{W} - k^{\text{SS}}_{\text{Top}} \times N^{\text{SS}}_{\text{Top}}), \tag{6.4}$$

where R_{QCD} is defined as the ratio of OS to SS for QCD events. This ratio is measured on data in the dedicated QCD control region after the subtraction of all non-QCD contributions:

$$R_{\text{QCD}} = \frac{(\text{Data} - \text{MC})^{\text{OS}}}{(\text{Data} - \text{MC})^{\text{SS}}}$$

Inserting Eq. 6.4 into Eq. 6.3, and regrouping the resulting terms leads to

$$N^{\text{OS}}_{\text{data}} = R_{\text{QCD}} \times N^{\text{SS}}_{\text{data}} + N^{\text{add-on}}_{Z\to\tau\tau} + N^{\text{add-on}}_{Z\to\ell\ell} + N^{\text{add-on}}_{\text{W}} + N^{\text{add-on}}_{\text{Top}},$$

with the following add-on terms:

- $N^{\text{add-on}}_{Z\to\tau\tau} = N^{\text{OS}}_{Z\to\tau\tau} - R_{\text{QCD}} \times N^{\text{SS}}_{Z\to\tau\tau}$,
- $N^{\text{add-on}}_{Z\to\ell\ell} = N^{\text{OS}}_{Z\to\ell\ell} - R_{\text{QCD}} \times N^{\text{SS}}_{Z\to\ell\ell}$,
- $N^{\text{add-on}}_{\text{W}} = k^{\text{OS}}_{\text{W}} \times N^{\text{OS}}_{W} - R_{\text{QCD}} \times k^{\text{SS}}_{W} \times N^{\text{SS}}_{W}$,
- $N^{\text{add-on}}_{\text{Top}} = k^{\text{OS}}_{\text{Top}} \times N^{\text{OS}}_{\text{Top}} - R_{\text{QCD}} \times k^{\text{SS}}_{\text{Top}} \times N^{\text{SS}}_{\text{Top}}$.

Due to the structure of these add-on terms, this method is called the 'OS-SS method'. Figure 6.4 shows the p_{T}- and τ_{had}-ID-inclusive distributions of $|\Delta\eta(\mu, \tau_{\text{had-vis}})|$ for 1- and 3-prong as well as for signal and high-m_{vis} control region. The different event contributions were estimated with the OS-SS method. The distributions of the BDT- and RNN-based τ_{had}-ID score in the signal region are depicted in Figure 6.5 and Figure 6.6, respectively. A mismodelling of the BDT-based τ_{had}-ID score in the low-$|\eta|$ signal region is apparent, justifying the scale factor binning described in the introduction of Chapter 6. For the QCD estimate, the R_{QCD} factor accounts for a possible normalization difference between the SS and the OS contribution. It does, however, not cover a possible discrepancy regarding the distribution of $|\Delta\eta(\mu, \tau_{\text{had-vis}})|$. For this reason, an additional shape uncertainty is introduced. It is derived as the ratio of OS to SS distribution in the QCD control region after normalizing both and depicted in Figure 6.7. The QCD shape uncertainty is derived p_{T}-inclusively to decrease the influence of statistical fluctuation.

6.3. Fit strategy

Be μ_i the predicted event yield in the i-th bin of a given distribution. Then, the probability to observe n_i events in that bin can be expressed by the Poisson probability

$$P(n_i|\mu_i) = \frac{\mu_i^{n_i} e^{-\mu_i}}{n_i!}.$$

When considering a distribution with N bins, the probability to observe a given set of event yields in data can be written as

$$P = \prod_{i=1}^{N} P(n_i|\mu_i).$$

Normally, a model depends on a set of M nuisance parameters (NPs) contained in the vector $\boldsymbol{\theta}$. In that case, the likelihood function quantifies how compatible a set of values for these parameters is with the observed data. Assuming that each of these NPs, θ_j, is constrained by a Gaussian probability distribution function $\mathcal{N}(\theta_j|\tilde{\theta}_j, \sigma_{\theta_j})$ with expectation value $\tilde{\theta}_j$ and uncertainty σ_{θ_j}, the likelihood function can be written as the product of the Poisson probabilities of each bin and the Gaussian constraint for each NP:

$$L(\theta) = \prod_{i=1}^{N} P(n_i|\mu_i(\boldsymbol{\theta})) \cdot \prod_{j=1}^{M} \mathcal{N}(\theta_j|\tilde{\theta}_j, \sigma_{\theta_j}). \tag{6.5}$$

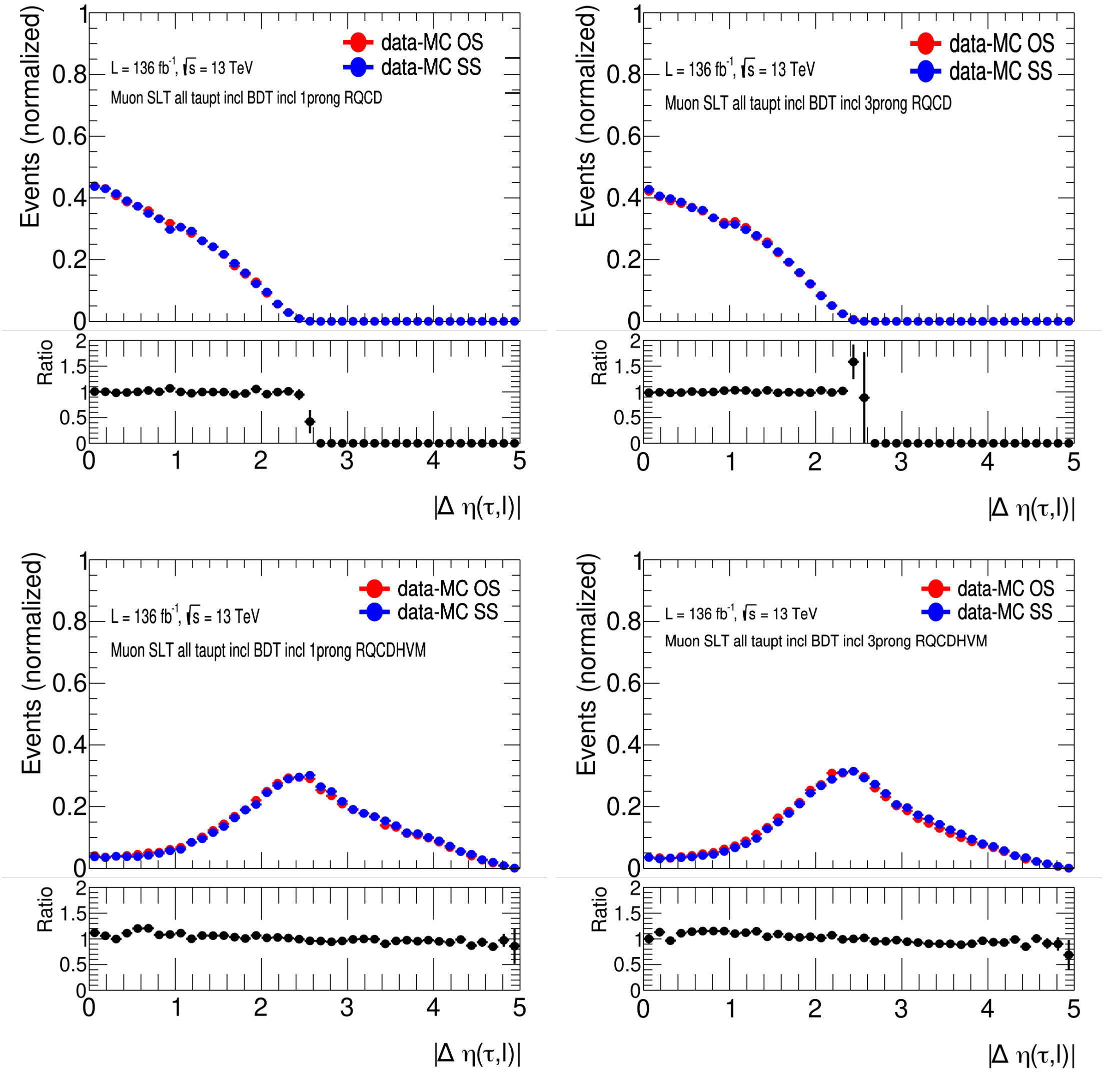

Figure 6.7.: Shape comparison between the normalized OS and SS $|\Delta\eta(\mu, \tau_{\text{had-vis}})|$ distributions in QCD control region for 1-prong (left), 3-prong (right), the Z-mass-window (top) and the high-m_{vis} region (bottom). Only statistical uncertainties are shown.

The likelihood function according to Eq. 6.5 is numerically maximized to find the set of NPs that is most compatible with the observed data. This is also referred to as *fitting* the model to the data. This maximum-likelihood fit to estimate the number of true $\tau_{\text{had-vis}}$ candidates on data uses $|\Delta\eta(\mu, \tau_{\text{had-vis}})|$ as the input variable and is conducted independently for BDT- and RNN-based τ_{had}-ID. Simulated $Z \rightarrow \tau_\mu \tau_{\text{had}}$ events, where the $\tau_{\text{had-vis}}$ candidate is truth-matched, are treated as the only signal. As it can be seen in Figure 6.4, the signal has predominantly small values of $|\Delta\eta(\mu, \tau_{\text{had-vis}})|$ while the background dominates for higher values, making $|\Delta\eta(\mu, \tau_{\text{had-vis}})|$ a well-separating variable. This effectively increases the degree of determination when maximizing the likelihood, resulting in more robust fit results with smaller uncertainties. Other distributions were tested, but the fit was found to perform best when based on $|\Delta\eta(\mu, \tau_{\text{had-vis}})|$.

The overall likelihood is a single function defined as the product of the likelihood functions of all bins of the signal and high-m_{vis} regions. All in all, 129 (191) nuisance parameters (NPs) are considered in the case of the BDT(RNN)-based classifier. Correlations between NPs can lead to correlations between the uncertainties of τ_{had}-ID scale factors. Therefore, the NPs correlated over the number of charged tracks and the p_{T} ($|\eta|$) of the $\tau_{\text{had-vis}}$ candidate are grouped in the case of RNN(BDT)-based classifier. In the group of correlated NPs are, for example, the uncertainty on the luminosity, cross section uncertainties, pile-up-reweighting uncertainty, and QCD shape uncertainties. On the other hand, k- and R_{QCD}-factors are calculated for each p_{T} ($|\eta|$) bin, and their uncertainties are therefore treated as uncorrelated across the bins of the scale factors. The likelihood is first maximized using the entire parameter space of all NPs to gauge what fraction of the uncertainty can be assigned to the group of (un-)correlated NPs. Then, the NPs of one group are fixed at the post-fit value of the first iteration. The fit is repeated where only the NPs of the other group can be varied. The fit converges at the same nominal values, and the post-fit uncertainty on the signal yield is attributed to the optimized group of NPs. The procedure is then repeated for the other group of NPs.

Designated NPs allow migration of the signal events between the different disjoint ID slices of the signal region. This strategy was chosen to ensure that the analysis is only sensitive to relative signal yield adjustments due to a possible mismodelling of the τ_{had}-ID score, rather than normalization effects such as a mismodelled reconstruction efficiency. For the BDT-based τ_{had}-ID, the migration from *not-loose* to *loose-not-medium* is restricted to help the fit converge.

Figure 6.8 and Figure 6.9 show the post-fit distribution of the BDT- and RNN-based τ_{had}-ID score, respectively. The plots were made by applying the post-fit values of all NPs from the fit in $|\Delta\eta(\mu, \tau_{\text{had-vis}})|$ to the pre-fit estimates of the corresponding variables. As expected, the agreement between data and model is better after the fit. Nonetheless, the BDT-based τ_{had}-ID score in the low-$|\eta|$ signal region is still mismodelled, which is observed as a rising slope in the ratio plot for high values of the τ_{had}-ID score fully contained within an interval that falls into the *tight* working point. This is not surprising as the fit can only vary the relative signal contributions between the disjoint ID slices and has no handle on the shape of the τ_{had}-ID score distribution within each slice. However, the overall shift of the signal from the tight to the looser categories indicates that the

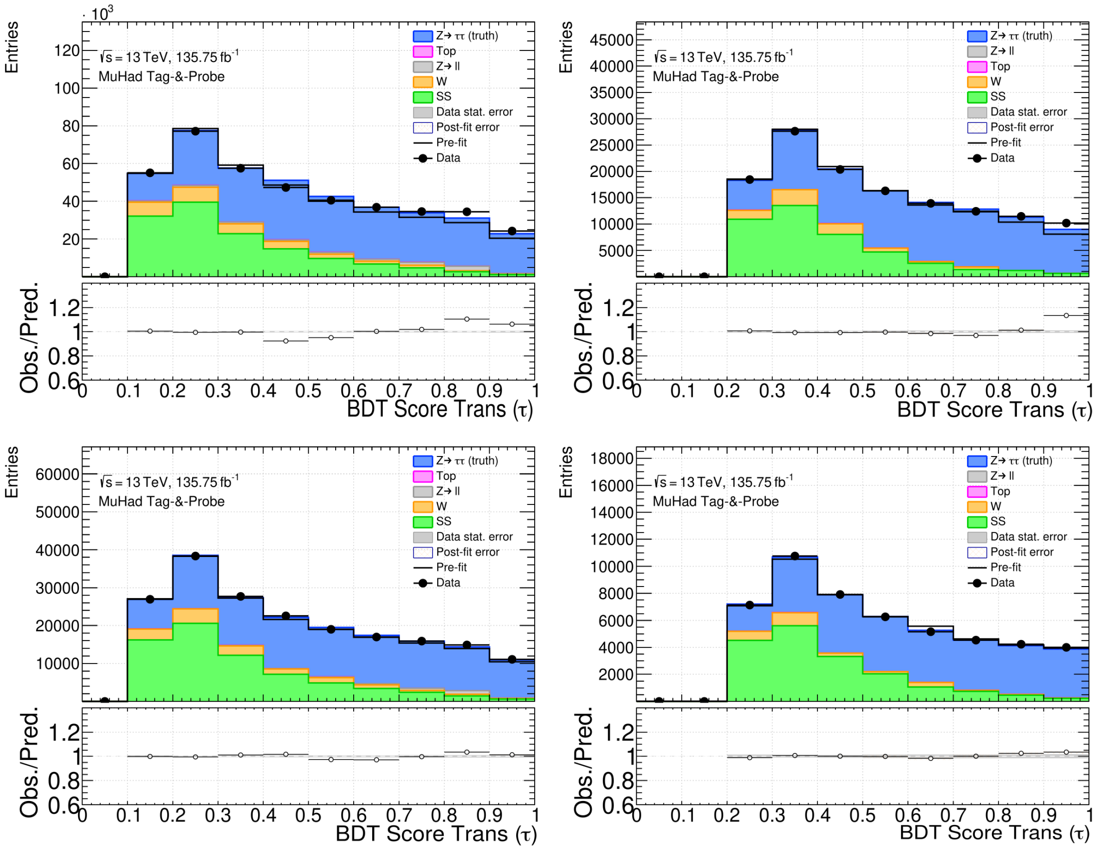

Figure 6.8.: Post-fit τ_{had}-ID score distribution for the BDT-based classifier in the p_{T} inclusive signal region. The figure is split into 1-prong versus 3-prong (left and right) and low versus high $|\eta|$ (top and bottom).

corresponding scale factor will be significantly different from 1, which can be observed in Figure 6.10.

The mismodelling of the BDT-based τ_{had}-ID score for $\tau_{\text{had-vis}}$ candidates in the detector barrel sparked some interest. The choice was made to not investigate this issue any further since the RNN-based classifier will be used in all future analyses at ATLAS, and its τ_{had}-ID score is well modelled.

6.4. Scale factor extraction

The scale factor is defined as the ratio of the efficiency on data and MC generated events (see Eq. 6.1 and Eq. 6.2). The amount of true $\tau_{\text{had-vis}}$ candidates that pass the identification can be calculated from the yields of truth-matched $Z \to \tau_\mu \tau_{\text{had}}$ contribution by summing over the disjoint τ_{had}-ID slices. For example, the yield for the medium working point, M, can be written as $M = MNT + T$, where MNT and T denote

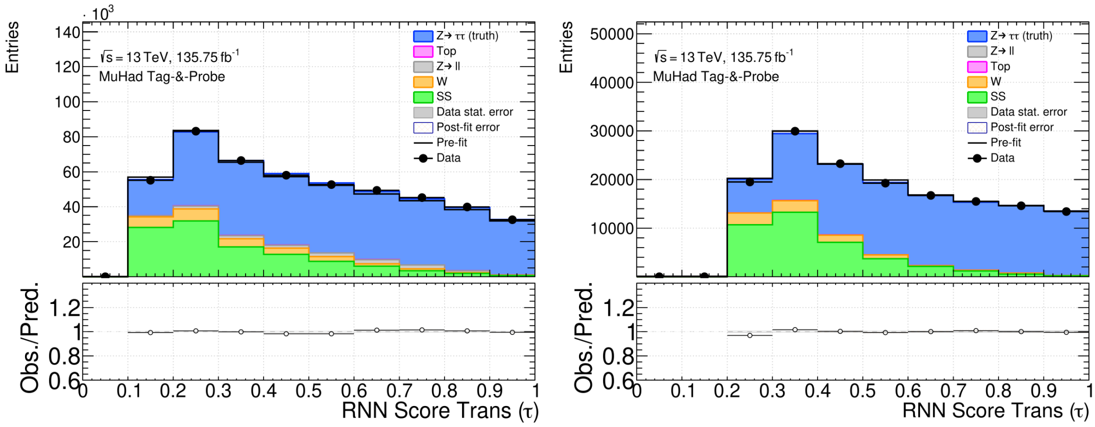

Figure 6.9.: Post-fit τ_{had}-ID score distribution for the RNN-based classifier in the p_{T} inclusive signal region. The figure is split into 1-prong versus 3-prong (left and right).

the yields in the *medium-not-tight* and *tight* slice of the signal region, respectively. On MC simulated events, these yields can be extracted directly from the truth-matched $Z \rightarrow \tau_\mu \tau_{\text{had}}$ events. On data, the number of true $\tau_{\text{had-vis}}$ candidates is the post-fit value of the truth-matched $Z \rightarrow \tau_\mu \tau_{\text{had}}$ contribution. The efficiency for the medium working point can be expressed as

$$\epsilon(M) = \frac{N_{MNT} + N_T}{N_{NL} + N_{LNM} + N_{MNT} + N_T}. \tag{6.6}$$

The efficiency is calculated analogously for the other working points of the τ_{had}-ID. When calculating the uncertainty of the efficiency, one has to consider that the numerator and the denominator are correlated. However, the efficiency of any working point can be expressed in terms of two uncorrelated terms A and B:

$$\epsilon = \frac{B}{A+B},$$

where B is the sum of terms that occur in numerator and denominator, and A is the sum of terms that only occur in the denominator. With this, the uncertainty of the efficiency can be expressed as:

$$\sigma_\epsilon = \frac{1}{(A+B)^2}\sqrt{B^2\sigma_A^2 + A^2\sigma_B^2}.$$

When calculating the uncertainty of the scale factor, the uncertainties ϵ_{data} and ϵ_{MC} are treated as uncorrelated:

$$\sigma_{SF} = SF \times \sqrt{\left(\frac{\sigma_{\epsilon_{MC}}}{\epsilon_{MC}}\right)^2 + \left(\frac{\sigma_{\epsilon_{data}}}{\epsilon_{data}}\right)^2}.$$

The final scale factors and their overall uncertainties can be seen in Figure 6.10 and Figure 6.11 for the BDT- and RNN-based classifier, respectively.

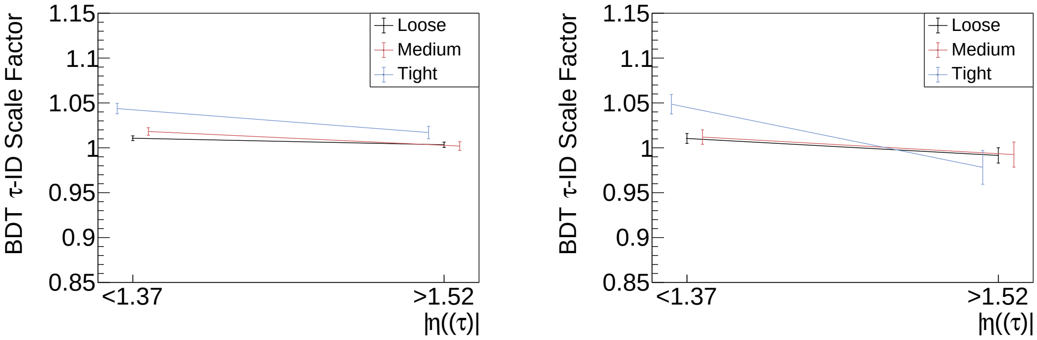

Figure 6.10.: BDT-based τ_{had}-ID scale factors for 1-prong (left) and 3-prong (right) as a function of $|\eta(\tau)|$. The scale factors are evaluated for the barrel ($|\eta(\tau)| < 1.37$) and endcap ($|\eta(\tau)| > 1.52$) region of the detector. The uncertainties include all statistical and systematic uncertainties except for the one dedicated to the lower τ−ID score cut value explained in Section 6.5.1.

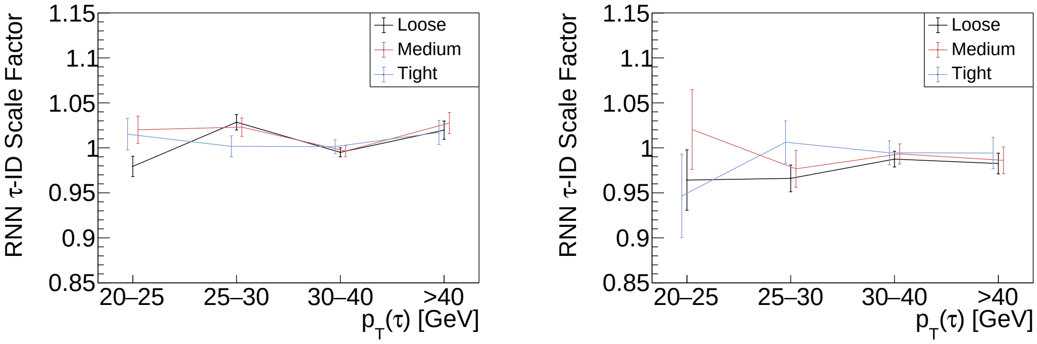

Figure 6.11.: RNN-based τ_{had}-ID scale factors for 1-prong (left) and 3-prong (right). The scale factors are evaluated for four bins of $p_{\text{T}}(\tau)$. The uncertainties include all statistical and systematic uncertainties except for the one dedicated to the lower τ−ID score cut value explained in Section 6.5.1.

6.5. Systematic uncertainties

The uncertainties on the scale factors play an important role as they have to be considered by any ATLAS analysis involving simulated events containing τ_{had} in the final state.
The overall uncertainties on the scale factors are predominantly of statistical nature. In particular, the low signal contribution in the *not-loose* bins of the signal region has a significant impact. The systematic uncertainties are differentiated into two groups: those that are correlated across the bins of the scale factor, and those that are not. As explained in Section 6.3, the grouping is different for the BDT- and RNN-based classifier. However, the systematic uncertainties are dominated by the effect of a cut on the τ_{had}-ID score applied to any $\tau_{\mathrm{had\text{-}vis}}$ candidate, treated as correlated across all bins. This uncertainty is described in the following.

6.5.1. Lowest cut on τ_{had}-ID score

By default, any $\tau_{\mathrm{had\text{-}vis}}$ candidate is required to have a τ_{had}-ID score of greater than 0.005 (0.01), corresponding to neglecting 0.5(1)% of real hadronically decaying τ leptons for the BDT(RNN)-based τ_{had}-ID. To account for a possible mismodelling of the neglected hadronic τ-decays, an additional uncertainty is assigned. This uncertainty is evaluated by running the complete analysis with different values of this lowest cut and comparing the resulting scale factors as it is displayed in Figure 6.12 for the RNN-based τ_{had}-ID. The effect is shown in the 30-40 GeV 1-prong and the 20-25 GeV 3-prong bin as they represent the bins with lowest and highest fluctuation, respectively. The largest difference between the scale factors of any two values for the lowest cut on τ_{had}-ID score is taken as a conservative estimate of the resulting uncertainty. The 20-25 GeV 3-prong bin is the only case were this additional uncertainty is larger than the statistical uncertainty on the scale factor.

6.6. Alternative scale factor estimates and outlook

Additional versions of the scale factors were calculated to account for different conditions. The default $Z \to \tau\tau$ sample used in the analysis was replaced by an alternative generated with a different MC generator. The complete analysis was conducted again to derive an alternative set of scale factors that analyses can apply depending on the MC generator used to produce their samples. The corresponding p_{T}-inclusive pre-fit $\tau-$ID score distributions for the loose working point can be seen in Appendix B.2 in Figure B.1 and Figure B.1 for the BDT- and the RNN-based $\tau-$ID, respectively.
Apart from the MC generator, the choice of the detector simulation can impact the τ_{had}-ID performance on simulated data. Therefore, the default detector simulation used in producing the $Z \to \tau\tau$ signal sample (FullSim) was replaced with AF2. Again, the entire analysis is conducted with the alternative signal sample. However, the resulting scale

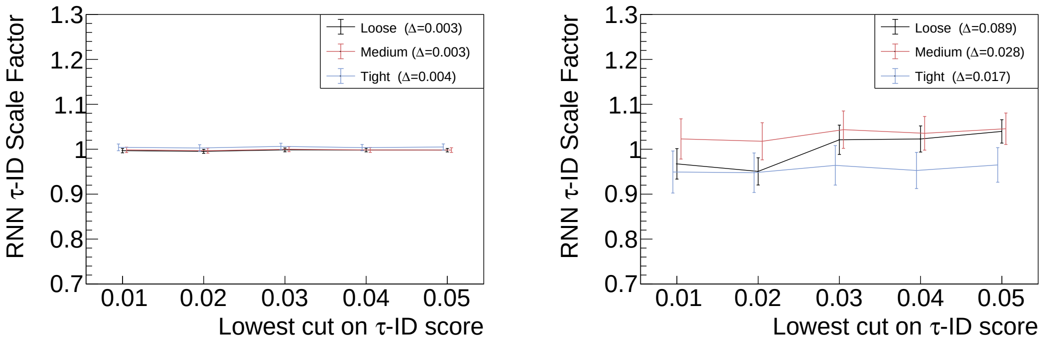

Figure 6.12.: RNN-based τ_{had}-ID scale factors for different lowest cuts on the τ_{had}-ID score for the 30-40 GeV 1-prong bin on the left, and the 20-25 GeV 3-prong bin on the right. The relative difference between highest and lowest nominal scale factor for each working point is displayed in the legend.

factors are comparable to the default, so only the difference is provided as an additional uncertainty. This systematic uncertainty has to be applied if AF2 is used to simulate hadronically decaying τ-leptons. The corresponding p_{T}-inclusive pre-fit $\tau-$ID score distributions for the loose working point can be seen in Appendix B.2 in Figure B.2 and Figure B.2 for the BDT- and the RNN-based $\tau-$ID, respectively.
Figure B.5 and Figure B.6 in Appendix B.3 show several sets of scale factors for BDT- and the RNN-based $\tau-$ID, respectively. Displayed at once are the default with the $Z \to \tau\tau$ sample simulated with Powheg and GEANT4, the alternative where Sherpa is used instead of Powheg, and the second alternative where AF2 is used instead of GEANT4.
As mentioned in Section 6.1, the signal region of this scale factor measurement is split into four disjoint τ_{had}-ID slices. Some analyses could benefit from applying the same cuts on the τ_{had}-ID score instead of using the default working points, making dedicated scale factors necessary. A set of such scale factors were calculated by replacing the sum in the numerator of Eq. 6.6 by the corresponding single term. However, the resulting uncertainties on the scale factors were vast, so the decision was not to apply that set of scale factors.

CHAPTER 7

Search for BSM $A/H \to \tau\tau$ in the fully hadronic decay channel

As mentioned in Chapter 1, the decay into a pair of τ-leptons is auspicious for searches for heavy Higgs bosons. The analysis described in the following considers the fully hadronic final state, $\tau_{\mathrm{had}}\tau_{\mathrm{had}}$, and the semileptonic one, $\tau_{\mathrm{lep}}\tau_{\mathrm{had}}$. Emphasis will be put on the former. Although BSM Higgs bosons could be produced via the same processes as their SM-like counterpart (see Figure 2.3), the increased mass and modified couplings could change the hierarchy of these processes. In particular, large values of $\tan\beta$ would enhance the production of heavy Higgs bosons in association with a b-quark. Therefore, this search considers BSM Higgs bosons produced via gluon-gluon-fusion and b-associated production as depicted in Figure 7.1.
The event selection is designed to suppress backgrounds from SM processes while providing high efficiency for hypothetical BSM signals. The dominant background comes from fakes estimated with a mixture of fake factor and fake rate approaches. A maximum-likelihood fit is conducted before upper limits on the product of production cross section and branching ratio, $\sigma \times BR$, are set. Limitations on the parameters of a given model can then be derived. The substeps of the analysis will be discussed in more detail in the following. Results are presented at the end.

7.1. Event selection

The analysis considers the complete Run 2 dataset recorded from 2015 to 2018 and corresponding to an integrated luminosity of roughly 139 fb^{-1}. The event selection can be divided into three steps. The trigger requirements and the preselection are applied to any event that is considered for this analysis. Then, the remaining events are categorized

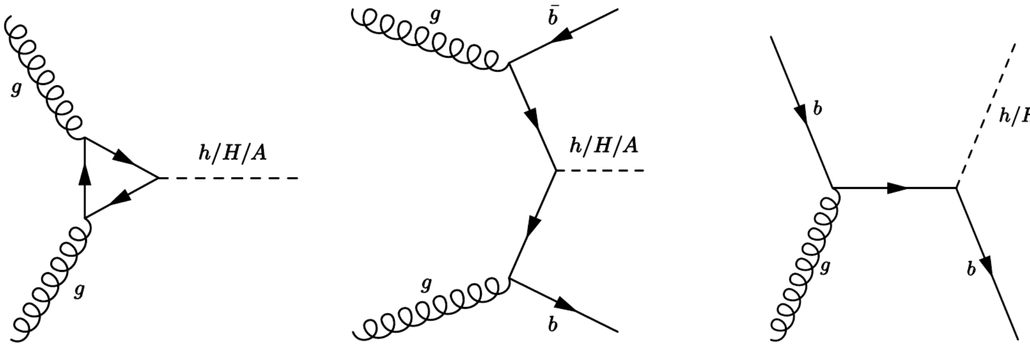

Figure 7.1.: Strong Higgs production via gluon-gluon-fusion and b-associated production in the four and five flavour scheme[1](from left to right) [107].

in various signal regions. If not specifically specified otherwise, the following description refers to the $\tau_{\text{had}}\tau_{\text{had}}$ channel exclusively. The combination with the $\tau_{\text{lep}}\tau_{\text{had}}$ channel is discussed in Section 7.5.

7.1.1. Trigger

An event is accepted if the lowest unprescaled single-tau trigger (STT) of the corresponding run number has fired. The p_{T} threshold of the lowest unprescaled trigger increases with the instantaneous luminosity. For each data-taking period, there is one considered single-tau trigger as listed in Table 7.1, showing a list of the considered triggers.
When investigating the names of the various triggers, the number `X` in `tauX` refers to the p_{T} threshold of the trigger. The term `medium1` specifies the working point of the online ID based on a BDT. Any of the listed triggers requires 1-3 tracks in the core region ($\Delta R < 0.2$) and no more than one track in the isolation region ($0.2 < \Delta R < 0.4$). If the term `tracktwoEF` appears in a trigger's name, that requirement is only posted for tracks reconstructed by the Event Filter (EF) algorithm [108]. The term `tracktwoEF`, on the other hand, implicates that the same requirements are also posted for tracks that were reconstructed by the fast track-finding algorithm (FTF). Lastly, the number `Y` in `L1TAUY` refers to lower cut on the transverse energy that is applied at the L1 stage.
For the event selection, there must be at least two reconstructed $\tau_{\text{had-vis}}$ candidates in the event, and they are sorted by their p_{T}. The $\tau_{\text{had-vis}}$ candidate with the highest p_{T} is referred to as the *leading* one (τ_1), the *subleading* $\tau_{\text{had-vis}}$ candidate (τ_2) is that with the second-highest p_{T}. The leading $\tau_{\text{had-vis}}$ candidate is required to be geometrically matched to the trigger within a $\Delta R = 0.2$ cone, and its p_{T} must exceed the trigger threshold by 5 GeV.
On simulated data, an event is accepted if any trigger of the corresponding data-taking

---

[1] Four and five flavour scheme are two different approximations for calculating production cross sections. In the five flavour scheme, top quarks are neglected as possible partons in the protons. In the four flavour scheme, top and bottom quarks are neglected.

Table 7.1.: List of single-tau triggers used in the $\tau_{\mathrm{had}}\tau_{\mathrm{had}}$ channel for each data taking period.

Period 2015-16

`HLT_tau80_medium1_tracktwo_L1TAU60`
`HLT_tau125_medium1_tracktwo`
`HLT_tau160_medium1_tracktwo`

Period 2017
`HLT_tau160_medium1_tracktwo` `HLT_tau160_medium1_tracktwo_L1TAU100`
Period 2018
`HLT_tau160_medium1_tracktwoEF_L1TAU100`

period has fired regardless of the simulated run number. The geometrical matching and p_{T} requirements are the same as for recorded data. Simulated events are scaled according to the relative luminosities recorded by each trigger to account for the fact that not all of these triggers were recording data for the entire data-taking period. This procedure is possible since all triggers listed in Table 7.1 deploy the same identification algorithm and only differ in p_{T} requirements, allowing for increased statistical power of the background estimate.

7.1.2. Event preselection

Any event considered in this analysis must fulfill the following criteria:

- at least one primary vertex with at least two associated tracks,
- at least two reconstructed $\tau_{\text{had-vis}}$ candidates. The p_{T} of the leading $\tau_{\text{had-vis}}$ must exceed 85 GeV, the subleading 65 GeV,
- the leading and subleading $\tau_{\text{had-vis}}$ candidates must pass the *medium* and *loose* working points of the BDT-based τ_{had}-ID, respectively,
- the two leading $\tau_{\text{had-vis}}$ candidates must be back-to-back ($\Delta\phi(\tau_1, \tau_2) > 2.7$),
- the two leading $\tau_{\text{had-vis}}$ candidates must have opposing charges ($q_{\tau_1} \times q_{\tau_2} == -1$). (Analogous to the convention in Section 6.1, this requirement is referred to as ‘OS’. Again, ‘SS’ refers to the case where both $\tau_{\text{had-vis}}$ candidates bear the same charge.)

7.1.3. Categorization

The signal region is split into the b-veto and b-tag categories. The latter is dedicated to heavy Higgs bosons produced in association with b-quarks. For the b-tag channel, events are required to contain at least one jet whose p_{T} exceeds 20 GeV and is tagged as

b-jet by the MV2c10 algorithm tuned to the efficiency of 70% for b-jets in simulated $t\bar{t}$ events [99]. The b-veto category is complementary to the b-tag category. Its purpose is the search for heavy Higgs bosons produced via gluon-gluon-fusion. Splitting the signal region into these two disjoint categories provides an additional experimental handle on the value of $\tan\beta$.
Apart from the two categories of the signal region, numerous control regions are considered for the background estimate deployed by the analysis. Their names and selection criteria are summarized in Table 7.2. In the DJ-FR, the fake factor is measured. It is then applied in the CR-1 to arrive at the estimate of the multijet contribution in the signal region. Fake rates for processes involving b-tagged jets are derived in the T-FR. All other fake rates are evaluated in the W-FR (see Section 7.3). DJ-FR, T-FR, and W-FR are denoted as *fake regions*. A validation region similar to the signal region but with a significantly lower expected signal purity is introduced by inverting the OS to an SS requirement. This region is referred to as the SS-VR and is used to validate the estimation of the backgrounds caused by fakes.

Table 7.2.: Definition of signal, control and fake regions used in the $\tau_{\text{had}}\tau_{\text{had}}$ channel. The symbol τ_1 (τ_2) represents the leading (sub-leading) $\tau_{\text{had-vis}}$ candidate.

Region	Selection
SR	τ_1 (trigger, medium), τ_2 (loose), $q(\tau_1) \times q(\tau_2) < 0$, $\lvert\Delta\phi(\tau_1, \tau_2)\rvert > 2.7$
CR-1	Pass SR except: τ_2 (fail loose)
DJ-FR	jet trigger, τ_1+τ_2 (no identification), $q(\tau_1) \times q(\tau_2) < 0$, $\lvert\Delta\phi(\tau_1, \tau_2)\rvert > 2.7$, $p_{\mathrm{T}}^{\tau_2}/p_{\mathrm{T}}^{\tau_1} > 0.3$
W-FR	μ (trigger, isolated), τ_1 (no identification), $\lvert\Delta\phi(\mu, \tau_1)\rvert > 2.4$, $m_{\mathrm{T}}(\mu, E_{\mathrm{T}}^{\text{miss}}) > 40\text{GeV}$ b-veto category only, exactly one $\tau_{\text{had-vis}}$ candidate
T-FR	Pass W-FR except: b-tag category only
SS-VR	Pass SR except: $q(\tau_1) \times q(\tau_2) == 1$ (SS)

7.1.4. Di-τ mass reconstruction

The mass of a resonance decaying into a pair of τ-leptons is challenging to reconstruct since the neutrinos in the final state carry away an unknown amount of energy and momentum. Various algorithms for this task were compared in a previous version of the analysis [109]. The total transverse mass was found to perform best in this context. It is defined as

$$\begin{aligned} m_{\mathrm{T}}^{\text{tot}} &= \sqrt{(p_{\mathrm{T}}^{\tau_1} + p_{\mathrm{T}}^{\tau_2} + E_{\mathrm{T}}^{\text{miss}})^2 - (\mathbf{p}_{\mathrm{T}}^{\tau_1} + \mathbf{p}_{\mathrm{T}}^{\tau_2} + \mathbf{E}_{\mathrm{T}}^{\text{miss}})^2} \\ &= \sqrt{m_T^2(E_{\mathrm{T}}^{\text{miss}}, \tau_1) + m_{\mathrm{T}}^2(E_{\mathrm{T}}^{\text{miss}}, \tau_2) + m_{\mathrm{T}}^2(\tau_1, \tau_2)}, \end{aligned}$$

where the transverse mass between two momentum-vectors is defined as

$$m_{\mathrm{T}}(\vec{a}, \vec{b}) = \sqrt{2p_{\mathrm{T}}(\vec{a})p_{\mathrm{T}}(\vec{b})(1 - \cos\Delta\phi(\vec{a}, \vec{b}))}.$$

Table 7.3.: Overview of the generators, PDFs, parton showering models, hadronization, underlying event, and approximation order used in this analysis. V represents either W or Z gauge bosons [111].

Process	Generator	PDF	UEPS	Cross section order
ggF	Powheg-Box v2 [112–116]	CT10 [117]	Pythia 8.1 [118]	NLO[2]
bbH	MG5_aMC@NLO 2.1.2 [119, 120]	CT10	Pythia 8.2 [121]	NLO[2]
W+jets	Sherpa 2.2.1 [122]	NNPDF 3.0 NNLO [123]	Sherpa 2.2.1 [124]	NNLO [125]
Z+jets	Powheg-Box v1 [112–114, 126]	CT10	Pythia 8.1	NNLO [125]
$VV/V\gamma^*$	Sherpa 2.2	NNPDF 3.0 NNLO	Sherpa 2.2	NLO
$t\bar{t}$	Powheg-Box v2 [112–114, 127]	NNPDF 3.0 NLO	Pythia 8.2	NNLO+NNLL [128–134]
Single t	Powheg-Box v2 [112–114, 135–137]	NNPDF 3.0 NLO	Pythia 8.2	NNLO+NNLL [138, 139]

The approach of $m_{\mathrm{T}}^{\mathrm{tot}}$ is relatively simple compared to more elaborate di-τ mass reconstruction algorithms such as the missing-mass-calculator (`MMC`) [110] or `MOSAIC` [109]. However, for the high transverse momenta of the τ-leptons considered in this analysis, the advantage of such algorithms is negligible. The MMC, for example, estimates the most likely momentum vectors of the neutrinos based on the kinematics of the $\tau_{\text{had-vis}}$ candidates. The large boost of τ-leptons considered in this analysis makes the neutrino and the other decay products travel in almost the same direction seen from the lab frame, making $m_{\mathrm{T}}^{\mathrm{tot}}$ a good approximation for the actual transverse mass. Furthermore, the computation time for $m_{\mathrm{T}}^{\mathrm{tot}}$ is significantly lower than for the `MMC` and `MOSAIC` algorithms, so it was chosen as the final discriminant of the analysis. Its distribution in the signal region after the fit described in Section 7.5 can be seen in Figure 7.2 for the $\tau_{\text{had}}\tau_{\text{had}}$ and $\tau_{\text{lep}}\tau_{\text{had}}$ channel, separately.

7.2. Samples

An overview of the generators used to simulate signal and background processes can be seen in Table 7.3. It also shows the assumed PDF sets for the hard process as well as the models for parton showering, hadronization, and the underlying event (UEPS). The last column shows the order to which the cross sections were calculated. A complete list of all samples used in this analysis can be found in Appendix C.5.

7.3. Background estimate

The background contributions in this analysis can be distinguished between those originating from true τ-leptons and those from fakes. The former are estimated directly from MC simulation. The latter, however, are estimated via partially data-driven techniques since the misidentification probability is not well modelled on simulated events. The dominant background contribution comes from fakes from multijet processes and is estimated with a purely data-driven *fake factor* approach. MC simulations of this contribution are not feasible due to the combination of a high cross section and low acceptance,

---

[2] NNLO corrections for the contribution from top quarks are considered

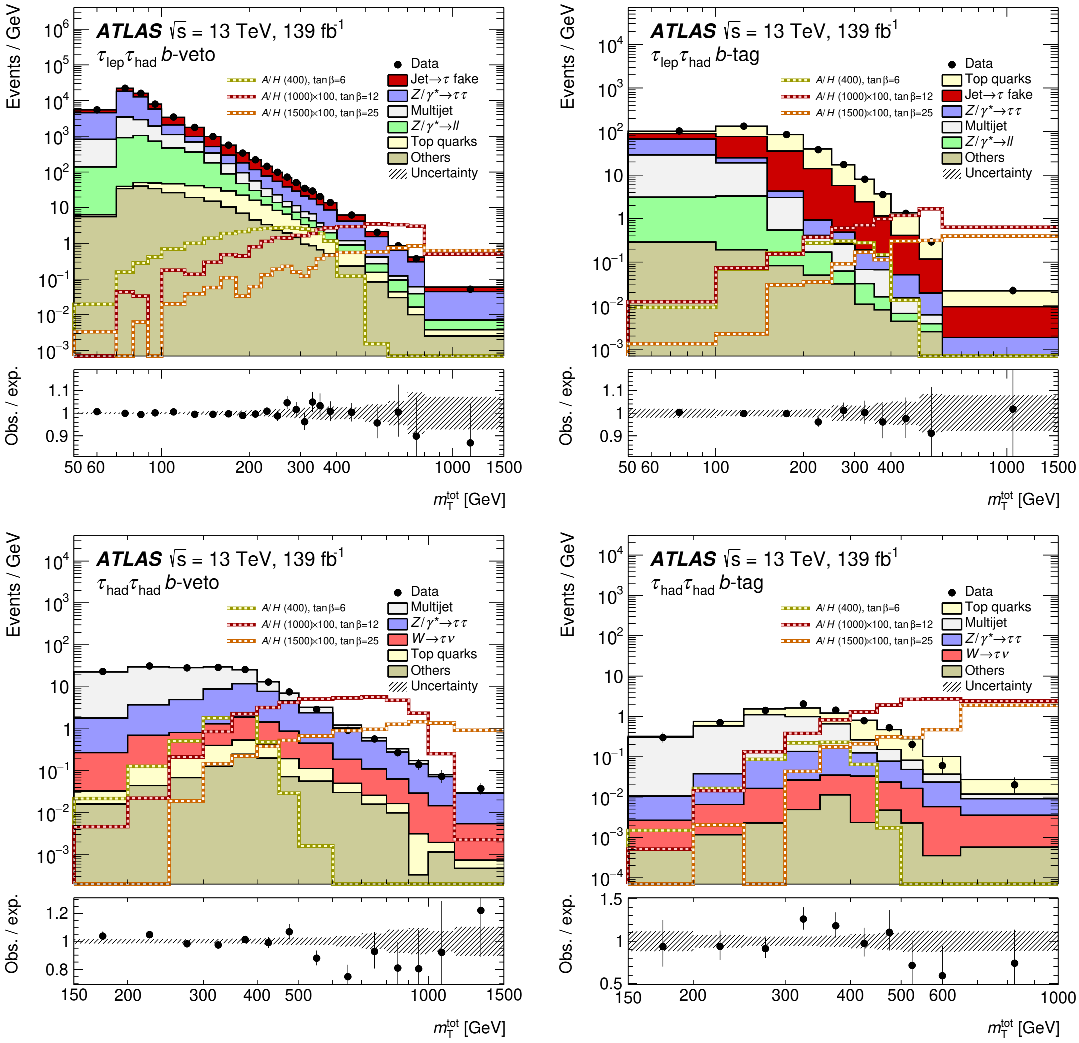

Figure 7.2.: The distribution of $m_{\mathrm{T}}^{\mathrm{tot}}$ in the signal regions of the $\tau_{\mathrm{lep}}\tau_{\mathrm{had}}$ channel (top) and the $\tau_{\mathrm{had}}\tau_{\mathrm{had}}$ (bottom) channel. The figure is also split into the b-veto (left) and b-tag (right) categories. The prediction for the background processes is obtained from the fit described in Section 7.5 assuming the background-only hypothesis. Expectations from signal processes are superimposed. Overflows are included in the last bin of the distributions [111].

requiring vast amounts of simulated events for sufficient statistical power. Fakes from all other processes are estimated via a semi data-driven *fake rate* approach. The difference between the semi data-driven fake rate approach and the fully data-driven fake factor approach will be explained in the following.

7.3.1. Fake rate approach

A significant background contribution comes from fake $\tau_{\text{had-vis}}$ candidates in processes that are estimated via MC simulation. In particular, the dominant background in the b-tag signal region for large values of $m_{\mathrm{T}}^{\text{tot}}$ emerges from fake $\tau_{\text{had-vis}}$ candidates from processes involving top quarks. In the b-veto region, the $W(\rightarrow \mu\nu)$+jets contribution is the main source for MC simulated fake $\tau_{\text{had-vis}}$ candidates.
The probability of a jet being misidentified by the $\tau-$ID algorithm is known as the *fake rate*. The fake rate is often poorly modelled in MC simulations. Therefore, it is evaluated on data via a tag-and-probe approach in a $W(\rightarrow \mu\nu)$+jets control region.

W-FR and Top-FR construction The $W(\rightarrow \mu\nu)$+jets control region where the fake rates are measured, is split into a b-tag (T-FR) and a b-veto case (W-FR). The same b-tagging definitions as in the signal region are deployed. A muon candidate tags the event, and the fake rate is evaluated on the jet (the tag). The control region is defined by requiring the `HLT_mu50` trigger to have fired. There must be exactly one reconstructed muon that is matched to the trigger, passes the *medium* identification, and whose transverse momentum exceeds 55 GeV. It must also fulfill a gradient isolation requirement tuned to 90(99)% efficiency for muons at $p_{\mathrm{T}} = 25(60)$ GeV.
Furthermore, there must be exactly one $\tau_{\text{had-vis}}$ candidate (and no electron) in the event, making this region orthogonal to the signal region. The tag object and the probe object must be back-to-back, although this requirement is slightly loosened concerning the signal region at $\Delta\phi(\mu, \tau_{\text{had-vis}}) > 2.4$. A cut on the transverse mass further suppresses contributions from multijet and signal: $m_{\mathrm{T}}(\mu, E_{\mathrm{T}}^{\text{miss}}) > 40$ GeV. The event selection mentioned above leads to a $W(\rightarrow \mu\nu)$+jets purity of 92% in the W-FR and an 82% Top purity in the T-FR, where the purity is defined as the ratio of the respective MC simulated event yield divided by the overall data yield in that control region.

Fake rate definition The fake rate of a given $\tau-$ID working point is defined as the ratio of events where the $\tau_{\text{had-vis}}$ candidate passes the $\tau-$ID requirement to all events. The fake rate is binned in the transverse momentum of the $\tau_{\text{had-vis}}$ candidate and calculated for 1-prong and 3-prong cases, separately:

$$FR_{\tau-\text{ID}}(p_{\mathrm{T}}, N_{\text{track}}) \equiv \left. \frac{N^{\text{pass }\tau-\text{ID}}(p_{\mathrm{T}}, N_{\text{track}})}{N^{\text{all }\tau-\text{ID}}(p_{\mathrm{T}}, N_{\text{track}})} \right|_{\mathrm{W}(\rightarrow\mu\nu)+\text{jets,Top}}, \tag{7.1}$$

where the denominator can be expressed as the sum of $\tau_{\text{had-vis}}$ candidates failing the $\tau-$ID, $N^{\text{fail }\tau-\text{ID}}(p_{\mathrm{T}}, N_{\text{track}})$, and those passing it, $N^{\text{pass }\tau-\text{ID}}(p_{\mathrm{T}}, N_{\text{track}})$. All truth-matched $\tau_{\text{had-vis}}$ candidates from MC simulation are subtracted before calculating the fake rate to ensure that it is evaluated exclusively on fake $\tau_{\text{had-vis}}$ candidates. Two different fake rate versions are calculated since fake rates are deployed for the leading and the subleading $\tau_{\text{had-vis}}$ candidate in the signal region. For the leading $\tau_{\text{had-vis}}$ candidate, the *medium* $\tau-$ID working point in combination with the trigger-based identification is required in the numerator of Eq. 7.1. When calculating the fake rates for the subleading $\tau_{\text{had-vis}}$ candidate, only the *loose* $\tau-$ID working point is required in the numerator.

Figure 7.3 shows a comparison of the OS fake rates evaluated on data and MC simulated events as a function of the transverse momentum of the $\tau_{\text{had-vis}}$ candidate. The two plots show the 1-prong W-FR and 3-prong T-FR cases, respectively. These two were chosen as they represent the fake rates with the highest (lowest) statistical power. All other relevant fake rate comparisons can be found in Appendix C.1 in Figure C.1 and Figure C.2. All plots contain only statistical uncertainties.

Generally, the agreement between the fake rates evaluated on MC simulated events and those evaluated on data is good. For the b-veto case, the fake rates evaluated on data are deployed for the background estimate in the signal region as their uncertainties are lower. In the case of b-tag, however, the data fake rate exhibits large statistical uncertainties. Therefore, the fake rate evaluated on MC simulated Top events is used with a correction factor normalizing it to the mean value of the fake rate on data. All resulting fake rates are displayed in Figure 7.4. The difference between OS and SS fake rates is due to the different fractions of quark- and gluon-initiated jets, a phenomenon discussed in detail in Section 7.3.2. Although only the OS fake rate is used directly for the background estimate in the signal region, the SS fake rate is applied when estimating the background in the SS-VR.

Fake rate application The dedicated fake rates for leading and subleading $\tau_{\text{had-vis}}$ candidates are only applied to fake $\tau_{\text{had-vis}}$ candidates from MC simulated events instead of requiring the $\tau-$ID. The distribution of given variable x in the signal region is estimated via:

$$N_{\text{W/Top}}(p_{\text{T}}, N_{\text{track}}, x) = FR_{\tau-\text{ID}}(p_{\text{T}}, N_{\text{track}}) \times \Big(N^{\text{all } \tau-\text{ID}}(p_{\text{T}}, N_{\text{track}}, x)\Big).$$

If the leading $\tau_{\text{had-vis}}$ candidate is fake, the *medium* + trigger fake rate is applied. If the subleading $\tau_{\text{had-vis}}$ candidate is fake, the *loose* fake rate is applied. If leading and subleading $\tau_{\text{had-vis}}$ candidates are fake, the product of both fake rates is applied. Only truth-matched $\tau_{\text{had-vis}}$ candidates have to pass trigger and the *medium* (*loose*) $\tau-$ID working point. The b-tag fake rate is applied to $\tau_{\text{had-vis}}$ candidates from MC simulated processes containing top quarks, meaning $t\bar{t}$ and single Top processes. The b-veto fake rate is applied to $\tau_{\text{had-vis}}$ candidates from all other MC simulated contributions. This procedure is summarized in Table 7.4 in combination with the trigger strategy. The first row lists the procedure for data, where no scaling factors are applied. The other four rows correspond to the four possible combinations true and fake for the leading and subleading $\tau_{\text{had-vis}}$ candidates.

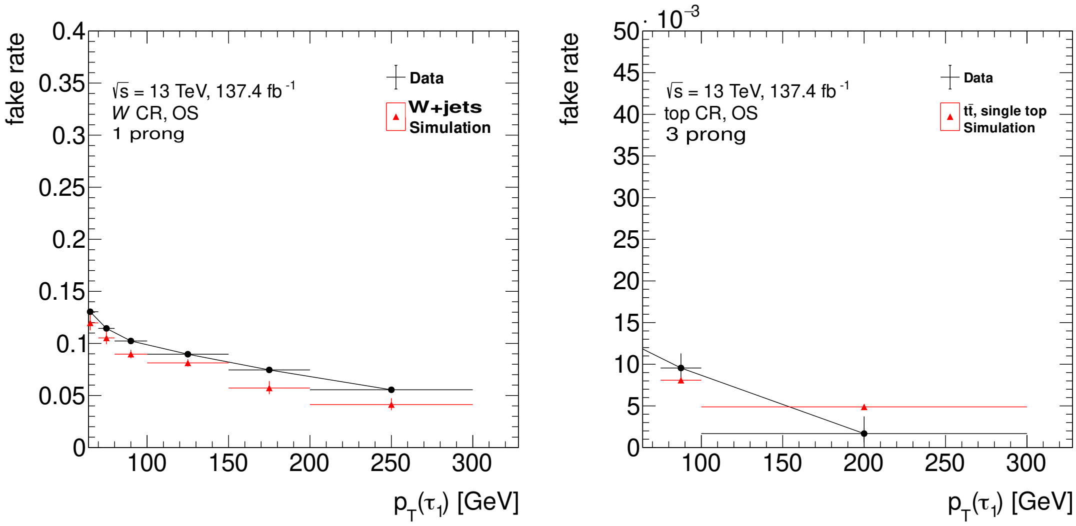

Figure 7.3.: Comparison of OS fake rates evaluated on data and MC simulated events. On the left, the fake rate is shown for the 1-prong W-FR. The right hand side shows the fake rates in the 3-prong T-FR.

7.3.2. Multijet estimate - fake factor approach

Because of the low acceptance for contributions from multijet processes, the MC simulation of the latter requires large computational efforts to achieve sufficient statistical power. Furthermore, QCD is difficult to describe perturbatively at low energy scales, leading to significant additional systematic uncertainties. For this reason, many analyses at ATLAS deploy data-driven techniques to estimate the contribution from multijet processes. This analysis deploys an approach where fake factors are measured in a di-jet control region and applied to events in the CR-1, which is the signal region with an inverted τ−ID requirement on the subleading $\tau_{\text{had-vis}}$ candidate.

τ_0	τ_1	trigger	ID_0	ID_1	SF_0	SF_1
data	data	STT & match(lead)	Med	Loose	1.	1.
truth	truth	STT & match(lead)	Med	Loose	$\text{SF}_{\text{trig}} * \text{SF}_{\text{ID}}$	SF_{ID}
truth	fake	STT & match(lead)	Med	-	$\text{SF}_{\text{trig}} * \text{SF}_{\text{ID}}$	FR_{Loose}
fake	truth	-	-	Loose	$FR^{\text{Trig}}_{\text{Med}}$	SF_{ID}
fake	fake	-	-	-	$FR^{\text{Trig}}_{\text{Med}}$	FR_{Loose}

Table 7.4.: Scheme of how trigger and offline τ−ID decisions are processed for events in the signal region, also listing the applied scale factors and fake rates.

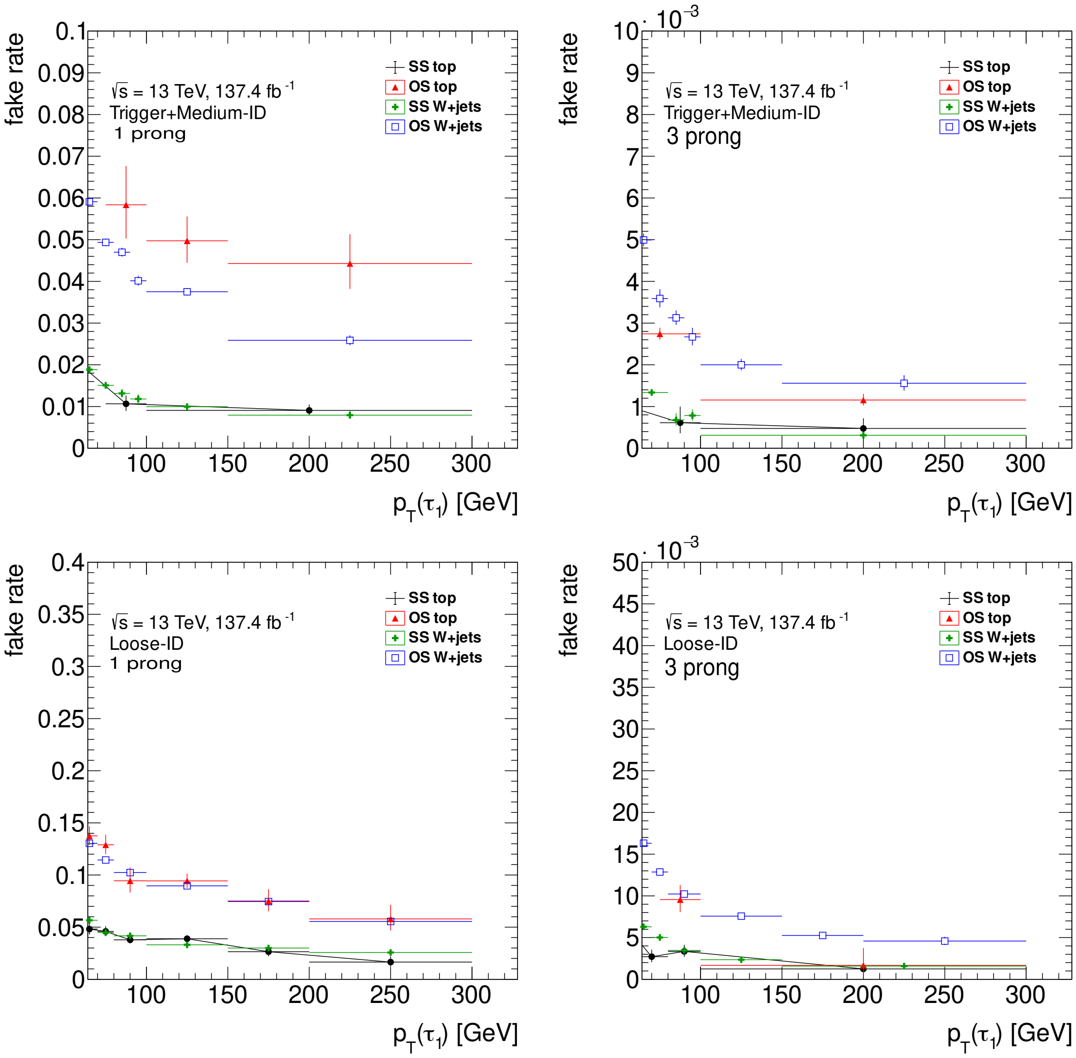

Figure 7.4.: Fake rates evaluated on data in the W-FR and the T-FR for the combination of the *medium* $\tau-$ID working point and the trigger requirement (top) and the *loose* $\tau-$ID requirement (bottom). The plot is also split into 1-prong (left) and 3-prong (right) $\tau_{\text{had-vis}}$ candidates.

Di-jet control region The fake factor is measured in a di-jet tag-and-probe approach. To be unbiased, the fake factor is evaluated on fake $\tau_{\text{had-vis}}$ candidates that have not passed any identification. An event is selected if any of the following single-jet triggers has fired: `HLT_j420`, `HLT_j400`, `HLT_j380`, `HLT_j360`, `HLT_j260`, `HLT_j175`, `HLT_j110`, `HLT_j85`, `HLT_j60`, `HLT_j55`, `HLT_j45`, `HLT_j35`, `HLT_j25`, or `HLT_j15`. Here, the number `X` in `HLT_jX` denotes the p_{T} threshold of the considered trigger.

Like in the signal region, at least two $\tau_{\text{had-vis}}$ candidates are required. The leading one must be matched to the trigger that fired and fail the *medium* working point of the BDT-based $\tau-$ID. The subleading $\tau_{\text{had-vis}}$ candidate is used as the probe on which the fake factor is evaluated. For better compatibility between signal region and di-jet control region, the transverse momenta of leading and subleading $\tau_{\text{had-vis}}$ candidates must exceed 85 GeV and 65 GeV, respectively, and they must be back-to-back ($\Delta\phi(\tau_1, \tau_2) > 2.7$). Furthermore, the transverse momentum of the subleading $\tau_{\text{had-vis}}$ candidate must be at least 30% of that of the leading one.

Fake factor evaluation The fake factor is defined as the number of fake $\tau_{\text{had-vis}}$ candidates that pass the $\tau-$ID, $N^{\text{pass } \tau-\text{ID}}$, divided by the number that fail it, $N^{\text{fail } \tau-\text{ID}}$. This ratio is binned in the number of tracks, N_{track}, and the transverse momentum of the $\tau_{\text{had-vis}}$ candidate, p_{T}:

$$\text{FF}_{\tau-\text{ID}}(p_{\text{T}}, N_{\text{track}}) \equiv \left. \frac{N^{\text{pass } \tau-\text{ID}}(p_{\text{T}}, N_{\text{track}})}{N^{\text{fail } \tau-\text{ID}}(p_{\text{T}}, N_{\text{track}})} \right|_{\text{di-jet}} . \tag{7.2}$$

MC simulated $\tau_{\text{had-vis}}$ candidates coming from all contributions apart from multijet processes are subtracted before calculating the fake factor in the DJ-FR to guarantee that it is evaluated on fake $\tau_{\text{had-vis}}$ candidates from multijet processes only.

The fake factor of a sample not only depends on the transverse momentum and the number of tracks. The types of particles that initiated the jets can also have an influence. Quark-initiated jets tend to be misidentified as a hadronically decaying τ-lepton with a higher probability than those initiated by a gluon. Therefore, the ratio of quark- to gluon-initiated jets in a pure multijet sample impacts the overall fake factor. The modelling is biased if the sample on which the fake factor is evaluated has different fractions of quark- and gluon-initiated jets than the signal region.

For this reason, a lower cut on the $\tau-$ID score is introduced in both regions, rejecting most gluon-initiated fake $\tau_{\text{had-vis}}$ candidates, resulting in the fake $\tau_{\text{had-vis}}$ candidates in the di-jet control and the signal region being predominantly initiated by quarks. Figure 7.5 shows the comparison of the distributions of the BDT-based $\tau-$ID score of the subleading $\tau_{\text{had-vis}}$ candidate in the signal region and the DJ-FR. The slopes in the ratio plots for low values of the $\tau-$ID score indicate the increased fraction of gluon-initiated jets in the di-jet control region with respect to the signal region. The lower cut on the $\tau-$ID score is set to 0.03, corresponding to 97% signal efficiency. This choice is justified by the mostly flat distribution of the ratio plots for $\tau-$ID scores above that value.

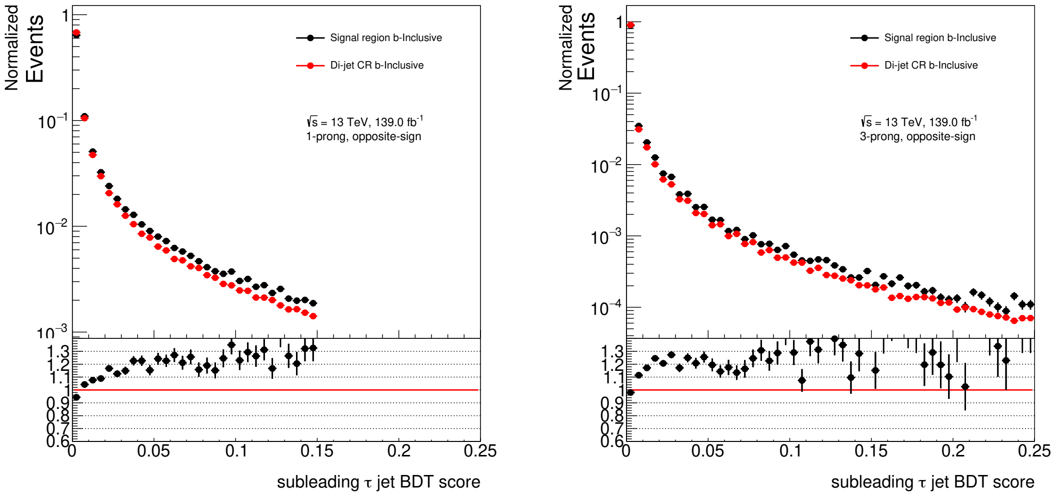

Figure 7.5.: Normalized distribution of the BDT-based $\tau-$ID score of the subleading $\tau_{\text{had-vis}}$ candidate in the di-jet control region and the signal region. The $\tau_{\text{had-vis}}$ candidates are required to fail the *loose* working point and possess one (left) or three charged tracks (right).

Furthermore, the fake factors are derived inclusively regarding the number of b-tagged jets to increase the statistical power. An additional corresponding uncertainty must be considered when estimating the multijet contribution in the b-veto or the b-tag signal region. These uncertainties are defined as the difference between the inclusive and the b-veto and b-tag fake factor, respectively. In the b-tag case, this uncertainty can be dominant. However, for the b-veto fake factors, the leading source of uncertainty is the limited statistical power in the di-jet control region. Other sources of uncertainty are the limited statistical power and systematic uncertainties of the MC simulated events, such as the uncertainty on the integrated luminosity. These uncertainties are evaluated by varying the MC simulated contributions within the respective uncertainty and subtracting them from data before re-calculating the fake factors, but found to be negligible.
The b-veto, b-tag, and b-inclusive OS fake factors are displayed in Figure 7.6 for 1-prong and 3-prong candidates, separately. The corresponding SS fake factors can be found in the Appendix C.2 in Figure C.3. In the same Appendix, Figure C.4 and Figure C.5 show the fake factors and their uncertainties in the b-tag and b-veto case, respectively.

Fake factor application The multijet contribution in the signal region is estimated by applying the fake factor in the CR-1 region, which corresponds to the signal region after inverting the *loose* $\tau-$ID requirement. The distribution of a given variable x can be

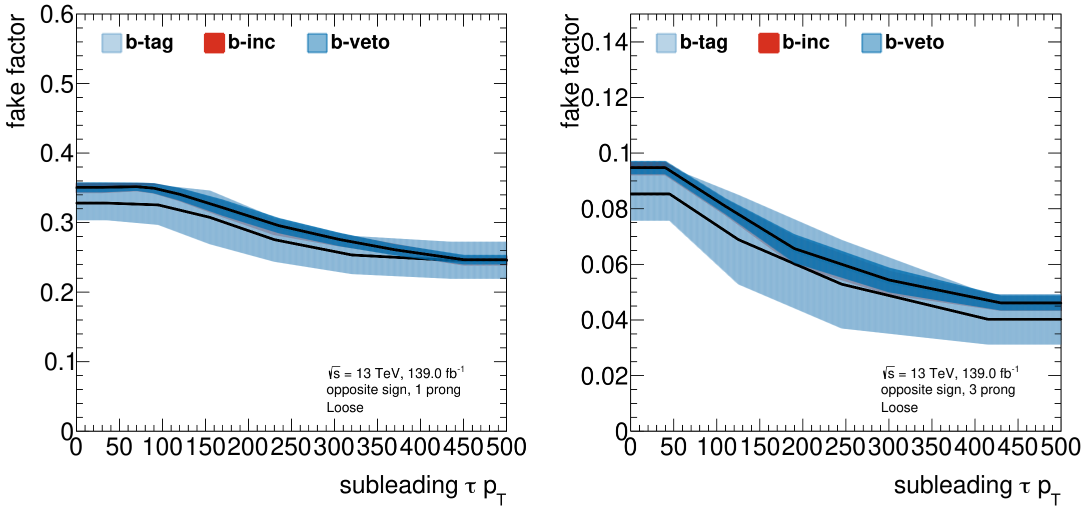

Figure 7.6.: Fake factors derived in the OS di-jet control region for 1-prong (left) and 3-prong (right) $\tau_{\text{had-vis}}$ candidates. A comparison between b-veto, b-tag, and b-inclusive fake factors is made.

estimated via

$$N_{\text{multijet}}(p_{\text{T}}, N_{\text{track}}, x) = \text{FF}_{\tau-\text{ID}}(p_{\text{T}}, N_{\text{track}}) \times \left(N_{\text{data}}^{\text{fail }\tau-\text{ID}}(p_{\text{T}}, N_{\text{track}}, x)\right), \tag{7.3}$$

where the fake factor is interpolated between the bin centers of p_{T}, improving the modelling. $N_{\text{data}}^{\text{fail }\tau-\text{ID}}$ is the number of fake $\tau_{\text{had-vis}}$ candidates in recorded data coming from the multijet contribution. It is retrieved by subtracting $\tau_{\text{had-vis}}$ candidates from all background contributions apart from multijet processes from recorded data.

By inverting the OS requirement of the signal region, a validation region for the multijet estimate with a meagre expected signal contribution is created. Figure 7.7 shows the distribution of $m_{\text{T}}^{\text{tot}}$ in this SS-VR for b-veto and b-tag case, separately. The background modelling matches the observed data well, validating the multijet estimate.

Distributions of additional variables in the validation region can be seen in the Appendix C.3. in Figure C.6 and Figure C.7 for the b-veto and the b-tag case, respectively.

7.3.3. Fake factor interpolation

Since almost any analysis that considers hadronically decaying τ-leptons must estimate the background coming from fake $\tau_{\text{had-vis}}$ candidates, the fake factor approach is a widespread technique. A *fake tau task force* (FTTF) was founded to synergize these efforts across τ_{had}-based measurements and searches and provide a universal tool within ATLAS.

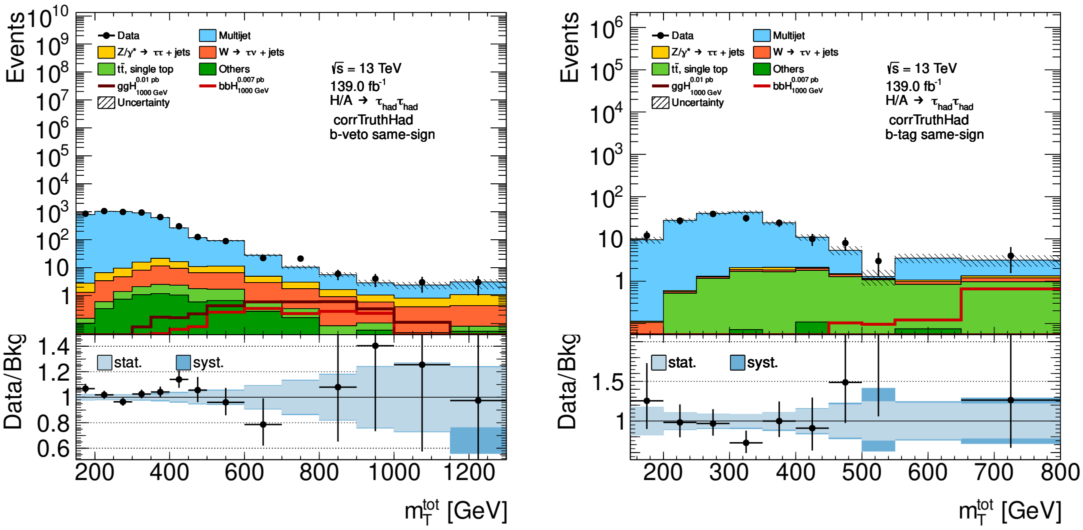

Figure 7.7.: Distribution of $m_{\mathrm{T}}^{\mathrm{tot}}$ in the b-veto (left) and b-tag (right) SS validation region before the fit. The background modelling matches the observed data well, validating the multijet estimate.

When developing such a universal approach, the main challenge is to contemplate the effects of varying fractions of quark- and gluon-initiated jets being reconstructed as $\tau_{\text{had-vis}}$ candidates. The FTTF aims to provide universal fake factors as a function of that ratio so that analyses can apply them after determining this ratio in the corresponding region. The fake factors' dependence on the ratio of quark- and gluon-initiated jets is determined by interpolating it between two regions where this ratio is known. Assuming that the sample consists exclusively of quark- and gluon-initiated jets faking $\tau_{\text{had-vis}}$ candidates, the fake factor of that sample can be expressed as

$$\mathrm{FF}_{\mathrm{SR}} = \frac{N_q^{\text{pass }\tau-\text{ID}} + N_g^{\text{pass }\tau-\text{ID}}}{N_q^{\text{fail }\tau-\text{ID}} + N_g^{\text{fail }\tau-\text{ID}}}, \tag{7.4}$$

where N_q and N_g are the number of quark- and gluon-initiated jets, respectively. This can be rewritten as

$$\mathrm{FF}_{\mathrm{SR}} = \frac{N_q^{\text{fail }\tau-\text{ID}}}{N_q^{\text{fail }\tau-\text{ID}} + N_g^{\text{fail }\tau-\text{ID}}} \cdot \frac{N_q^{\text{pass }\tau-\text{ID}}}{N_q^{\text{fail }\tau-\text{ID}}} + \frac{N_g^{\text{fail }\tau-\text{ID}}}{N_q^{\text{fail }\tau-\text{ID}} + N_g^{\text{fail }\tau-\text{ID}}} \cdot \frac{N_g^{\text{pass }\tau-\text{ID}}}{N_g^{\text{fail }\tau-\text{ID}}}.$$

Identifying the fake factors for samples of pure quark- and gluon-initiated jets,

$$\mathrm{FF}_q \equiv \frac{N_q^{\text{pass }\tau-\text{ID}}}{N_q^{\text{fail }\tau-\text{ID}}}, \qquad \mathrm{FF}_g \equiv \frac{N_g^{\text{pass }\tau-\text{ID}}}{N_g^{\text{fail }\tau-\text{ID}}},$$

and introducing the fraction of quark-initiated jets among those failing the $\tau-$ID,

$$q_f \equiv \frac{N_q^{\text{fail }\tau-\text{ID}}}{N_q^{\text{fail }\tau-\text{ID}} + N_g^{\text{fail }\tau-\text{ID}}},$$

Equation 7.4 can finally be expressed as

$$\mathrm{FF}_{\mathrm{SR}} = q_f \cdot \mathrm{FF}_q + (1 - q_f) \cdot \mathrm{FF}_g.$$

Hence, the fake factor linearly depends on the fraction of quark-initiated jets failing the τ−ID. Measuring it in two regions with quark fractions $q_{f,1}$ and $q_{f,2}$ then allows interpolating the fake factor to any region with quark fraction $q_{f,\mathrm{SR}}$ as displayed in Figure 7.8.

A fit is conducted to estimate the fraction of quark-initiated jets on data in a given region. Templates of pure quark- and gluon-initiated jets faking $\tau_{\text{had-vis}}$ candidates as a function of a chosen kinematic variable are taken from MC simulated events. A linear combination of the two templates is created and compared to the distribution on data. The estimate on q_f is achieved by minimizing χ^2 of this comparison. The templates are randomly varied within their uncertainties, and the minimization is repeated. After enough repetitions of this procedure, the width of the distribution of the fit results converges, delivering an estimate for the uncertainty on the fraction of quark-initiated jets on data. This uncertainty is minimized by conducting the fit for a well-separating variable, exploiting the shape difference of the quark and gluon templates. One such variable is the *jet width*, defined as the weighted average ΔR of all objects within the jet:

$$j = \frac{\sum_i \Delta R^i p_T^i}{\sum_i p_T^i}.$$

Figure 7.9 shows examples of template fits using the jet width conducted in the dijet control region and the signal region separately. The lower cut on the τ−ID score mentioned in Section 7.3.2 was not applied before conducting the fit. Although only showing a single iteration of the fit, the results hint at the difference in the fraction of quark-initiated jets in these two regions, further justifying the application of that cut.

The fake factor evaluated in the dijet control was corrected according to the fraction of quark-initiated jets on data. The modelling of the multijet contribution in the validation region was found to be consistent with the approach of applying the lower cut on the τ−ID score. Although not deployed in the final version of the analysis, the studies on the fake factor interpolation were an important confirmation of the background estimate. They also marked the beginning of the efforts of the FTTF, providing a proof of concept and a solid fit strategy, including a correct treatment of uncertainties.

7.4. Systematic uncertainties

The systematic uncertainties considered by the analysis can be categorized into four groups: experimental uncertainties, theoretical uncertainties on the background and signal modelling, and uncertainties on the data-driven background estimate.

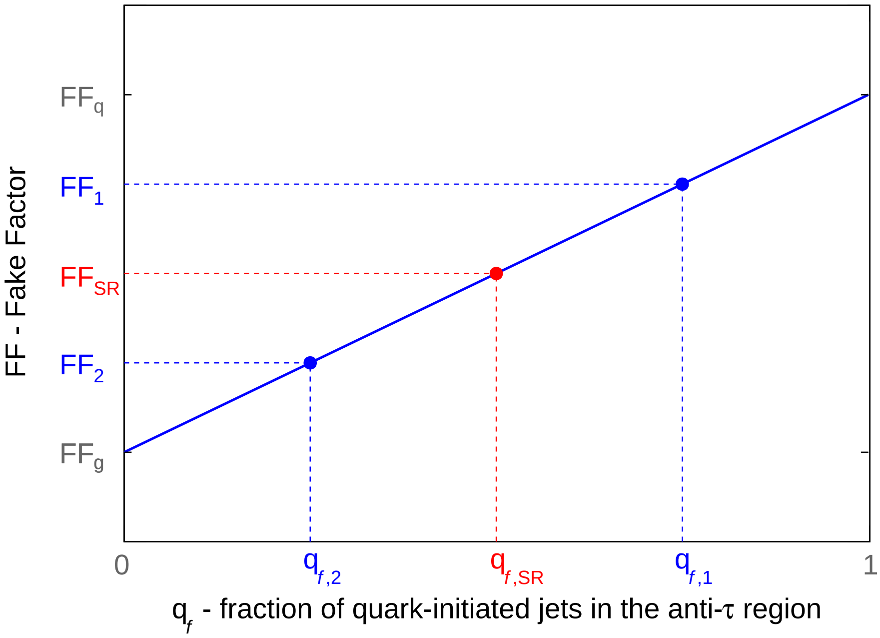

Figure 7.8.: Illustration of the FTTF interpolation approach. Measuring the fake factor in two regions with known fractions of quark-initiated jets, $q_{f,1}$ and $q_{f,2}$, allows interpolating the factor to a given region with fraction $q_{f,\mathrm{SR}}$.

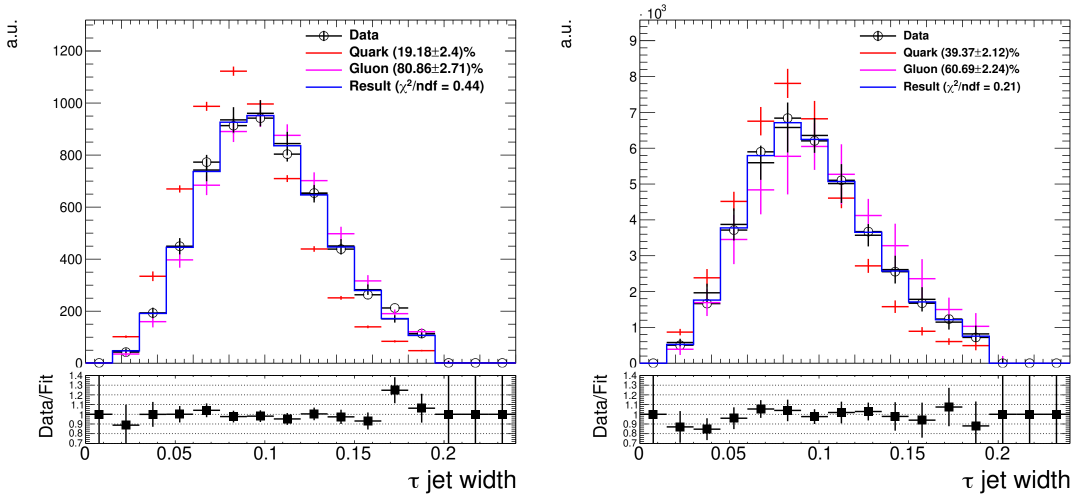

Figure 7.9.: Results of template fits of the jet width in the 3-prong, 50 GeV $< p_\mathrm{T} <$ 70 GeV, di-jet control region (left) and signal region (right). The ratio plot only shows statistical uncertainties. The first and the last three bins were excluded before conducting the fit due to modelling issues [140].

Table 7.5.: Summary of experimental systematic uncertainties considered by the analysis.

NP name	Description
“Lumi”	Integrated luminosity measurement
“TAU”	τ_{had} reconstruction, identification, electron-veto and energy scale
“METSoft”	$E_{\text{T}}^{\text{miss}}$ soft terms
“JER, JES, Jvt”	jet energy scale and resolution
“btag”	flavour-tagging
“PRW”	pile-up

Experimental uncertainties relate to the detector simulation and the evaluation of the integrated luminosity [141, 142] and are applied to every contribution estimated via MC simulated samples. The uncertainties that were found not to be negligible are categorized into six groups. A summary of these groups can be found in Table 7.5.

The theoretical uncertainties on the background modelling include a relative cross section uncertainty of 6% [143,144] for the processes involving top quarks and a dedicated systematic uncertainty on the cross-section for the Z+jets processes. All considered theoretical uncertainties on the background modelling are summarized in Table 7.6. The background contribution from $t\bar{t}$ events is affected by additional dedicated systematic uncertainties to cover the dependence on the configuration of the MC generators. These uncertainties consider the effects of initial- and final state radiation, as well as the results of different matrix element generators. They are derived by replacing the nominal sample used to estimate the $t\bar{t}$ contribution with an alternative and evaluating the resulting difference. For the matrix element, Powheg is replaced by MC@NLO [119], and for the parton shower, Pythia is replaced by Herwig++ [145]. The list of alternative samples considered is summarized in Table 7.7.

The theoretical uncertainties on the signal modelling consider initial- and final state radiation, the renormalization and factorization scale, and multi parton interactions. The resulting combined relative uncertainties on the signal acceptance for various assumed resonance masses are summarized in Table 7.8.

NP name	Description
“LPX”	(Mainly on Z+jets) systematics on PDF choose, QCD scale, strong interaction coefficient
“xsec_top”	Cross section prediction uncertainty
“TTBAR”	Top modeling sys (mainly shape sys)

Table 7.6.: Summary of theoretical systematic uncertainties related to the background modelling of the analysis.

Table 7.7.: List of sample DSIDs and names used to calculate top background uncertainty.

Variation		Sample
FSR		mc16_13TeV.410472.PhPy8EG_A14_ttbar_hdamp258p75_dilep
ISR	up	mc16_13TeV.410482.PhPy8EG_A14_ttbar_hdamp517p5_dil
	down	mc16_13TeV.410472.PhPy8EG_A14_ttbar_hdamp258p75_dilep
ME		mc16_13TeV.410465.aMcAtNloPy8EvtGen_MEN30NLO_A14N23LO_ttbar_noShWe_dil
PS		mc16_13TeV.410558.PowhegHerwig7EvtGen_H7UE_tt_hdamp258p75_704_dil

category	200 GeV	400 GeV	600 GeV	800 GeV	1000 GeV	1200 GeV	1400 GeV	1750 GeV	2000 GeV	2500 GeV
b-associated production										
b-tag	7.39	2.45	2.46	2.33	2.24	2.3	1.82	1.64	1.97	1.97
b-veto	6.42	2.07	2.97	2.19	1.65	2.87	2.07	2.63	2.45	2.18
gluon fusion										
b-tag	23.07	11.68	7.29	8.31	7.3	7.41	6.39	6.42	8.08	6.74
b-veto	4.68	1.94	2.01	2.07	1.99	1.55	1.39	1.25	1.2	1.2

Table 7.8.: Combined relative signal acceptance uncertainties (in percent).

The uncertainties on the data-driven background estimations are summarized in Table 7.9. While the uncertainty on the fake rates only considers the limited statistical power of data and simulated events in the W-FR and T-FR, the uncertainties on the fake factors are more elaborate. Here, all experimental uncertainties listed in Table 7.5 are considered when calculating the fake factors in addition to the statistical uncertainty in the DJ-FR and the dedicated b-tagging uncertainty explained in Section 7.3.2.
Table 7.10 lists the most impactful systematic uncertainties quantified by the relative increase in the expected 95% CL upper limits on $\sigma \times BR$ with respect to the statistical only expected limit. The procedure the derive such limits is described in Section 7.5. It can be seen that, depending on the assumed resonance mass and whether ggF or bbH production is considered, the leading source of uncertainty stems from the τ_{had} energy calibration, the efficiency of the τ_{had}-ID, or the theoretical uncertainty on the modelling of the Z+jets contribution.

NP name	Description
“HHFAKERATE”	Fake rate sys in $\tau_{\text{had}}\tau_{\text{had}}$
“QCDFF_BINC ”	Fake factor sys in $\tau_{\text{had}}\tau_{\text{had}}$

Table 7.9.: Summary of systematic uncertainties related to the data-driven background estimates of the analysis.

7.5. Statistical analysis

Similar to the procedure described in Section 6.3, a maximum-likelihood fit is performed to finalize the estimation of the contributions of the various processes and set limits on $\sigma \times BR$. Analogous to Eq. 6.5, the likelihood is defined as the product of the Poisson

Table 7.10.: Most impactful systematic uncertainties and the relative increase in the expected 95% CL upper limits on $\sigma \times BR$ with respect to the statistical only expected limit. The values are shown for scalar bosons with masses of 400 GeV and 1 TeV produced via ggF and bbH production.

Source	ggF (400 GeV)	ggF (1 TeV)	bbH (400 GeV)	bbH (1 TeV)
Tau id. efficiency	0.14	0.16	0.12	0.08
Tau energy scale	0.33	0.09	0.22	0.03
Z+jets bkg. modeling	0.27	0.19	0.08	0.04
Mis-id. $\tau_{\text{had-vis}}$ bkg.	0.22	0.01	0.14	0.03
Others	0.09	0.04	0.11	0.02
Total	0.54	0.28	0.45	0.13

probability terms of all bins in the final discriminant, $m_{\mathrm{T}}^{\mathrm{tot}}$. Additionally, the Gaussian constraints of the NPs governing the systematic uncertainties are factored in. The parameter of interest is the signal strength μ. It is defined as the ratio of post-fit to assumed pre-fit signal cross section. A value of $\mu = 0$ corresponds to the background-only hypothesis. In the case of $\mu = 1$, the signal strength is as predicted by the considered BSM model.

When only considering the $\tau_{\text{had}}\tau_{\text{had}}$ channel, the fit is conducted simultaneously in the b-veto and b-tag signal region. For the combined limit, the fit is conducted in the b-veto and b-tag signal regions of the $\tau_{\text{had}}\tau_{\text{had}}$ and $\tau_{\text{lep}}\tau_{\text{had}}$ channel and two dedicated control regions of the $\tau_{\text{lep}}\tau_{\text{had}}$ channel designed to constrain the Top background. The $m_{\mathrm{T}}^{\mathrm{tot}}$ distribution after this simultaneous fit assuming the background-only hypothesis can be seen in Figure 7.2. The binning displayed was used to construct the likelihood function of the simultaneous fit.

7.5.1. Limit setting

Exclusion limits are derived using the modified frequentist method, CL$_s$ [146] deploying the asymptotic approximation [147] and the test statistic, $\tilde{q}_\mu$, defined as the following likelihood ratio:

$$\tilde{q}_\mu = \begin{cases} -2\ln(L(\mu,\hat{\hat{\theta}})/L(0,\hat{\hat{\theta}})) & \text{if } \hat{\mu} < 0, \\ -2\ln(L(\mu,\hat{\hat{\theta}})/L(\hat{\mu},\hat{\theta})) & \text{if } 0 \leq \hat{\mu} \leq \mu, \\ 0 & \text{if } \hat{\mu} > \mu, \end{cases}$$

where $L(\mu,\theta)$ denotes the likelihood function, and μ and θ refer to the parameter of interest and the vector containing all NPs, respectively. Furthermore, $(\hat{\mu},\hat{\theta})$ is defined as the argument of the global maximum of $L(\mu,\theta)$, while $(\mu,\hat{\hat{\theta}})$ maximizes $L(\mu,\theta)$ conditionally for a given value of μ. According to the Neyman-Pearson-Lemma [148], such a ratio of likelihood functions is an optimal test statistic, meaning that the power is maximized for

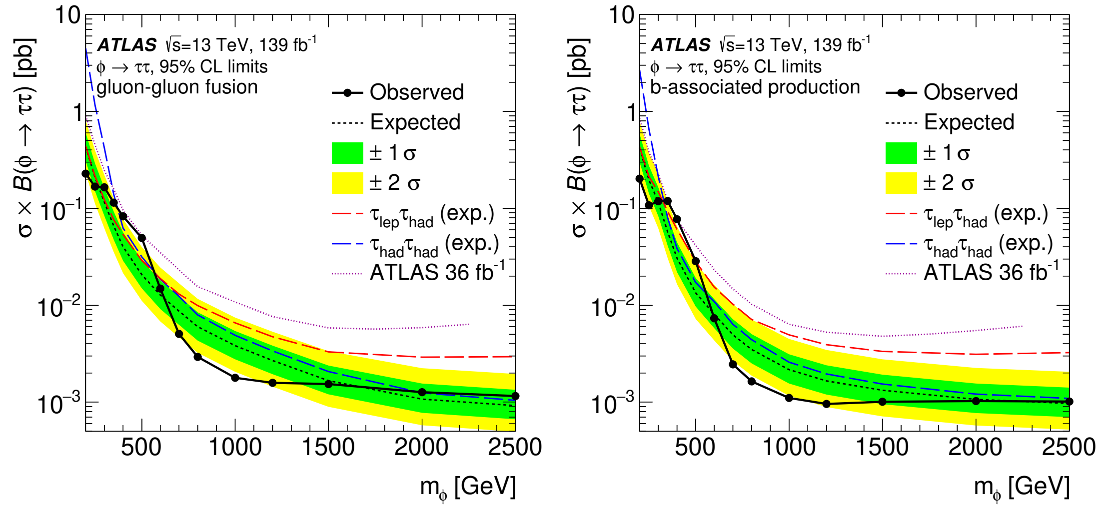

Figure 7.10.: Model independent observed and expected 95% CL upper limits on $\sigma \times BR$ for a scalar boson ϕ produced via gluon-gluon-fusion (left) and b-associated production (right). The limits were derived from a statistical combination of all considered channels. The pure $\tau_{\text{lep}}\tau_{\text{had}}$ and $\tau_{\text{had}}\tau_{\text{had}}$ limits are also shown. Additionally, the purple dotted line indicates the area excluded by the previous analysis, considering 2015-2016 ATLAS data [111].

a given significance[3]. The factor of -2 as well as the application of the natural logarithm in the definition of $\tilde{q}_\mu$ are purely convention.

Model independent exclusion limits on the production cross section times branching fraction are calculated for 14 mass points ranging from 0.2 TeV to 2.5 TeV and displayed in Figure 7.10. For comparison, the combined results are shown alongside the pure $\tau_{\text{lep}}\tau_{\text{had}}$ and $\tau_{\text{had}}\tau_{\text{had}}$ limits. It becomes apparent that for assumed resonance masses below roughly 500 GeV, the $\tau_{\text{lep}}\tau_{\text{had}}$ channel provides the dominant exclusion limit, before the $\tau_{\text{had}}\tau_{\text{had}}$ channel takes over for higher masses. Furthermore, the area excluded by the combined previous analysis, considering 2015-2016 ATLAS data, is shown for comparison.

The p-value corresponds to the probability of observing something that is equally or less compatible with the null hypothesis (SM, background-only) than the observed data. It is calculated for each excess over the background-only hypothesis. For this, a simplified test statistic, q_0, is analyzed. Using the same notation as above, it is defined as

$$q_0 = \begin{cases} -2\ln(L(0,\hat{\hat{\theta}})/L(\hat{\mu},\hat{\theta})) & \text{if } \hat{\mu} \geq 0, \\ 0 & \text{if } \hat{\mu} < 0. \end{cases}$$

---

[3] In hypothesis testing, the significance, α, corresponds to the probability of falsely rejecting the null hypothesis, whereas the power, $1-\beta$, quantifies the probability of correctly accepting the alternative hypothesis.

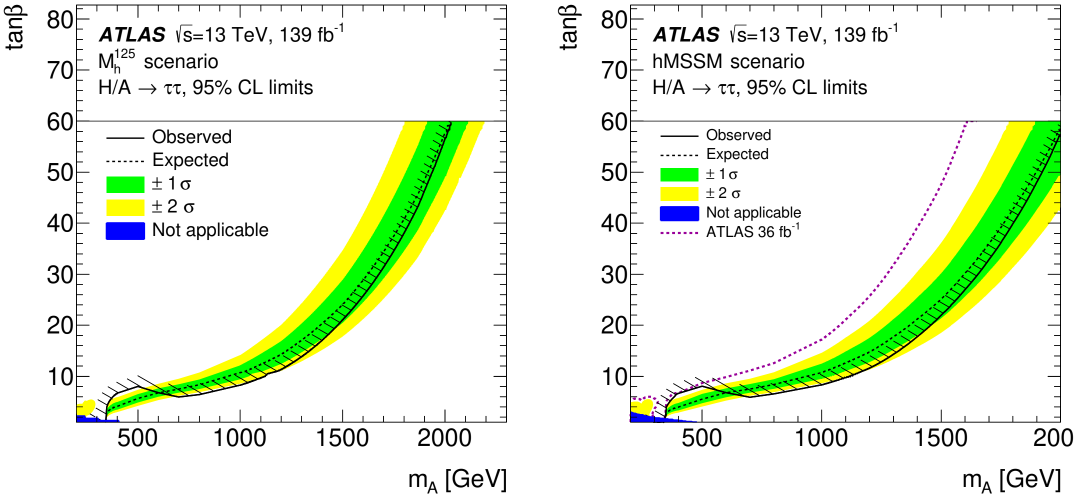

Figure 7.11.: The observed and expected 95% CL upper limits on $\tan\beta$ as a function of m_A in the M_h^{125} scenario (left) and the hMSSM scenario (right). For the regions shown in solid blue, the mass splitting between A and H bosons is above 50% of the mass resolution, making the simple addition of the cross sections invalid. The hatched area indicates that everything above the curve is excluded by the search [111].

The most significant excess over the background for a heavy resonance produced via gluon-gluon-fusion occurs at $m_\phi = 500$ GeV with a significance of 2.2σ, corresponding to a p-value of 0.014. The lowest p-value for the b-associated production is 0.003 (2.7σ), reached at $m_\phi = 400$ GeV. Hence, all in all, the data is in good agreement with the background prediction and no excess over the Standard Model with a significance of over 3σ was observed.

Limits on the production cross section times branching fraction are also derived for various assumed combinations of gluon-gluon-fusion and b-associated production. Therefore, the model-independent limits are derived as a function of the fraction of b-associated production in steps of 0.05, where 0 corresponds to pure gluon-gluon-fusion and 1 corresponds to pure b-associated production. This scan of limits is still model-independent but can be translated into various model interpretations. It is graphically displayed in Appendix C.4 in Figure C.8.

The results are interpreted in the context of different MSSM scenarios. Figure 7.11 shows the regions of the $m_A - \tan\beta$ phase space excluded at the 95% CL for the M_h^{125} and the hMSSM scenarios explained in Section 3.2.5.

CHAPTER 8

Improvements to the search for BSM $A/H/Z' \rightarrow \tau\tau$ in the fully hadronic decay channel

The analysis strategy described in Chapter 7 was used to publish the first results based on the full Run 2 dataset [111]. More refined techniques will be deployed to analyze the same dataset and publish final results with improved limits on the parameter space in question. The improvements to the search include general updates to object reconstruction and identification at ATLAS, the consideration of previously neglected events, and a multivariate analysis approach for the limit setting. Furthermore, additional BSM scenarios are considered. The various changes are explained in the following.

8.1. Updates to object reconstruction and identification

Since the last results were published, many combined performance groups at ATLAS have disclosed new algorithms and scale factors. Out of these, the switch from the BDT- to the RNN-based $\tau-$ID algorithm [104] has the most significant impact on this analysis. As mentioned in Section 5.5.3, the background from jets being misidentified as hadronically decaying τ-leptons is reduced by a factor of roughly four for $\tau_{\text{had}}\tau_{\text{had}}$ final states while maintaining the same signal efficiency. Additionally, the scale factors for the $\tau-$ID algorithm have been derived using the complete Run 2 dataset, leading to decreased uncertainties compared to the ones used in Chapter 7.

The energy calibration of $\tau_{\text{had-vis}}$ candidates now deploys a machine learning approach as described in Section 5.5.2, resulting in improved precision and decreased uncertainties.

The RNN-based DL1r algorithm [100] has replaced the BDT-based MV2c10 b-tagging

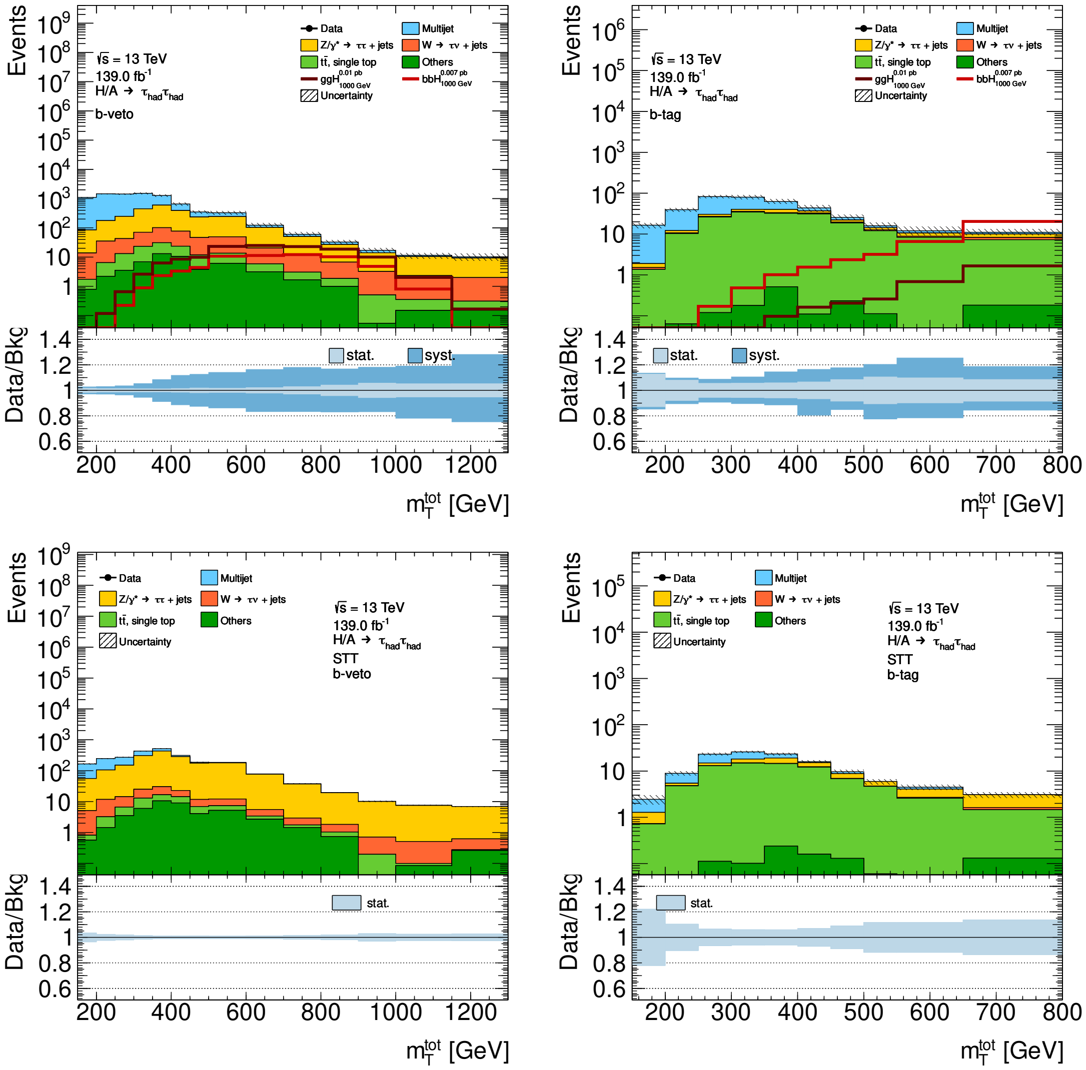

Figure 8.1.: The pre-fit distribution of $m_{\mathrm{T}}^{\mathrm{tot}}$ in the blinded in the b-veto (left) and b-tag signal region (right). At the top, the distribution is as it was used for the analysis described in Chapter 7 and the error band in the ratio plots includes systematic uncertainties. The updates to the object reconstruction and identification mentioned in the text were deployed for the two bottom plots. Here, the error band only includes statistical uncertainties and only single-tau trigger events are shown for better comparability.

algorithm. The better performance of the latter for high transverse momenta mentioned in Section 5.4.4 plays a crucial role for searches for heavy resonances produced in association with b-quarks as is the case for this analysis.
Figure 8.1 shows the impact of the changes to the object reconstruction and identification. At the top, the pre-fit distribution of $m_{\mathrm{T}}^{\mathrm{tot}}$ in the signal region as it was used for the analysis described in Chapter 7 is shown. At the bottom, the distribution of the same variable in the same signal region is shown after deploying the updates to the object reconstruction and identification mentioned above. The data is blinded for the latter since the results have not been published yet. It becomes evident that the background contribution - in particular that from multijet processes - is vastly reduced.
Since the new object reconstruction and identification algorithms are tuned to the same signal efficiencies as their predecessors, the reduction in the background does not come at a cost and is expected to increase the sensitivity significantly, contributing to stricter limits in the end.

8.2. Inclusion of di-tau trigger events

The analysis described in Chapter 7 considers events for the $\tau_{\mathrm{had}}\tau_{\mathrm{had}}$ channel if a single-tau trigger has fired. This strategy was chosen because the high p_{T} thresholds of the lowest unprescaled single-tau triggers as listed in Table 7.1 are not considerable drawbacks for searches for heavy resonances. Additionally, this approach allows a more straightforward implementation of the fake factor method.
For the improved Run-2 analysis, events recorded by the di-tau triggers (DTT) listed in Table 8.1 are also considered. The lower p_{T} of the lowest unprescaled di-tau triggers compared to the single-tau triggers increases the sensitivity for lower resonance masses. Figure 8.2 shows the pre-fit $m_{\mathrm{T}}^{\mathrm{tot}}$ distribution for events in the new di-tau trigger signal region. When comparing it to the corresponding distribution for single-tau trigger events, it becomes apparent that the di-tau triggered events predominantly contribute to values of $m_{\mathrm{T}}^{\mathrm{tot}} < 400$ GeV. As mentioned in Section 7.5.1, the $\tau_{\mathrm{lep}}\tau_{\mathrm{had}}$ channel set the stricter limits in this regime when the last results were published. The reason for this was the vast contribution of background from multijet processes in the $\tau_{\mathrm{had}}\tau_{\mathrm{had}}$ channel for low values of $m_{\mathrm{T}}^{\mathrm{tot}}$. However, the lowest resonance mass at which the $\tau_{\mathrm{had}}\tau_{\mathrm{had}}$ channel sets the stricter limit is decreased by introducing the RNN-based $\tau-$ID. Therefore, the introduction of di-tau triggered events is expected to improve the limit set by the combined analysis as well.
Events are pre-classified according to the transverse momentum of the leading $\tau_{\text{had-vis}}$ candidate before considering the triggers to simplify the background estimate and prevent overlap between the di-tau and single-tau trigger regions. This revised event selection is explained in Section 8.2.1.
Even with the increased background rejection of the RNN-based $\tau-$ID algorithm, the most prominent background in the $\tau_{\mathrm{had}}\tau_{\mathrm{had}}$ channel is the multijet contribution. In particular, the di-tau category of the signal region is dominated by this process. The

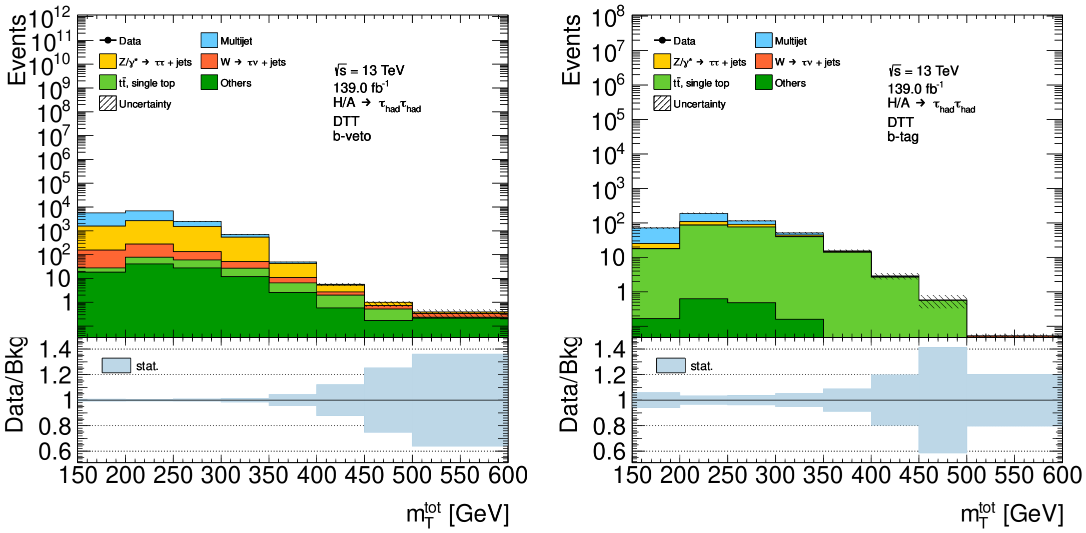

Figure 8.2.: Blinded pre-fit $m_{\mathrm{T}}^{\mathrm{tot}}$ distributions for events in the new di-tau trigger signal region. The b-veto (left) and b-tag category (right) is shown.

estimation of the multijet contribution in the single-tau trigger category of the signal region deploys the same fake factor approach as described in Section 7.3.2. For the di-tau trigger events, however, some changes to this method are necessary, as explained in Section 8.2.2.

The fake rate approach to estimate backgrounds coming from fake $\tau_{\text{had-vis}}$ candidates in simulated events remains mostly unchanged concerning the procedure described in Section 7.3.1 for single-tau trigger events. The procedure for di-tau trigger events is explained in Section 8.2.3.

8.2.1. Event selection

Apart from the updates to object reconstruction and identification explained in Section 8.1 and the introduction of di-tau trigger events, the event selection has remained unchanged from what is described in Section 7.1. Events are required to be accepted by any of the single tau or di-tau triggers that were active during the data-taking periods. The considered single-tau triggers remain unchanged concerning the last published results (see Table 7.1). The considered di-tau triggers are listed in Table 8.1. Any di-tau trigger is the combination of two single-tau triggers. Using the same naming convention as in Section 7.1.1, there are only two new terms: `mediumRNN` refers to a newly introduced RNN-based online-ID replacing the BDT-based one indicated by `medium1`. The RNN-based ID is always deployed in combination with loosened requirements on the tracks denoted by `tracktwoMVA`, where 0-3 tracks must exist on EF level.

Generally, there is always one unique lowest unprescaled single tau and di-tau trigger for each luminosity block except for the period after the TS1 in 2018, where all listed

Table 8.1.: List of di-tau triggers used in the $\tau_{\text{had}}\tau_{\text{had}}$ channel for each data taking period.

Period 2015-16

`HLT_tau35_loose1_tracktwo_tau25_loose1_tracktwo`
`HLT_tau35_medium1_tracktwo_tau25_medium1_tracktwo`
`HLT_tau80_medium1_tracktwo_L1TAU60_tau50_medium1_tracktwo_L1TAU12`

Period 2017
`HLT_tau80_medium1_tracktwo_L1TAU60_tau50_medium1_tracktwo_L1TAU12` `HLT_tau80_medium1_tracktwo_L1TAU60_tau60_medium1_tracktwo_L1TAU40`
Period 2018
`HLT_tau80_medium1_tracktwoEF_L1TAU60_tau60_medium1_tracktwoEF_L1TAU40` `HLT_tau80_mediumRNN_tracktwoMVA_L1TAU60_tau60_mediumRNN_tracktwoMVA_L1TAU40`

single- and di-tau triggers were active and unprescaled. A logical OR between the two single-tau (di-tau) triggers is used as the lowest unprescaled single-tau (di-tau) trigger during this period.

For the event selection, firstly, the data-taking period of the event and the offline p_{T} of the leading $\tau_{\text{had-vis}}$ candidate are considered. If the offline p_{T} exceeds the online p_{T} threshold of the lowest unprescaled single-tau trigger of that data-taking period by more than 5 GeV, the event is classified as a possible single-tau trigger event. Otherwise, it is classified as a possible di-tau trigger event.

For possible single-tau trigger events on data, the lowest unprescaled trigger must have fired. Furthermore, the leading $\tau_{\text{had-vis}}$ candidate must be matched to the trigger within an angular distance of $\Delta R = 0.2$. Simulated events with a truth-matched leading $\tau_{\text{had-vis}}$ candidate are treated the same. Simulated events where the leading $\tau_{\text{had-vis}}$ candidate is not truth matched are accepted in the signal region regardless of trigger decisions and weighted by the corresponding fake rate as described in Section 7.3.1.

For possible di-tau trigger events, leading and subleading $\tau_{\text{had-vis}}$ candidates must exceed the online p_{T} trigger threshold of the leading and subleading trigger leg by 5 GeV, respectively. On recorded data, the lowest unprescaled di-tau trigger must have fired, and the leading and subleading $\tau_{\text{had-vis}}$ candidates must be matched to it within an angular distance of $\Delta R = 0.2$. It does not matter whether the leading $\tau_{\text{had-vis}}$ candidate is matched to the leading or subleading leg of the di-tau trigger. Simulated events where the leading and subleading $\tau_{\text{had-vis}}$ candidates are truth matched are treated like data events. For simulated events where either the leading or the subleading $\tau_{\text{had-vis}}$ candidate is not truth-matched, one of the legs of the lowest unprescaled trigger must have fired, and the truth-matched $\tau_{\text{had-vis}}$ candidate must be matched to it. A fake rate then weights the event according to the properties of the fake $\tau_{\text{had-vis}}$ candidate. For simulated events where leading and subleading $\tau_{\text{had-vis}}$ candidate are not truth-matched, no trigger decisions are required. These events are scaled by the product of the fake rates for the leading and subleading $\tau_{\text{had-vis}}$ candidates. More details on this can be found in Section 8.2.3.

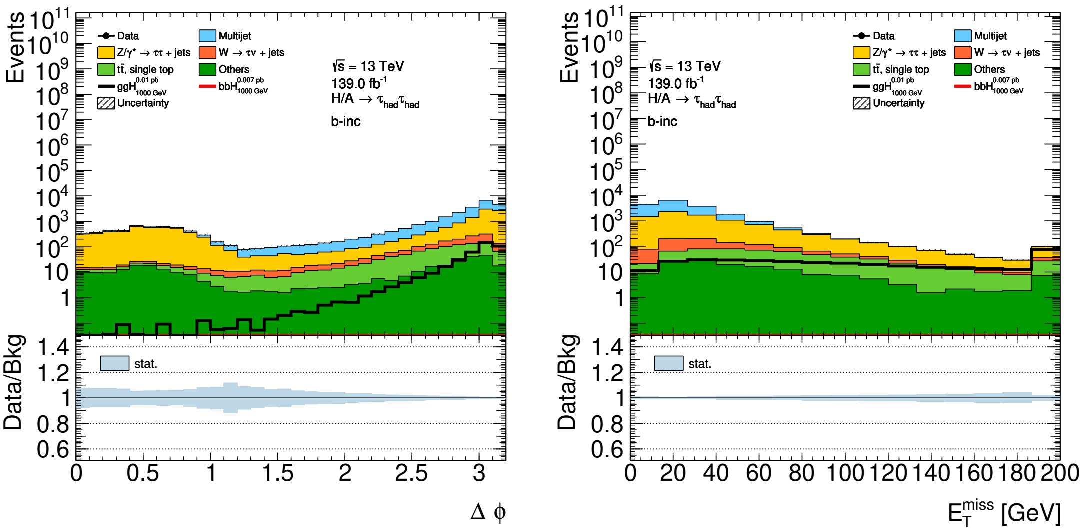

Figure 8.3.: The pre-fit distributions of $\Delta\phi(\tau_1, \tau_2)$ and $E_{\mathrm{T}}^{\mathrm{miss}}$ in the blinded signal region. These distributions motivated the set of selections defining the QCD-CR.

The event categorization listed in Table 7.2 still holds with the addition of a newly introduced control region to validate the modelling of the multijet background contribution, the QCD-CR. It is retrieved from the signal region by replacing the back-to-back requirement by $1.2 < \Delta\phi(\tau_1, \tau_2) < 2.7$ to suppress a possible signal and introducing the additional cut $E_{\mathrm{T}}^{\mathrm{miss}} < 60$ GeV to suppress the contributions from all other backgrounds. Figure 8.3 shows the pre-fit distributions of $\Delta\phi(\tau_1, \tau_2)$ and $E_{\mathrm{T}}^{\mathrm{miss}}$ in the signal region to motivate the choice of cuts. Furthermore, the requirement $\Delta R(\tau_1, \tau_2) > 2.7$ is introduced to improve the modelling in the QCD-CR. The necessity for this new control region stems from the consideration of di-tau trigger events and is explained in more detail in Section 8.2.2.

8.2.2. Fake factor approach for di-tau trigger events

As for the analysis described in Chapter 7, the multijet contribution is estimated via a data-driven fake factor approach. Unlike in the single-tau trigger category of the signal region, the subleading $\tau_{\text{had-vis}}$ candidate in the di-tau trigger category has to fulfill an online $\tau-$ID requirement to fire the trigger. Therefore, the fake factor derived in the di-jet control region is not applicable in this case. It is instead evaluated in a region that is like the signal region but with the OS requirement inverted into a SS requirement, leading to minimal possible signal contamination.

Generally, the multijet contribution is estimated via what is referred to as an 'ABCD' method. For this, four disjoint regions are considered. Then, the ratio of event yields between the two control regions 'D' and 'C' is used to weight events in control sample

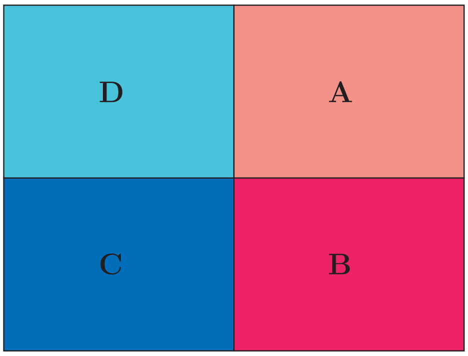

Figure 8.4.: Schematic depiction of the regions that contribute to a generalized ABCD background estimate.

'B' to arrive at the estimate of the respective background in the signal region, 'A':

$$N_A = \frac{N_D}{N_C} \times N_B. \tag{8.1}$$

For an unbiased estimate of a background contribution with the ABCD method, the ratio $\frac{N_D}{N_C}$ must be evaluated in dependence of appropriate variables and the same background contribution must dominate all three control regions. Furthermore, the regions A and B must be in a similar relation to each other as the regions C and D[1]. The latter is often achieved by defining the four regions as the combinatorial possibilities of two selection criteria and their negations. For this reason, the regions of the ABCD method can be schematically depicted as four rectangles within a single larger one as can be seen in Figure 8.4.

In the case of a fake factor approach, the top row of the ABCD matrix is defined by passing the $\tau-$ID requirement while the bottom row fails it and the ratio $\frac{N_D}{N_C}$ is evaluated binned in p_{T} and N_{track} of the $\tau_{\text{had-vis}}$ candidate. The difference between the estimates of the multijet contribution for single- and di-tau trigger events becomes apparent when schematically displaying them as in Figure 8.5. Both deploy a fake factor approach, but different cuts are used to split the left and right columns of the ABCD matrix: For the fake factor applied to single-tau trigger events, the left column differs from the right column by requiring a single-jet trigger instead of a single-tau trigger and the $\tau-$ID ID requirement on the leading $\tau_{\text{had-vis}}$ candidate is inverted to make the two columns orthogonal. For the fake factor that is applied to di-tau trigger events, the left column implies an SS requirement in contrast to the OS requirement of the right column. Since the fake factors for di-tau trigger events in the signal region are evaluated on SS events, the SS validation region cannot be used to validate the modelling of the multijet contribution as it was done for the last results (see Figure 7.7). Instead, the new QCD-CR is introduced for this validation. Figure 8.6 shows this validation in the QCD-CR for

---

[1] 'In a similar relation' means that the ratio of event yields between regions D and C is the same as between regions A and B for the process to be estimated.

1-prong and 3-prong decays, separately. The background modelling describes the data well, validating the estimate of the multijet contribution.

Systematic uncertainties In principle, all systematic uncertainties that apply to the fake factors evaluated in the DJ-FR (see Section 7.4) also apply to the fake factors evaluated on di-tau triggered events. However, the multijet estimate for di-tau trigger events evaluates fake factors on SS events and applies them to OS events, possibly introducing a bias. This bias is accounted for by a dedicated systematic uncertainty applied to the SS fake factors. It is evaluated by comparing fake factors evaluated on OS and SS events in the DJ-FR, as can be seen in Figure 8.7.
OS and SS fake factors evaluated in the DJ-FR are compatible within their uncertainties. Nonetheless, their relative difference is evaluated bin-by-bin and applied to the SS di-tau trigger fake factors as an additional shape uncertainty. The impact of that new uncertainty compared to all other uncertainties affecting these fake factors can be seen in Figure 8.8.

R_{QCD} estimate For di-tau trigger events, an alternative to the fake factor approach was also tested. It deployed an ABCD method similar to that described in Section 6.2, where instead of a fake factor, the R_{QCD}-factor is used, defined as the ratio of OS to SS events. It is evaluated on di-tau trigger events, where the subleading $\tau_{\text{had-vis}}$ candidate fails the loose τ−ID requirement and binned in $\Delta\phi(\tau_1, \tau_2)$:

$$R_{\mathrm{QCD}}(\Delta\phi(\tau_1,\tau_2)) \equiv \left.\frac{N_{OS}(\Delta\phi(\tau_1,\tau_2))}{N_{SS}(\Delta\phi(\tau_1,\tau_2))}\right|_{\mathrm{CR-1_{DTT}}} . \tag{8.2}$$

The multijet contribution in the signal region is estimated by applying the R_{QCD}-factor in the SS-SR region, which corresponds to the signal region after inverting the OS re-

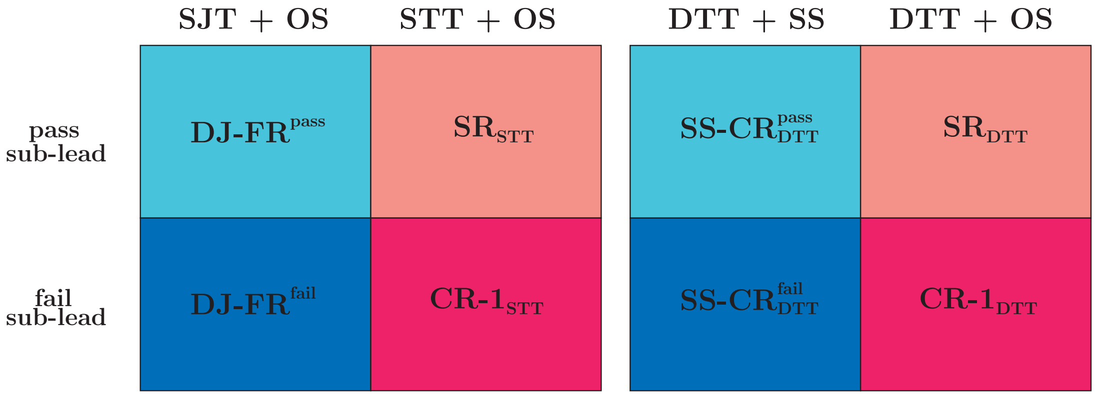

	SJT + OS	STT + OS	DTT + SS	DTT + OS
pass sub-lead	$\mathrm{DJ\text{-}FR^{pass}}$	$\mathrm{SR_{STT}}$	$\mathrm{SS\text{-}CR^{pass}_{DTT}}$	$\mathrm{SR_{DTT}}$
fail sub-lead	$\mathrm{DJ\text{-}FR^{fail}}$	$\mathrm{CR\text{-}1_{STT}}$	$\mathrm{SS\text{-}CR^{fail}_{DTT}}$	$\mathrm{CR\text{-}1_{DTT}}$

Figure 8.5.: Schematic depiction of the regions that contribute to estimation of the multijet contribution in the single-tau trigger (left) and di-tau trigger category of the signal region.

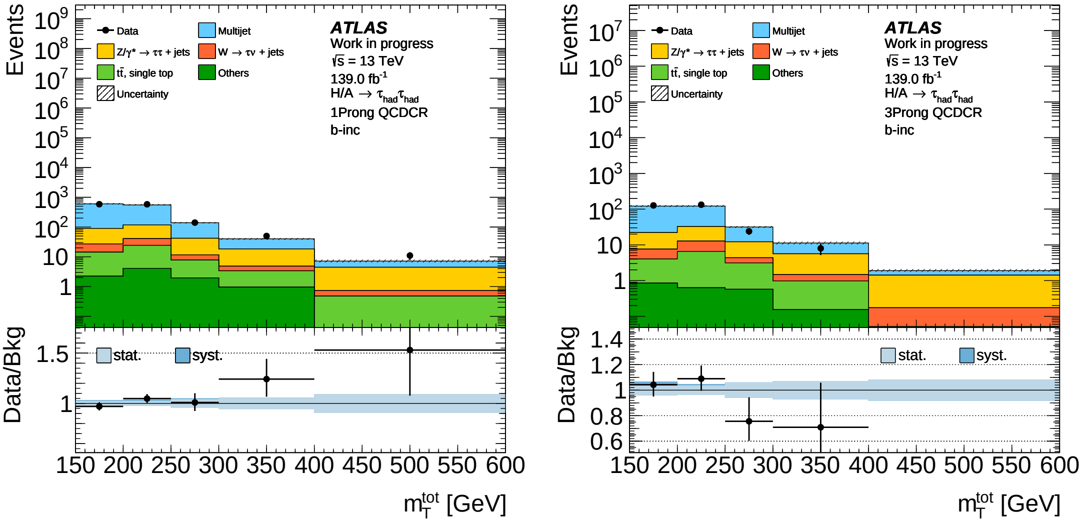

Figure 8.6.: The pre-fit distribution of $m_{\mathrm{T}}^{\mathrm{tot}}$ in the QCD-CR for 1-prong (left) and 3-prong subleading $\tau_{\text{had-vis}}$ candidates (right). The plot is trigger-inclusive, where the single-tau trigger and di-tau trigger multijet contributions are estimated with the fake factor evaluated in the DJ-FR and the SS-CR, respectively. The uncertainty band includes statistical uncertainties and systematic uncertainties that affect the fake factors.

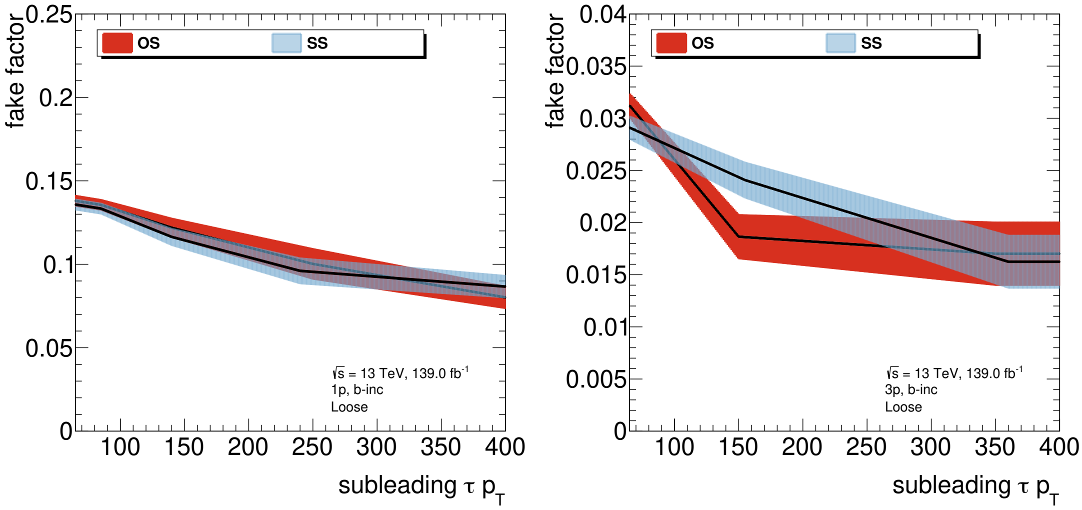

Figure 8.7.: Comparison of b-inclusive OS and SS fake factors evaluated in the di-jet region. The comparison is shown for the 1-prong (left) and 3-prong case (right). The error band includes only statistical uncertainties.

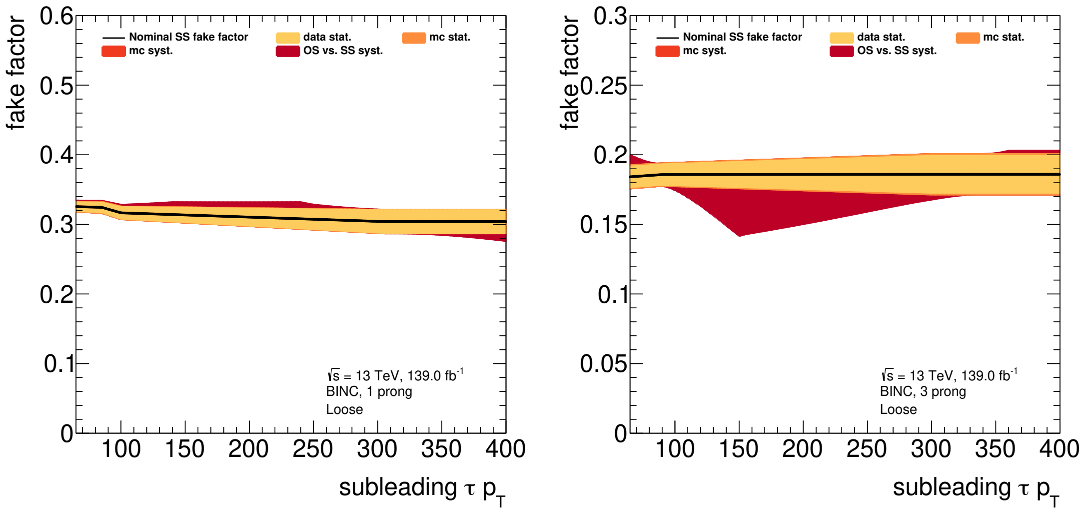

Figure 8.8.: Fake factors evaluated on SS di-tau trigger events for the 1-prong (left) and 3-prong case (right). Statistical and systematic uncertainties are shown that include the uncertainty dedicated to the possible difference between OS and SS fake factors derived by a comparison in the di-jet control region graphically depicted in Fig. 8.7.

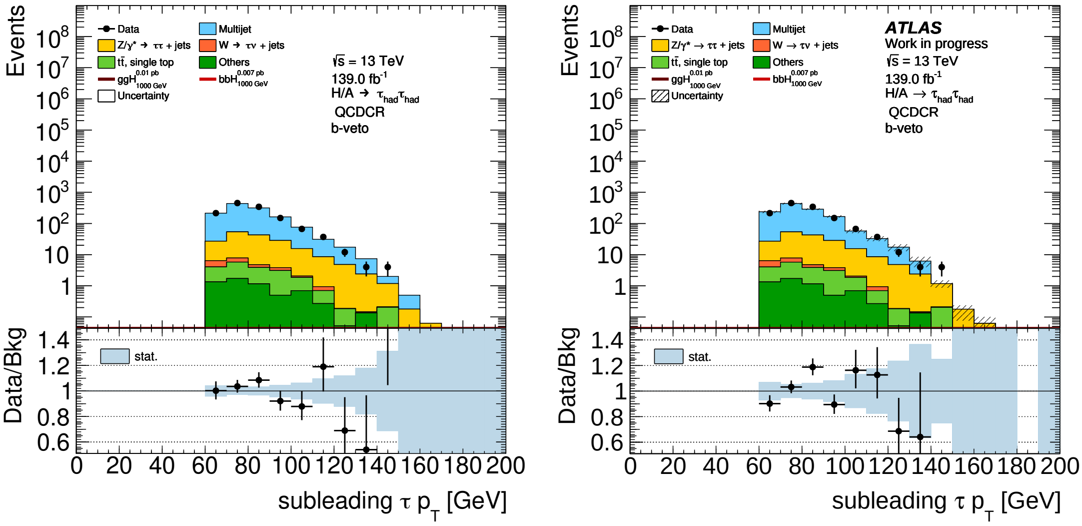

Figure 8.9.: The pre-fit p_{T} distribution of the subleading $\tau_{\text{had-vis}}$ candidate in QCD-CR for di-tau trigger events. On the left, the fake factor approach is deployed for the multijet estimate. On the right, the R_{QCD} estimate is used.

quirement. The distribution of a given variable x can be estimated via

$$N_{\text{multijet}}(\Delta\phi(\tau_1,\tau_2),x) = R_{\text{QCD}}(\Delta\phi(\tau_1,\tau_2)) \times \Big(N_{SS}(\Delta\phi(\tau_1,\tau_2),x)\Big). \tag{8.3}$$

When using the nomenclature of Figure 8.4 and the regions as depicted in Figure 8.5, the R_{QCD} estimate is an ABCD method that uses the same regions as the fake factor method, but Eq. 8.1 has to be modified to

$$N_A = \frac{N_B}{N_C} \times N_D. \tag{8.4}$$

Figure 8.9 compares the performance of the two different ways to estimate the multijet contribution. The pre-fit p_{T} distribution of the subleading $\tau_{\text{had-vis}}$ candidate is shown in the QCD-CR deploying the R_{QCD} and the fake factor approach separately. Although the modelling of the multijet contribution is acceptable for both methods, the choice was made in favour of the fake factor approach, as the statistical uncertainties are significantly smaller.

8.2.3. Fake rate approach for di-tau trigger events

As in the analysis described in Chapter 7, a partially data-driven fake rate approach is deployed to estimate the contribution from fake $\tau_{\text{had-vis}}$ candidates coming from non-multijet contributions. These are predominantly Top processes in the b-tag category and $Z/\gamma^* \to \tau\tau$ in the b-veto category.

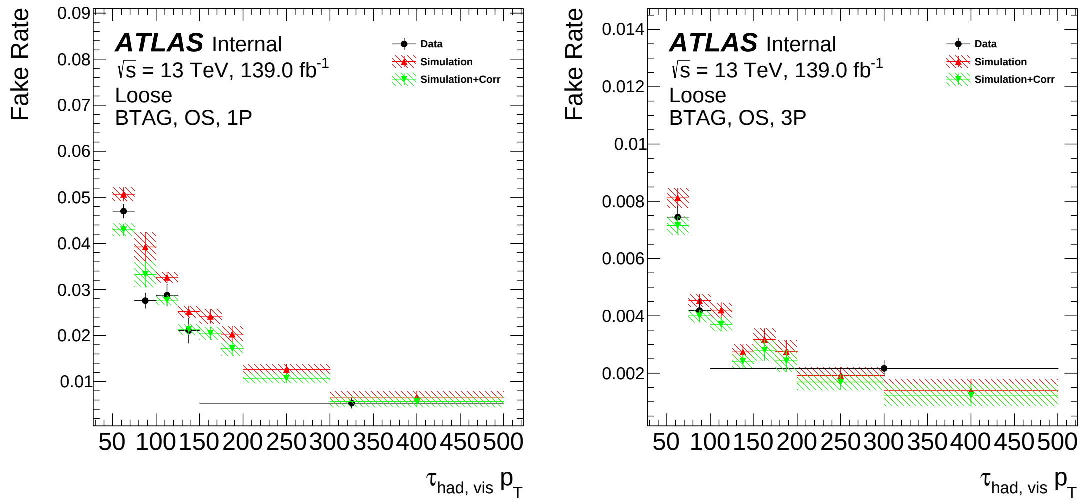

Figure 8.10.: Fake rate for the loose ID working point in the Top-FR in data compared to the top MC simulated sample, also showing the MC fake rate after normalization to data. It is split into 1-prong (left) and 3-prong (right).

The fake rate approach for single-tau trigger events in this analysis only mildly differs from the one described in Section 7.3.1. One detail is that all b-tag fake rates are now evaluated on MC simulated events in the Top-FR and normalized to the average value of those evaluated on recorded data. The reason for this is that the agreement between MC simulated and recorded data b-tag fake rates is significantly reduced, as can be seen in Figure 8.10.
The origin of this improvement of modelling of the fake rate on MC simulated top events remains unclear. It might be due to the updated b-tagging algorithm and the RNN-based $\tau-$ID algorithm mentioned in Section 8.1.
Another change with respect to the analysis described in Chapter 7 is the introduction of fake rates for the CR-1 region where the subleading $\tau_{\text{had-vis}}$ candidate is required to fail the *loose* $\tau-$ID requirement to improve the modelling and keep the semi data-driven approach consistent across all considered regions of the analysis. The corresponding fake rates can be seen in Appendix D.2 in Figure D.1. This was neglected in the previous version of the analysis as the CR-1 is dominated by the multijet contribution, rendering the influence of a mismodelled fake rate on simulated events almost negligible.
With the introduction of di-tau trigger events, fake rates have to be provided for additional combinations of trigger and $\tau-$ID requirements. All in all, these are *loose* (for subleading $\tau_{\text{had-vis}}$ in SR_{STT}), *medium*+trigger (for leading $\tau_{\text{had-vis}}$ in SR_{STT} and SR_{DTT}), *loose*+trigger (for subleading $\tau_{\text{had-vis}}$ in SR_{DTT}), *fail-loose* (for subleading $\tau_{\text{had-vis}}$ in CR-1_{STT}), and *fail-loose*+trigger (for subleading $\tau_{\text{had-vis}}$ in CR-1_{DTT}). Figure 8.11 shows all fake rates that are applied directly in the signal region.

For single-tau trigger events, the application of fake rates remains unchanged with respect to the analysis described in Chapter 7. For di-tau trigger events, however, a new approach was developed that works as follows. Analogous to the single-tau trigger category, if leading and subleading $\tau_{\text{had-vis}}$ candidates are not truth matched, no trigger is required to have fired, and the product of *medium* + trigger and *loose* fake rates is applied as an event weight. If, however, only the leading $\tau_{\text{had-vis}}$ candidate is truth-matched, the subleading leg of the considered di-tau trigger must have fired, and the leading $\tau_{\text{had-vis}}$ candidate must be matched to it. Although prescaled on data, this leg is unprescaled for simulated events as it did not have to be processed in real-time. The event is then weighed by the *loose* + trigger fake rate. If only the subleading $\tau_{\text{had-vis}}$ candidate is truth-matched, then the subleading leg of the di-tau trigger must have fired, and the subleading $\tau_{\text{had-vis}}$ candidate must be matched to it. The event is weighted by the *medium* + trigger fake rate. This scheme is summarized in Table 8.2.

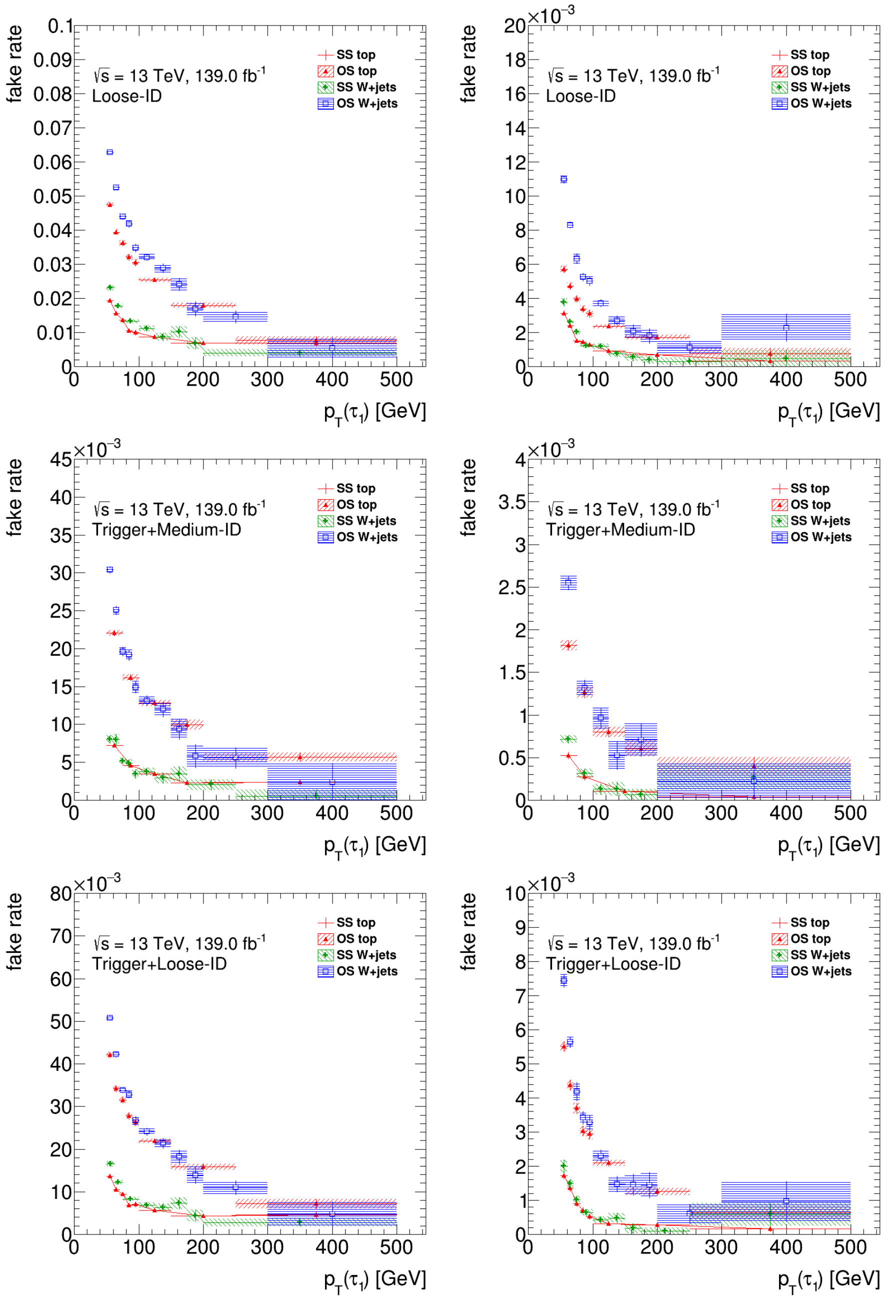

Figure 8.11.: Tau fake rates measured in the $W(\rightarrow \mu\nu)$+jets and top control regions in data for the loose working point (top) and medium working point including the trigger (middle), as well as the loose working point including the trigger (bottom). It is split in 1-prong (left) and 3-prong (right) and according to the charge product of the tag and the probe.

Table 8.2.: Scheme of how trigger and offline τ−ID decisions are processed for di-tau trigger events in the signal region. The scale factors applied for each $\tau_{\text{had-vis}}$ candidate are also listed. The overall scaling factor of the event can be written as the product $\text{SF}_0 \times \text{SF}_1$. See Table 7.4 for the corresponding scheme for single-tau trigger events.

τ_0	τ_1	trigger	ID_0	ID_1	SF_0	SF_1
data	data	DTT & match(τ_0, τ_1)	Med	Loose	1.	1.
truth	truth	DTT & match(τ_0, τ_1)	Med	Loose	$\text{SF}_{\text{trig}} * \text{SF}_{\text{ID}}$	$\text{SF}_{\text{trig}} * \text{SF}_{\text{ID}}$
truth	fake	one leg & match(τ_0)	Med	-	$\text{SF}_{\text{trig}} * \text{SF}_{\text{ID}}$	$FR^{\text{Trig}}_{\text{Loose}}$
fake	truth	one leg & match(τ_1)	-	Loose	$FR^{\text{Trig}}_{\text{Med}}$	$\text{SF}_{\text{trig}} * \text{SF}_{\text{ID}}$
fake	fake	-	-	-	$FR^{\text{Trig}}_{\text{Med}}$	$FR^{\text{Trig}}_{\text{Loose}}$

8.3. Z' signal interpretation

A hypothetical heavier version of the Z boson, usually denoted as Z', would also be able to decay into two τ leptons. Because of this, the analysis is suited to set limits on BSM Z' models (see Section 3.3) as well. A search for $Z' \to \tau\tau$ has been performed [109] but not with the full Run 2 dataset. Therefore, it will be considered for this analysis again. The kinematic properties of τ-leptons coming from $Z' \to \tau\tau$ decays are expected to be very similar to those from BSM $A/H \to \tau\tau$ decays assuming the same resonance mass. Figure 8.13 shows simulated truth-level comparisons of τ-lepton kinematics coming from the different parent particles. As expected, the distributions for $A \to \tau\tau$ and $H \to \tau\tau$ are virtually indistinguishable. $Z' \to \tau\tau$ decays, on the other hand, lead to the τ-leptons possessing slightly lower momenta on average. They are, however, also more back-to-back.

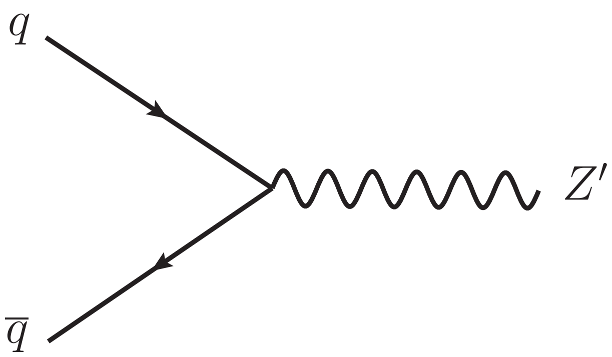

Figure 8.12.: Feynman diagram of the quark-quark-fusion Z' production process.

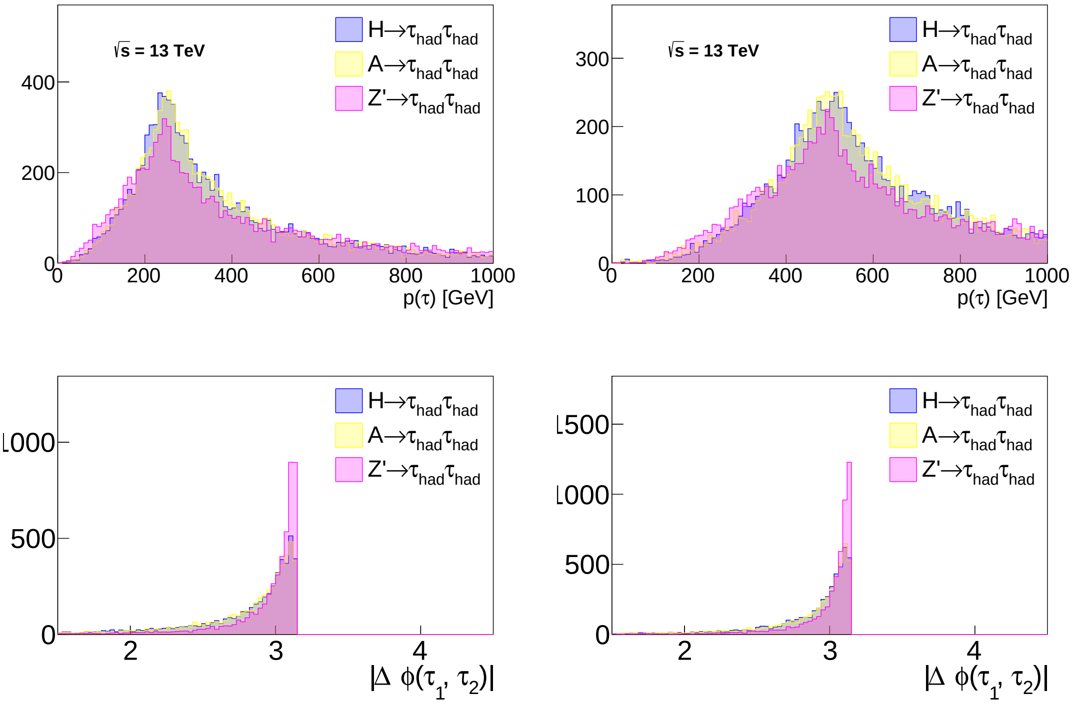

Figure 8.13.: Truth-level distributions for $H/A/Z' \to \tau\tau$ with the same number of simulated decays. The top row shows the momentum of τ-leptons, the bottom shows the distribution of $|\Delta\phi(\tau_1, \tau_2)|$. On the left (right), all parent particles are assumed to have a resonance mass of 500(1000) GeV.

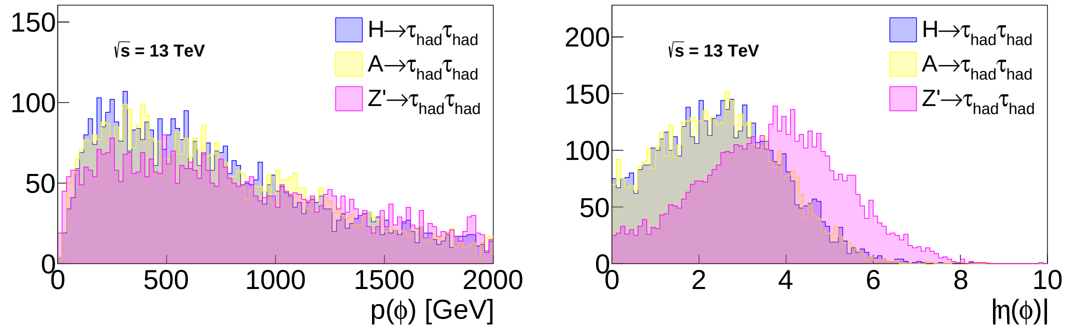

Figure 8.14.: Truth-level distributions for $H/A/Z'$ particles with the same number of simulated decays. The momentum ($|\eta|$) of the heavy resonance is depicted on the left (right). In each case, a resonance mass of 1000 GeV was assumed.

The kinematic differences between A/H and Z' decays are only partly explained by the different spin values of the parent particles. Another critical factor is the kinematics of the parent particles themselves. Figure 8.14 shows truth-level momentum and $|\eta|$ distributions of simulated A, H and Z' particles. Since Z' particles can only be produced via quark-quark-fusion as depicted in Figure 8.12, they possess, on average, slightly higher momenta and significantly larger values of $|\eta|$ than A/H produced via gluon-gluon-fusion. This can be explained by the shape of the PDFs in Figure 4.9. The momentum of quarks along the z-axis has a wider probability distribution function than that of gluons, leading to larger differences of that variable when comparing two quarks of colliding protons compared to two gluons chosen in the same fashion. Therefore, particles produced via quark-quark-fusion will, on average, have a larger boost along the z-axis than particles produced in gluon-gluon-fusion, and decay products of the former will appear more back-to-back in the transverse plane for that reason.

Instead of using MC simulation directly to produce Z' signal samples, the TauSpinner algorithm [149] can be used to reweight LO Drell-Yann ($Z/\gamma^* \to \tau\tau$) samples event by event and emulate Z' samples that way. $Z/\gamma^* \to \tau\tau$ samples can be generated in slices of the resonance mass, providing low statistical uncertainties after the reweighting. This procedure has the advantage that an arbitrary mass grid of Z' samples can be generated with relatively small computing efforts.

Figure 8.15 displays truth-level distributions for unweighted LO $Z/\gamma^* \to \tau\tau$ samples, showing their sliced nature. All in all, 19 mass slices of such samples are considered, ranging from 120 GeV to 5000 GeV in increasing mass intervals.

The TauSpinner reweighting algorithm is validated by comparing reweighted $Z/\gamma^* \to \tau_{\text{had}}\tau_{\text{had}}$ samples to $Z' \to \tau_{\text{had}}\tau_{\text{had}}$ samples directly from MC simulation. Figure 8.16 shows the truth-level distribution of the invariant mass of the $\tau_{\text{had}}\tau_{\text{had}}$ system for this comparison and an assumed resonance mass of 1 TeV. The comparison is shown for two different assumed decay widths (0.1 GeV and 10 GeV).

The difference in kinematic distributions between $Z' \to \tau_{\text{had}}\tau_{\text{had}}$ and $H \to \tau_{\text{had}}\tau_{\text{had}}$ observed is too small to be observed on reconstruction level as can be seen in Figure 8.17.

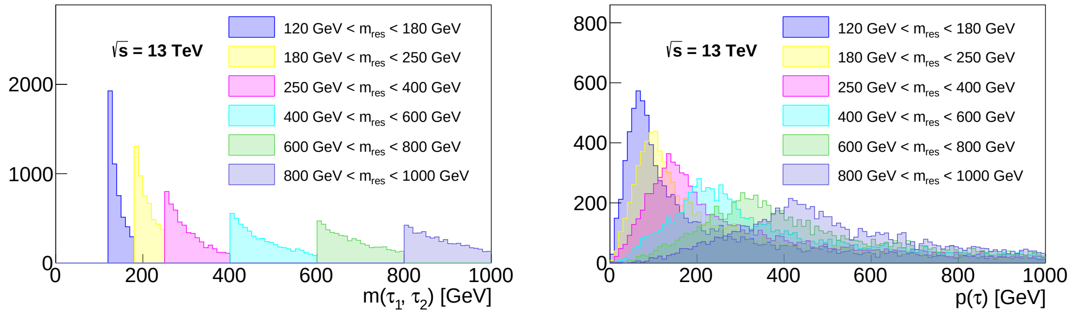

Figure 8.15.: Unweighted truth level distributions for LO $Z/\gamma^* \to \tau_{\text{had}}\tau_{\text{had}}$ produced in slices of the resonance mass. The invariant mass of the $\tau_{\text{had}}\tau_{\text{had}}$ system (left) and the momentum of the τ leptons (right) are displayed.

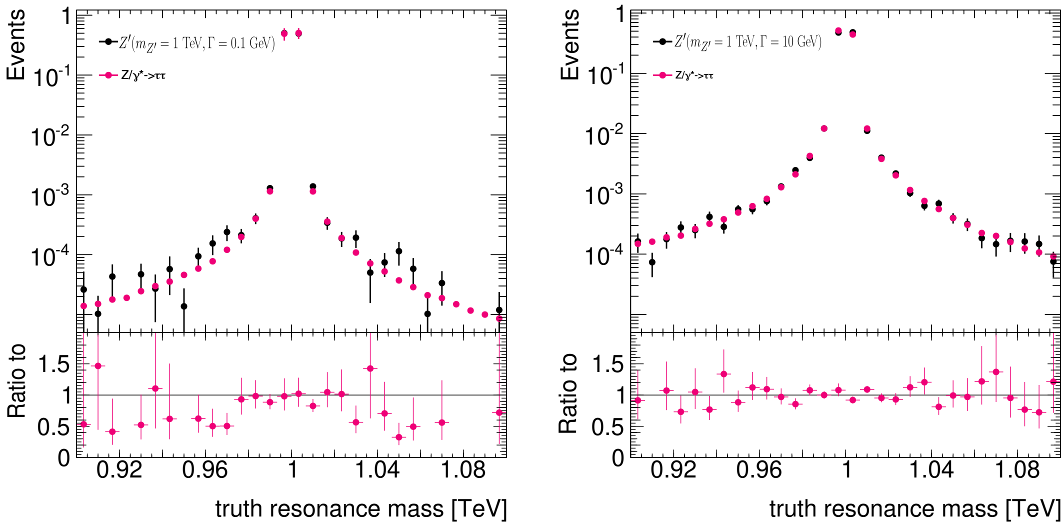

Figure 8.16.: The resonance mass distribution for actual Z' samples and those that were created from LO $Z/\gamma^* \to \tau\tau$ samples using TauSpinner for reweighting. The comparison is shown for two different assumed decay widths (0.1 GeV (left) and 10 GeV (right)).

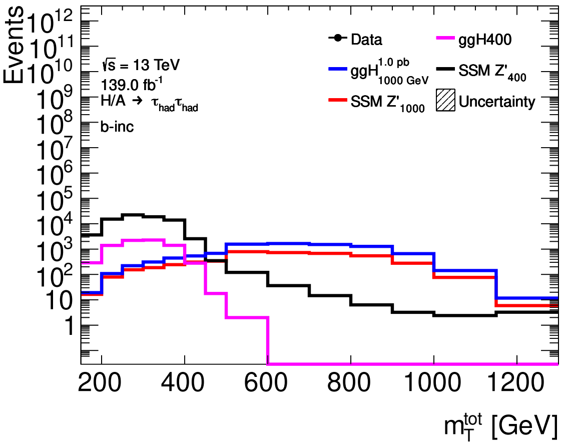

Figure 8.17.: The distribution of $m_{\mathrm{T}}^{\mathrm{tot}}$ on reconstruction level for ggH and Z' samples in the trigger-inclusive signal region. Both resonances are produced for a mass of 400 GeV and 1000 GeV, each.

8.4. Multivariate analysis

Unlike the analysis described in Chapter 7, this analysis deploys a multivariate technique to distinguish possible signal from background instead of a cut-based one with $m_{\mathrm{T}}^{\mathrm{tot}}$ as the final discriminant. Improvements in the sensitivity are expected.

8.4.1. Basic model architecture

A single parametrized neural network (PNN) [150] that takes the assumed resonance mass as an input parameter is simultaneously trained across all assumed signal masses. This approach takes advantage of the similarity between the kinematic distributions of the various signal scenarios and the smooth transition between the kinematic distributions of them. Although not expected to yield better results for one signal mass point than a dedicated NN purely trained on this scenario, the PNN will also perform well on signal masses not used for the training. This property of the PNN justifies additional credibility for the interpolation between the signal masses and reduces the computing resources needed for the training.

The PNN contains two dense ReLU[2] layers with 16 outputs each, followed by a single output dense layer with a sigmoid activation function.

The complete list of considered variables aims to take into account the kinematic features of the events and is shown in Table 8.3.

---

[2] ReLU is short for 'Rectified Linear Unit' and is a simple non-linear activation function of the form $f(x) = \max(0, x)$. A layer is dense if all of its neurons are connected to all neurons of the preceeding layer. A dense ReLU layer is a dense layer where each neuron has a ReLU activation function.

Table 8.3.: List of variables considered in the MVA training split into categories.

Mass or Combined	τ	$E_{\mathrm{T}}^{\mathrm{miss}}$	Jets	Angular
$m_{\mathrm{T}}^{\mathrm{tot}}$	$p_T(\tau_0)$	$E_{\mathrm{T}}^{\mathrm{miss}}$	N_{jets}	$\Delta\phi(\tau_0,\tau_1)$
$m_T(\tau_0, E_{\mathrm{T}}^{\mathrm{miss}})$	$p_T(\tau_1)$	ΣE_T	Σp_T(up to 3 lead jets)	$\Delta\eta(\tau_0,\tau_1)$
$m_T(\tau_1, E_{\mathrm{T}}^{\mathrm{miss}})$	$p_T(\tau_1)/p_T(\tau_0)$			$\Delta R(\tau_0,\tau_1)$
m_{vis}	$p_T(\tau_0) - p_T(\tau_1)$			$\Delta\phi(E_{\mathrm{T}}^{\mathrm{miss}},\tau_0)$
$\Sigma p_T(\tau_0,\tau_1,E_{\mathrm{T}}^{\mathrm{miss}})$	τ_0 width			$\Delta\phi(E_{\mathrm{T}}^{\mathrm{miss}},\tau_1)$
				$\sum_i \cos(\phi(E_{\mathrm{T}}^{\mathrm{miss}}) - \phi(\tau_i))$

8.4.2. PNN training

The first step of training is optimizing the number of training rounds. The data is initially split into a training and test sample containing 90% and 10% percent of the events, respectively. The model is then trained until the ROC AUC score on the test sample stops increasing, ensuring optimal performance while avoiding overtraining.
The training is then run using k-fold cross-validation, splitting the data into ten different sub-sets. Each subset is used for training once, while the other nine are used for testing. A dedicated model is trained for the b-tag and the b-veto category, each. Only the main backgrounds for each are considered. These are for the b-veto category MC simulated $Z/\gamma^* \to \tau\tau$ and $Z \to \tau\tau$ processes, and the MC simulated top contribution for the b-tag category. The multijet contribution on data in the SS-CR is used as background for the training in both categories.

8.4.3. Performance evaluation

Figure 8.18 and Figure 8.19 show the output scores and ROC curves for the PNN in the b-veto and the b-tag region, respectively. As mentioned above, the multijet contribution is taken from the SS-CR. No signs of overtraining are observed. The separation between signal and background works well and improves with increasing resonance mass.

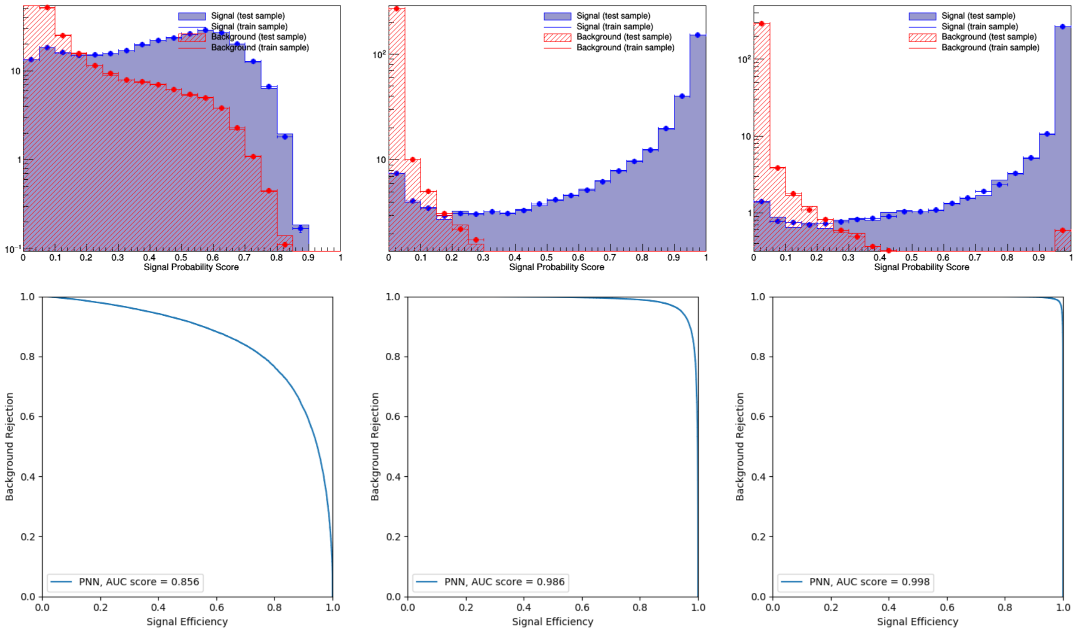

Figure 8.18.: Results of the PNN in the b-veto category. The output scores for the 400, 1200, and 2000 GeV signal mass points are shown from left to right in the top row. The histograms are split into signal and background, as well as train and test samples that were not used in the training. The bottom row shows the obtained ROC curves for the same assumed resonance masses.

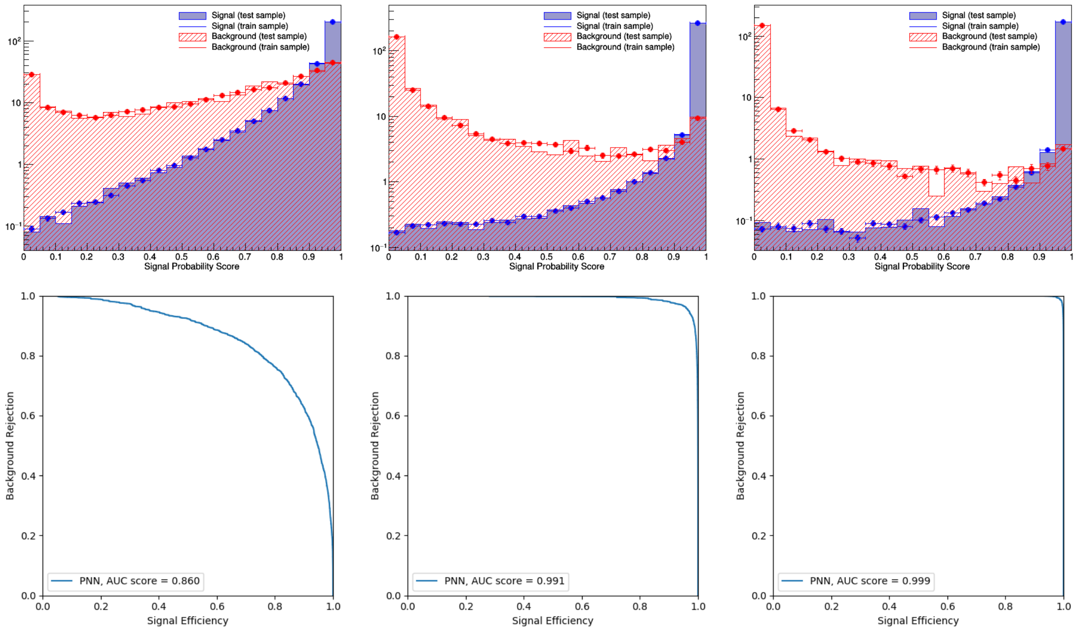

Figure 8.19.: Results of the PNN in the b-tag category. The output scores for the 400, 1200, and 2000 GeV signal mass points are shown from left to right in the top row. The histograms are split into signal and background, as well as train and test samples that were not used in the training. The bottom row shows the obtained ROC curves for the same assumed resonance masses.

8.5. Analysis Outlook

The impact of the improvements described in Sections 8.2 to 8.4 on the exclusion limits is difficult to gauge without explicitly deriving them. They will, however, be estimated in the following. The ratio of hypothetical signal to the square root of the background, $\frac{s}{\sqrt{b}}$ can be used as a metric. Assuming only statistical uncertainties of Poissonian nature, this metric is inversely proportional to the limit on $\sigma \times BR$.

Updates to object reconstruction and identification It is safe to assume that a hypothetical signal yield in this analysis would be very similar to that in the analysis described in Chapter 7 since the newly deployed identification algorithms are tuned to the same signal efficiency. Therefore, the analysis mainly benefits from the increase in background rejection. Figure 8.1 shows a roughly five-fold reduction of the multijet contribution in the b-veto category and a tenfold reduction in the b-tag category, corresponding to increasing $\frac{s}{\sqrt{b}}$ by a factor of $\sqrt{5}$ and $\sqrt{10}$ in the b-veto and b-tag signal region, respectively. The object reconstruction and identification updates also significantly reduce various systematic uncertainties, such as the tau energy scale, further improving the limits.

Inclusion of di-tau triggered events Comparing the pre-fit $m_{\mathrm{T}}^{\mathrm{tot}}$ distributions for single- and di-tau trigger events in the blinded signal region as displayed in Figure 8.1 and Figure 8.2, respectively, reveals that the newly introduced di-tau trigger events significantly contribute to the signal region in the region $m_{\mathrm{T}}^{\mathrm{tot}} < 400$ GeV. For $m_{\mathrm{T}}^{\mathrm{tot}} < 300$ GeV, the di-tau trigger events dominate the signal region, contributing roughly ten times, corresponding to increasing $\frac{s}{\sqrt{b}}$ by the factor $\sqrt{10}$. Combined with the updates to object reconstruction and identification, this would mean lowering the statistics only limit on $\sigma \times BR$ for a heavy resonance produced via gluon-gluon-fusion and b-associated production by factors of roughly seven and ten, respectively.

MVA approach The PNN trained to discriminate background from a potential signal contribution provides better separation than the default final discriminant $m_{\mathrm{T}}^{\mathrm{tot}}$. The additional sensitivity from this MVA approach will be most strongly pronounced for lower assumed resonance masses, as $m_{\mathrm{T}}^{\mathrm{tot}}$ already provides strong separation otherwise. It is not straightforward to quantify the impact on the limit setting based on a single numerical value.

Z' interpretation Considering the analysis described in Chapter 7 improved the limit on $\sigma \times BR$ tenfold with respect to the previous results (see Figure 7.10), a similar effect is expected for the limits on Z'. When factoring in the expected improvements described in Sections 8.2 to 8.4, a roughly 70- to 100-fold improvement over the previous best limit from the analysis considering 36.1 fb^{-1} can be expected.

CHAPTER 9

Conclusion

Many promising BSM theories predict the existence of heavy resonances that would preferably decay into τ-leptons, making the latter a vital part in the search for deviations from the SM. Three analyses considering final states with hadronically decaying τ-leptons were presented in this thesis. These measurements are based on each other. Evaluating the performance of the $\tau-$ID algorithm was crucial for the search for BSM $A/H \to \tau\tau$ in the fully hadronic decay channel, and the improvements to the latter will further increase the sensitivity to promising BSM scenarios such as SUSY or GUTs predicting the existence of Z' bosons.

Since the LHC is a proton-proton collider, purely hadronic interactions are an important source of background for most analyses at ATLAS, especially when reconstructing final states with hadronically decaying τ-leptons whose signatures in the detector are similar to those of quark- or gluon-initiated jets. The $\tau-$ID algorithm identifies actual hadronic τ-lepton decays, discriminating against the background, and is widely used within ATLAS.

The measurement of scale factors for the $\tau-$ID algorithm described in Chapter 6 was the first of its kind that used the full Run 2 dataset. It was also the first such measurement deploying an elaborate maximum-likelihood approach, significantly reducing the previously lowest uncertainty. A mismodelling of the BDT-based $\tau-$ID score on simulated $Z \to \tau_\mu\tau_{\text{had}}$ events was discovered, which is corrected by applying the corresponding scale factor and its uncertainties. For the newly introduced RNN-based $\tau-$ID algorithm, no significant difference in efficiency on simulated and recorded hadronic τ-lepton decays was observed.

The scale factors were implemented into the common ATLAS software framework, decreasing the systematic uncertainties on simulated hadronic τ-lepton decays for analyses considering the BDT-based $\tau-$ID algorithm, and allowing to deploy the RNN-based algorithm for the first time. In particular, the latter will significantly reduce the amount of background when considering hadronically decaying τ-leptons and, therefore, improve the sensitivity of many measurements within ATLAS.

The search for BSM $A/H \to \tau\tau$ in the fully hadronic decay channel described in Chapter 7 was conducted for the first time considering the full Run 2 dataset. The results were combined with the semi-leptonic decay channel. No excess over the SM was observed. However, the limits set on the product of production cross section and branching fraction for a heavy resonance are the strictest for this process up to date. Consequently, the analysis excluded significantly larger phase space regions of the $\tan\beta$-m_A-plane of various MSSM benchmark scenarios. In particular, for large values of m_A and $\tan\beta$, this search sets the strictest limits on the hMSSM compared to other measurements sensitive to these parameters, as can be seen in Figure 3.6.

The fully hadronic decay channel set stricter limits than its semi-leptonic counterpart for assumed resonance masses above roughly 400 GeV. Below that, the sensitivity is limited by the background from the vast multijet contribution, which was estimated via an elaborate data-driven fake factor technique. Improvements to this method were investigated and provide the possibility for a unified approach for all analyses dealing with this background. For very high masses, the main background comes from the irreducible $Z/\gamma^* \to \tau_{\text{had}}\tau_{\text{had}}$ contribution in the b-veto category and Top processes in the b-tag category.

After the first results of the search for BSM $A/H \to \tau\tau$ based on the full Run 2 dataset were published, the goal is to increase the measurement's sensitivity further by deploying more elaborate data analysis techniques on the same dataset, as detailed in Chapter 8. This is referred to as the legacy analysis, and different aspects of the search were revised. Updates to object reconstruction and identification at ATLAS that were introduced since the previous set of results were published include a new b-tagging algorithm and the switch from the BDT- to the RNN-based $\tau-$ID algorithm. The $\tau_{\text{had}}\tau_{\text{had}}$ channel of the search will especially benefit from the increased background rejection of the latter, rendering the multijet contribution almost negligible for $m_{\text{T}}^{\text{tot}} > 400$ GeV.

Another improvement is the inclusion of events triggered by di-tau triggers, expanding the considered kinematical phase space towards lower τ-lepton momenta. This new part of the signal region required a new background estimate, which was implemented and validated. Also, a PNN was trained to discriminate background from a potential signal contribution, providing better separation than the default final discriminant $m_{\text{T}}^{\text{tot}}$. The additional sensitivity from this MVA approach will be most strongly pronounced for lower assumed resonance masses, as $m_{\text{T}}^{\text{tot}}$ already provides strong separation otherwise. The combination of the measures mentioned above is expected to significantly increase the sensitivity of the combined search and shift the point at which the $\tau_{\text{had}}\tau_{\text{had}}$ channel becomes dominant towards lower resonance masses.

The introduction of a Z' signal interpretation will most likely improve the previous best limits on several models since no search for a di-tau final state has considered the full Run 2 dataset yet. The approach of reweighting simulated $Z/\gamma^* \to \tau\tau$ events to emulate a $Z' \to \tau\tau$ signal with an arbitrary resonance mass has been validated. Also, efforts are ongoing to train the MVA approach for a dedicated version to distinguish Z' signals from background.

The ATLAS detector will continue to deliver more data. Especially after the upgrade towards the High Luminosity LHC (HL-LHC), which is planned to be installed in 2025, the instantaneous luminosity will increase significantly [151]. There are also promising developments regarding the simulation to keep up with the increased data rate. For example, generative models [152] might replace the classical approach, significantly accelerating the detector simulation, and an increasing number of tasks will be fulfilled by quantum algorithms [153].

The additional data will also be used for searches for heavy Higgs bosons. Perhaps, an excess over the SM background will be discovered, proving physics beyond the Standard Model. If not, bigger parts of the parameter space of various models will be excluded. In any case, exciting times lie ahead.

Acknowledgements

Life in general, but particle physics in particular, is a team effort. The following acknowledgements mention only a tiny fraction of the people who made this thesis possible.
I am immensely grateful for everything that my supervisor, Stan Lai, has done for me. This thesis would never have converged without just the right amount of micromanagement. I admire his based supervision style of being a bit strict at first and then enduring even the hardest cringe in the later stages of my PhD.
A huge thank you goes to Michel Janus, the perfect mentor for a young, clueless scientist. He conveyed an unbelievable amount of insight and talked me out of many mistakes.
Thanks also to Jason Veatch and Kira Abeling, who always offered open ears and cookies, respectively. Actually, Kira only offered a single cookie. I had to smuggle the rest via an undisclosed mule (I happen to have a talent for such operations).
Petar Bokan and Serhat Ördek have become my role models in terms of science and humour. Our friendship will outlive particle physics. Thank you both for having a cultural background and granting me the k- and g- word pass.
I would also like to thank Liron Barak, Luca Fiorini, Antonio de Maria, Max Märker, and Adam Bailey for the fruitful cooperation outside of the Göttingen institute.
I hereby invite Arnulf Quadt to all my future birthday parties. Thank you very much for acting as my second referee and let me know if you're in Geneva on the 10th of March.
Most importantly, my gratitude goes to my family, especially to Sushi and Taffi, for frequently reminding me that there is more to life than getting a PhD and to Thore for proofreading this thesis.

Danke Thors, dass du mich für Physik begeistert hast. Entschuldige, dass ich bei einem Experiment promoviert habe, das fast ausschließlich Hintergrund produziert. In Zukunft werde ich mich Neutrinos widmen.

Dzięki Ewie. Pokazałeś mi, że niewidomi też widzą.

Bibliography

[1] ATLAS Collaboration, G. Aad et al., *Observation of a new particle in the search for the Standard Model Higgs boson with the ATLAS detector at the LHC*, Phys. Lett. **B716** (2012) 1–29.

[2] S. Chatrchyan, et al., *Observation of a new boson at a mass of 125 GeV with the CMS experiment at the LHC*, Physics Letters B **716** (2012) 30–61.

[3] ATLAS, CMS Collaboration, G. Aad et al., *Combined Measurement of the Higgs Boson Mass in pp Collisions at* $\sqrt{s} = 7$ *and 8 TeV with the ATLAS and CMS Experiments*, Phys. Rev. Lett. **114** (2015) 191803.

[4] ATLAS Collaboration, M. Aaboud et al., *Cross-section measurements of the Higgs boson decaying into a pair of* τ*-leptons in proton-proton collisions at* $\sqrt{s} = 13$ *TeV with the ATLAS detector*, Phys. Rev. D **99** (2019) 072001.

[5] J. F. Gunion, et al., *The Higgs Hunter's Guide*, vol. 80. 2000.

[6] S. L. Glashow, *Partial Symmetries of Weak Interactions*, Nucl. Phys. **22** (1961) 579–588.

[7] S. Weinberg, *A Model of Leptons*, Phys. Rev. Lett. **19** (1967) 1264–1266.

[8] A. Salam, *Weak and Electromagnetic Interactions*, ed. Nobel Symposium No. 8 (Almqvist & Wiksell, Stockholm, 1968).

[9] Particle Data Group Collaboration, P. Zyla et al., *Review of Particle Physics*, PTEP **2020** (2020) 083C01.

[10] C.-N. Yang and R. L. Mills, *Conservation of Isotopic Spin and Isotopic Gauge Invariance*, Phys. Rev. **96** (1954) 191–195.

[11] G. Hooft, *Renormalizable Lagrangians for massive Yang-Mills fields*, Nuclear Physics B **35** (1971) 167–188.

[12] G. 't Hooft and M. Veltman, *Regularization and renormalization of gauge fields*, Nuclear Physics B **44** (1972) 189–213.

[13] F. Englert and R. Brout, *Broken Symmetry and the Mass of Gauge Vector Mesons*, Phys. Rev. Lett. **13** (1964) 321–323.

[14] P. Higgs, *Broken symmetries, massless particles and gauge fields*, Physics Letters **12** (1964) 132–133.

[15] P. W. Higgs, *Broken Symmetries and the Masses of Gauge Bosons*, Phys. Rev. Lett. **13** (1964) 508–509.

[16] G. Aad, et al., *Study of the spin and parity of the Higgs boson in diboson decays with the ATLAS detector*, The European Physical Journal C **75** (2015).

[17] S. Chatrchyan, et al., *Study of the Mass and Spin-Parity of the Higgs Boson Candidate via Its Decays to Z Boson Pairs*, Physical Review Letters **110** (2013).

[18] ATLAS Collaboration, G. Aad et al., *LHC Higgs Cross Section Working Group*, `https://twiki.cern.ch/twiki/bin/view/lhcphysics/lhchwg`, 2020.

[19] ATLAS Collaboration, G. Aad et al., *Combined measurements of Higgs boson production and decay using up to* 80 *fb^{-1} of proton-proton collision data at $\sqrt{s} = 13$ TeV collected with the ATLAS experiment*, Phys. Rev. D **101** (2020) 012002.

[20] H. Hamber, *Quantum Gravitation: The Feynman Path Integral Approach*. 01, 2009.

[21] V. Faraoni, *Three new roads to the Planck scale*, `arXiv:1705.09749 [gr-qc]`.

[22] J. Polchinski, *String theory. Vol. 2: Superstring theory and beyond*. Cambridge Monographs on Mathematical Physics. Cambridge University Press, 12, 2007.

[23] F. Zwicky, *On the Masses of Nebulae and of Clusters of Nebulae*, The Astrophysical Journal **86** (1937) 217.

[24] A. T. Bajkova and V. V. Bobylev, *Rotation curve and mass distribution in the Galaxy from the velocities of objects at distances up to 200 kpc*, Astron. Lett. **42** (2016) 567–582.

[25] T. Clifton, et al., *Modified gravity and cosmology*, Physics Reports **513** (2012) 1–189.

[26] V. Trimble, *Existence and nature of dark matter in the universe.*, Annual Review of Astronomoy and Astrophysics **25** (1987) 425–472.

[27] N. Vittorio and J. Silk, *Fine-scale anisotropy of the cosmic microwave background in a universe dominated by cold dark matter*, Astrophysical Journal Letters **285** (1984) L39–L43.

[28] A. H. G. Peter, *Dark Matter: A Brief Review*, ArXiv e-prints (2012).

[29] S. P. Martin, *A Supersymmetry primer*, Adv. Ser. Direct. High Energy Phys. **18** (1998) 1–98.

[30] S. Dimopoulos, S. Raby, and F. Wilczek, *Supersymmetry and the Scale of Unification*, Phys. Rev. D **24** (1981) 1681–1683.

[31] M. Jankiewicz, *Various aspects of gravity*. PhD thesis, Vanderbilt University, Dec., 2007.

[32] R. Haag, J. T. Lopuszanski, and M. Sohnius, *All Possible Generators of Supersymmetries of the s Matrix*, Nucl. Phys. **B88** (1975) 257.

[33] A. Djouadi, et al., *Fully covering the MSSM Higgs sector at the LHC*, JHEP **06** (2015) 168.

[34] R. Barbieri and G. F. Giudice, *Upper bounds on supersymmetric particle masses*, Nucl. Phys. B **306** (1987).

[35] M. Carena, et al., *MSSM Higgs Boson Searches at the LHC: Benchmark Scenarios after the Discovery of a Higgs-like Particle*, Eur. Phys. J. **C73** (2013) 2552.

[36] O. Stal, *Prospects for Higgs boson scenarios beyond the Standard ModelProspects for Higgs boson scenarios beyond the standard model*, Int. J. Mod. Phys. Conf. Ser. **31** (2014) 1460289.

[37] A. Djouadi, et al., *The post-Higgs MSSM scenario: Habemus MSSM?*, Eur. Phys. J. **C73** (2013) 2650.

[38] ATLAS Collaboration, *Summary plots from the ATLAS SUSY physics group*, 2021. `https://twiki.cern.ch/twiki/bin/view/AtlasPublic/SupersymmetryPublicResults`.

[39] J. L. Hewett and T. G. Rizzo, *Low-energy phenomenology of superstring-inspired E6 models*, Physics Reports **183** (1989) 193–381.

[40] M. Cvetic and S. Godfrey, *Discovery and identification of extra gauge bosons*. 3, 1995. `arXiv:hep-ph/9504216`.

[41] A. Leike, *The phenomenology of extra neutral gauge bosons*, Physics Reports **317** (1999) 143–250.

[42] R. Diener, S. Godfrey, and T. A. W. Martin, *Unravelling an extra neutral gauge boson at the LHC using third generation fermions*, Physical Review D **83** (2011).

[43] P. Langacker, *The physics of heavy Z' gauge bosons*, Reviews of Modern Physics **81** (2009) 1199–1228.

[44] T. Jezo, et al., *NLO+NLL limits on W' and Z' gauge boson masses in general extensions of the Standard Model*, Journal of High Energy Physics **2014** (2014) .

[45] K. R. Lynch, et al., *Finding Z' bosons coupled preferentially to the third family at CERN LEP and the Fermilab Tevatron*, Physical Review D **63** (2001).

[46] E. Malkawi, T. Tait, and C.-P. Yuan, *A model of strong flavor dynamics for the top quark*, Physics Letters B **385** (1996) 304–310.

[47] K. Hsieh, et al., *Global analysis of general$SU(2)\times SU(2)\times U(1)$models with precision data*, Physical Review D **82** (2010).

[48] D. J. Muller and S. Nandi, *Topflavor: a separate SU(2) for the third family*, Physics Letters B **383** (1996) 345–350.

[49] R. Cashmore, L. Maiani, and J.-P. Revol, *Prestigious Discoveries at CERN: 1973 Neutral Currents 1983 W & Z Bosons*. 01, 2003.

[50] M. Caffo, R. Gatto, and E. Remiddi, *Neutrino counting in e^+e^- collisions*, Nuclear Physics B **286** (1987) 293–305.

[51] V. Fanti, et al., *A new measurement of direct CP violation in two pion decays of the neutral kaon*, Physics Letters B **465** (1999) 335–348.

[52] L. Evans and P. Bryant, *LHC Machine*, JINST **3** (2008) S08001.

[53] ATLAS Collaboration, A. Airapetian et al., *ATLAS: Detector and physics performance technical design report. Volume 2*,.

[54] E. Mobs, *The CERN accelerator complex - 2019. Complexe des accélérateurs du CERN - 2019*, `https://cds.cern.ch/record/2684277`, General Photo.

[55] ATLAS Collaboration, G. Aad et al., *Luminosity Public Results Run 2*, `https://twiki.cern.ch/twiki/bin/view/AtlasPublic/LuminosityPublicResultsRun2`, 2021.

[56] ATLAS Collaboration, G. Aad et al., *The ATLAS Experiment at the CERN Large Hadron Collider*, JINST **3** (2008) S08003.

[57] CMS Collaboration, S. Chatrchyan et al., *The CMS Experiment at the CERN LHC*, JINST **3** (2008) S08004.

[58] LHCb Collaboration, A. A. Alves, Jr. et al., *The LHCb Detector at the LHC*, JINST **3** (2008) S08005.

[59] ALICE Collaboration, K. Aamodt et al., *The ALICE experiment at the CERN LHC*, JINST **3** (2008) S08002.

[60] TOTEM Collaboration, V. Berardi, et al., *Total cross-section, elastic scattering and diffraction dissociation at the Large Hadron Collider at CERN: TOTEM Technical Design Report*, tech. rep., Geneva, 2004. `https://cds.cern.ch/record/704349`.

[61] MoEDAL Collaboration, J. Pinfold, et al., *Technical Design Report of the MoEDAL Experiment*, tech. rep., Jun, 2009. `https://cds.cern.ch/record/1181486`.

[62] A. Tricomi, et al., *The LHCf experiment at the LHC: Physics Goals and Status*, Nucl. Phys. B, Proc. Suppl. **196** (2009) 30–35.

[63] M. Schott and M. Dunford, *Review of single vector boson production in pp collisions at* $\sqrt{s} = 7\ TeV$, Eur. Phys. J. **C74** (2014) 2916.

[64] ATLAS Collaboration, M. Capeans, et al., *ATLAS Insertable B-Layer Technical Design Report*, tech. rep., Sep, 2010. `https://cds.cern.ch/record/1291633`.

[65] A. Ruiz-Martinez and ATLAS Collaboration, *The Run-2 ATLAS Trigger System*, tech. rep., CERN, Geneva, Feb, 2016. `https://cds.cern.ch/record/2133909`.

[66] G. Aad, et al., *The ATLAS Simulation Infrastructure*, The European Physical Journal C **70** (2010) 823–874.

[67] NNPDF Collaboration, R. D. Ball et al., *Parton distributions from high-precision collider data*, Eur. Phys. J. C **77** (2017) 663.

[68] A. Buckley, et al., *General-purpose event generators for LHC physics*, Physics Reports **504** (2011) 145–233.

[69] B. Andersson, et al., *Parton fragmentation and string dynamics*, Physics Reports **97** (1983) 31–145.

[70] B. Webber, *A QCD model for jet fragmentation including soft gluon interference*, Nuclear Physics B **238** (1984) 492–528.

[71] A. Buckley, et al., *Systematic event generator tuning for the LHC*, The European Physical Journal C **65** (2009) 331–357.

[72] P. Z. Skands, *Tuning Monte Carlo generators: The Perugia tunes*, Physical Review D **82** (2010).

[73] T. Sjöstrand and P. Skands, *Multiple Interactions and the Structure of Beam Remnants*, Journal of High Energy Physics **2004** (2004) 053–053.

[74] M. Bähr, S. Gieseke, and M. H. Seymour, *Simulation of multiple partonic interactions in Herwig++*, Journal of High Energy Physics **2008** (2008) 076–076.

[75] GEANT4 Collaboration, S. Agostinelli et al., *GEANT4–a simulation toolkit*, Nucl. Instrum. Meth. A **506** (2003) 250–303.

[76] W. Lukas, *Fast Simulation for ATLAS: Atlfast-II and ISF*, tech. rep., CERN, Geneva, Jun, 2012. `https://cds.cern.ch/record/1458503`.

[77] J. Shiers, *The Worldwide LHC Computing Grid (worldwide LCG)*, Computer Physics Communications **177** (2007) 219–223, Proceedings of the Conference on Computational Physics 2006.

[78] K. Bos, et al., *LHC computing Grid: Technical Design Report. Version 1.06 (20 Jun 2005).* Technical design report. LCG. CERN, Geneva, 2005. `http://cds.cern.ch/record/840543`.

[79] CERN, *The Grid: A system of tiers*, `https://home.cern/science/computing/grid-system-tiers`.

[80] I. Bird, *Computing for the Large Hadron Collider*, Annual Review of Nuclear and Particle Science **61** (2011) 99–118.

[81] ATLAS Collaboration, M. Aaboud et al., *Performance of the ATLAS Track Reconstruction Algorithms in Dense Environments in LHC Run 2*, Eur. Phys. J. C **77** (2017) 673.

[82] A. Rosenfeld and J. L. Pfaltz, *Sequential Operations in Digital Picture Processing*, J. ACM **13** (1966) 471–494.

[83] ATLAS Collaboration, M. Aaboud et al., *Reconstruction of primary vertices at the ATLAS experiment in Run 1 proton–proton collisions at the LHC*, Eur. Phys. J. C **77** (2017) 332.

[84] ATLAS Collaboration, G. Aad et al., *Performance of primary vertex reconstruction in proton-proton collisions at* $\sqrt{s}=7$ *TeV in the ATLAS experiment*, tech. rep., CERN, Geneva, Jul, 2010. `https://cds.cern.ch/record/1281344`.

[85] ATLAS Collaboration, M. Aaboud et al., *Electron reconstruction and identification in the ATLAS experiment using the 2015 and 2016 LHC proton-proton collision data at* $\sqrt{s} = 13$ *TeV*, Eur. Phys. J. C **79** (2019) 639.

[86] W. Lampl, et al., *Calorimeter Clustering Algorithms: Description and Performance*, tech. rep., CERN, Geneva, Apr, 2008. `https://cds.cern.ch/record/1099735`.

[87] ATLAS Collaboration, G. Aad et al., *Electron efficiency measurements with the ATLAS detector using the 2015 LHC proton-proton collision data*, tech. rep., CERN, Geneva, Jun, 2016. `https://cds.cern.ch/record/2157687`.

[88] ATLAS Collaboration, G. Aad et al., *Electron and photon energy calibration with the ATLAS detector using data collected in 2015 at* $\sqrt{s} = 13$ TeV, tech. rep., CERN, Geneva, Aug, 2016. `https://cds.cern.ch/record/2203514`.

[89] ATLAS Collaboration, G. Aad et al., *Electron and photon performance measurements with the ATLAS detector using the 2015–2017 LHC proton-proton collision data*, JINST **14** (2019) P12006.

[90] ATLAS Collaboration, G. Aad et al., *Muon reconstruction performance of the ATLAS detector in proton–proton collision data at* $\sqrt{s}$ *=13 TeV*, Eur. Phys. J. C **76** (2016) 292.

[91] ATLAS Collaboration, G. Aad et al., *Topological cell clustering in the ATLAS calorimeters and its performance in LHC Run 1*, Eur. Phys. J. C **77** (2017) 490.

[92] M. Cacciari, G. P. Salam, and G. Soyez, *The anti-*k_t *jet clustering algorithm*, JHEP **04** (2008) 063.

[93] S. D. Ellis and D. E. Soper, *Successive combination jet algorithm for hadron collisions*, Phys. Rev. D **48** (1993) 3160–3166.

[94] Y. L. Dokshitzer, et al., *Better jet clustering algorithms*, JHEP **08** (1997) 001.

[95] ATLAS Collaboration, M. Aaboud et al., *Jet energy scale measurements and their systematic uncertainties in proton-proton collisions at* $\sqrt{s} = 13$ *TeV with the ATLAS detector*, Phys. Rev. D **96** (2017) 072002.

[96] M. Cacciari and G. P. Salam, *Pileup subtraction using jet areas*, Phys. Lett. B **659** (2008) 119–126.

[97] *Tagging and suppression of pileup jets with the ATLAS detector*, tech. rep., CERN, Geneva, May, 2014. `https://cds.cern.ch/record/1700870`.

[98] ATLAS Collaboration, M. Aaboud et al., *Identification and rejection of pile-up jets at high pseudorapidity with the ATLAS detector*, Eur. Phys. J. C **77** (2017) 580.

[99] ATLAS Collaboration, G. Aad et al., *Performance of b-Jet Identification in the ATLAS Experiment*, JINST **11** (2016) P04008.

[100] ATLAS Collaboration, G. Aad et al., *Search for new resonances in mass distributions of jet pairs using 139 fb*$^{-1}$ *of pp collisions at* $\sqrt{s} = 13$ *TeV with the ATLAS detector*, JHEP **03** (2020) 145.

[101] ATLAS Collaboration, G. Aad et al., *Reconstruction, Energy Calibration, and Identification of Hadronically Decaying Tau Leptons in the ATLAS Experiment for Run-2 of the LHC*, Tech. Rep. ATL-PHYS-PUB-2015-045, CERN, Geneva, Nov, 2015. `http://cds.cern.ch/record/2064383`.

[102] ATLAS Collaboration, G. Aad et al., *Measurement of the tau lepton reconstruction and identification performance in the ATLAS experiment using pp collisions at* $\sqrt{s} = 13$ *TeV*, tech. rep., CERN, Geneva, May, 2017. `https://cds.cern.ch/record/2261772`.

[103] ATLAS Collaboration, G. Aad et al., *Reconstruction of hadronic decay products of tau leptons with the ATLAS experiment*, Eur. Phys. J. C **76** (2016) 295.

[104] ATLAS Collaboration, G. Aad et al., *Identification of hadronic tau lepton decays using neural networks in the ATLAS experiment*, Tech. Rep. ATL-PHYS-PUB-2019-033, CERN, Geneva, Aug, 2019. `http://cds.cern.ch/record/2688062`.

[105] S. Hochreiter and J. Schmidhuber, *Long Short-Term Memory*, Neural Computation **9** (1997) 1735–1780.

[106] ATLAS Collaboration, G. Aad et al., *Performance of Missing Transverse Momentum Reconstruction in Proton-Proton Collisions at 7 TeV with ATLAS*, Eur. Phys. J. C **72** (2012) 1844.

[107] ATLAS Collaboration, M. Aaboud et al., *Search for Minimal Supersymmetric Standard Model Higgs bosons H/A and for a Z' boson in the $\tau\tau$ final state produced in pp collisions at $\sqrt{s} = 13$ TeV with the ATLAS Detector*, Eur. Phys. J. C **76** (2016) 585.

[108] ATLAS Collaboration, G. Aad et al., *Performance of the ATLAS Trigger System in 2010*, Eur. Phys. J. C **72** (2012) 1849.

[109] ATLAS Collaboration, *Search for neutral MSSM Higgs bosons $H/A \to \tau_{lep}\tau_{had}$ and $Z' \to \tau_{lep}\tau_{had}$ produced in 13 TeV collisions with the ATLAS detector*, `https://cds.cern.ch/record/2131232`.

[110] A. Elagin, P. Murat, A. Pranko and A. Safonov, *A new mass reconstruction technique for resonances decaying to di-τ*, Nucl. Instrum. Meth. **A 654** (2011) 481–489.

[111] ATLAS Collaboration, G. Aad et al., *Search for heavy Higgs bosons decaying into two tau leptons with the ATLAS detector using pp collisions at $\sqrt{s} = 13$ TeV*, Phys. Rev. Lett. **125** (2020) 051801.

[112] P. Nason, *A New method for combining NLO QCD with shower Monte Carlo algorithms*, JHEP **11** (2004) 040.

[113] S. Frixione, P. Nason, and C. Oleari, *Matching NLO QCD computations with parton shower simulations: the POWHEG method*, JHEP **11** (2007) 070.

[114] S. Alioli, et al., *A general framework for implementing NLO calculations in shower Monte Carlo programs: the POWHEG BOX*, JHEP **06** (2010) 043.

[115] S. Alioli, et al., *NLO Higgs boson production via gluon fusion matched with shower in POWHEG*, JHEP **04** (2009) 002.

[116] E. Bagnaschi, G. Degrassi, P. Slavich and A. Vicini, *Higgs production via gluon fusion in the POWHEG approach in the SM and in the MSSM*, JHEP **02** (2012) 088.

[117] H.-L. Lai et al., *New parton distributions for collider physics*, Phys. Rev. D **82** (2010) 074024.

[118] T. Sjöstrand, S. Mrenna, and P. Skands, *A brief introduction to PYTHIA 8.1*, Comput. Phys. Commun. **178** (2008) 852–867.

[119] J. Alwall et al., *The automated computation of tree-level and next-to-leading order differential cross sections, and their matching to parton shower simulations*, JHEP **07** (2014) 079.

[120] M. Wiesemann, et al., *Higgs production in association with bottom quarks*, JHEP **02** (2015) 132.

[121] T. Sjöstrand, et al., *An introduction to PYTHIA 8.2*, Comput. Phys. Commun. **191** (2015) 159.

[122] E. Bothmann et al., *Event generation with Sherpa 2.2*, SciPost Phys. **7** (2019) 034.

[123] NNPDF Collaboration, R. D. Ball et al., *Parton distributions for the LHC run II*, JHEP **04** (2015) 040.

[124] S. Schumann and F. Krauss, *A parton shower algorithm based on Catani-Seymour dipole factorisation*, JHEP **03** (2008) 038.

[125] C. Anastasiou, et al., *High-precision QCD at hadron colliders: Electroweak gauge boson rapidity distributions at next-to-next-to leading order*, Phys. Rev. D **69** (2004) 094008.

[126] S. Alioli, et al., *NLO vector-boson production matched with shower in POWHEG*, JHEP **07** (2008) 060.

[127] S. Frixione, P. Nason, and G. Ridolfi, *A positive-weight next-to-leading-order Monte Carlo for heavy flavour hadroproduction*, JHEP **09** (2007) 126.

[128] M. Beneke, et al., *Hadronic top-quark pair production with NNLL threshold resummation*, Nucl. Phys. B **855** (2012) 695–741.

[129] M. Cacciari, et al., *Top-pair production at hadron colliders with next-to-next-to-leading logarithmic soft-gluon resummation*, Phys. Lett. B **710** (2012) 612–622.

[130] P. Bärnreuther, M. Czakon, and A. Mitov, *Percent-Level-Precision Physics at the Tevatron: Next-to-Next-to-Leading Order QCD Corrections to* $q\bar{q} \to t\bar{t} + X$, Phys. Rev. Lett. **109** (2012) 132001.

[131] M. Czakon and A. Mitov, *NNLO corrections to top-pair production at hadron colliders: the all-fermionic scattering channels*, JHEP **12** (2012) 054.

[132] M. Czakon and A. Mitov, *NNLO corrections to top pair production at hadron colliders: the quark-gluon reaction*, JHEP **01** (2013) 080.

[133] M. Czakon, P. Fiedler, and A. Mitov, *Total Top-Quark Pair-Production Cross Section at Hadron Colliders Through $O(\alpha_S^4)$)*, Phys. Rev. Lett. **110** (2013) 252004.

[134] M. Czakon and A. Mitov, *Top++: A program for the calculation of the top-pair cross-section at hadron colliders*, Comput. Phys. Commun. **185** (2014) 2930.

[135] E. Re, *Single-top Wt-channel production matched with parton showers using the POWHEG method*, Eur. Phys. J. C **71** (2011) 1547.

[136] R. Frederix, E. Re, and P. Torrielli, *Single-top t-channel hadroproduction in the four-flavour scheme with POWHEG and aMC@NLO*, JHEP **09** (2012) 130.

[137] S. Alioli, et al., *NLO single-top production matched with shower in POWHEG: s- and t-channel contributions*, JHEP **09** (2009) 111.

[138] M. Aliev et al., *HATHOR: HAdronic Top and Heavy quarks crOss section calculatoR*, Comput. Phys. Commun. **182** (2011) 1034.

[139] P. Kant, et al., HATHOR *for single top-quark production: Updated predictions and uncertainty estimates for single top-quark production in hadronic collisions*, Comput. Phys. Commun. **191** (2015) 74.

[140] L. Gerlach, *Search for BSM $H \to \tau\tau$ in the fully hadronic decay channel with ATLAS*, Master's thesis, University of Göttingen. II.Physik-UniGö-MSc-2017/06.

[141] G. Avoni et al., *The new LUCID-2 detector for luminosity measurement and monitoring in ATLAS*, JINST **13** (2018) P07017.

[142] ATLAS Collaboration, M. Aaboud et al., *Luminosity determination in pp collisions at $\sqrt{s} = 8$ TeV using the ATLAS detector at the LHC*, Eur. Phys. J. C **76** (2016) 653.

[143] LHC Top Physics Working Group, *ATLAS-CMS recommended predictions for single-top cross sections using the Hathor v2.1 program* , `https://twiki.cern.ch/twiki/bin/view/LHCPhysics/SingleTopRefXsec`.

[144] LHC Top Physics Working Group, *ATLAS-CMS recommended predictions for top-quark-pair cross sections using the Top++v2.0 program* , `https://twiki.cern.ch/twiki/bin/view/LHCPhysics/TtbarNNLO`.

[145] J. Bellm et al., *Herwig 7.0/Herwig++ 3.0 release note*, Eur. Phys. J. C **76** (2016) 196.

[146] A. L. Read, *Presentation of search results: the CL_s technique*, J. Phys. **G 28** (2002) 2693–2704.

[147] G. Cowan, K. Cranmer, E. Gross and O. Vitells, *Asymptotic formulae for likelihood-based tests of new physics*, Eur. Phys. J. **C 71** (2011) 1554.

[148] J. Neyman and E. S. Pearson, *IX. On the problem of the most efficient tests of statistical hypotheses*, Philosophical Transactions of the Royal Society of London.

Series A, Containing Papers of a Mathematical or Physical Character **231** (1933) 289–337.

[149] T. Przedzinski, E. Richter-Was, and Z. Was, *Documentation of TauSpinner algorithms: program for simulating spin effects in τ -lepton production at LHC*, Eur. Phys. J. C **79** (2019) 91.

[150] P. Baldi, et al., *Parameterized neural networks for high-energy physics*, Eur. Phys. J. C **76** (2016) 235.

[151] G. Apollinari, et al., *High Luminosity Large Hadron Collider HL-LHC*, CERN Yellow Rep. (2015) 1–19.

[152] Chapman, John, et al., *Fast simulation methods in ATLAS: from classical to generative models*, EPJ Web Conf. **245** (2020) 02035.

[153] C. W. Bauer, et al., *Quantum Algorithm for High Energy Physics Simulations*, Phys. Rev. Lett. **126** (2021) 062001.

Appendices

APPENDIX A

Author's contribution

The purpose of this Appendix is to point out what exactly the author's contributions were, as large teams derived the presented results.

The author conducted the measurement of the BDT-based $\tau-$ID scale factors as described in Chapter 6 as the sole analyzer to qualify as an ATLAS author. During the second year of his PhD studies, the author refined this measurement and conducted it for the RNN-based version of the classifier. This effort included optimizing the event selection in the signal region and the existing control regions and introducing new control regions altogether. Although the OS-SS background estimate had been deployed in other tag-and-probe measurements, significant adjustments to it were made by the author. The fit strategy for the maximum-likelihood estimation of the signal yield was developed from scratch by the author. The same holds for the extraction of the final scale factors and the propagation of the uncertainties. The author also developed and implemented the method to estimate the systematic uncertainty stemming from the lower cut on the $\tau-$ID score and conducted all cross-checks with alternative configurations of the signal simulation. The procedure to split the uncertainties into those of statistical and systematic nature as well as applying the fit results to a variable that was not used for the likelihood maximization were also implemented by the author.

The author has been one of the main contributors to the efforts of searching for a heavy Higgs boson decaying to a pair of τ-leptons in the fully hadronic decay channel over the last four years. For the first results based on the full Run 2 dataset published in early 2020 [111] and described in Chapter 7, the author mainly contributed to the multijet estimate. The author implemented the fake factor interpolation in the context of the analysis that ultimately led to the introduction of the lower cut on the $\tau-$ID score in the signal and di-jet control region and sparked the founding of the Fake Tau Task Force. As one of the founding members of that task force, the author provided the first iteration of the χ^2 minimization strategy deployed to estimate the fraction of quark- and gluon-initiated jets on data.

Furthermore, the author worked on a *pseudo-continous* $\tau-$ID approach, splitting the signal region into disjoint slices of the $\tau-$ID (e.g. *loose-not-medium* instead of *loose*) to increase the sensitivity. As a member of the tau working group, the author derived an experimental set of scale factors to accompany the pseudo-continuous approach. However, the uncertainties on these scale factors were vast, and the approach was dismissed. After the first results based on the full Run 2 dataset were published, the author became the main analyzer of the search for BSM $A/H \to \tau\tau$ and was responsible for all improvements for the legacy analysis described in Chapter 8 except for the MVA approach. The author requested and validated hypothetical signal samples such as the Z' samples and implemented and validated the TauSpinnerTool in the context of the analysis. The author implemented the inclusion of di-tau trigger events and developed a new background estimate for these. The computationally intensive 'ntuple' production was run by the author, who had access to significant computing resources to do so. Also, all the changes to the analysis were documented in the internal note by the author.

APPENDIX B

Measurement of τ_{had} identification efficiency

B.1. MC Samples

This section contains a list of all the MC samples used in the analysis. The following endings to the file names were omitted:

- mc16a: _s3126_r9364_p3759
- mc16d: _s3126_r10239_p3759
- mc16d: _s3126_r11152_p3759

B.1.1. mc16a

$Z \rightarrow \tau\tau$

`mc16_13TeV.425201.PowhegPythia8EvtGen_AZNLOCTEQ6L1_Ztautau_l22h10_filter.deriv.DAOD_TAUP3.e6465`

$Z \rightarrow \tau\tau$ (alternative)

`mc16_13TeV.364128.Sherpa_221_NNPDF30NNLO_Ztautau_MAXHTPTV0_70_CVetoBVeto.deriv.DAOD_TAUP3.e5307`

`mc16_13TeV.364129.Sherpa_221_NNPDF30NNLO_Ztautau_MAXHTPTV0_70_CFilterBVeto.deriv.DAOD_TAUP3.e5307`

`mc16_13TeV.364130.Sherpa_221_NNPDF30NNLO_Ztautau_MAXHTPTV0_70_BFilter.deriv.DAOD_TAUP3.e5307`

`mc16_13TeV.364131.Sherpa_221_NNPDF30NNLO_Ztautau_MAXHTPTV70_140_CVetoBVeto.deriv.DAOD_TAUP3.e5307`

`mc16_13TeV.364132.Sherpa_221_NNPDF30NNLO_Ztautau_MAXHTPTV70_140_CFilterBVeto.deriv.DAOD_TAUP3.e5307`

`mc16_13TeV.364133.Sherpa_221_NNPDF30NNLO_Ztautau_MAXHTPTV70_140_BFilter.deriv.DAOD_TAUP3.e5307`

`mc16_13TeV.364134.Sherpa_221_NNPDF30NNLO_Ztautau_MAXHTPTV140_280_CVetoBVeto.deriv.DAOD_TAUP3.e5307` `mc16_13TeV.364135.Sherpa_221_NNPDF30NNLO_Ztautau_MAXHTPTV140_280_CFilterBVeto.deriv.DAOD_TAUP3.e5307`

`mc16_13TeV.364136.Sherpa_221_NNPDF30NNLO_Ztautau_MAXHTPTV140_280_BFilter.deriv.DAOD_TAUP3.e5307`

`mc16_13TeV.364137.Sherpa_221_NNPDF30NNLO_Ztautau_MAXHTPTV280_500_CVetoBVeto.deriv.DAOD_TAUP3.e5307`

`mc16_13TeV.364138.Sherpa_221_NNPDF30NNLO_Ztautau_MAXHTPTV280_500_CFilterBVeto.deriv.DAOD_TAUP3.e5313`

`mc16_13TeV.364139.Sherpa_221_NNPDF30NNLO_Ztautau_MAXHTPTV280_500_BFilter.deriv.DAOD_TAUP3.e5313`

`mc16_13TeV.364140.Sherpa_221_NNPDF30NNLO_Ztautau_MAXHTPTV500_1000.deriv.DAOD_TAUP3.e5307`

`mc16_13TeV.364141.Sherpa_221_NNPDF30NNLO_Ztautau_MAXHTPTV1000_E_CMS.deriv.DAOD_TAUP3.e5307`

W+jets

`mc16_13TeV.361100.PowhegPythia8EvtGen_AZNLOCTEQ6L1_Wplusenu.deriv.DAOD_TAUP3.e3601`

`mc16_13TeV.361101.PowhegPythia8EvtGen_AZNLOCTEQ6L1_Wplusmunu.deriv.DAOD_TAUP3.e3601`

`mc16_13TeV.361102.PowhegPythia8EvtGen_AZNLOCTEQ6L1_Wplustaunu.deriv.DAOD_TAUP3.e3601`

`mc16_13TeV.361103.PowhegPythia8EvtGen_AZNLOCTEQ6L1_Wminusenu.deriv.DAOD_TAUP3.e3601`

`mc16_13TeV.361104.PowhegPythia8EvtGen_AZNLOCTEQ6L1_Wminusmunu.deriv.DAOD_TAUP3.e3601`

`mc16_13TeV.361105.PowhegPythia8EvtGen_AZNLOCTEQ6L1_Wminustaunu.deriv.DAOD_TAUP3.e3601`

$Z \to \ell\ell$

`mc16_13TeV.361106.PowhegPythia8EvtGen_AZNLOCTEQ6L1_Zee.deriv.DAOD_TAUP3.e3601`

`mc16_13TeV.361107.PowhegPythia8EvtGen_AZNLOCTEQ6L1_Zmumu.deriv.DAOD_TAUP3.e3601`

top

`mc16_13TeV.410470.PhPy8EG_A14_ttbar_hdamp258p75_nonallhad.deriv.DAOD_TAUP3.e6337`

`mc16_13TeV.410471.PhPy8EG_A14_ttbar_hdamp258p75_allhad.deriv.DAOD_TAUP3.e6337`

`mc16_13TeV.410644.PowhegPythia8EvtGen_A14_singletop_schan_lept_top.deriv.DAOD_TAUP3.e6527`

`mc16_13TeV.410645.PowhegPythia8EvtGen_A14_singletop_schan_lept_antitop.deriv.DAOD_TAUP3.e6527`

`mc16_13TeV.410646.PowhegPythia8EvtGen_A14_Wt_DR_inclusive_top.deriv.DAOD_TAUP3.e6552`

`mc16_13TeV.410647.PowhegPythia8EvtGen_A14_Wt_DR_inclusive_antitop.deriv.DAOD_TAUP3.e6552`

`mc16_13TeV.410658.PhPy8EG_A14_tchan_BW50_lept_top.deriv.DAOD_TAUP3.e6671`

`mc16_13TeV.410659.PhPy8EG_A14_tchan_BW50_lept_antitop.deriv.DAOD_TAUP3.e6671`

B.2. Additional $\tau-$ID score prefit distributions

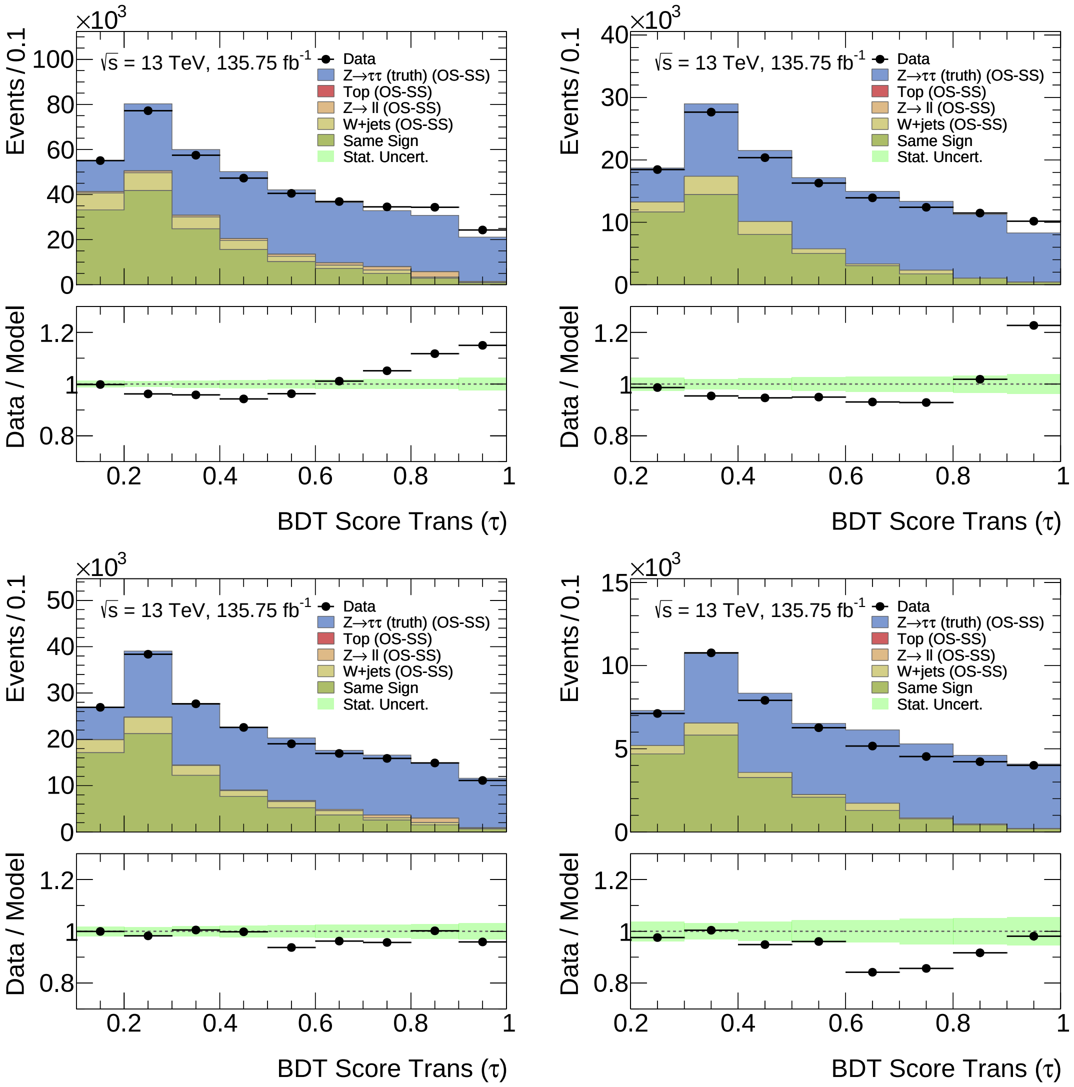

Figure B.1.: Prefit τ_{had}-ID score distribution for the BDT-based classifier in the p_{T} inclusive signal region. The figure is split into 1-prong versus 3-prong (left and right) and low versus high $|\eta|$ (top and bottom). The $Z \to \tau\tau$ sample is generated with Sherpa.

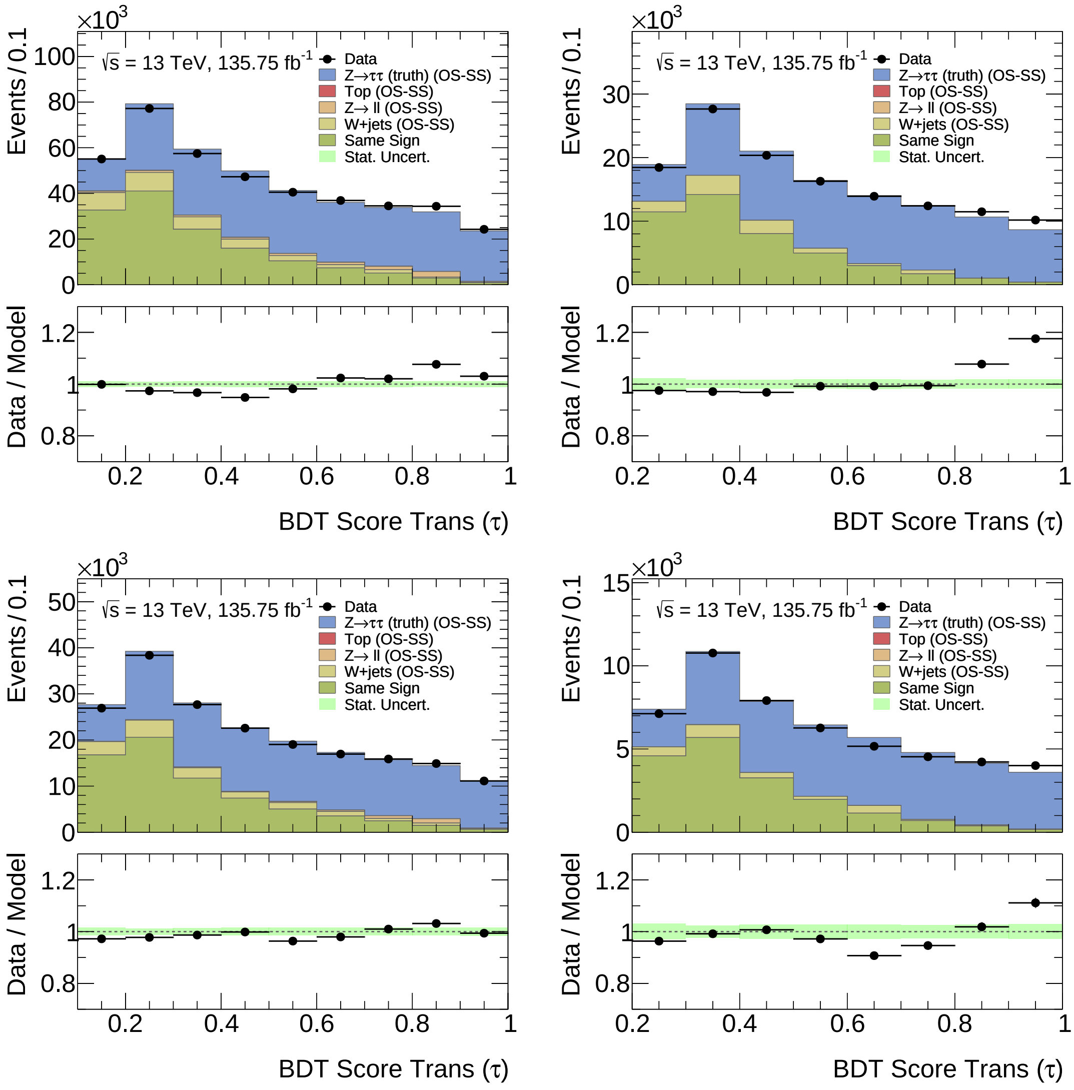

Figure B.2.: Prefit τ_{had}-ID score distribution for the BDT-based classifier in the p_{T} inclusive signal region. The figure is split into 1-prong versus 3-prong (left and right) and low versus high $|\eta|$ (top and bottom). AF2 is used to simulate the detector response for the $Z \to \tau\tau$ sample.

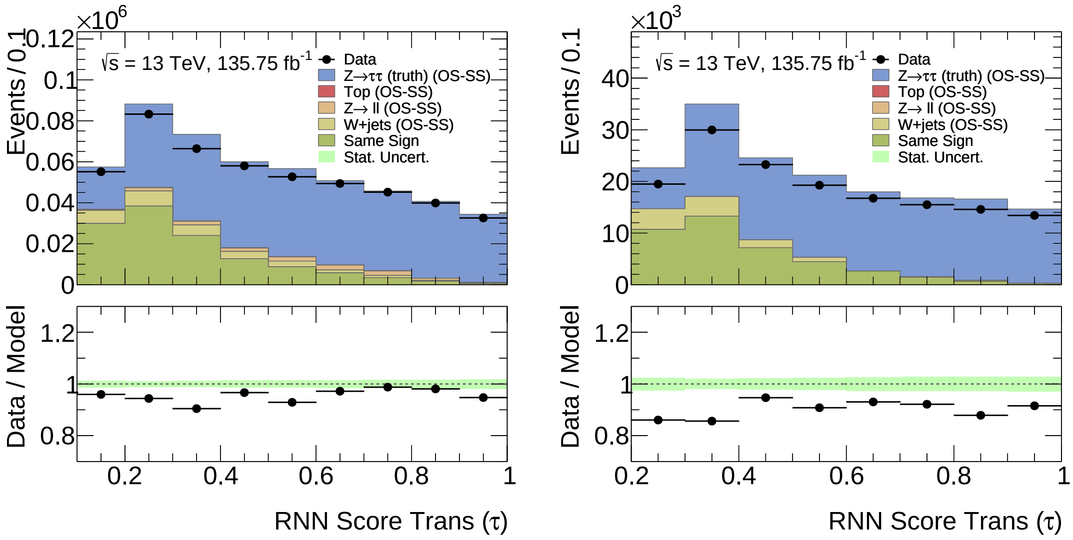

Figure B.3.: Prefit τ_{had}-ID score distribution for the RNN-based classifier in the p_{T} inclusive signal region. The figure is split into 1-prong versus 3-prong (left and right). The $Z \to \tau\tau$ sample is generated with Sherpa.

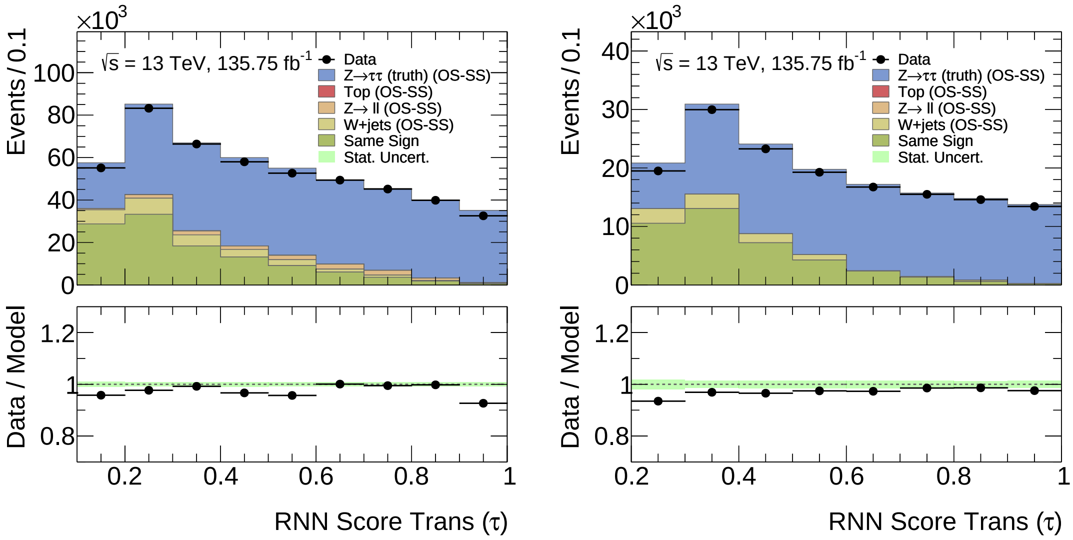

Figure B.4.: Prefit τ_{had}-ID score distribution for the RNN-based classifier in the p_{T} inclusive signal region. The figure is split into 1-prong versus 3-prong (left and right). AF2 is used to simulate the detector response for the $Z \to \tau\tau$ sample.

B.3. Additional scale factor plots

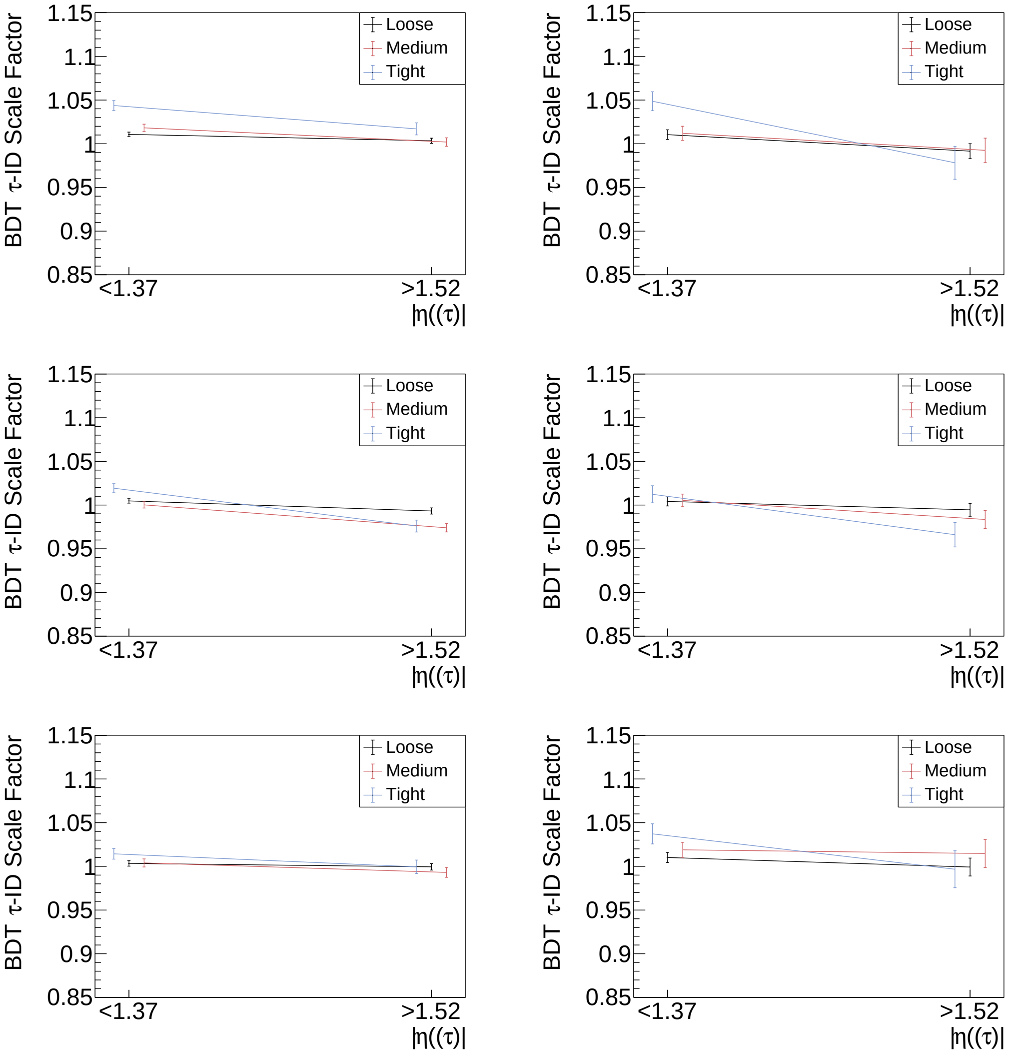

Figure B.5.: Comparison of different BDT-based τ_{had}-ID scale factors for 1-prong (left) and 3-prong (right). The top row shows the default result, using Powheg MC generated $Z \to \tau\tau$ samples and the GEANT4 detector simulation. In the middle, the MC generator was replaced with an alternative (Sherpa) and in the bottom, AF2 was used as an alternative detector simulation. The scale factors are evaluated for four bins of $p_{\mathrm{T}}(\tau)$. The uncertainties include all statistical and systematic uncertainties except for the one dedicated to the lower $\tau-$ID score cut value explained in Section 6.5.1.

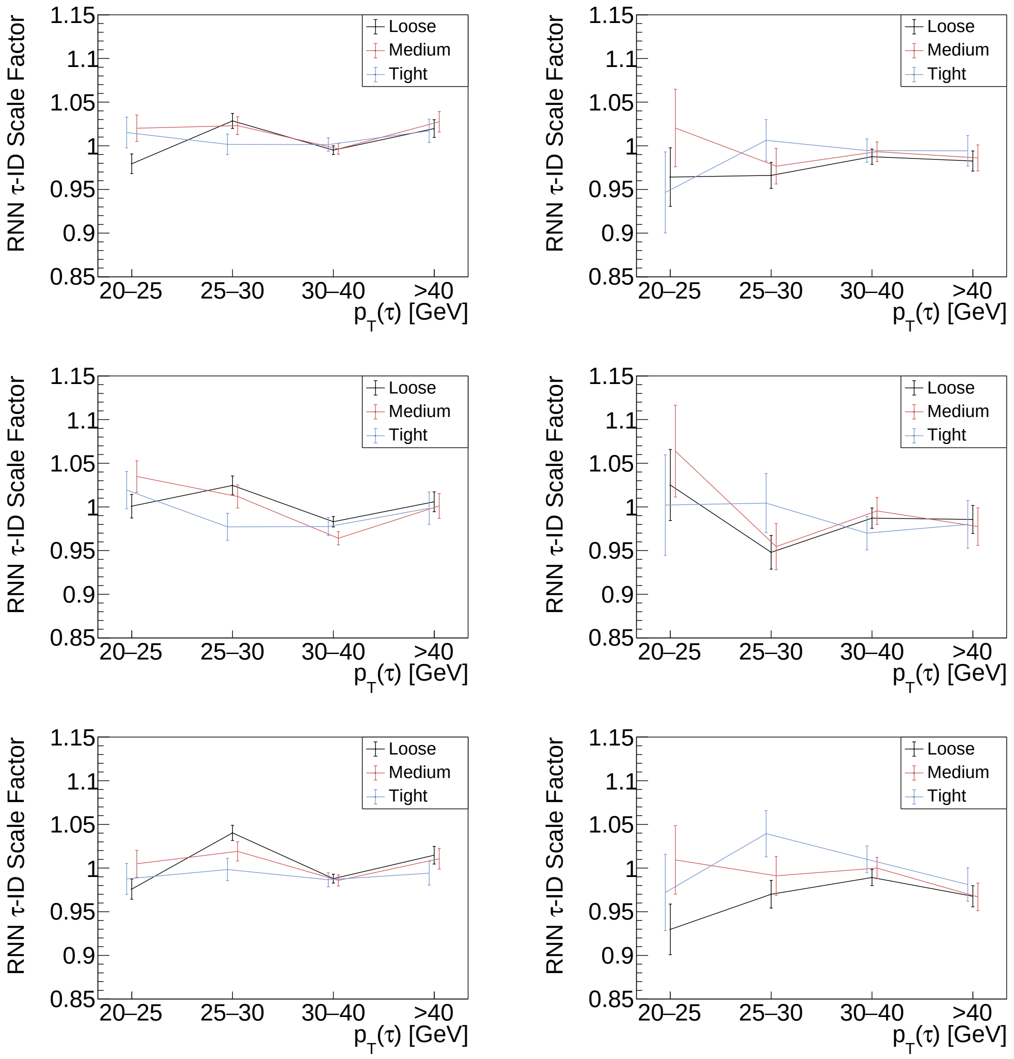

Figure B.6.: RNN-based τ_{had}-ID scale factors for 1-prong (left) and 3-prong (right). The top row shows the default result, using Powheg MC generated $Z \to \tau\tau$ samples and the GEANT4 detector simulation. In the middle, the MC generator was replaced with an alternative (Sherpa) and in the bottom, AF2 was used as an alternative detector simulation. The scale factors are evaluated for four bins of $p_{\text{T}}(\tau)$. The uncertainties include all statistical and systematic uncertainties except for the one dedicated to the lower τ−ID score cut value explained in Section 6.5.1..

APPENDIX C

Search for BSM $A/H/ \rightarrow \tau\tau$ in the fully hadronic decay channel

C.1. Fake rates

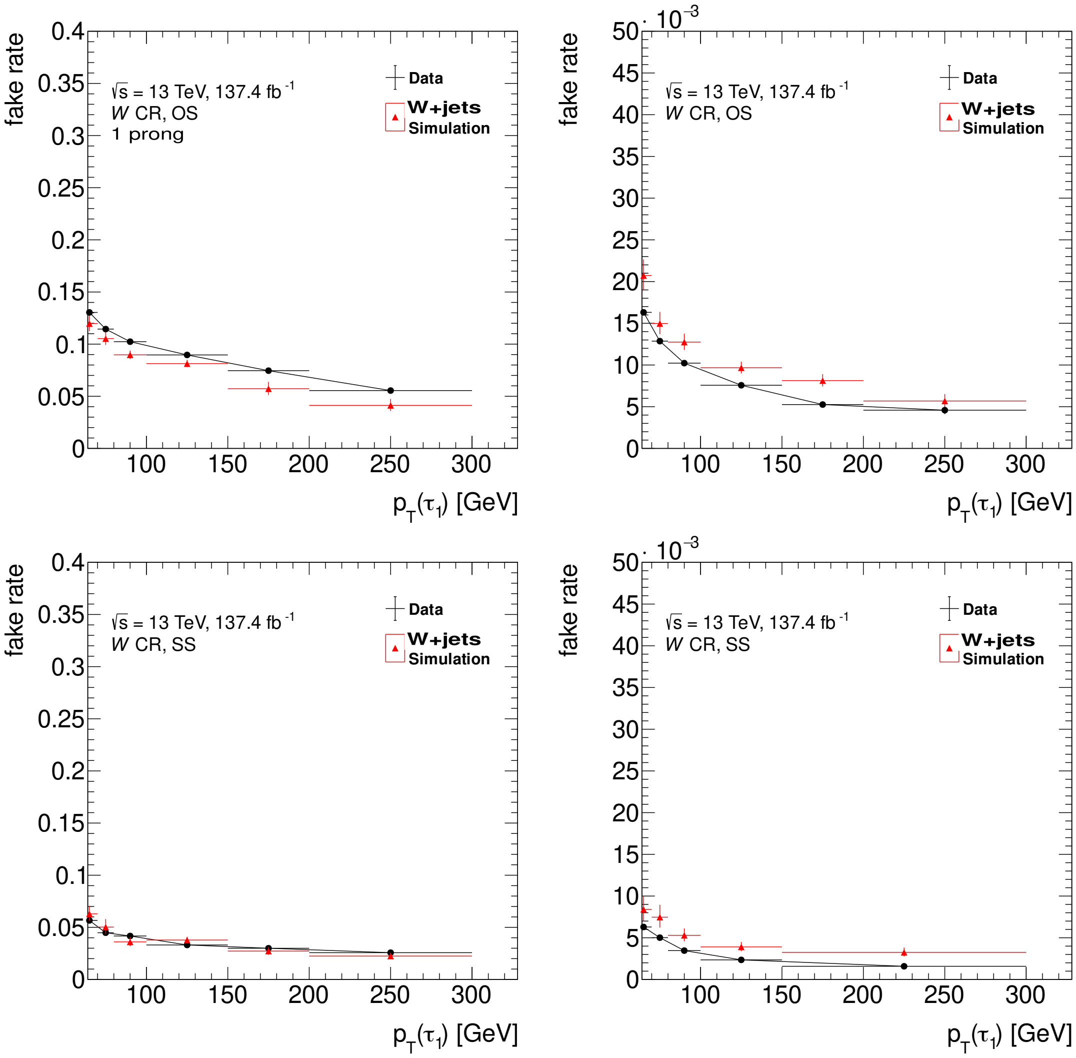

Figure C.1.: Fake rates evaluated on data in the OS (top) and SS (bottom) W-FR for the *loose* $\tau-$ID requirement. The plot shows the comparison between MC simulated and recorded data.

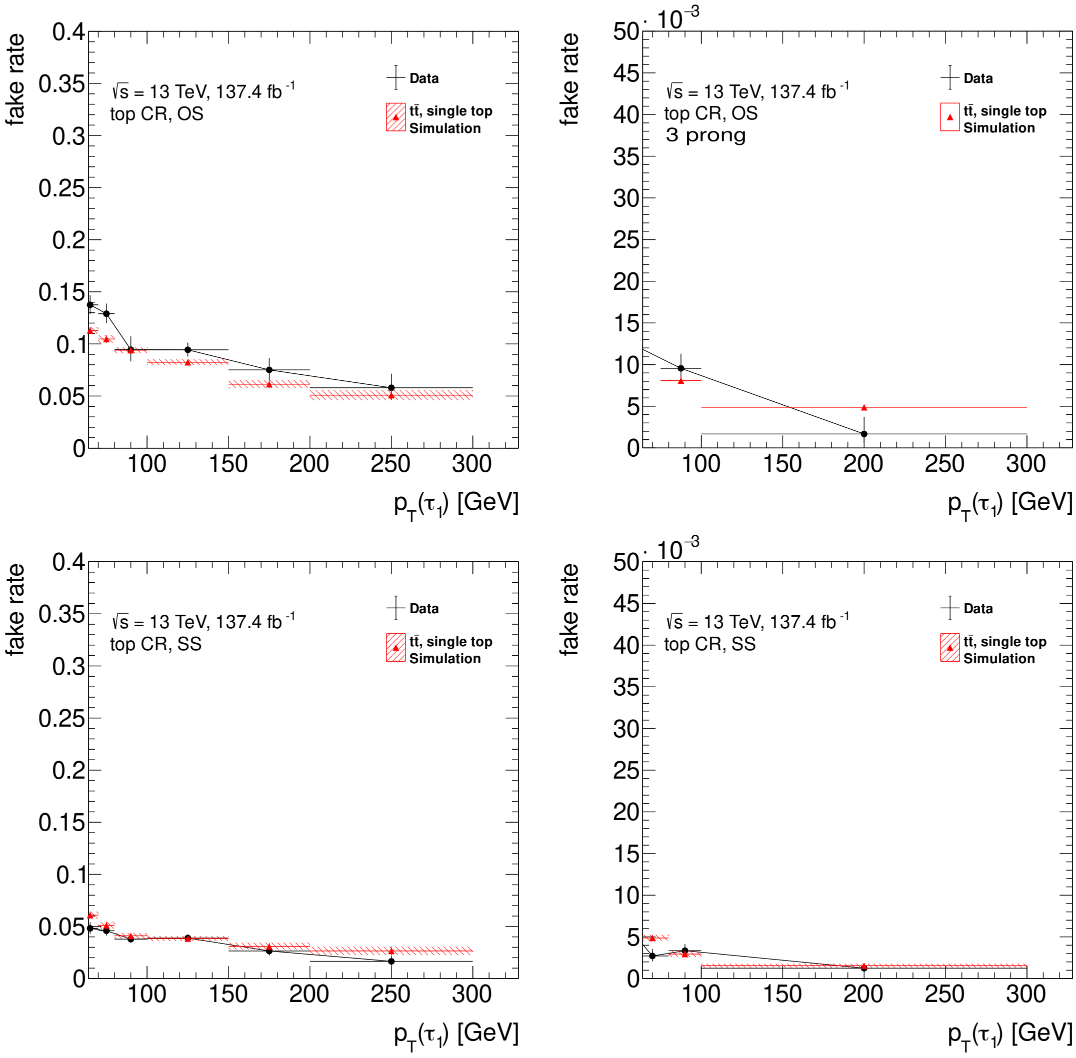

Figure C.2.: Fake rates evaluated on data in the OS (top) and SS (bottom) T-FR for the *loose* τ−ID requirement. The plot shows the comparison between MC simulated and recorded data.

C.2. Fake factors

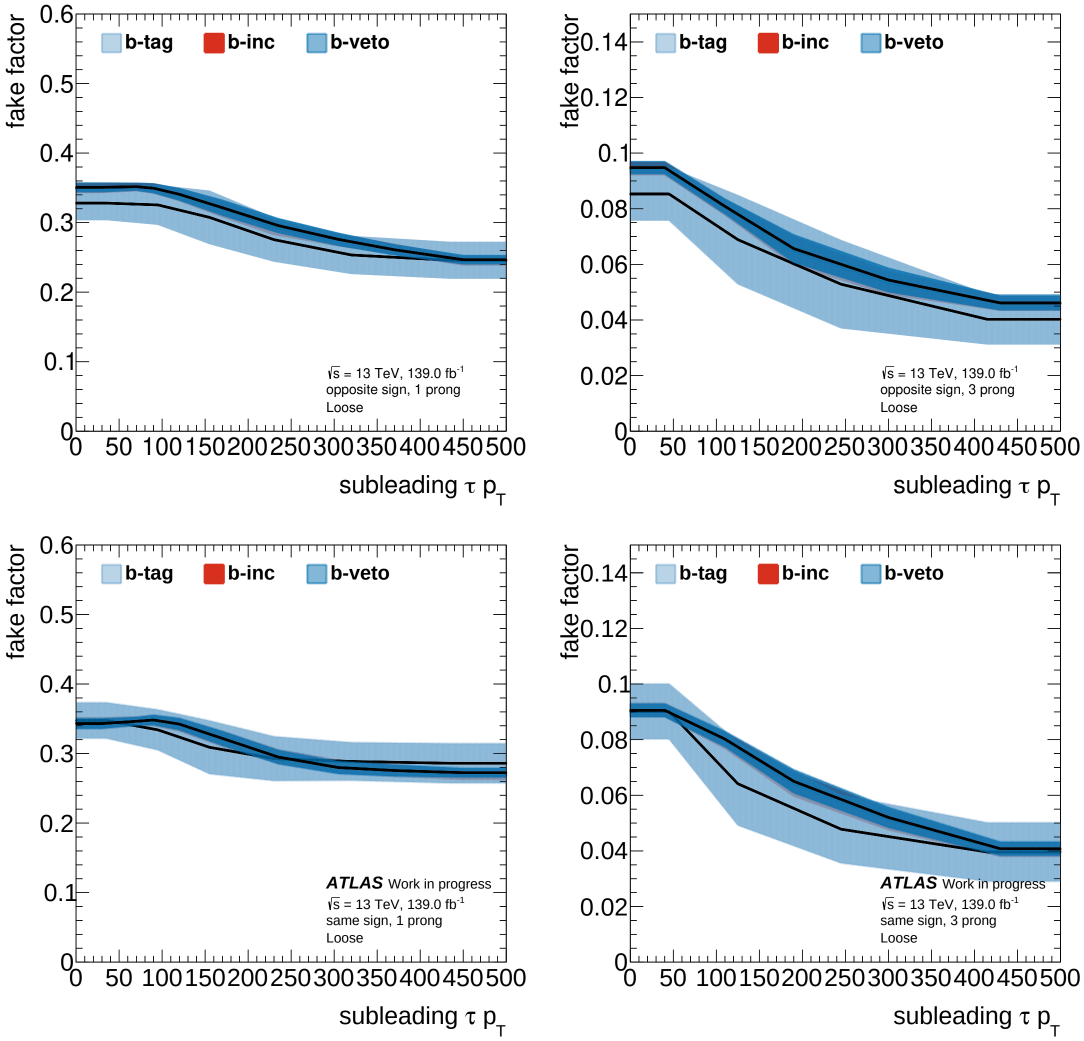

Figure C.3.: Fake factors derived in the OS (top) and SS (bottom) di-jet control region for 1-prong (left) and 3-prong (right) $\tau_{\text{had-vis}}$ candidates. A comparison between b-veto, b-tag, and b-inclusive fake factors is made.

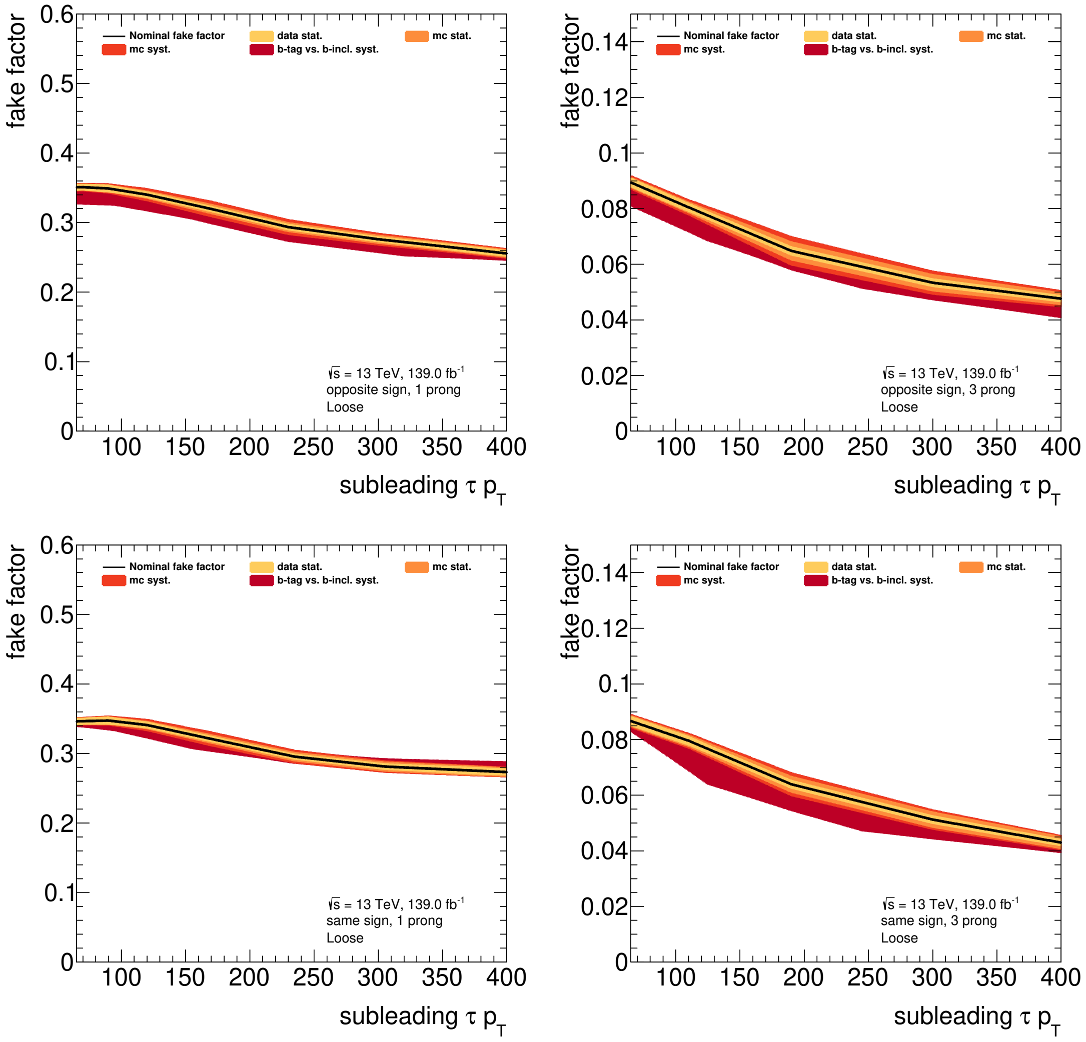

Figure C.4.: Fake factors and their uncertainties in the OS (top) and SS (bottom) case for 1-prong (left) and 3-prong (right) $\tau_{\text{had-vis}}$ candidates. The dark red shade indicates the uncertainty that is considered when using the *b*-inclusive fake factors in the *b*-tag signal region.

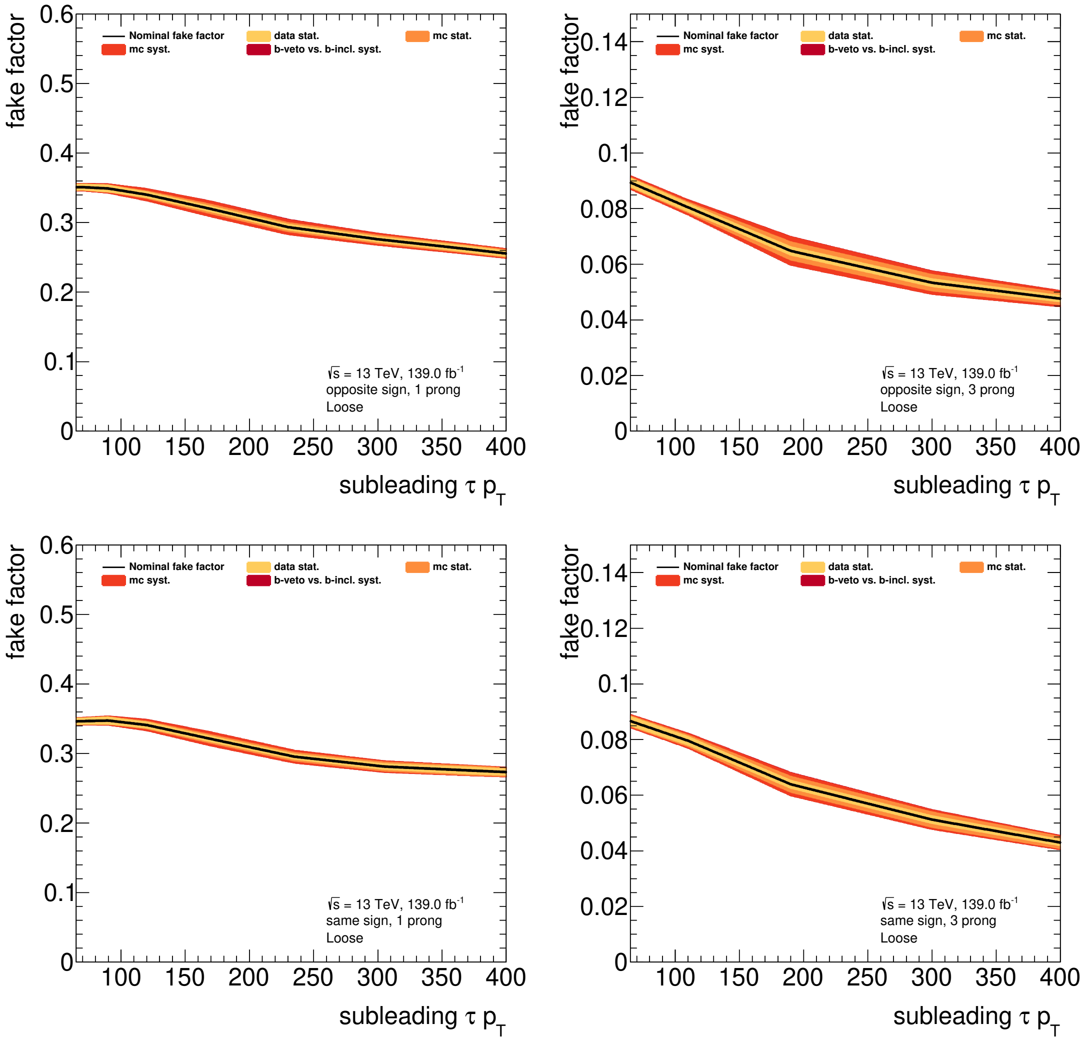

Figure C.5.: Fake factors and their uncertainties in the OS (top) and SS (bottom) case for 1-prong (left) and 3-prong (right) $\tau_{\text{had-vis}}$ candidates. The dark red shade indicates the uncertainty that is considered when using the b-inclusive fake factors in the b-veto signal region.

C.3. Additional pre-fit distributions in the validation region

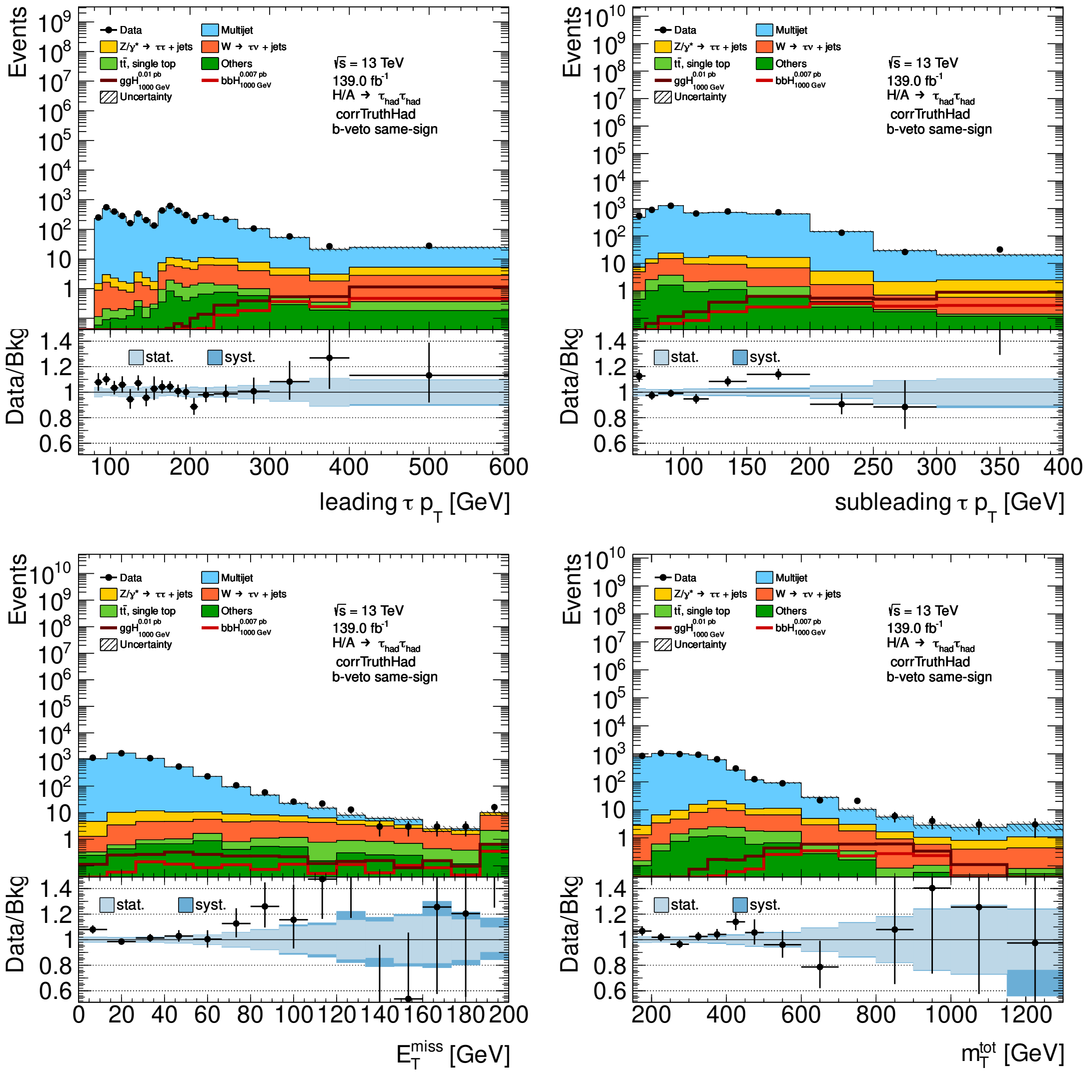

Figure C.6.: Distributions of various variables in the b-veto validation region. These are: p_{T} of leading $\tau_{\text{had-vis}}$ candidate (top left), p_{T} of subleading $\tau_{\text{had-vis}}$ candidate (top right), $E_{\mathrm{T}}^{\mathrm{miss}}$ (bottom left), and $m_{\mathrm{T}}^{\mathrm{tot}}$ (bottom right).

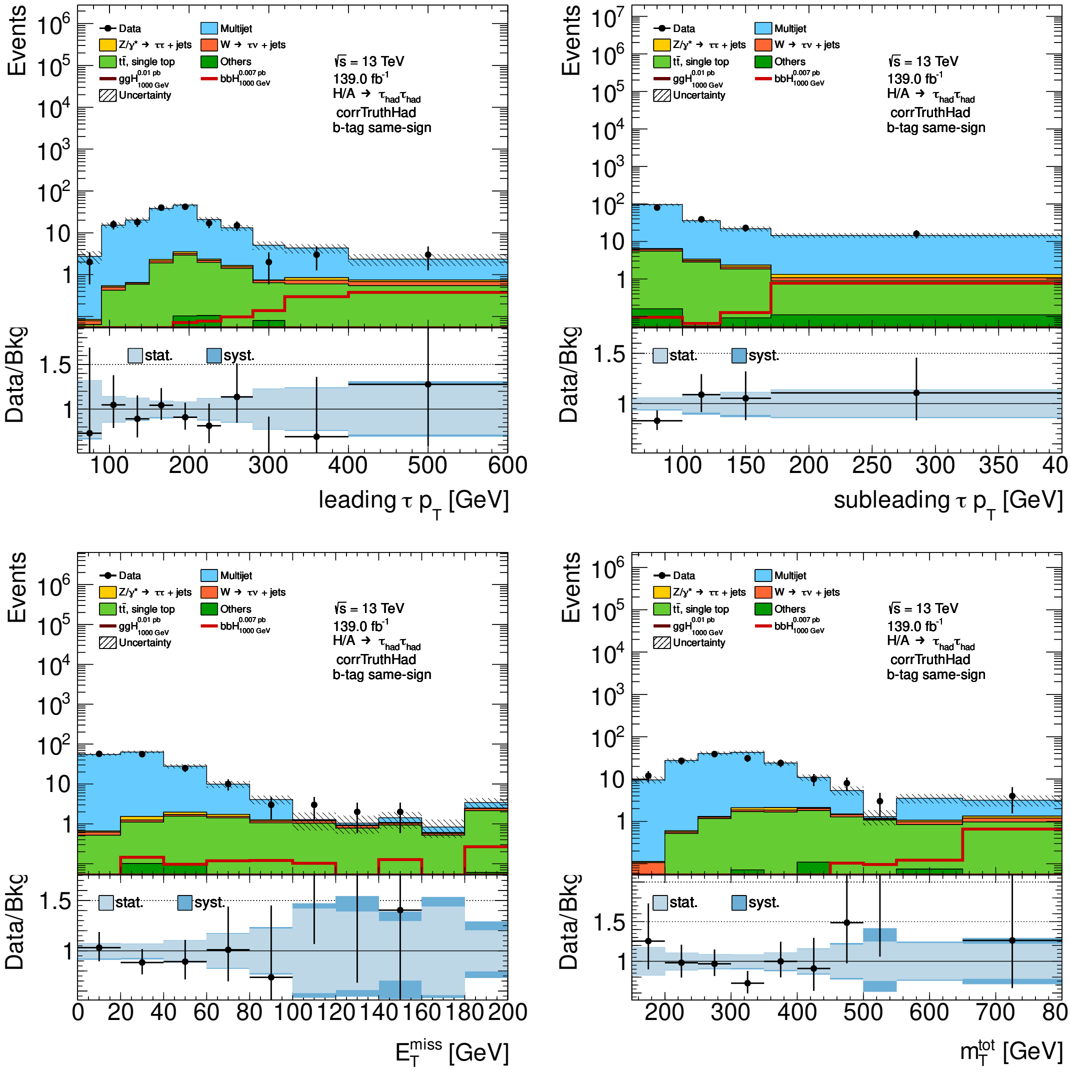

Figure C.7.: Distributions of various variables in the b-tag validation region. These are: p_{T} of leading $\tau_{\text{had-vis}}$ candidate (top left), p_{T} of subleading $\tau_{\text{had-vis}}$ candidate (top right), $E_{\mathrm{T}}^{\text{miss}}$ (bottom left), and $m_{\mathrm{T}}^{\text{tot}}$ (bottom right).

C.4. Limits

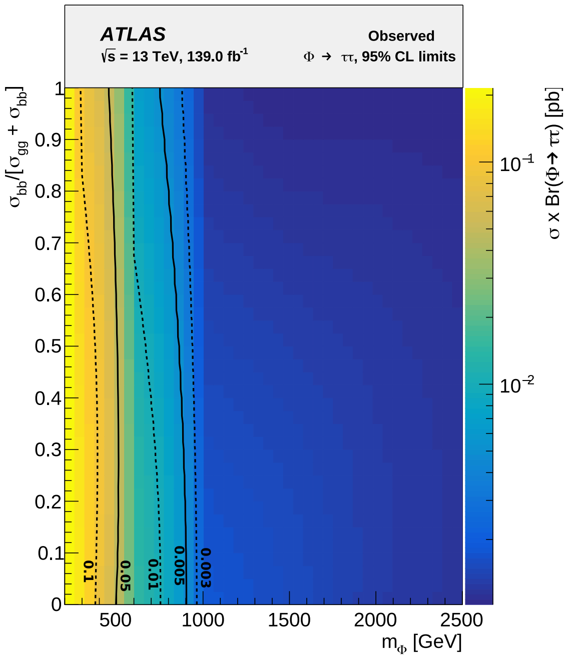

Figure C.8.: The model-independent observed 95% upper limit on the production cross section times branching fraction for a heavy resonance, ϕ, as a function of the assumed resonance mass, m_ϕ, and the fraction of b-associated production, $\sigma_{bb}/[\sigma_{gg} + \sigma_{bb}]$

C.5. MC samples

This section contains a list of all the MC samples used in the analysis. The following file endings were omitted:

- mc16a: _s3126_r9364
- mc16d: _s3126_r10201
- mc16e: _s3126_r10724

gluon-fusion H/A production

```
mc16_13TeV.342305.PowhegPythia8EvtGen_CT10_AZNLOCTEQ6L1_ggH200W1_tautaulh.recon.AOD.e4284
mc16_13TeV.342306.PowhegPythia8EvtGen_CT10_AZNLOCTEQ6L1_ggH200W1_tautauhh.recon.AOD.e4284
mc16_13TeV.342308.PowhegPythia8EvtGen_CT10_AZNLOCTEQ6L1_ggH250W1_tautaulh.recon.AOD.e4284
mc16_13TeV.342309.PowhegPythia8EvtGen_CT10_AZNLOCTEQ6L1_ggH250W1_tautauhh.recon.AOD.e4284
mc16_13TeV.342310.PowhegPythia8EvtGen_CT10_AZNLOCTEQ6L1_ggH300W2_tautaulh.recon.AOD.e4284
mc16_13TeV.342311.PowhegPythia8EvtGen_CT10_AZNLOCTEQ6L1_ggH300W2_tautauhh.recon.AOD.e4284
mc16_13TeV.342312.PowhegPythia8EvtGen_CT10_AZNLOCTEQ6L1_ggH350W3_tautaulh.recon.AOD.e4284
mc16_13TeV.342313.PowhegPythia8EvtGen_CT10_AZNLOCTEQ6L1_ggH350W3_tautauhh.recon.AOD.e4284
mc16_13TeV.342314.PowhegPythia8EvtGen_CT10_AZNLOCTEQ6L1_ggH400W5_tautaulh.recon.AOD.e4284
mc16_13TeV.342315.PowhegPythia8EvtGen_CT10_AZNLOCTEQ6L1_ggH400W5_tautauhh.recon.AOD.e4284
mc16_13TeV.342316.PowhegPythia8EvtGen_CT10_AZNLOCTEQ6L1_ggH500W5_tautaulh.recon.AOD.e4284
mc16_13TeV.342317.PowhegPythia8EvtGen_CT10_AZNLOCTEQ6L1_ggH500W5_tautauhh.recon.AOD.e4284
mc16_13TeV.342318.PowhegPythia8EvtGen_CT10_AZNLOCTEQ6L1_ggH600W10_tautaulh.recon.AOD.e4284
mc16_13TeV.342319.PowhegPythia8EvtGen_CT10_AZNLOCTEQ6L1_ggH600W10_tautauhh.recon.AOD.e4284
mc16_13TeV.342320.PowhegPythia8EvtGen_CT10_AZNLOCTEQ6L1_ggH700W20_tautaulh.recon.AOD.e4284
mc16_13TeV.342321.PowhegPythia8EvtGen_CT10_AZNLOCTEQ6L1_ggH700W20_tautauhh.recon.AOD.e4284
mc16_13TeV.342322.PowhegPythia8EvtGen_CT10_AZNLOCTEQ6L1_ggH800W20_tautaulh.recon.AOD.e4284
mc16_13TeV.342323.PowhegPythia8EvtGen_CT10_AZNLOCTEQ6L1_ggH800W20_tautauhh.recon.AOD.e4284
mc16_13TeV.342326.PowhegPythia8EvtGen_CT10_AZNLOCTEQ6L1_ggH1000W30_tautaulh.recon.AOD.e4284
mc16_13TeV.342327.PowhegPythia8EvtGen_CT10_AZNLOCTEQ6L1_ggH1000W30_tautauhh.recon.AOD.e4284
mc16_13TeV.342330.PowhegPythia8EvtGen_CT10_AZNLOCTEQ6L1_ggH1200W40_tautaulh.recon.AOD.e4284
mc16_13TeV.342331.PowhegPythia8EvtGen_CT10_AZNLOCTEQ6L1_ggH1200W40_tautauhh.recon.AOD.e4284
mc16_13TeV.342336.PowhegPythia8EvtGen_CT10_AZNLOCTEQ6L1_ggH1500W60_tautaulh.recon.AOD.e4284
mc16_13TeV.342337.PowhegPythia8EvtGen_CT10_AZNLOCTEQ6L1_ggH1500W60_tautauhh.recon.AOD.e4284
mc16_13TeV.345296.PowhegPythia8EvtGen_CT10_AZNLOCTEQ6L1_ggH2000W80_tautauhh.recon.AOD.e5685
mc16_13TeV.345297.PowhegPythia8EvtGen_CT10_AZNLOCTEQ6L1_ggH2000W80_tautaulh.recon.AOD.e5685
mc16_13TeV.345300.PowhegPythia8EvtGen_CT10_AZNLOCTEQ6L1_ggH2500W100_tautauhh.recon.AOD.e5685
mc16_13TeV.345301.PowhegPythia8EvtGen_CT10_AZNLOCTEQ6L1_ggH2500W100_tautaulh.recon.AOD.e5685
```

b-associated H/A production

```
mc16_13TeV.341856.aMcAtNloPythia8EvtGen_A14NNPDF23LO_bbH125_yb2_tautaulh.recon.AOD.e4482
mc16_13TeV.341857.aMcAtNloPythia8EvtGen_A14NNPDF23LO_bbH150_yb2_tautaulh.recon.AOD.e5686
mc16_13TeV.341858.aMcAtNloPythia8EvtGen_A14NNPDF23LO_bbH200_yb2_tautaulh.recon.AOD.e4482
mc16_13TeV.341860.aMcAtNloPythia8EvtGen_A14NNPDF23LO_bbH300_yb2_tautaulh.recon.AOD.e4482
```

mc16_13TeV.341862.aMcAtNloPythia8EvtGen_A14NNPDF23LO_bbH400_yb2_tautaulh.recon.AOD.e4298

mc16_13TeV.341864.aMcAtNloPythia8EvtGen_A14NNPDF23LO_bbH600_yb2_tautaulh.recon.AOD.e4482

mc16_13TeV.341868.aMcAtNloPythia8EvtGen_A14NNPDF23LO_bbH1000_yb2_tautaulh.recon.AOD.e4298

mc16_13TeV.341873.aMcAtNloPythia8EvtGen_A14NNPDF23LO_bbH1500_yb2_tautaulh.recon.AOD.e5314

mc16_13TeV.341874.aMcAtNloPythia8EvtGen_A14NNPDF23LO_bbH125_yb2_tautauhh.recon.AOD.e4482

mc16_13TeV.341875.aMcAtNloPythia8EvtGen_A14NNPDF23LO_bbH200_yb2_tautauhh.recon.AOD.e4482

mc16_13TeV.341877.aMcAtNloPythia8EvtGen_A14NNPDF23LO_bbH300_yb2_tautauhh.recon.AOD.e4482

mc16_13TeV.341879.aMcAtNloPythia8EvtGen_A14NNPDF23LO_bbH400_yb2_tautauhh.recon.AOD.e4298

mc16_13TeV.341881.aMcAtNloPythia8EvtGen_A14NNPDF23LO_bbH600_yb2_tautauhh.recon.AOD.e4482

mc16_13TeV.341885.aMcAtNloPythia8EvtGen_A14NNPDF23LO_bbH1000_yb2_tautauhh.recon.AOD.e4298

mc16_13TeV.341920.aMcAtNloPythia8EvtGen_A14NNPDF23LO_bbH1500_yb2_tautauhh.recon.AOD.e5314

mc16_13TeV.345288.aMcAtNloPythia8EvtGen_A14NNPDF23LO_bbH2000_yb2_tautauhh.recon.AOD.e5686

mc16_13TeV.345289.aMcAtNloPythia8EvtGen_A14NNPDF23LO_bbH2000_yb2_tautaulh.recon.AOD.e5686

mc16_13TeV.345292.aMcAtNloPythia8EvtGen_A14NNPDF23LO_bbH2500_yb2_tautauhh.recon.AOD.e5686

mc16_13TeV.345293.aMcAtNloPythia8EvtGen_A14NNPDF23LO_bbH2500_yb2_tautaulh.recon.AOD.e5686

$Z/\gamma^* \to \tau\tau$+jets

mc16_13TeV.301040.PowhegPythia8EvtGen_AZNLOCTEQ6L1_DYtautau_120M180.recon.AOD.e3649

mc16_13TeV.301041.PowhegPythia8EvtGen_AZNLOCTEQ6L1_DYtautau_180M250.recon.AOD.e3649

mc16_13TeV.301042.PowhegPythia8EvtGen_AZNLOCTEQ6L1_DYtautau_250M400.recon.AOD.e3649

mc16_13TeV.301043.PowhegPythia8EvtGen_AZNLOCTEQ6L1_DYtautau_400M600.recon.AOD.e3649

mc16_13TeV.301044.PowhegPythia8EvtGen_AZNLOCTEQ6L1_DYtautau_600M800.recon.AOD.e3649

mc16_13TeV.301045.PowhegPythia8EvtGen_AZNLOCTEQ6L1_DYtautau_800M1000.recon.AOD.e3649

mc16_13TeV.301046.PowhegPythia8EvtGen_AZNLOCTEQ6L1_DYtautau_1000M1250.recon.AOD.e3649

mc16_13TeV.301047.PowhegPythia8EvtGen_AZNLOCTEQ6L1_DYtautau_1250M1500.recon.AOD.e3649

mc16_13TeV.301048.PowhegPythia8EvtGen_AZNLOCTEQ6L1_DYtautau_1500M1750.recon.AOD.e3649

mc16_13TeV.301049.PowhegPythia8EvtGen_AZNLOCTEQ6L1_DYtautau_1750M2000.recon.AOD.e3649

mc16_13TeV.301050.PowhegPythia8EvtGen_AZNLOCTEQ6L1_DYtautau_2000M2250.recon.AOD.e3649

mc16_13TeV.301051.PowhegPythia8EvtGen_AZNLOCTEQ6L1_DYtautau_2250M2500.recon.AOD.e3649

mc16_13TeV.301052.PowhegPythia8EvtGen_AZNLOCTEQ6L1_DYtautau_2500M2750.recon.AOD.e3649

mc16_13TeV.301053.PowhegPythia8EvtGen_AZNLOCTEQ6L1_DYtautau_2750M3000.recon.AOD.e3649

mc16_13TeV.301054.PowhegPythia8EvtGen_AZNLOCTEQ6L1_DYtautau_3000M3500.recon.AOD.e3649

mc16_13TeV.301055.PowhegPythia8EvtGen_AZNLOCTEQ6L1_DYtautau_3500M4000.recon.AOD.e3649

mc16_13TeV.301056.PowhegPythia8EvtGen_AZNLOCTEQ6L1_DYtautau_4000M4500.recon.AOD.e3649

mc16_13TeV.301057.PowhegPythia8EvtGen_AZNLOCTEQ6L1_DYtautau_4500M5000.recon.AOD.e3649

mc16_13TeV.301058.PowhegPythia8EvtGen_AZNLOCTEQ6L1_DYtautau_5000M.recon.AOD.e3649

mc16_13TeV.361108.PowhegPythia8EvtGen_AZNLOCTEQ6L1_Ztautau.recon.AOD.e3601

$W \to \tau\nu$+jets

mc16_13TeV.364184.Sherpa_221_NNPDF30NNLO_Wtaunu_MAXHTPTV0_70_CVetoBVeto.recon.AOD.e5340

mc16_13TeV.364185.Sherpa_221_NNPDF30NNLO_Wtaunu_MAXHTPTV0_70_CFilterBVeto.recon.AOD.e5340

mc16_13TeV.364186.Sherpa_221_NNPDF30NNLO_Wtaunu_MAXHTPTV0_70_BFilter.recon.AOD.e5340

mc16_13TeV.364187.Sherpa_221_NNPDF30NNLO_Wtaunu_MAXHTPTV70_140_CVetoBVeto.recon.AOD.e5340

mc16_13TeV.364188.Sherpa_221_NNPDF30NNLO_Wtaunu_MAXHTPTV70_140_CFilterBVeto.recon.AOD.e5340

mc16_13TeV.364189.Sherpa_221_NNPDF30NNLO_Wtaunu_MAXHTPTV70_140_BFilter.recon.AOD.e5340
mc16_13TeV.364190.Sherpa_221_NNPDF30NNLO_Wtaunu_MAXHTPTV140_280_CVetoBVeto.recon.AOD.e5340
mc16_13TeV.364191.Sherpa_221_NNPDF30NNLO_Wtaunu_MAXHTPTV140_280_CFilterBVeto.recon.AOD.e5340
mc16_13TeV.364192.Sherpa_221_NNPDF30NNLO_Wtaunu_MAXHTPTV140_280_BFilter.recon.AOD.e5340
mc16_13TeV.364193.Sherpa_221_NNPDF30NNLO_Wtaunu_MAXHTPTV280_500_CVetoBVeto.recon.AOD.e5340
mc16_13TeV.364194.Sherpa_221_NNPDF30NNLO_Wtaunu_MAXHTPTV280_500_CFilterBVeto.recon.AOD.e5340
mc16_13TeV.364195.Sherpa_221_NNPDF30NNLO_Wtaunu_MAXHTPTV280_500_BFilter.recon.AOD.e5340
mc16_13TeV.364196.Sherpa_221_NNPDF30NNLO_Wtaunu_MAXHTPTV500_1000.recon.AOD.e5340
mc16_13TeV.364197.Sherpa_221_NNPDF30NNLO_Wtaunu_MAXHTPTV1000_E_CMS.recon.AOD.e5340

$t\bar{t}$, single top

mc16_13TeV.410470.PhPy8EG_A14_ttbar_hdamp258p75_nonallhad.recon.AOD.e6337
mc16_13TeV.410471.PhPy8EG_A14_ttbar_hdamp258p75_allhad.recon.AOD.e6337
mc16_13TeV.410472.PhPy8EG_A14_ttbar_hdamp258p75_dil.recon.AOD.e6348
mc16_13TeV.410644.PowhegPythia8EvtGen_A14_singletop_schan_lept_top.recon.AOD.e6527
mc16_13TeV.410645.PowhegPythia8EvtGen_A14_singletop_schan_lept_antitop.recon.AOD.e6527
mc16_13TeV.410646.PowhegPythia8EvtGen_A14_Wt_DR_inclusive_top.recon.AOD.e6552
mc16_13TeV.410647.PowhegPythia8EvtGen_A14_Wt_DR_inclusive_antitop.recon.AOD.e6552
mc16_13TeV.410658.PhPy8EG_A14_tchan_BW50_lept_top.recon.AOD.e6671
mc16_13TeV.410659.PhPy8EG_A14_tchan_BW50_lept_antitop.recon.AOD.e6671

Others

mc16_13TeV.301000.PowhegPythia8EvtGen_AZNLOCTEQ6L1_DYee_120M180.recon.AOD.e3649
mc16_13TeV.301001.PowhegPythia8EvtGen_AZNLOCTEQ6L1_DYee_180M250.recon.AOD.e3649
mc16_13TeV.301002.PowhegPythia8EvtGen_AZNLOCTEQ6L1_DYee_250M400.recon.AOD.e3649
mc16_13TeV.301003.PowhegPythia8EvtGen_AZNLOCTEQ6L1_DYee_400M600.recon.AOD.e3649
mc16_13TeV.301004.PowhegPythia8EvtGen_AZNLOCTEQ6L1_DYee_600M800.recon.AOD.e3649
mc16_13TeV.301005.PowhegPythia8EvtGen_AZNLOCTEQ6L1_DYee_800M1000.recon.AOD.e3649
mc16_13TeV.301006.PowhegPythia8EvtGen_AZNLOCTEQ6L1_DYee_1000M1250.recon.AOD.e3649
mc16_13TeV.301007.PowhegPythia8EvtGen_AZNLOCTEQ6L1_DYee_1250M1500.recon.AOD.e3649
mc16_13TeV.301008.PowhegPythia8EvtGen_AZNLOCTEQ6L1_DYee_1500M1750.recon.AOD.e3649
mc16_13TeV.301009.PowhegPythia8EvtGen_AZNLOCTEQ6L1_DYee_1750M2000.recon.AOD.e3649
mc16_13TeV.301010.PowhegPythia8EvtGen_AZNLOCTEQ6L1_DYee_2000M2250.recon.AOD.e3649
mc16_13TeV.301011.PowhegPythia8EvtGen_AZNLOCTEQ6L1_DYee_2250M2500.recon.AOD.e3649
mc16_13TeV.301012.PowhegPythia8EvtGen_AZNLOCTEQ6L1_DYee_2500M2750.recon.AOD.e3649
mc16_13TeV.301013.PowhegPythia8EvtGen_AZNLOCTEQ6L1_DYee_2750M3000.recon.AOD.e3649
mc16_13TeV.301014.PowhegPythia8EvtGen_AZNLOCTEQ6L1_DYee_3000M3500.recon.AOD.e3649
mc16_13TeV.301015.PowhegPythia8EvtGen_AZNLOCTEQ6L1_DYee_3500M4000.recon.AOD.e3649
mc16_13TeV.301016.PowhegPythia8EvtGen_AZNLOCTEQ6L1_DYee_4000M4500.recon.AOD.e3649
mc16_13TeV.301017.PowhegPythia8EvtGen_AZNLOCTEQ6L1_DYee_4500M5000.recon.AOD.e3649
mc16_13TeV.301018.PowhegPythia8EvtGen_AZNLOCTEQ6L1_DYee_5000M.recon.AOD.e3649
mc16_13TeV.301020.PowhegPythia8EvtGen_AZNLOCTEQ6L1_DYmumu_120M180.recon.AOD.e3649
mc16_13TeV.301021.PowhegPythia8EvtGen_AZNLOCTEQ6L1_DYmumu_180M250.recon.AOD.e3649
mc16_13TeV.301022.PowhegPythia8EvtGen_AZNLOCTEQ6L1_DYmumu_250M400.recon.AOD.e3649

```
mc16_13TeV.301023.PowhegPythia8EvtGen_AZNLOCTEQ6L1_DYmumu_400M600.recon.AOD.e3649
mc16_13TeV.301024.PowhegPythia8EvtGen_AZNLOCTEQ6L1_DYmumu_600M800.recon.AOD.e3649
mc16_13TeV.301025.PowhegPythia8EvtGen_AZNLOCTEQ6L1_DYmumu_800M1000.recon.AOD.e3649
mc16_13TeV.301026.PowhegPythia8EvtGen_AZNLOCTEQ6L1_DYmumu_1000M1250.recon.AOD.e3649
mc16_13TeV.301027.PowhegPythia8EvtGen_AZNLOCTEQ6L1_DYmumu_1250M1500.recon.AOD.e3649
mc16_13TeV.301028.PowhegPythia8EvtGen_AZNLOCTEQ6L1_DYmumu_1500M1750.recon.AOD.e3649
mc16_13TeV.301029.PowhegPythia8EvtGen_AZNLOCTEQ6L1_DYmumu_1750M2000.recon.AOD.e3649
mc16_13TeV.301030.PowhegPythia8EvtGen_AZNLOCTEQ6L1_DYmumu_2000M2250.recon.AOD.e3649
mc16_13TeV.301031.PowhegPythia8EvtGen_AZNLOCTEQ6L1_DYmumu_2250M2500.recon.AOD.e3649
mc16_13TeV.301032.PowhegPythia8EvtGen_AZNLOCTEQ6L1_DYmumu_2500M2750.recon.AOD.e3649
mc16_13TeV.301033.PowhegPythia8EvtGen_AZNLOCTEQ6L1_DYmumu_2750M3000.recon.AOD.e3649
mc16_13TeV.301034.PowhegPythia8EvtGen_AZNLOCTEQ6L1_DYmumu_3000M3500.recon.AOD.e3649
mc16_13TeV.301035.PowhegPythia8EvtGen_AZNLOCTEQ6L1_DYmumu_3500M4000.recon.AOD.e3649
mc16_13TeV.301036.PowhegPythia8EvtGen_AZNLOCTEQ6L1_DYmumu_4000M4500.recon.AOD.e3649
mc16_13TeV.301037.PowhegPythia8EvtGen_AZNLOCTEQ6L1_DYmumu_4500M5000.recon.AOD.e3649
mc16_13TeV.301038.PowhegPythia8EvtGen_AZNLOCTEQ6L1_DYmumu_5000M.recon.AOD.e3649
mc16_13TeV.361106.PowhegPythia8EvtGen_AZNLOCTEQ6L1_Zee.recon.AOD.e3601
mc16_13TeV.361107.PowhegPythia8EvtGen_AZNLOCTEQ6L1_Zmumu.recon.AOD.e3601
mc16_13TeV.363355.Sherpa_221_NNPDF30NNLO_ZqqZvv.recon.AOD.e5525
mc16_13TeV.363356.Sherpa_221_NNPDF30NNLO_ZqqZll.recon.AOD.e5525
mc16_13TeV.363357.Sherpa_221_NNPDF30NNLO_WqqZvv.recon.AOD.e5525
mc16_13TeV.363358.Sherpa_221_NNPDF30NNLO_WqqZll.recon.AOD.e5525
mc16_13TeV.363359.Sherpa_221_NNPDF30NNLO_WpqqWmlv.recon.AOD.e5583
mc16_13TeV.363360.Sherpa_221_NNPDF30NNLO_WplvWmqq.recon.AOD.e5983
mc16_13TeV.363489.Sherpa_221_NNPDF30NNLO_WlvZqq.recon.AOD.e5525
mc16_13TeV.364250.Sherpa_222_NNPDF30NNLO_llll.recon.AOD.e5894
mc16_13TeV.364253.Sherpa_222_NNPDF30NNLO_lllv.recon.AOD.e5916
mc16_13TeV.364254.Sherpa_222_NNPDF30NNLO_llvv.recon.AOD.e5916
mc16_13TeV.364255.Sherpa_222_NNPDF30NNLO_lvvv.recon.AOD.e5916
mc16_13TeV.364156.Sherpa_221_NNPDF30NNLO_Wmunu_MAXHTPTV0_70_CVetoBVeto.recon.AOD.e5340
mc16_13TeV.364157.Sherpa_221_NNPDF30NNLO_Wmunu_MAXHTPTV0_70_CFilterBVeto.recon.AOD.e5340
mc16_13TeV.364158.Sherpa_221_NNPDF30NNLO_Wmunu_MAXHTPTV0_70_BFilter.recon.AOD.e5340
mc16_13TeV.364159.Sherpa_221_NNPDF30NNLO_Wmunu_MAXHTPTV70_140_CVetoBVeto.recon.AOD.e5340
mc16_13TeV.364160.Sherpa_221_NNPDF30NNLO_Wmunu_MAXHTPTV70_140_CFilterBVeto.recon.AOD.e5340
mc16_13TeV.364161.Sherpa_221_NNPDF30NNLO_Wmunu_MAXHTPTV70_140_BFilter.recon.AOD.e5340
mc16_13TeV.364162.Sherpa_221_NNPDF30NNLO_Wmunu_MAXHTPTV140_280_CVetoBVeto.recon.AOD.e5340
mc16_13TeV.364163.Sherpa_221_NNPDF30NNLO_Wmunu_MAXHTPTV140_280_CFilterBVeto.recon.AOD.e5340
mc16_13TeV.364164.Sherpa_221_NNPDF30NNLO_Wmunu_MAXHTPTV140_280_BFilter.recon.AOD.e5340
mc16_13TeV.364165.Sherpa_221_NNPDF30NNLO_Wmunu_MAXHTPTV280_500_CVetoBVeto.recon.AOD.e5340
mc16_13TeV.364166.Sherpa_221_NNPDF30NNLO_Wmunu_MAXHTPTV280_500_CFilterBVeto.recon.AOD.e5340
mc16_13TeV.364167.Sherpa_221_NNPDF30NNLO_Wmunu_MAXHTPTV280_500_BFilter.recon.AOD.e5340
mc16_13TeV.364168.Sherpa_221_NNPDF30NNLO_Wmunu_MAXHTPTV500_1000.recon.AOD.e5340
mc16_13TeV.364169.Sherpa_221_NNPDF30NNLO_Wmunu_MAXHTPTV1000_E_CMS.recon.AOD.e5340
```

```
mc16_13TeV.364170.Sherpa_221_NNPDF30NNLO_Wenu_MAXHTPTV0_70_CVetoBVeto.recon.AOD.e5340
mc16_13TeV.364171.Sherpa_221_NNPDF30NNLO_Wenu_MAXHTPTV0_70_CFilterBVeto.recon.AOD.e5340
mc16_13TeV.364172.Sherpa_221_NNPDF30NNLO_Wenu_MAXHTPTV0_70_BFilter.recon.AOD.e5340
mc16_13TeV.364173.Sherpa_221_NNPDF30NNLO_Wenu_MAXHTPTV70_140_CVetoBVeto.recon.AOD.e5340
mc16_13TeV.364174.Sherpa_221_NNPDF30NNLO_Wenu_MAXHTPTV70_140_CFilterBVeto.recon.AOD.e5340
mc16_13TeV.364175.Sherpa_221_NNPDF30NNLO_Wenu_MAXHTPTV70_140_BFilter.recon.AOD.e5340
mc16_13TeV.364176.Sherpa_221_NNPDF30NNLO_Wenu_MAXHTPTV140_280_CVetoBVeto.recon.AOD.e5340
mc16_13TeV.364177.Sherpa_221_NNPDF30NNLO_Wenu_MAXHTPTV140_280_CFilterBVeto.recon.AOD.e5340
mc16_13TeV.364178.Sherpa_221_NNPDF30NNLO_Wenu_MAXHTPTV140_280_BFilter.recon.AOD.e5340
mc16_13TeV.364179.Sherpa_221_NNPDF30NNLO_Wenu_MAXHTPTV280_500_CVetoBVeto.recon.AOD.e5340
mc16_13TeV.364180.Sherpa_221_NNPDF30NNLO_Wenu_MAXHTPTV280_500_CFilterBVeto.recon.AOD.e5340
mc16_13TeV.364181.Sherpa_221_NNPDF30NNLO_Wenu_MAXHTPTV280_500_BFilter.recon.AOD.e5340
mc16_13TeV.364182.Sherpa_221_NNPDF30NNLO_Wenu_MAXHTPTV500_1000.recon.AOD.e5340
mc16_13TeV.364183.Sherpa_221_NNPDF30NNLO_Wenu_MAXHTPTV1000_E_CMS.recon.AOD.e5340
```

APPENDIX D

Improvements to the search for BSM $A/H/Z' \to \tau\tau$ in the fully hadronic decay channel

D.1. MC samples

This section contains a list of the MC samples used in the analysis that are not listed in C.5. The following file endings were omitted:

- mc16a: _s3126_r9364
- mc16d: _s3126_r10201
- mc16e: _s3126_r10724

LO $Z/\gamma^* \to \tau\tau$

```
mc16_13TeV.800302.Py8EG_A14NNPDF23LO_DYtautau_120MLL180.deriv.DAOD_HIGG4D4.e8118
mc16_13TeV.800303.Py8EG_A14NNPDF23LO_DYtautau_180MLL250.deriv.DAOD_HIGG4D4.e8118
mc16_13TeV.800304.Py8EG_A14NNPDF23LO_DYtautau_250MLL400.deriv.DAOD_HIGG4D4.e8118
mc16_13TeV.800305.Py8EG_A14NNPDF23LO_DYtautau_400MLL600.deriv.DAOD_HIGG4D4.e8118
mc16_13TeV.800306.Py8EG_A14NNPDF23LO_DYtautau_600MLL800.deriv.DAOD_HIGG4D4.e8118
mc16_13TeV.800307.Py8EG_A14NNPDF23LO_DYtautau_800MLL1000.deriv.DAOD_HIGG4D4.e8118
mc16_13TeV.800308.Py8EG_A14NNPDF23LO_DYtautau_1000MLL1250.deriv.DAOD_HIGG4D4.e8118
mc16_13TeV.800309.Py8EG_A14NNPDF23LO_DYtautau_1250MLL1500.deriv.DAOD_HIGG4D4.e8118
mc16_13TeV.800310.Py8EG_A14NNPDF23LO_DYtautau_1500MLL1750.deriv.DAOD_HIGG4D4.e8118
mc16_13TeV.800311.Py8EG_A14NNPDF23LO_DYtautau_1750MLL2000.deriv.DAOD_HIGG4D4.e8118
mc16_13TeV.800312.Py8EG_A14NNPDF23LO_DYtautau_2000MLL2250.deriv.DAOD_HIGG4D4.e8118
mc16_13TeV.800313.Py8EG_A14NNPDF23LO_DYtautau_2250MLL2500.deriv.DAOD_HIGG4D4.e8118
```

```
mc16_13TeV.800314.Py8EG_A14NNPDF23LO_DYtautau_2500MLL2750.deriv.DAOD_HIGG4D4.e8118
mc16_13TeV.800315.Py8EG_A14NNPDF23LO_DYtautau_2750MLL3000.deriv.DAOD_HIGG4D4.e8118
mc16_13TeV.800316.Py8EG_A14NNPDF23LO_DYtautau_3000MLL3500.deriv.DAOD_HIGG4D4.e8118
mc16_13TeV.800317.Py8EG_A14NNPDF23LO_DYtautau_3500MLL4000.deriv.DAOD_HIGG4D4.e8118
mc16_13TeV.800318.Py8EG_A14NNPDF23LO_DYtautau_4000MLL4500.deriv.DAOD_HIGG4D4.e8118
mc16_13TeV.800319.Py8EG_A14NNPDF23LO_DYtautau_4500MLL5000.deriv.DAOD_HIGG4D4.e8118
mc16_13TeV.800320.Py8EG_A14NNPDF23LO_DYtautau_5000MLL.deriv.DAOD_HIGG4D4.e8118
```

D.2. Fake rates

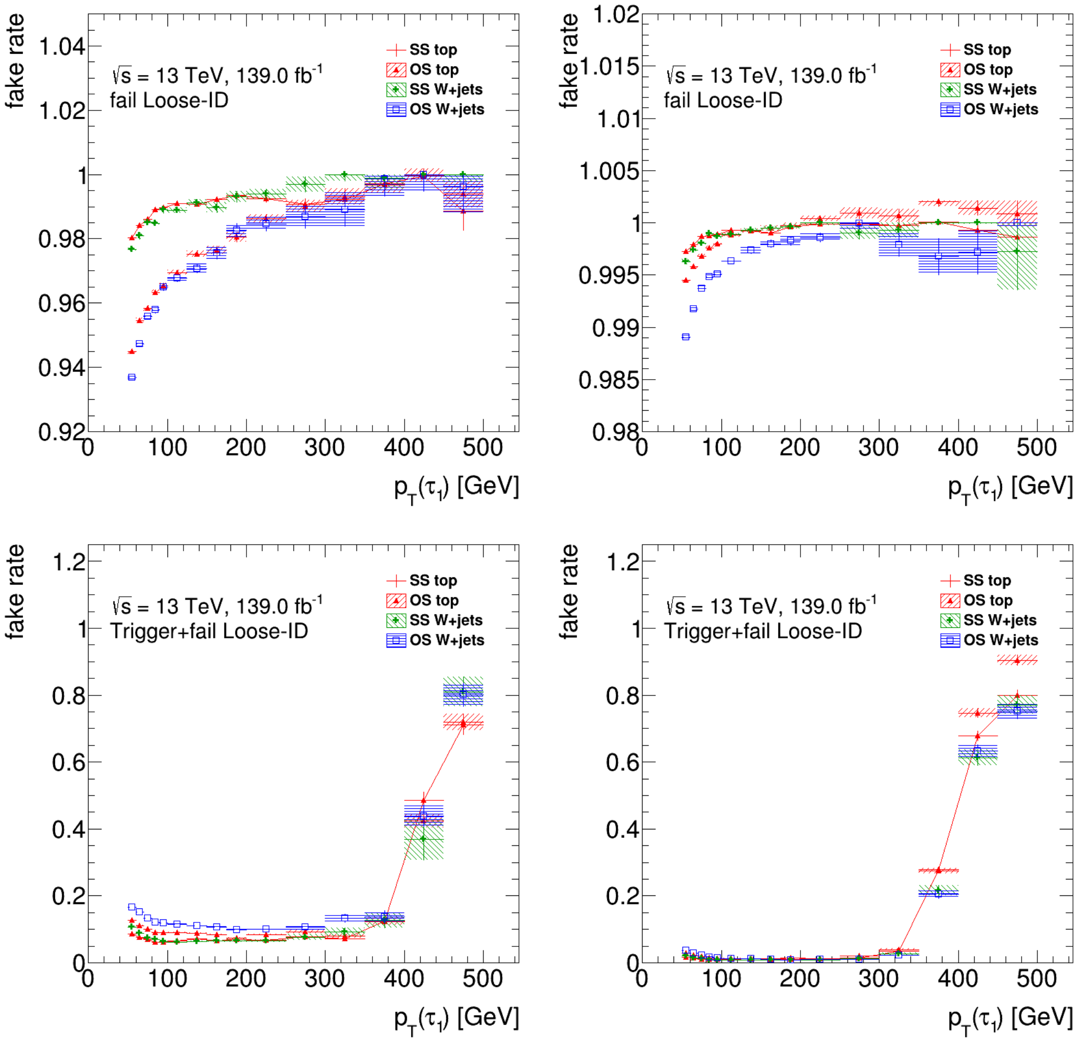

Figure D.1.: Fake rates measured in the $W(\rightarrow \mu\nu)$+jets and top control regions in data for the *fail-loose* working point (top) and the *fail-loose* working point including the trigger (bottom). It is split in 1-prong (left) and 3-prong (right) and according to the charge product of the tag and the probe.